

1 UNIVERSITY OF OKLAHOMA

2 GRADUATE COLLEGE

3 SEARCHING FOR SUPERSYMMETRIC PARTICLES AT THE LARGE HADRON

4 COLLIDER USING THE ATLAS DETECTOR

5 A DISSERTATION

6 SUBMITTED TO THE GRADUATE FACULTY

7 in partial fulfillment of the requirements for the

8 Degree of

9 DOCTOR OF PHILOSOPHY

10 By

11 OTHMANE RIFKI

12 Norman, Oklahoma

13 2016

¹⁴ SEARCHING FOR SUPERSYMMETRIC PARTICLES AT THE LARGE HADRON
¹⁵ COLLIDER USING THE ATLAS DETECTOR

¹⁶ A DISSERTATION APPROVED FOR THE
¹⁷ HOMER L. DODGE DEPARTMENT OF PHYSICS AND ASTRONOMY

¹⁸ BY

¹⁹ Dr. Brad Abbott, Chair

Dr. Peter Barker, Outside Member

Dr. Mike Strauss

Dr. Chung Kao

Dr. Eric Abraham

²⁰

²¹

© Copyright by OTHMANE RIFKI 2016
All Rights Reserved.

23 Table of Contents

24 Acknowledgments	vii
25 Abstract	viii
26 Preface	ix
27 1 Introduction	1
28 2 Theoretical Background	11
29 2.1 The Standard Model of Particle Physics	11
30 2.1.1 Quantum Chromodynamics	12
31 2.1.2 The Electroweak Theory	12
32 2.1.3 Limitations of the Standard Model	15
33 2.2 Supersymmetry	20
34 2.2.1 Principles of Supersymmetry	20
35 2.2.2 Supersymmetric Phenomenology	23
36 2.2.3 The Hierarchy Problem	27
37 2.3 Discovery at the LHC	28
38 3 Experimental Apparatus	31
39 3.1 The Large Hadron Collider	31
40 3.2 A Toroidal LHC Apparatus (ATLAS)	35
41 3.2.1 Co-ordinate System	36
42 3.2.2 Inner detector	37
43 3.2.3 Calorimeters	40
44 3.2.4 Muon System	43
45 3.3 ATLAS Trigger and Data Acquisition System	44
46 3.3.1 Hardware Trigger (L1)	46
47 3.3.2 Dataflow Challenges in Run-2	48
48 3.3.3 ATLAS Dataflow Design	49
49 3.4 ATLAS Operations	52
50 3.4.1 ATLAS Operation	52
51 3.5 Event Simulation	54
52 3.6 Reconstruction and Identification Techniques	57
53 3.6.1 Basic Principle	57
54 3.6.2 Electrons	61
55 3.6.3 Muons	63
56 3.6.4 Jets	65
57 3.6.5 Heavy flavor	67
58 3.6.6 Missing transverse momentum	67
59 4 The Region of Interest Builder	71
60 4.1 Overview	71
61 4.2 VMEbus based RoIB	72
62 4.2.1 Hardware implementation	72
63 4.2.2 System Performance and Evolution	74

64	4.3	PC based RoIB	75
65	4.3.1	The Common Readout Receiver Card	76
66	4.3.2	Readout System Firmware and Software	76
67	4.3.3	RoIB Software	79
68	4.4	Prototype Tests	79
69	4.4.1	Standalone Tests	80
70	4.4.2	Full System Tests	80
71	4.5	Online Performance in Run-2	83
72	5	Analysis Strategy	86
73	5.1	Overview	86
74	5.2	Benchmarking Models	88
75	5.3	Dataset and Simulated Event Samples	96
76	5.3.1	Collision Data	96
77	5.3.2	Simulated Event Samples	97
78	5.4	Event Selection	104
79	5.4.1	Pre-selection and event cleaning	104
80	5.4.2	Trigger strategy	106
81	5.4.3	Object definition	107
82	5.4.4	Data-MC comparisons	111
83	5.5	Signal Regions	112
84	5.6	Analysis Acceptance and Efficiency	117
85	6	Data-driven Background Estimation Techniques	130
86	6.1	The problem of fakes	130
87	6.2	Common processes for faking leptons	131
88	6.3	The Monte Carlo Template Method	133
89	6.3.1	Motivation	133
90	6.3.2	Description of the method	134
91	6.3.3	Correction factors	135
92	6.3.4	Control regions	136
93	6.4	Matrix Method	138
94	6.4.1	Events with one object	141
95	6.4.2	Dynamic matrix method	143
96	6.4.3	Propagation of uncertainties	148
97	7	Background Estimation	149
98	7.1	Overview	149
99	7.2	Irreducible Backgrounds	149
100	7.2.1	Expected yields in the signal regions	149
101	7.2.2	Validation regions	150
102	7.2.3	Validation of irreducible background estimates	155
103	7.3	Reducible Backgrounds	156
104	7.3.1	Charge-flip Background	157
105	7.3.2	Matrix Method	165
106	7.3.3	MC Template Method	178
107	7.3.4	Reducible Background Validation	180
108	7.4	Systematic uncertainties	184

109	7.4.1 Theoretical Uncertainties	185
110	7.4.2 Experimental Uncertainties	187
111	8 Statistical Treatment	201
112	8.1 Likelihood Function	202
113	8.2 Limit Setting Procedure	204
114	8.2.1 Profile Likelihood Ratio	204
115	8.2.2 The p -value	205
116	8.2.3 The CL_s Prescription	207
117	8.2.4 Approximate Sampling Distributions	209
118	8.3 Statistical Implementation	211
119	9 Results and Interpretation	212
120	9.1 Predictions and Observations	212
121	9.2 Statistical Interpretation	215
122	9.2.1 Model independent discovery and upper limits	218
123	9.2.2 Model dependent exclusion limits	218
124	10 Conclusions	227
125	A Auxiliary material	228
126	A.1 Signal region with best exclusion	228
127	A.2 Upper limit on cross section	230
128	A.3 Signal region cutflow	231
129	A.4 Acceptance and Efficiency	231
130	References	249

¹³¹ Acknowledgments

¹³² I would like to acknowledge...

¹³³ **Abstract**

¹³⁴ My abstract ...

¹³⁵ Preface

¹³⁶ My preface here...

¹³⁷ Over the past five years, I have always been asked by family, friends, and
¹³⁸ people I meet, what do you do. I have written the introduction with a general
¹³⁹ audience in mind to answer this question.

¹⁴⁰ **Chapter 1**

¹⁴¹ **Introduction**

¹⁴² **Historical Background**

¹⁴³ Of what is the universe made? A question that has intrigued the human curiosity
¹⁴⁴ since the dawn of time. Today, we are confident that we do not know the answer
¹⁴⁵ to this question. However, a lot of progress has been made with the aim of
¹⁴⁶ reducing the diversity of the physical phenomena observed around us to a limited
¹⁴⁷ number of constituents following fundamental principles. Over two thousands
¹⁴⁸ years ago, the ancient Greeks postulated that all is made of Earth, Air, Fire
¹⁴⁹ and Water. Fast-forward to the end of the 19th century, Mendeleev and others
¹⁵⁰ made the astonishing remark that by organizing the relative atomic masses of
¹⁵¹ chemical elements, elements with similar chemical properties followed a pattern.
¹⁵² The periodic table of elements was born. The predictive power of the periodic
¹⁵³ table led to the anticipation of new elements that were later discovered. However,
¹⁵⁴ the table lacked compactness and necessitated a more fundamental underlying
¹⁵⁵ structure that could connect the different elements together.

¹⁵⁶ At the turn of the 20th century, several important discoveries established the
¹⁵⁷ existence of the atom and its constituents. The atom was formed by electrons
¹⁵⁸ bound via the electromagnetic force to a nucleus, where nearly all the mass
¹⁵⁹ resides. The nucleus itself is formed from protons and neutrons that are “glued”
¹⁶⁰ together by the strong nuclear force (or strong force). These elements formed the
¹⁶¹ underlying substructure that explained qualitatively the systematic organization

162 of the periodic table. Moreover, quantum ideas were applied to the atom offering a
 163 quantitative description of the origin of structure in atoms and molecules, including
 164 the chemical elements and their properties. The decades that followed refined
 165 our understanding of the composition of matter through a series of experimental
 166 results. By studying the collisions of protons and neutrons in the 1950's and
 167 1960's, a plethora of new particles were discovered which belonged to the same
 168 family as the proton and neutron, called *hadrons*. These particles could not all
 169 be elementary ¹. By invoking the same argument that atoms were composite
 170 based on Mendeleev's table, a new layer of structure was unfolded to reveal the
 171 existence of *quarks* as basic constituents of all hadrons. Six types of quarks were
 172 discovered over the years with the latest, the top quark, being the most massive
 173 elementary particle discovered at Fermilab in Chicago, Illinois in 1995 [1, 2].

174 The observation of the continuous energy spectra in the radioactive β decay of
 175 nuclei led to the discovery of neutrinos to remedy the energy conservation law in the
 176 decay. Neutrinos are very light neutral particles that interact via the weak nuclear
 177 force responsible for radioactivity and nuclear fusion, the process that powers the
 178 stars. Electrons and neutrinos had other relatives collectively called *leptons*. The
 179 quarks and leptons are referred to as *fermions* and have a half integer spin, an
 180 intrinsic property of elementary particles. The strong, weak, and electromagnetic
 181 interactions are mediated by gluons, W and Z bosons, and photons, respectively.
 182 These particles have an integer spin and are called *bosons*. The latest addition
 183 to the known elementary particles happened in 2012 with the discovery of a new

¹Elementary particles refer to particles that cannot be decomposed into further constituents.

¹⁸⁴ boson, the Higgs boson, that allows the quarks and leptons and the W and Z
¹⁸⁵ bosons to acquire mass[3, 4].

¹⁸⁶ The Standard Model

¹⁸⁷ The physics of elementary particles became the most ambitious and organized
¹⁸⁸ attempt to answer the question of what the universe is made out of. Through a
¹⁸⁹ mixture of both theoretical insight and experimental input, we now know that
¹⁹⁰ everything we see in our daily life is formed from quarks and leptons that interact
¹⁹¹ via the strong, weak, and electromagnetic forces.² The forms of these forces are
¹⁹² determined from basic principles of symmetry and invariance. As a result, a
¹⁹³ theoretical framework was constructed to synthesize all these developments in a
¹⁹⁴ quantitative calculational tool that became known as the *standard model of particle*
¹⁹⁵ *physics* (SM). The only inputs needed by the SM are the interaction strengths of
¹⁹⁶ the forces and quark and lepton masses to make very accurate predictions about
¹⁹⁷ the behavior of elementary particles. Over the past 30 years, the SM has been
¹⁹⁸ vigorously tested by many experiments and has been shown to accurately describe
¹⁹⁹ particle interactions at the highest energies produced in the laboratory. Yet, we
²⁰⁰ know it is not the complete story.

²⁰¹ Limitations

²⁰² In 1933, an observation of the Coma Cluster by Zwicky suggested that the
²⁰³ galaxies in the cluster were moving too fast to be explained by the luminous

² The fourth fundamental force of gravity is extremely weak and only acts at the macroscopic scale.

matter present[5]. The same observation was repeated when looking at the rotation speeds of individual galaxies which suggested a dark component of mass, dark matter. The experimental evidence established that dark matter is not made out of baryons and is more abundant than ordinary matter. For example, anisotropies in the cosmic microwave background, a radiation left over from the Big Bang, were consistent with quantum fluctuations from an inflationary epoch [6, 7]. These fluctuations encoded details about the density of matter in the form of cosmological parameters as they traveled through space and time to reach our experiments. The astonishing conclusion was that the universe has nearly five times as much dark matter as ordinary matter [8]. The supernovae surveys gave direct evidence for an accelerating universe [9], a view that was cemented by the measurement of cosmological parameters [10, 11] which led to the startling discovery that most of the energy density of the universe is in the form of an unknown negative-pressure, called dark energy [12]. There is an extensive program of experiments which will probe the dark energy. Astrophysics and cosmology told us about the existence of dark matter and measured its density to a remarkable precision. Particle physics holds the hope to uncover what dark matter is. In short, all experimental evidence are consistent with a universe constructed of

• baryons (everyday matter): $\sim 5\%$

• dark matter: $\sim 20\%$

• dark energy: $\sim 75\%$

• neutrinos, photons: a tiny fraction

²²⁶ Today, we are in front of many puzzles related to our view of the universe.

²²⁷ Everything we know of, namely all particles of the standard model, constitutes

²²⁸ only 5% of the energy budget of the universe. The universe is also predominately

²²⁹ composed of matter as opposed to anti-matter even though at the start of the

²³⁰ universe, they were in equal amounts. The standard model describes the content

²³¹ of everyday matter and how it interacts but without telling us why it is that

²³² way. Moreover, the standard model only describes these phenomena up to an

²³³ energy scale of $\mathcal{O}(100)$ GeV, called the weak scale. Beyond this scale lies the

²³⁴ realm of phenomena not described by the standard model that extend all the way

²³⁵ to the Planck scale of $\mathcal{O}(10^{19})$ GeV. There is no mechanism to generate mass for

²³⁶ neutrinos in the standard model. Last but not least, the standard model does not

²³⁷ incorporate gravity, the fourth fundamental force. The SM is unable to account

²³⁸ for these observed features in the universe. Thus, there is a need for a theory

²³⁹ beyond the standard model.

²⁴⁰ Supersymmetry

²⁴¹ One of the most prominent extensions of the standard model, that addresses many

²⁴² of the shortcomings mentioned above, is a theory based on a new symmetry, called

²⁴³ supersymmetry. This symmetry is between the matter particles, fermions, and

²⁴⁴ particles whose exchange mediates the forces, bosons. Our current description of

²⁴⁵ the world treats fermions and bosons differently. Supersymmetry puts forward

²⁴⁶ the idea that fermions and bosons can be treated in a fully symmetric way. In

²⁴⁷ other words, if we exchange fermions and bosons in the equations of the theory,

248 the equations will still look the same. An immediate consequence of the theory is
 249 that every standard model particle will have a “superpartner.” As a result, we
 250 can design experiments to search for these supersymmetric particles. The work
 251 presented in this dissertation is about the search for supersymmetric particles
 252 with a specific signature. The many benefits of supersymmetry will be discussed
 253 later but here it is worth mentioning two important features of the theory: it
 254 unifies the three interactions, electromagnetic, strong, and weak forces, at very
 255 high energies and it provides a dark matter candidate particle. Now that we
 256 understand what we are trying to do, it is time to address the question of how to
 257 do it.

258 **Experimental techniques**

259 The human eye can resolve pieces of dust up to 10^{-5} m. The subatomic distances
 260 we are interested in probing range from 10^{-15} m, the size of a proton, down to
 261 10^{-18} m, the size of a quark. Instruments are needed to extend our senses to probe
 262 these very small scales. For instance, light microscopes can reveal the structure
 263 of things down to 10^{-6} m, the scale of bacteria and molecules. A special type of
 264 microscope is needed to probe smaller distances, a particle accelerator. The basic
 265 idea is that in order to see an object, a wave must scatter off this object and must
 266 have a wavelength smaller than the object being probed. Since particles have a
 267 wavelike character, they can be used to probe ever shorter distances according to

$$E = \frac{hc}{\lambda}$$

268 where E is the energy of the particle, λ is its wavelength, and $hc \sim 10^{-6} eVm$.
 269 As a result, the higher the speed of the particles, the greater their energy and
 270 momentum and the shorter their associated wavelength. Modern accelerators can
 271 generate energy in the TeV scale and thus probe a distance of 10^{-18} m. All the
 272 development that we have made describes phenomena happening at distances
 273 larger than about 10^{-18} m. Thus, it is possible that electrons and quarks have
 274 some structure which are beyond our ability to resolve in experiment. For this
 275 reason, we consider them as not having any deeper structure, i.e. they are called
 276 pointlike objects.

277 Over the last century, beams of particles were used to study the composition of
 278 matter. Initially, beams originated from phenomena that were already naturally
 279 occurring, such as alpha and beta particles coming from radioactive decays and
 280 cosmic rays. Some cosmic rays are much more energetic than what we can produce
 281 in the laboratory today, however, they occur at random and with a low intensity.
 282 Instead, high energy particle accelerators were used to deliver high intensity beams
 283 of electrons, protons, and other particles under controlled conditions. For this
 284 reason, particle physics is also known as high energy physics. By colliding two
 285 sufficiently energetic particles, new particles will be created according to Einstein's
 286 equation $E = mc^2$ (or more generally $E = \sqrt{(mc^2)^2 + (pc)^2}$), where energy can
 287 be exchanged for mass, and vice versa, the exchange rate being c^2 , the square
 288 of the speed of light. For example, an electron has a mass of 0.5 MeV and can
 289 only be created in an electron-positron pair, thus 1 MeV of energy is needed for
 290 an electron-positron pair to be produced at rest. Energies in the TeV range

291 were present about a billionth of a second after the Big Bang. In other words, by
 292 colliding high energy particles, it is possible to recreate momentarily conditions
 293 similar to those of the universe when it was newly born. At such energies, particles
 294 and antiparticles were created, including exotic forms no longer common today.
 295 Most of the particles generated in these collisions are extremely short lived with
 296 lifetimes less than 10^{-20} seconds, producing radiation and decaying to stable
 297 particles, such as electrons and quarks, that make up most of what we see today.
 298 One of the exotic forms of matter that may exist is supersymmetry. The search
 299 for evidence for supersymmetric particles using data collected at a high energy
 300 particle accelerator is the subject of this dissertation.

301 The Large Hadron Collider (LHC) is the world's most energetic particle
 302 accelerator and the pinnacle of colliding beam technology. Is it located at CERN,
 303 the European Laboratory for Particle Physics ³, near Geneva, Switzerland. The
 304 LHC accelerates counter rotating beams of protons (and even atomic nuclei) to
 305 99.9999991% the speed of light in a 27 km ring reaching an energy of 6.5 TeV per
 306 beam. The most important part of the design is the magnets, cooled by the
 307 largest cryogenic system in the world to 1.9 K (-271.3 °C), that keep the protons
 308 on track and bring the counter-rotating needle-like beams to meet head on 40
 309 million times per second. The debris of each collision fly off in all directions,
 310 briefly producing less common exotic forms of matter captured by large particle
 311 detectors in the form of “snapshots” of these collisions, called events. The teams

³ The acronym comes from French “Conseil Européen pour la Recherche Nucléaire” which was established to do fundamental physics research. In 1952, this research concentrated on understanding the atom and its nucleus, hence the word “nuclear”. Today, our knowledge goes deeper than the nucleus which motivates the modified name.

312 of scientists analyze these events to identify the different particles that were
313 produced and reconstruct the full collision process. With this information, it is
314 possible to make precision measurements of rare standard model processes, like the
315 production of the Higgs boson, or search for beyond the standard model physics,
316 like evidence for supersymmetry. ATLAS is one of the general-purpose particle
317 detectors at the LHC that supplied the events analyzed in this dissertation to
318 search for supersymmetry. The ATLAS detector is the largest-volume particle
319 detector ever built – the size of a seven-story building 46 meters high and 26
320 meters in diameter, weights 7000 tonnes, and able to measure particle trajectories
321 down to 0.01 meters. Bunches of protons pass through each other at the heart of
322 the ATLAS detector 40 million times per second. Each time they cross there are
323 on average 25 proton-proton collisions, leading to about a billion proton collisions
324 per second. The data generated in these collisions amounts to about 60 terabytes
325 per second, an amount far beyond what is technologically possible to store. In
326 fact, the processes of interest are extremely rare. For example, the Higgs boson is
327 produced once in 20 million million collisions. In more practical terms, a Higgs
328 boson might appear once a day during the LHC operations. ATLAS has a big
329 computational challenge to recognize this one Higgs event and record it to tape out
330 of 35 million million other collisions each day. The topic of this dissertation is to
331 search for supersymmetric particles that are even rarer and thus more challenging
332 to look for.

333 This dissertation will give a detailed explanation on how we searched for
334 supersymmetric particles using the ATLAS detector. First, the motivation behind

335 the work will begin with an overview of the standard model of particle physics
336 and supersymmetry in Chapter 2 followed by the design of the ATLAS detector at
337 the LHC in Chapter 3. The Region of Interest Builder that processes every event
338 recorded by ATLAS is covered in Chapter 4. The detailed description of the search
339 starts in Chapter 5 covering the basic analysis strategy and the supersymmetric
340 models considered. The most important part of the analysis is the estimation
341 of standard model and detector backgrounds with novel techniques developed
342 by the author and covered in Chapters 6 and 7. The statistical methodology
343 and interpretation of the results is presented in Chapters 8 and 9. This analysis
344 represents an important search for supersymmetric particles with the early data-
345 set collected by ATLAS at a new center of mass energy of 13TeV. The strength
346 of the search lies in exploring regions of the parameter space with a small mass
347 difference between the supersymmetric particles, regions that are difficult to probe
348 with other searches for new physics.

³⁴⁹ **Chapter 2**

³⁵⁰ **Theoretical Background**

³⁵¹ **2.1 The Standard Model of Particle Physics**

³⁵² The Standard Model (SM) of particle physics is a description of the physical world
³⁵³ around us in terms of fundamental particles and their interactions. The develop-
³⁵⁴ ment of the SM has been guided by both theoretical predictions and experimental
³⁵⁵ discoveries. The SM includes three of the four fundamental forces: electromag-
³⁵⁶ netism, the strong interaction, and the weak interaction. The mathematical
³⁵⁷ formalism used relies on quantum field theory.

³⁵⁸ The fundamental particles are represented by the states of quantized fields.

³⁵⁹ Quarks and leptons constitute matter and are associated with fields of half
³⁶⁰ integer spin, called fermion fields. The dynamics of the system is defined by the
³⁶¹ Lagrangian, \mathcal{L} , a quantity that describes the motion and excitations in the fields.

³⁶² The Lagrangian of the SM is invariant under spacetime dependent continuous
³⁶³ internal transformations of the group $SU(3) \times SU(2) \times U(1)$. This invariance is
³⁶⁴ called gauge invariance and is necessary to ensure that the theory is renormalizable.

³⁶⁵ The renormalizability condition guarantees the predictive power of the theory. To
³⁶⁶ preserve gauge invariance, additional quantum fields with spin one are required,
³⁶⁷ called gauge bosons. As a result, twelve gauge fields are required to write a gauge
³⁶⁸ invariant Lagrangian, eight for the generators of $SU(3)$, three for the generators
³⁶⁹ of $SU(2)$, and one for the $U(1)$ generator. The elements described are enough to

³⁷⁰ write down the Lagrangian of the SM.

³⁷¹ 2.1.1 Quantum Chromodynamics

³⁷² The $SU(3)$ gauge symmetry coupled to the quarks describes Quantum Chromo-
³⁷³ dynamics (QCD), the theory of strong interactions. The eight $SU(3)$ gauge fields
³⁷⁴ are associated to the different colored states of the gluon. The QCD Lagrangian
³⁷⁵ is given by

$$\mathcal{L}_{QCD} = -\frac{1}{4}G_{A\mu\nu}G_A^{\mu\nu} + \sum_{i=\text{flavors}} \bar{q}_i (iD - m_i) q_i, \quad (2.1)$$

³⁷⁶ where G 's are the gauge fields of QCD given by

$$G_{A\mu\nu} = \partial_\mu G_{A\nu} - \partial_\nu G_{A\mu} - g_S f_{ABC} G_{B\mu} G_{C\nu}, \quad (2.2)$$

³⁷⁷ and the covariant derivative, $D\mu$, defined as

$$D_\mu = \partial_\mu + ig_S \frac{\lambda_A}{2} G_{A\mu}, \quad (2.3)$$

³⁷⁸ where g_S is the strong coupling constant, and λ_A are the eight Gell-Mann matrices.
³⁷⁹ The indices of the quarks, $i = 1, 2, 3$, run over the colors: red, blue, green, and
³⁸⁰ their anticolors. While the indices of the gluons, $A, B, C = 1, \dots, 8$, correspond
³⁸¹ to the combinations of colors and anticolors. Color must be conserved in all
³⁸² QCD interactions, similar to the electric charge. Gluons have been observed
³⁸³ experimentally and interact with quarks as predicted by the SM [13].

³⁸⁴ 2.1.2 The Electroweak Theory

³⁸⁵ The $SU(2) \times U(1)$ gauge symmetry describes the electroweak theory that unifies
³⁸⁶ the electromagnetic and weak interactions. There are two problems with this

387 part of the SM. The four gauge fields of $SU(2)$ and $U(1)$ must be added without
 388 mass to preserve gauge invariance. However, the gauge bosons of the weak force
 389 have a large mass according to observation, and thus in direct contradiction with
 390 the prediction. In addition, the weak interaction violates parity where it couples
 391 differently to the left and right-handed quark and lepton helicity states. The
 392 solution is to treat the two helicity states of the leptons as different fields with
 393 different couplings. A fermion mass term in the Lagrangian would couple to
 394 these different fields but will break gauge invariance. Again to maintain gauge
 395 invariance, the fermion fields should be massless in direct contradiction with
 396 observation.

397 Both of the problems described can be resolved by introducing spontaneous
 398 symmetry breaking. The principle is to introduce new scalar fields with zero spin
 399 that couple to the electroweak $SU(2) \times U(1)$ gauge fields while preserving the
 400 gauge invariance of the Lagrangian. The form of the potential describing this new
 401 interaction is chosen in such a way that zero values of the fields do not correspond
 402 to the lowest energy state. As a consequence, the ground state of the field will
 403 “break” the $SU(2) \times U(1)$ symmetry even though the Lagrangian preserves it.
 404 The scalar fields will take a non-zero value, called the vacuum expectation value
 405 (vev), to allow the fermions and weak gauge bosons to appear as massive particles.
 406 A consequence of this mechanism is that one additional scalar field obtains mass
 407 and thus predicts a neutral massive spin zero particle, the Higgs boson.

408 The complete Lagrangian of the electroweak theory, including the mechanism

⁴⁰⁹ of electroweak symmetry breaking, can then be expressed as

$$\mathcal{L}_{EW} = \mathcal{L}_{\text{gauge}} + \mathcal{L}_{\text{matter}} + \mathcal{L}_{\text{Higgs}} + \mathcal{L}_{\text{Yukawa}}. \quad (2.4)$$

⁴¹⁰ The kinetic portion of the Lagrangian introduces the gauge isotriplet, $W_\mu^{i=1,2,3}$,

⁴¹¹ for $SU(2)$ and the gauge singlet, B_μ , of $U(1)$, in

$$\mathcal{L}_{\text{gauge}} = -\frac{1}{4} \mathbf{W}_{\mu\nu} \mathbf{W}^{\mu\nu} - B_{\mu\nu} B^{\mu\nu}, \quad (2.5)$$

⁴¹² where

$$\mathbf{W}^{\mu\nu} = \partial^\mu \mathbf{W}^\nu - \partial^\nu \mathbf{W}^\mu - g \mathbf{W}^\mu \times \mathbf{W}^\nu, \quad (2.6)$$

⁴¹³

$$B^{\mu\nu} = \partial^\mu B^\nu - \partial^\nu B^\mu \quad (2.7)$$

⁴¹⁴ and g is the $SU(2)$ gauge coupling constant. A linear superposition of the fields

⁴¹⁵ $W_\mu^{i=1,2,3}$ and B_μ lead to the SM W^\pm , Z , and photon. The matter Lagrangian is

$$\mathcal{L}_{\text{matter}} = i \bar{\psi} \not{D} \psi \quad (2.8)$$

⁴¹⁶ where the covariant derivative is defined as

$$D_\mu = \partial_\mu + ig \mathbf{W}_\mu \cdot \mathbf{T} + \frac{1}{2} ig' B_\mu Y. \quad (2.9)$$

⁴¹⁷ where g' is $U(1)$ gauge coupling constant, \mathbf{T} is the weak isospin, and Y is the

⁴¹⁸ weak hypercharge. The Higgs potential introduces a doublet of complex scalar

⁴¹⁹ fields, Φ , expressed as

$$\mathcal{L}_{\text{Higgs}} = (D\Phi)^\dagger (D\Phi) + \mu^2 \Phi^\dagger \Phi - \lambda (\Phi^\dagger \Phi)^2 \quad (2.10)$$

420

$$\Phi = \begin{pmatrix} \phi^+ \\ \phi^0 \end{pmatrix} \quad (2.11)$$

421 The shape of the Higgs potential is determined by the parameters μ and λ . If
 422 $\mu^2 < 0$, the Higgs field will acquire a set of identical minima with a vev of
 423 $v = -\frac{\mu^2}{2\lambda} \equiv \frac{v^2}{2}$. The physical mass of the Higgs particle in the SM is

$$m_h = \sqrt{-2\mu^2}, \quad (2.12)$$

424 observed by ATLAS and CMS in 2012 with a mass of
 425 $m_h = 125.09 \pm 0.24$ GeV [14, 15]. The Yukawa interactions are introduced to the
 426 Lagrangian manually to describe the interaction between the fermions and the
 427 Higgs field, expressed as

$$\mathcal{L}_{\text{Yukawa}} = \sum_{\text{generations}} \left[-\lambda_e \bar{L} \cdot \phi e_R - \lambda_d \bar{Q} \cdot \phi d_R - \lambda_u \epsilon^{ab} \bar{Q}_a \phi_b^\dagger u_R + h.c. \right] \quad (2.13)$$

428 where λ is the Yukawa coupling of the particular fermion, L and e_R are the lepton
 429 fields, Q , u_R , and d_R are the quark fields, ϵ^{ab} is the completely antisymmetric
 430 $SU(2)$ tensor with $\epsilon^{ab} = 1$

431 2.1.3 Limitations of the Standard Model

432 The SM has now been tested successfully over the past decades which validated
 433 its dynamics in the gauge sector and in the flavor structure. As an illustration
 434 of this remarkable achievement, Figure 2.1 shows the agreement between the
 435 SM total production cross section of several processes that spans twelve orders
 436 of magnitude, measured by ATLAS compared to theoretical expectations at 7

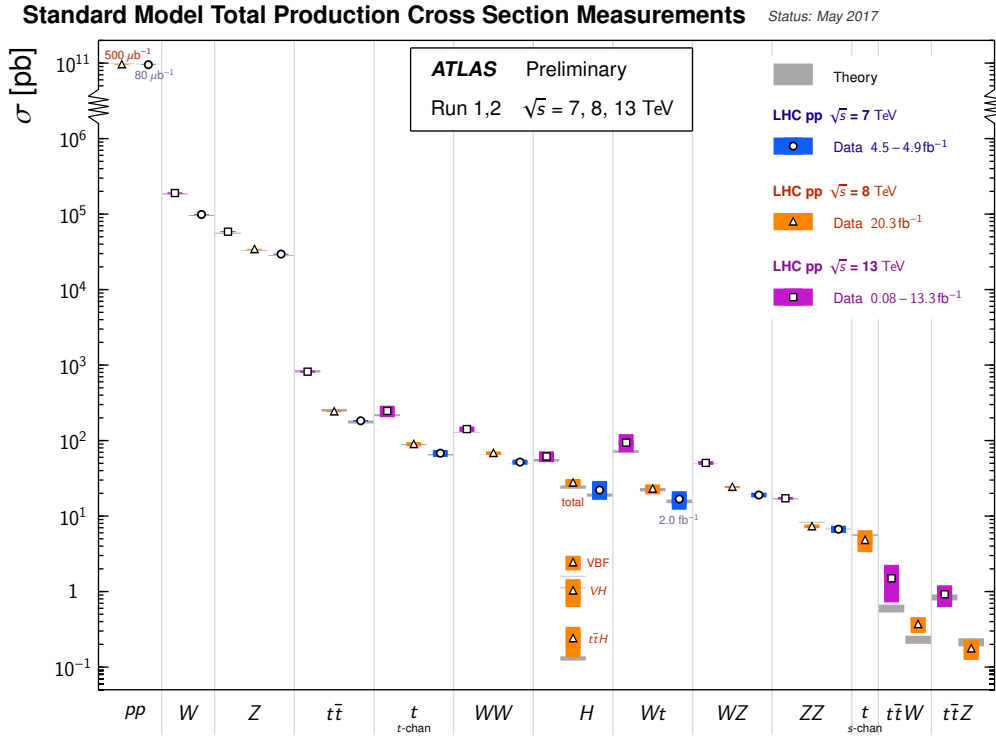


Figure 2.1: Summary of several Standard Model total production cross section measurements, corrected for leptonic branching fractions, compared to the corresponding theoretical expectations. All theoretical expectations were calculated at NLO or higher.

437 TeV, 8 TeV, and 13 TeV. The most obvious shortcoming is that the SM makes
 438 no attempt to include the fourth fundamental force of gravity. The reason
 439 is that the addition of the gravitational terms results in a theory that is not
 440 renormalizable, hence it loses its predictive power. In the energy regime explored
 441 by modern accelerators, the impact of gravity is negligible. However, these
 442 effects become important at the Planck scale that corresponds to energies of
 443 $E_{\text{Planck}} = m_{\text{Planck}} c^2 = \sqrt{\hbar c^5 / G_{\text{Newton}}} \sim 1.2 \times 10^{16} \text{ TeV}$ (the LHC reaches $\sqrt{s} = 13$
 444 TeV), which is well beyond our reach [16]. Putting this problem aside, there are

⁴⁴⁵ several problems in the energy range accessible to our accelerators:

⁴⁴⁶ • Dark matter: There is now overwhelming evidence for its existence; rotation

⁴⁴⁷ curves, Cosmic Microwave Background, primordial abundance of the light

⁴⁴⁸ elements, etc. Yet, the SM does not have a dark matter candidate[8].

⁴⁴⁹ • Baryon asymmetry: The ratio of matter to antimatter is asymmetric with

⁴⁵⁰ complete absence of antimatter except in cosmic rays. The asymmetry

⁴⁵¹ can be explained with the presence of CP - violating ¹ interactions. While

⁴⁵² the SM contains such CP violating terms in the form of the CKM matrix,

⁴⁵³ describing quark mixing, and the PMNS matrix, describing neutrino mixing,

⁴⁵⁴ the size of this effect is too small to account for the observed asymmetry

⁴⁵⁵ [17].

⁴⁶⁶ • Anomalous magnetic moment of the muon: The measurement of the mag-

⁴⁵⁷ netic moment anomaly $a_\mu = \frac{g-2}{2}$, where g is the gyromagnetic ratio of the

⁴⁵⁸ muon, deviates from the SM prediction by 3.3σ [18, 19].

⁴⁵⁹ • Neutrino masses: The direct consequence of the observation of solar and

⁴⁶⁰ atmospheric neutrino oscillations is that neutrinos are massive. The SM

⁴⁶¹ does not have a mechanism to include mass terms in its Lagrangian[20].

⁴⁶² These arguments are not considered flaws of the SM but rather limitations that

⁴⁶³ need to be overcome by adding new elements to the theory, i.e. new interactions

⁴⁶⁴ and new particles. None of the arguments mentioned address the question of

¹ CP refers to invariance under conjugation of (C) charge and (P) parity symmetries. The charge conjugation transforms a particle to its antiparticle while parity transforms the coordinate system to its mirror image.

465 the energy scale at which the new physics should appear. For this, we turn
 466 to the two known scales in physics: the scale of electroweak physics of $\mathcal{O}(10^2)$
 467 GeV and the scale of gravity of $\mathcal{O}(10^{19})$ GeV, also known as the Planck scale.
 468 The difference between the two scales is in the order of $\mathcal{O}(10^{16})$. Since the SM
 469 is a renormalizable theory, it can be effectively valid up to the Planck scale and
 470 used to evaluate radiative corrections to any precision. This causes a problem
 471 that can be best illustrated by calculating the mass of the Higgs boson in the SM.
 472 The physical mass of the Higgs boson ($m_{h,\text{physical}} \sim 125$ GeV) can be written as
 473 $m_{h,\text{physical}}^2 \simeq m_h^2 + \delta m_h^2$, where m_h is the Higgs mass parameter in the Lagrangian
 474 given in Eq.2.12, and δm_h is the one-loop radiative corrections obtained by
 evaluating the diagrams of Figure 2.2. The Higgs mass can then be expressed as

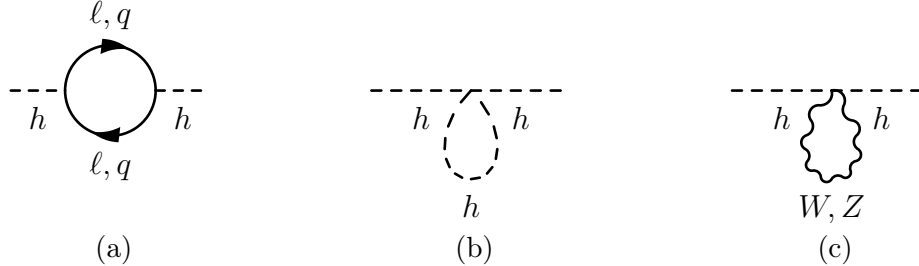


Figure 2.2: The one-loop contribution of (a) quarks and leptons, (b) Higgs bosons,
and (c) W, Z bosons to the mass of the Higgs bosons.

475

$$m_{h,\text{physical}}^2 \simeq m_h^2 + \frac{C}{16\pi^2} \Lambda^2, \quad (2.14)$$
 476 where the coefficient C embodies the various coupling constants of the SM². The
 477 diagrams contributing to the Higgs mass diverge quadratically with Λ , the cut-
 478 off scale at which the SM is no longer valid. If the diagrams do not mutually

²Expression can be found in equation (3) of [21].

479 compensate for one another, the cut-off of quadratic divergences, Λ , can be as
 480 high as the Planck scale ($\mathcal{O}(10^{18})$ GeV). In other words, the mass scale of the
 481 Higgs boson has to be of the order of the Planck scale, while the observation is
 482 sixteen orders of magnitude below. The mass parameter m_h must be “tuned” to
 483 cancel out this huge correction. This fine-tuning is regarded as *unnatural* and a
 484 sign of undiscovered principles that would explain this hierarchy paradox, known
 485 as the “hierarchy problem”. By requiring that the quantum corrections, encoded
 486 in the cut-off scale Λ , to be not too far off from the mass parameter m_h , we can
 487 make an educated guess that the SM can only be valid up to an energy scale
 of $\Lambda \sim \mathcal{O}(1)$ TeV as illustrated in Figure 2.3. This scale can be experimentally

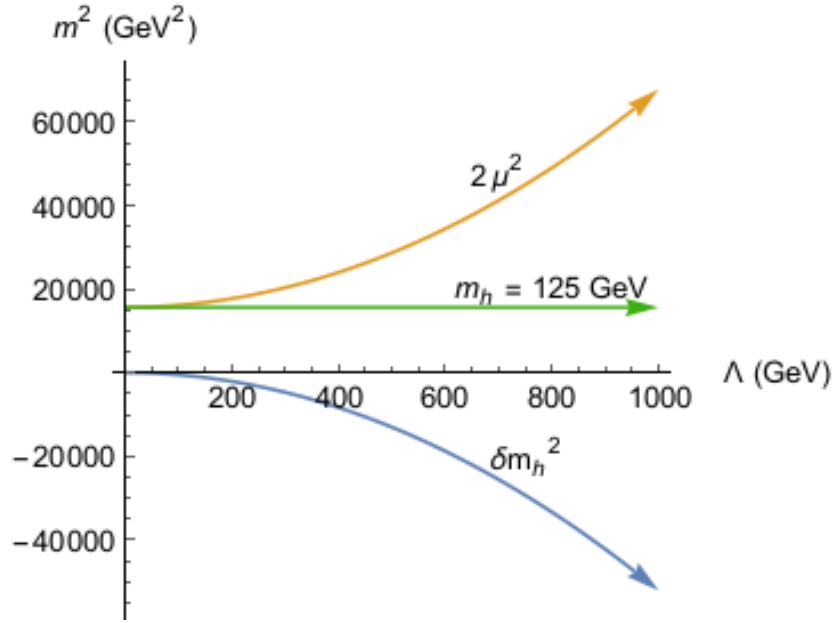


Figure 2.3: Illustration of how the Higgs mass parameter $m_h^2 = -2\mu^2$ needs
 to be adjusted to compensate for the quantum corrections δm_h^2 to ensure that
 $m_{h,\text{physical}} \sim 125$ GeV [22].

488
 489 probed with the LHC to verify if new physics exists. Hence, the work presented

⁴⁹⁰ in this dissertation is to search for new phenomena at this energy scale. It is time
⁴⁹¹ to address the model studied in this dissertation that would resolve the hierarchy
⁴⁹² problem and some of the other limitations of the SM described in this section.

⁴⁹³ 2.2 Supersymmetry

⁴⁹⁴ The hierarchy problem stated in the last section can be solved if the diagrams
⁴⁹⁵ of Figure 2.2 cancelled out. It is possible since the radiative contributions to
⁴⁹⁶ the Higgs mass coming from the fermion loop has a minus sign while the boson
⁴⁹⁷ loop contributes with a positive sign. By introducing a new symmetry between
⁴⁹⁸ fermions and bosons, directly linking matter and gauge fields, the diagrams can
⁴⁹⁹ mutually compensate one another. This new symmetry is called *supersymmetry*
⁵⁰⁰ and commonly referred to as SUSY. In this section, we describe briefly the
⁵⁰¹ principles of supersymmetry by focusing on the concepts rather than the technical
⁵⁰² implementation of the theory. We also cover the motivations for examining
⁵⁰³ supersymmetry and how it mitigates many of the problems of the SM. Last but
⁵⁰⁴ not least, we will cover the phenomenology of the theory and its implications in a
⁵⁰⁵ hadron collider like the LHC.

⁵⁰⁶ 2.2.1 Principles of Supersymmetry

⁵⁰⁷ The symmetries encountered in the SM are a direct product of the Poincare group
⁵⁰⁸ that encodes the symmetries of space-time (translations, rotations, and boosts)
⁵⁰⁹ and the internal symmetries ($SU(3) \times SU(2) \times U(1)$). These symmetries do not
⁵¹⁰ affect the space-time geometric properties of the transformed states. For instance,

511 an isotropic rotation can transform a neutron into a proton, preserving the same
 512 spin, but cannot transform a neutron into a pion, a particle with a different
 513 spin. Transformations of supersymmetry are very different in the sense that they
 514 directly associate fields of integer and half-integer spins, allowing fermions and
 515 bosons to be transformed into one another.

516 The development of the formalism of supersymmetry started with the famous
 517 no-go theorem from Coleman and Mandula [23] who showed that there is no
 518 non-trivial way to mix the space-time symmetry group with the internal symmetry
 519 group in four dimensions and maintain non-zero scattering amplitudes. In this
 520 theorem, only commuting symmetry generators were considered which describe
 521 bosonic generators with integer spin. Haag, Lopuszanski, and Sohnius generalized
 522 the theorem by extending the symmetry group to anticommutating generators that
 523 describe fermions [24]. The super-Poincare group, which includes supersymmetry
 524 transformations linking bosons and fermions in addition to the other space-time
 525 symmetries, was constructed. The conclusion is that the most general framework
 526 for the symmetries of physics is a direct product of the super-Poincare group with
 527 the internal symmetry group. This group is represented by four supersymmetry
 528 generators Q_α and $\bar{Q}_{\dot{\alpha}}$, where α and $\dot{\alpha}$ represent a left-handed and right-handed
 529 Weyl spinor index, respectively. They can act on a scalar state ϕ to obtain a
 530 spinor particle

$$Q_\alpha |\phi\rangle = |\psi_\alpha\rangle , \quad (2.15)$$

531 where the state ψ represents a fermion. The momentum operator and gauge
 532 transformation generators of internal symmetries commute with the operators Q

533 and \bar{Q} . As a result, the supersymmetric states contain bosonic and fermionic fields,
 534 commonly referred to as *supermultiplet*. The supermultiplets can be either chiral,
 535 containing a boson and a left-handed fermion, or anti-chiral, with a right-handed
 536 fermion. As a consequence of the commutation properties, the particles within
 537 a supermultiplet have identical charges, such as the electric charge and colour
 538 charge, under all gauge symmetries. The implication of this statement is that in
 539 a supersymmetric extension of the SM, there will be two superpartners, a boson
 540 and a fermion, with the same quantum numbers except spin.

541 SUSY breaking

542 The momentum operator P^μ also commutes with Q , $[Q, P^\mu] = 0$, which implies
 543 that if supersymmetry is exact, then that every bosonic state must have a
 544 corresponding fermionic partner with an identical mass. In other words, the
 545 supersymmetric partners must come in mass-degenerate pairs. However, this
 546 possibility has been ruled out experimentally since we know that there is no
 547 superpartners with similar masses as the SM particles. Supersymmetry must then
 548 be a broken symmetry. Supersymmetry breaking is not well understood, however,
 549 there is an appealing scheme that preserves most of the attractive features of
 550 supersymmetry which is known as *soft supersymmetry breaking*. In this scheme,
 551 the superpartner masses can be increased to an acceptable range with the current
 552 experimental bounds. Also, the scale of the mass splitting should be in the range
 553 of $\mathcal{O}(100)$ GeV to $\mathcal{O}(1)$ TeV, since it can be linked to electroweak symmetry
 554 breaking[25].

555 **2.2.2 Supersymmetric Phenomenology**

556 **Minimal Supersymmetric Standard Model**

557 The simplest implementation of a supersymmetric SM is known as the Minimal
 558 Supersymmetric Standard Model, or MSSM. It is minimal since it contains the
 559 smallest number of new particle states and new interactions necessary such that
 560 the SM particles still exist in their current forms and within a supersymmetric
 561 framework.

562 In this model, each SM fermion is placed within a supermultiplet containing
 563 an additional boson. These new particles are called the same as their fermionic
 564 counterpart with a prepended ‘*s*-’. For instance, an electron (e) is partnered with
 565 a selectron (\tilde{e}), a quark (q) with a generic squark (\tilde{q}), etc. On the other hand, the
 566 SM bosons with spin 1, that is B^0 , W^\pm , W^0 before electroweak symmetry breaking,
 567 are paired with fermionic superpartners with spin $\frac{1}{2}$ into gauge supermultiplets.
 568 These new particles are called the same as their bosonic counterpart but with the
 569 postfix ‘*-ino*’. So we obtain gluinos (\tilde{g}), winos (\tilde{W}) and binos (\tilde{B}).

570 The Higgs sector is chosen to consist of two left-chiral scalar superfields, H_u
 571 and H_d , with different charges under $U(1)_Y$, $Y = 1$ and $Y = -1$, respectively.
 572 The H_u and H_d supermultiplets are required since each gives mass to only the up
 573 or the down quarks. They are also introduced to ensure the cancellation of triangle
 574 anomalies in the SM, which would otherwise make the theory non-renormalizable.

575 The superpartners of the SM particles in the MSSM are shown in Table 2.1.
 576 Since SUSY is a broken symmetry, the gaugino eigenstates mix with the Higgs

Particle group	Spin	P_R	Gauge eigenstates	Mass eigenstates
Higgs bosons	0	+1	$H_u^0, H_d^0, H_u^+, H_d^-$	h^0, H^0, A^0, H^\pm
			$\tilde{u}_L, \tilde{u}_R, \tilde{d}_L, \tilde{d}_R$	(same)
squarks	0	-1	$\tilde{s}_L, \tilde{s}_R, \tilde{c}_L, \tilde{c}_R$	(same)
			$\tilde{t}_L, \tilde{t}_R, \tilde{b}_L, \tilde{b}_R$	$\tilde{t}_1, \tilde{t}_2, \tilde{b}_1, \tilde{b}_2$
			$\tilde{e}_L, \tilde{e}_R, \tilde{\nu}_e$	(same)
sleptons	0	-1	$\tilde{\mu}_L, \tilde{\mu}_R, \tilde{\nu}_\mu$	(same)
			$\tilde{\tau}_L, \tilde{\tau}_R, \tilde{\nu}_\tau$	$\tilde{\tau}_1, \tilde{\tau}_2, \tilde{\nu}_\tau$
Neutralinos	1/2	-1	$\tilde{B}^0, \tilde{W}^0, \tilde{H}_u^0, \tilde{H}_d^0$	$\tilde{\chi}_1^0, \tilde{\chi}_2^0, \tilde{\chi}_3^0, \tilde{\chi}_4^0$
Charginos			$\tilde{W}^\pm, \tilde{H}_u^+, \tilde{H}_d^-$	$\tilde{\chi}_1^\pm, \tilde{\chi}_2^\pm$
gluino	1/2	-1	\tilde{g}	(same)

Table 2.1: Superpartners of the SM particles in the Minimal Supersymmetric Standard Model showing the mass eigenstates and which gauge eigenstates are mixed. The two first generations of the squarks and sleptons are assumed to have negligible mixing.

577 multiplets to form a set of neutralinos ($\tilde{\chi}_i^0$, $i = 1, 2, 3, 4$), charginos ($\tilde{\chi}_i^\pm$, $i = 1, 2$),
 578 and Higgs bosons as a result of the SUSY breaking terms that are added. The
 579 neutralino and chargino states are ordered in terms of mass as $m_{\tilde{\chi}_1^0} \leq m_{\tilde{\chi}_2^0} \leq$
 580 $m_{\tilde{\chi}_3^0} \leq m_{\tilde{\chi}_4^0}$ and $m_{\tilde{\chi}_1^\pm} \leq m_{\tilde{\chi}_2^\pm}$. It is worth noting that the MSSM expects to have
 581 five physical Higgs bosons: two CP-even Higgs bosons h^0 and H^0 , one CP-odd
 582 state A^0 , and a pair of charged Higgs H^\pm . The observed Higgs boson of 125
 583 GeV can be one of the two CP-even Higgs bosons. Unlike in the SM where the
 584 Higgs mass is one free parameter, the masses of the Higgs bosons at tree level and
 585 the mixing angle are expressed in terms of two parameters chosen to be the mass
 586 of A^0 (m_A) and the ratio of the two vacuum expectation values ($\tan \beta = v_u/v_d$).
 587 These vacuum expectation values, v_u and v_d , correspond to the local minima of
 588 the scalar potential in which electroweak symmetry is spontaneously broken.

589 Simplified Models

590 The details given so far have described the particle content of the MSSM. As far
 591 as the free parameters are concerned, in contrast to the SM which has nineteen
 592 free parameters, the MSSM has 124 free parameters. While a large portion
 593 of the parameter space is excluded, there are many degrees of freedom still
 594 remaining. In principle, it is possible to reduce the number of parameters by
 595 making well-motivated assumptions on the physics at higher energy scales. In
 596 fact, model builders attempt to formulate reasonable and economical models that
 597 are phenomenologically viable and falsifiable based on the current experimental
 598 results.

599 Another strategy is to completely decouple many of the particles in the SUSY
 600 spectrum, and assume a 100% branching ratio for one specific decay mode, in
 601 what is known as *simplified models*. In practice, the decoupling is achieved by
 602 arbitrarily tuning the SUSY breaking parameters in the Lagrangian to include the
 603 desired mass terms and couplings. While such models are known to be not viable
 604 and may even break the renormalizability of the theory, they are considered as
 605 indicative of the reach of the analysis in probing the SUSY parameter space and
 606 can also be recast by theorists in terms of their own models. This is the strategy
 607 followed in most of the results shown in the analysis presented in this dissertation.

608 ***R-parity***

609 It is desirable to write down supersymmetric interactions that preserve baryon or
 610 lepton numbers since they are putatively good symmetries in the SM. This can
 611 be achieved by requiring the conservation of a new quantity called *R-parity*. For
 612 baryon number B , lepton number L , and particle spin s , the *R-parity* is defined
 613 as

$$P_R = (-1)^{3(B-L)+2s}. \quad (2.16)$$

614 The MSSM is formulated as an *R-parity* conserving (RPC) theory. However, it
 615 can be extended to include a superpotential for the *R-parity* violating (RPV)
 616 interactions that can be written as

$$W_{P_R} = \frac{1}{2} \lambda^{ijk} L_i L_j E_k + \lambda'^{ijk} L_i Q_j D_k - \kappa^i L_i H_d + \frac{1}{2} \lambda''^{ijk} U_i D_j D_k, \quad (2.17)$$

in which chiral quark and lepton superfields are denoted by Q , U , D and L , E , respectively, where i , j , and k are flavour indices. The terms show the only interactions that violate baryon or lepton number conservation where λ and λ' couplings break lepton number conservation, while λ'' coupling breaks baryon number conservation. The work presented in this dissertation will not address RPV scenarios [26].

2.2.3 The Hierarchy Problem

As described previously, there are scalar and fermion loops that contribute to the radiative corrections to the Higgs mass that diverges as Λ^2 . By introducing supersymmetric partners, the large fermionic contribution to the Higgs mass will be compensated by the scalar particle loop of the same mass but with an opposite sign. In the case of unbroken supersymmetry, this cancellation is exact and will thus eliminate the fine-tuning problem. However, we know that supersymmetry must be broken. Naturalness is introduced to place limits on the masses of certain superpartners in order not to replace the fine-tuning problem of the SM with another in a supersymmetric model. As a result, there is strong motivation for having supersymmetry in the weak scale which will inevitably stabilize the electroweak symmetry breaking of the SM which suffered from the fine-tuning problem.

There are other benefits of supersymmetry that are beyond the scope of this work. We refer the reader to the literature [27, 28, 29].

638 2.3 Discovery at the LHC

639 Some notable discoveries in particles physics are those of the W and Z bosons
 640 [30, 31], the top quark [1, 2], and the Higgs boson [14, 15]. The path towards the
 641 discovery of these particles was guided by theoretical insight which gave great
 642 confidence that these particles should exist. For instance, the features of the W
 643 and Z bosons, such as their mass and production rates, were known in advance.
 644 Their signals stood out from the backgrounds without ambiguity. The top quark
 645 discovery was harder, but its production and decay properties were predicted.
 646 For the Higgs, there was reasonable evidence for its existence. The production
 647 and decay of the Higgs were all known as a function of mass, the only missing
 648 parameter in the theory. In fact, these properties were also known for alternative
 649 models to the SM implementation of the Higgs mechanism.

650 Today, we do not have such theoretical guidance, and thus our task is notably
 651 more difficult. The strategy followed at the LHC is to aim at establishing
 652 significant deviations from the SM by carefully examining if the observed signal
 653 is not consistent with the standard model expectation. The second step is to
 654 understand what this deviation corresponds to in the vast space of possible beyond
 655 the SM scenarios.

656 There are three possible scenarios to establish a deviation from the SM
 657 expectation: invariant mass peaks, anomalous shapes of kinematic distributions,
 658 and excess in counting experiments. By examining invariant mass distributions of
 659 dilepton, diphoton, or dijet final states, a peak that stands out from the background

660 continuum that is not predicted by the SM is the most clear indication of a new
 661 physics signal. The benefit of this type of signal is that the background can be
 662 directly taken from data by mere extrapolation of the sidebands of the invariant
 663 mass below and above the peak. As a result, the simulation will not be important
 664 in this scenario, which is desirable to avoid any mis-modelling or inaccuracies of the
 665 simulation. The second strategy aims at establishing a clear difference in the shape
 666 of a given kinematic variable between the observed data from the expected SM
 667 background. Distributions, like the missing transverse momentum or the effective
 668 mass defined as the sum of all reconstructed objects and missing transverse
 669 momentum in the event, are chosen to be sensitive to new physics scenarios. This
 670 approach relies heavily on a precise knowledge of the SM background shapes.
 671 For this reason, special care must be taken to validate the accuracy of the SM
 672 modeling. The claim that a new signal exists is far too important to only rely on
 673 a direct comparison with Monte Carlo simulation. For this reason, a combination
 674 of data-driven and correction techniques are employed. Often times, data is used
 675 internally to correct the shape and normalization of the SM backgrounds and to
 676 validate the estimate before extrapolating to the search region represented by a
 677 kinematic distribution of a given variable. The last strategy aims at defining some
 678 selection criteria expected to increase the probability for observing a new signal,
 679 then counting the number of observed events passing the cuts and comparing
 680 it to the expected background. In a sense, this strategy is similar to the shape
 681 discrepancy case except that an integral over the full sample passing the cuts is
 682 taken since the statistics is typically low. As a consequence, counting experiments

683 require an even more careful assessment of the background to achieve the most
684 robust understanding of the expected prediction.

685 The work described in this dissertation follows the last strategy of designing
686 several counting experiments. The essential part of the work is in establishing a
687 reliable background estimate in these experiments to access the compatibility of
688 the observed data with the predicted background.

689 **Chapter 3**

690 **Experimental Apparatus**

691 **3.1 The Large Hadron Collider**

692 The Large Hadron Collider (LHC) is the largest particle accelerator and collider
693 in the world. The LHC is built in a circular tunnel 27 km in circumference that is
694 buried between 50 m to 175 m underground and straddles the Swiss and the French
695 borders at CERN. The LHC is a synchrotron that accelerates two counter-rotating
696 beams of protons to 6.5 TeV then brings them into head-on collisions at the center
697 of four large detectors: ALICE, ATLAS, CMS, and LHCb. The center of mass
698 energy of the proton-proton (or pp) collision is $\sqrt{s} = 13$ TeV, the energy of the
699 collision data analyzed in this dissertation. The beam itself has a total energy of
700 336 MJ requiring an accurate and careful steering of the beam at all times. This
701 is achieved by a strong magnetic field generated by superconducting magnets that
702 guide the protons around the accelerator. There are 1232 dipoles magnets, each
703 15 meters long operating at 1.9 K and generating a magnetic field of 8.33 T. The
704 dipoles are comprised of 7600 km of superconducting cable which is formed from
705 filaments of Niobium-titanium (NbTi).

706 A complex of smaller accelerators boost the protons before injecting them
707 to the LHC, the last accelerator in the chain as shown in Figure 3.1. Protons,
708 obtained from hydrogen atoms, start their journey in a linear accelerator called the
709 Linac2. The Linac2 accelerates the protons to 50 MeV. Then, they are injected

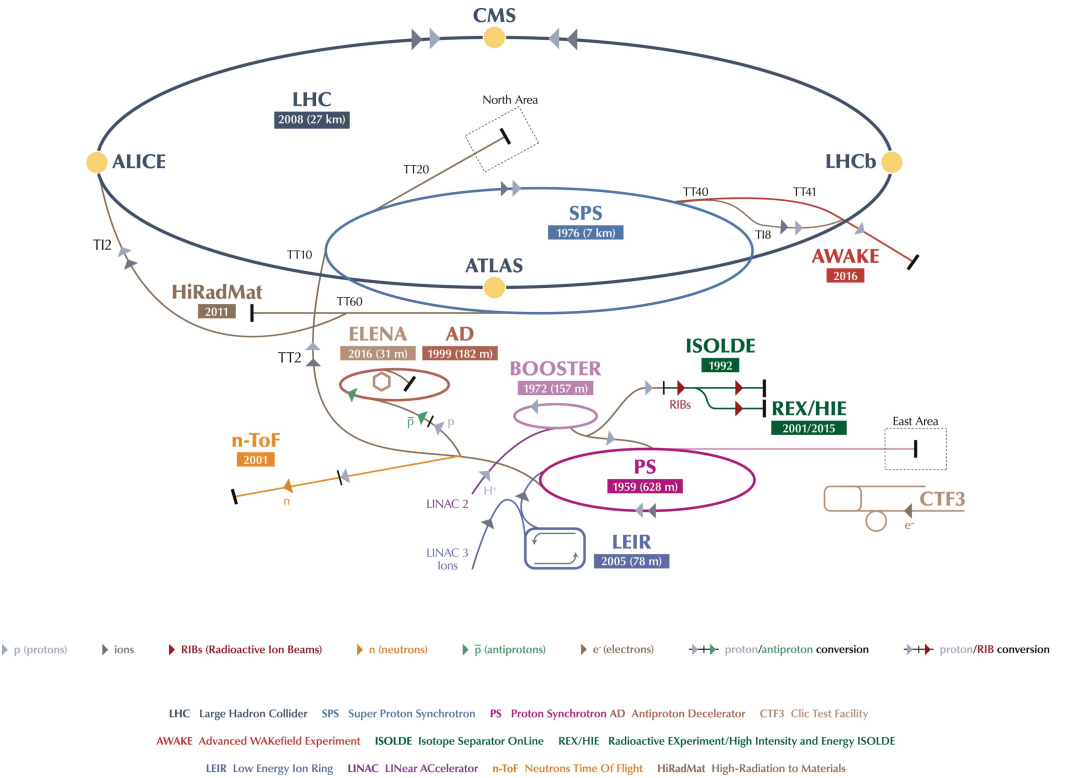


Figure 3.1: The CERN accelerator complex composed of a chain of particle accelerators with the LHC as the last ring (dark blue line) [32].

710 into the PS Booster, which accelerates them to 1.4 GeV. After the PS Booster,
 711 the protons are sent to the Proton Synchrotron where they are accelerated to
 712 25 GeV. They are then sent to the Super Proton Synchrotron (SPS) where they
 713 are accelerated to 450 GeV. At this stage, the protons are injected into the
 714 LHC and accelerated to the target energy of 6.5 TeV per proton. The beams are
 715 then focused at each of the interaction points to produce proton-proton collisions.
 716 Under normal operating conditions, the colliding beams will circulate for $\mathcal{O}(10)$
 717 hours at a time.

718 The protons are grouped in “bunches” when circulated in the LHC as a result

719 of the acceleration scheme. In normal operation of the LHC, each proton beam
 720 has 2808 bunches, with each bunch containing about 100 billion protons. These
 721 bunches are a few centimetres long and a few millimeters wide when they are far
 722 from a collision point but squeezed to about 16 micrometers when they collide.
 723 The rate of their interaction is defined in terms of the luminosity, a measure of
 724 the number of collisions produced per second by the accelerator. Generally, the
 725 event rate $\frac{dN}{dt}$ of a physics process with cross section σ is

$$\frac{dN}{dt} = \sigma \mathcal{L} \quad (3.1)$$

726 where the constant of proportionality, \mathcal{L} , is called the instantaneous luminosity, and
 727 has units of $cm^{-2}s^{-1}$. The LHC has exceeded its design luminosity of $10^{34}cm^{-2}s^{-1}$
 728 or $10nb^{-1}s^{-1}$ ($1 \text{ barn} = 10^{-24}cm^2$) by almost 40% as shown in Figure 3.2a. Given
 729 the total inelastic cross section of 60 mb, the collision rate of protons is then
 730 $\sigma\mathcal{L} \sim 10^9$ Hz: a billion proton interactions per second. The integral of the
 731 instantaneous luminosity, $L = \int \mathcal{L} dt$, refers to the amount of data collected. The
 732 large integrated luminosities allow for the study of rare processes, such as the
 733 search for supersymmetric particles. Figure 3.2b shows the data sets collected by
 734 the LHC, where the data collected in 2015 and 2016 at $\sqrt{s} = 13$ TeV is the basis
 735 of the work presented in this dissertation.

736 The other important characteristic of the LHC is that multiple pp interactions
 737 occur at every bunch crossing. This quantity is correlated with the instantaneous
 738 luminosity as can be seen by comparing Figure 3.2a and Figure 3.3a. Figure 3.3b
 739 shows that the mean number of interactions per bunch crossing was 25 in 2016

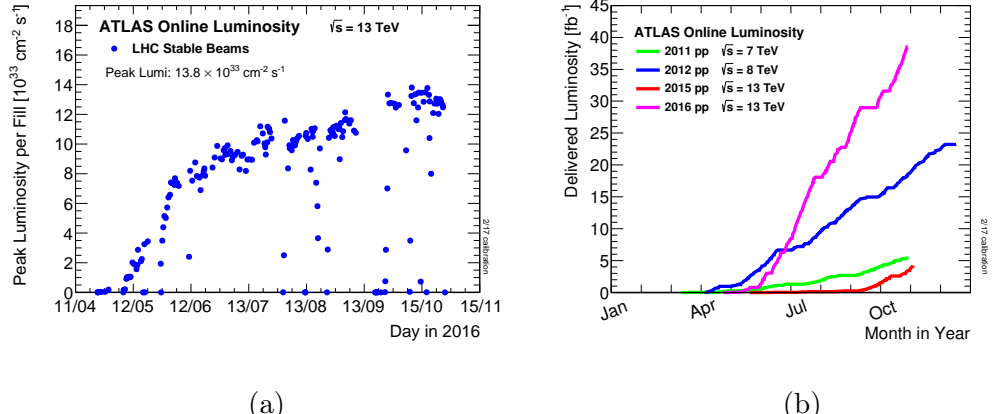


Figure 3.2: (a) The peak instantaneous luminosity delivered to ATLAS in 2016 and (b) the cumulative luminosity delivered to ATLAS between 2011 and 2016, during stable beams for pp collisions

740 with the peak number of interactions reaching up to 50. This causes a computa-
 741 tional challenge in reconstructing the physics objects coming from one interesting interaction. A typical hard scattering of two protons has a large impact parameter

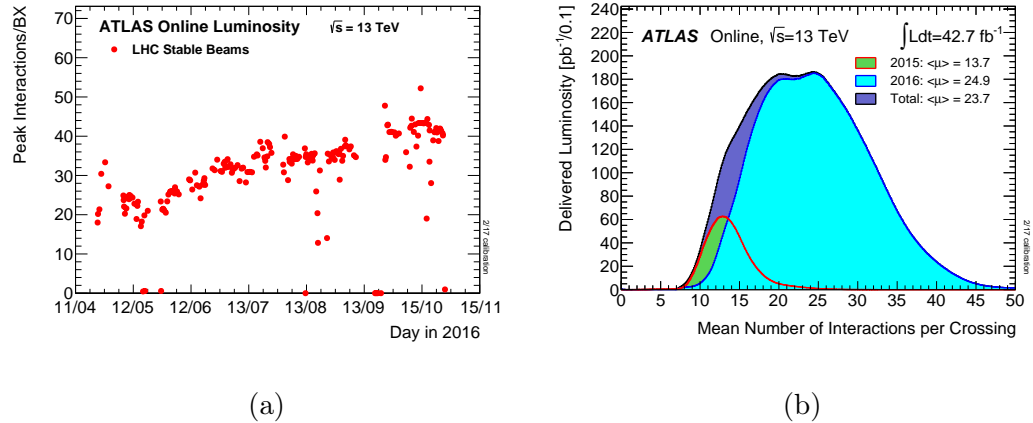


Figure 3.3: (a) the peak number of inelastic collisions per beam crossing during 2016 and (b) the mean number of these collisions per crossing for 2015 and 2016, during stable beams for pp collisions

743 leading to low momentum particles in the final state. These type of collisions are
 744 known as “minimum bias” collisions and are considered as background to the more
 745 spectacular hard scattering that is typical of an interesting event. The minimum
 746 bias is generally not well understood since it comes from nonperturbative QCD
 747 and is estimated using the LHC data.

748 3.2 A Toroidal LHC Apparatus (ATLAS)

749 ATLAS (**A**Toroidal **L**H_C **A**pparatu**S**) is a multi-purpose particle detector located
 750 at one of the LHC interaction points 100 meters underground. It is the largest
 751 particle detector ever built with a weight of about 7000 tonnes, a length of 44 m,
 752 and a diameter of 25 m as shown in Figure 3.4. It is designed to probe Higgs
 753 physics, QCD, flavour physics, as well as a multitude of beyond the Standard
 754 Model (BSM) physics scenarios including supersymmetry.

755 ATLAS covers a solid angle of almost 4Ω to capture as much information
 756 from the collisions as possible. It is composed of multiple layers of detectors to
 757 ensure that all particles produced in the collision are identified and measured
 758 with high accuracy. These subsystems are shown in Figure 3.4. The first detector
 759 resides in the part closest to the LHC pipe and is composed of silicon tracking
 760 sensors designed to reconstruct the paths of charged particles. Next, comes the
 761 electromagnetic and hadronic calorimeter cells that measure the energy of particles.
 762 Last comes the muon spectrometer in the outermost part of the detector to detect
 763 muons since they penetrate the calorimeters. An axial magnetic field of 2 T is

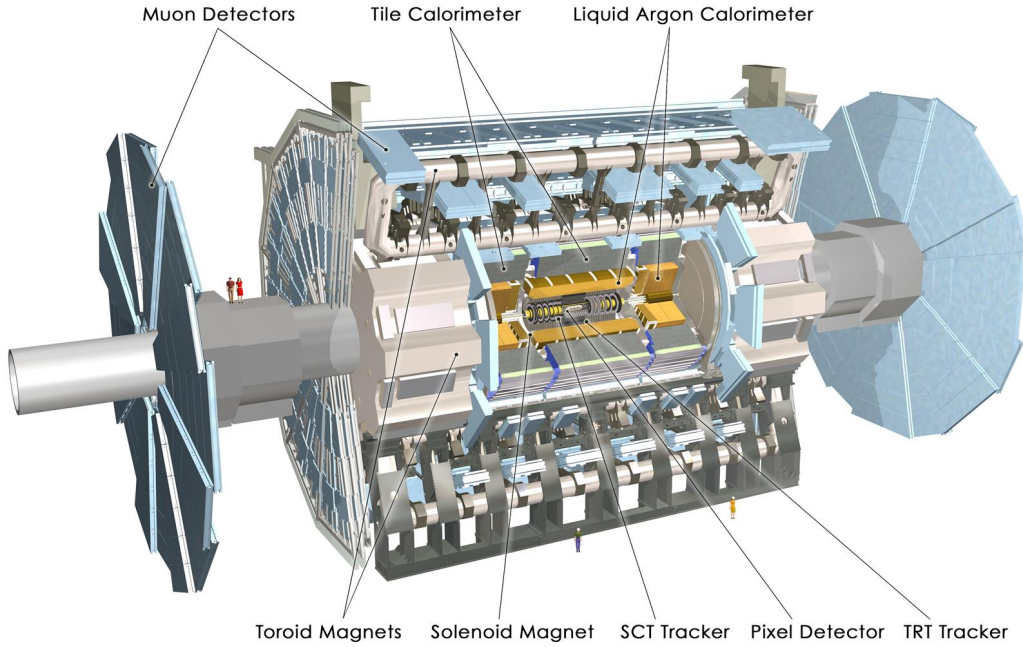


Figure 3.4: Overview of all the subsystems of the ATLAS detector.

764 applied across the inner detector while a toroidal magnetic field of approximately
 765 0.5 T is applied across the muon detectors. The remainder of this chapter will
 766 describe in more details these detectors.

767 3.2.1 Co-ordinate System

768 The common coordinate system of ATLAS is right-handed Cartesian, with its
 769 origin at the nominal interaction point. The axes are oriented such that the x -axis
 770 is pointing towards the center of the LHC ring, the y -axis is directed vertically
 771 upward, and the z -axis defines one of the beam directions. The (x, y) plane defines
 772 the transverse plane, usually represented by polar coordinates (r, ϕ) with $\phi = 0$
 773 on the x -axis. The polar angle θ is replaced by the pseudorapidity

$$\eta = -\ln \left(\tan \left(\frac{\theta}{2} \right) \right), \quad (3.2)$$

⁷⁷⁴ shown in Figure 3.5. It is named after the rapidity (y) since it yields the same
⁷⁷⁵ quantity for massless particles

$$y = \frac{1}{2} \ln \left(\frac{E + p_Z}{E - p_Z} \right), \quad (3.3)$$

⁷⁷⁶ which is invariant under boosts in the z -direction. It is common to describe the
⁷⁷⁷ separation between two physical objects in the detector by

$$\Delta R = \sqrt{\Delta\eta^2 + \Delta\phi^2} \quad (3.4)$$

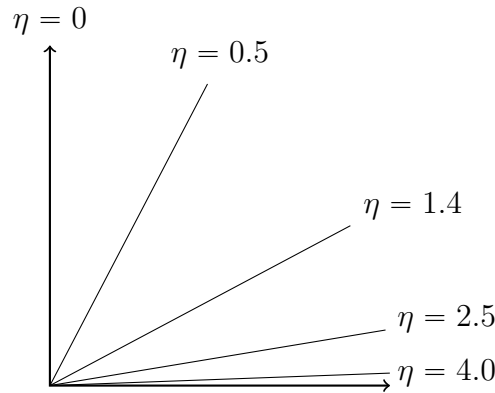


Figure 3.5: Illustration of some pseudorapidity values relevant for ATLAS.

⁷⁷⁸ 3.2.2 Inner detector

⁷⁷⁹ In the innermost part of ATLAS is placed a tracker referred to as the Inner
⁷⁸⁰ Detector (ID). It has finely segmented detectors to reconstruct the tracks of
⁷⁸¹ charged particles in the magnetic field of the solenoid. The main subsystems
⁷⁸² of the ID are the pixel detector, the SemiConductor Tracker (SCT), and the
⁷⁸³ Transition Radiation Tracker (TRT) shown in Figure 3.6. Overall these give
⁷⁸⁴ coverage of the solid angle defined by $|\eta| < 2.5$, and occupy the volume with

785 $33.25 < r < 1082$ mm. Using these systems, its purpose is to detect the path
 786 taken by charged particles as they bend through the magnetic field, and hence
 787 determine their momenta. Particles from the main pp interaction pass through
 788 several layers of silicon detectors each providing a 2-dimensional coordinate. To
 789 reduce correlations between individual points the layers are spread out evenly
 790 along the tracks. Figure 3.6b shows a charged particle with 10 GeV transverse
 791 momentum, denoted by p_T , that emerges from the interaction point and traverses
 792 the beam-pipe, four pixel layers, four double layers of SCT sensors, and around
 793 35 TRT straws. These elements will be described next.

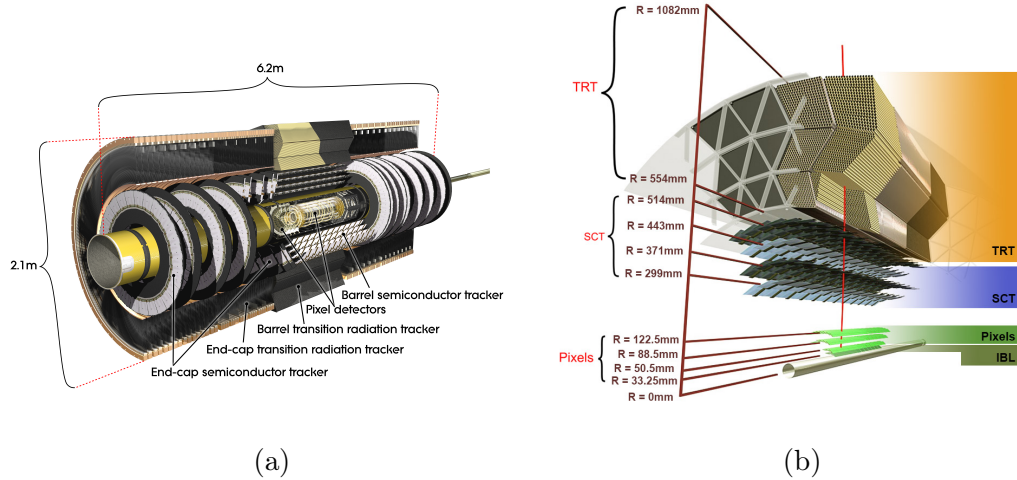


Figure 3.6: Overview of the subsystems of the inner detector of ATLAS in both (a) and (b). The radial locations of each component are shown in (b) as a charged particle with 10 GeV p_T traverses the barrel of the Inner Detector.

794 Pixel detector

795 Since the pixel detector is the closest to the beam pipe ($33.25 < r < 242$ mm
 796), it is the highest resolution detector. It contains 140 million semiconductor

797 pixels each of just $50 \times 400 \mu\text{m}$, thus giving a 2-dimensional coordinate with just
 798 one layer. The best resolution is in the φ coordinate. As a result, it is able to
 799 measure the charged particle track intersection position at the different layers up
 800 to a precision of $10 \times 115 \mu\text{m}$. This resolution is important since the area
 801 subtended by a given solid angle is at its smallest value near the interaction point.
 802 It is also designed to tolerate the very high radiation doses that it is exposed to
 803 at such proximity to the interaction point. The detector is formed of three barrel
 804 layers as well as two end-cap structures. Each of the end-caps comprises four discs
 805 of sensors, arranged such that most tracks are more likely to hit pixels in at least
 806 three distinct layers. The most important requirements for the pixel detectors
 807 are to provide the position of the main pp interaction, called the primary vertex,
 808 and subsequent vertices from B -meson decays. These are important parameters
 809 for the identification of jets originating from b -hadrons, essential for most of the
 810 physics program of ATLAS, including the search presented in this dissertation.
 811 Further details can be found in the corresponding technical design report [8].

812 **SCT**

813 The SCT surrounds the pixel layers. The SCT is formed of four such stereo layers
 814 in the barrel, along with nine discs in each end-cap. Each SCT layer is composed
 815 of a double layer of silicon strips, whose axes are tilted by 40 mrad with respect
 816 to one another. The pair of measurements at each SCT layer locates charged
 817 particles in $r - \phi$ with an accuracy of $17 \mu\text{m}$, and along z , with an accuracy of
 818 $580 \mu\text{m}$. The SCT provides between four and nine measurements per particle,

819 with coverage up to $|\eta| = 2.5$. Further details can be found in the technical design
 820 report of the inner detector [9, 10].

821 **TRT**

822 The TRT is the largest of the sub-detectors in the ID. It is composed of $\sim 300,000$
 823 straw drift tubes that provide position measurements with an accuracy of ~ 130
 824 μm in ϕ . A large number of hits, around 35 per particle, is provided, with coverage
 825 up to $|\eta|=2.0$. It operates based on the ionization of the gas inside the tubes ((

826 70% Xe, 27% CO₂ and 3% O₂) when traversed by charged particles; the ions then
 827 drift radially due to the potential difference, and the excess charge is collected and
 828 detected. The tubes are arranged parallel to the beam axis in the barrel region,
 829 and radially in the end-caps. In addition to providing particle tracks, the TRT
 830 also provides particle identification through the detection of transition radiation ¹
 831 . For example, electrons will emit more transition radiation photons than charged
 832 hadrons.

833 **3.2.3 Calorimeters**

834 The calorimeter system measures the energy of hadrons, electrons and photons.
 835 The ATLAS calorimeter is divided into an electromagnetic calorimeter based on
 836 liquid argon (LAr) and a hadronic calorimeter based on iron-scintillator “tiles”
 837 (Tile). The distinction is due to the different interaction behaviour between the
 838 calorimeter and electrons/photons on one side and hadrons on the other side. [12].

¹Transition radiation is emitted whenever a charged particle crosses the boundary between two media.

839 An overview of the calorimeter system can be seen in Figure 3.7. Overall they
 840 cover solid angles up to $|\eta| < 4.9$, with the electromagnetic calorimetry providing
 841 finer grained measurements to augment the inner detector for electron and photon
 842 measurements, while the hadronic calorimeter is coarser but sufficient for jet
 843 reconstruction and measurements of missing transverse momentum.

844 The ATLAS calorimeters are sampling calorimeters. Incident particles produce
 845 showers of energy in the calorimeter. Only a fraction of the energy produced
 846 by the particle is measured by active detector sensors. The energy of the full
 847 shower can be inferred from the observed energy. Thus a calibration must be
 848 used to estimate the true energy of any observed shower in the calorimeter. Each
 849 calorimeter is also segmented in η and ϕ to provide some directional information,
 850 although it is coarser than that from the inner detector. Finally, the calorimeter
 851 is designed to limit “punch-through” of high energy jets into the muon chambers.

852 LAr Calorimeters

853 The energies of electrons and photons are measured by the LAr electromagnetic
 854 calorimeters composed of the barrel section with $|\eta| < 1.475$, and end-cap sec-
 855 tions with $1.375 < |\eta| < 3.2$. These detectors provide complete ϕ coverage and
 856 fast readout, in addition to high granularity measurements, critical for parti-
 857 cle identification in the range $|\eta| < 2.5$. There is a region of slightly degraded
 858 performance where the barrel and end-cap sections do overlap. Most ATLAS
 859 analyses, including the one presented in this dissertation, ignore electron and
 860 photon candidates that fall into this “crack” region. Figure 3.8 shows a cut-away

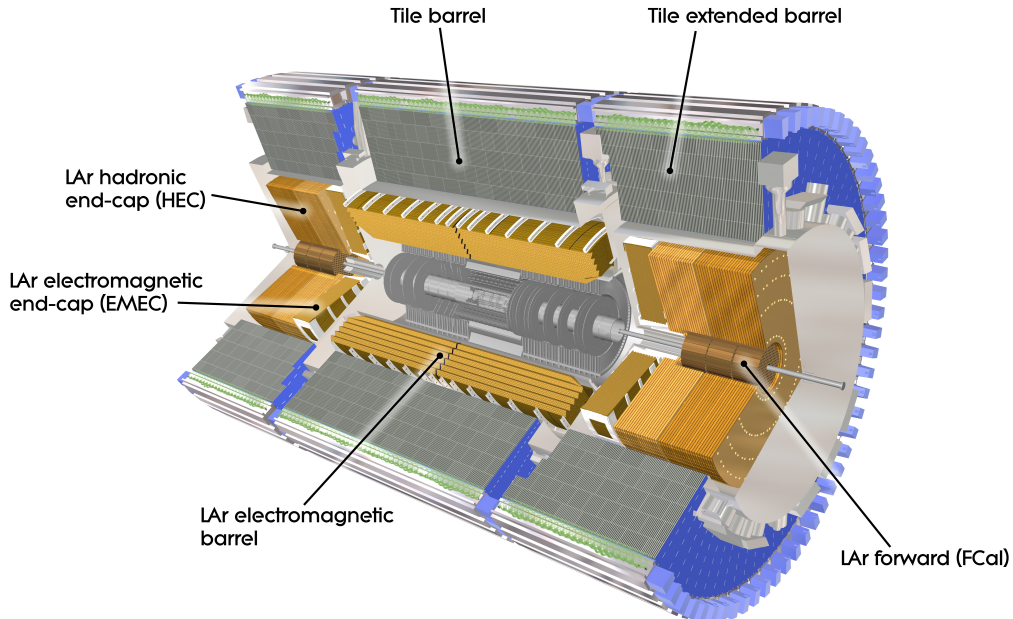


Figure 3.7: Overview of the different calorimeters in ATLAS.

861 of the different layers in the electromagnetic barrel calorimeter. The first layer,
 862 referred to as the “strips”, provides very fine segmentation in η . The strips can
 863 separate between showers initiated by electrons or photons and showers initiated
 864 by neutral pions. The second sampling provides most of the energy measurement
 865 and has fine segmentation in both η and ϕ . The third sampling is coarser and
 866 adds additional depth to the calorimeter.

867 Tile Calorimeters

868 The tile calorimeter is the hadron calorimeter covering the range of $|\eta| < 1.7$.
 869 The tile calorimeter uses steel tiles as an absorber and scintillating tiles as the
 870 detector. The scintillator tile calorimeter is separated into a barrel and two
 871 extended barrel cylinders. The light produced in the scintillators is read out

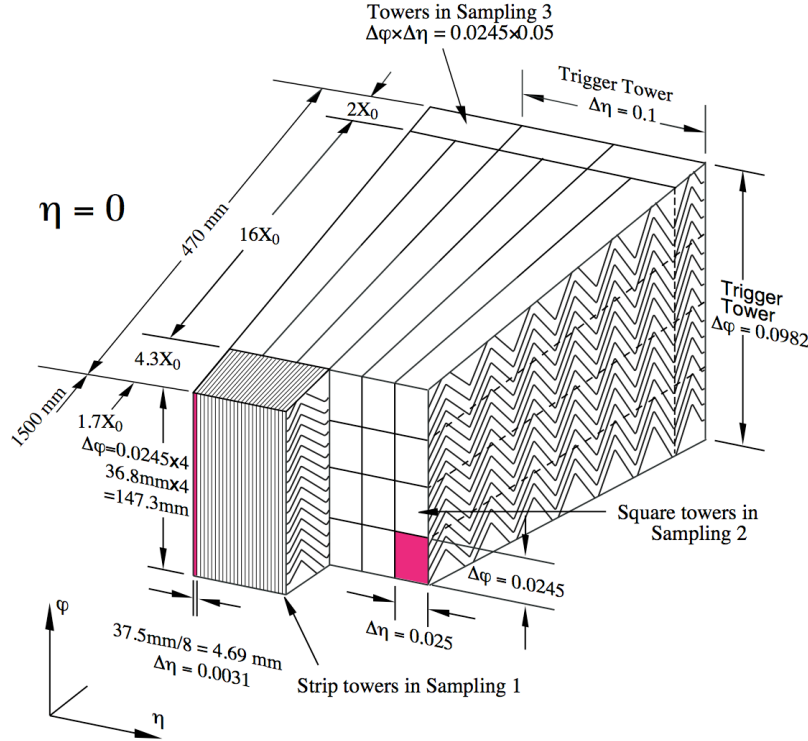


Figure 3.8: Sketch of the accordion structure of the LAr EM calorimeter where the different layers are clearly visible. The granularity in η and ϕ of the cells of each of the three layers is shown.

872 with wavelength-shifting optical fibers to photomultipliers (PMTs) placed on the
873 outside of the calorimeter.

874 3.2.4 Muon System

875 The ATLAS muon system is used as a trigger to select events with high energy
876 muons and to measure the position of muons as they traverse the detector.

877 The system covers the range of $|\eta| < 2.7$ and operates on the principle of
878 measuring the deflection of tracks due to magnetic fields. There is then a magnetic
879 field in the barrel section, $|\eta| < 1.4$, induced by the main barrel coils, and a

880 magnetic field in the end-cap region, $1.6 < |\eta| < 2.7$, induced by separate end-cap
 881 coils, as can be seen in Figure 3.9. In the region $1.4 < |\eta| < 1.6$, the bending will
 882 occur by a combination of the barrel and end-cap fields.

883 Several technologies are used to select the events and make measurements.
 884 The barrel region has resistive-plate chambers (RPC) for $|\eta| < 1.05$ that provide
 885 very fast timing information, ~ 10 ns, used for triggering. The barrel also has
 886 monitored drift tubes (MDT) for $|\eta| < 2.0$ that give precise measurements, $\sim 35\mu\text{m}$
 887 per chamber, in the (η, z) -plane where the bending occurs. The forward region
 888 of the detector, $2.0 < |\eta| < 2.7$, has Cathode strip detectors (CSCs) nearest
 889 to the interaction point, followed by thin-gap chambers (TGCs) and additional
 890 MDTs. The CSCs achieve a resolution of $40\mu\text{m}$ in the (η, z) -plane and 5 mm in
 891 the transverse plane. The layout of these components is more clearly shown in
 892 Figure 3.10.

893 3.3 ATLAS Trigger and Data Acquisition System

894 The ATLAS detector's data acquisition system, illustrated in Figure 3.14, makes
 895 use of a multi-tiered trigger to reduce the bandwidth from the LHC proton bunch
 896 crossing rate of 40 MHz to the 1 kHz written to disk [33, 34]. The first tier
 897 (Level-1 or L1) [35], implemented in real time with custom electronics, makes
 898 an early event selection to determine if any objects of interest are present and
 899 reduces the data flow to 100 kHz. The second tier, referred to as the High Level
 900 Trigger (HLT) [36], is implemented on a commodity computing cluster running

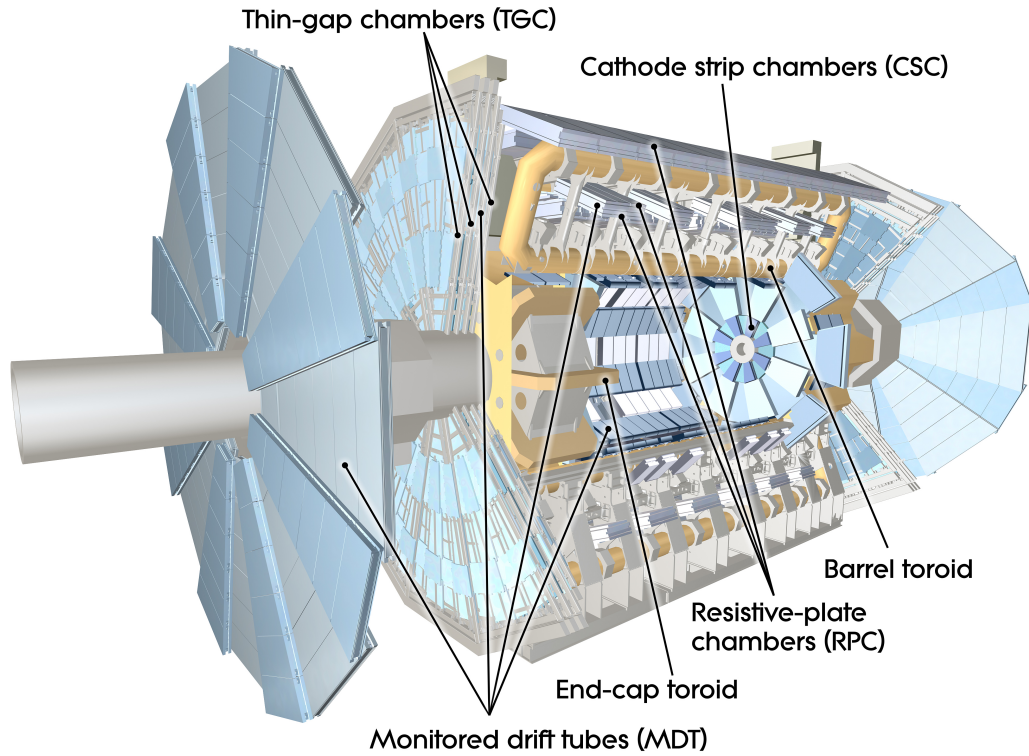


Figure 3.9: Overview of the ATLAS muon system.

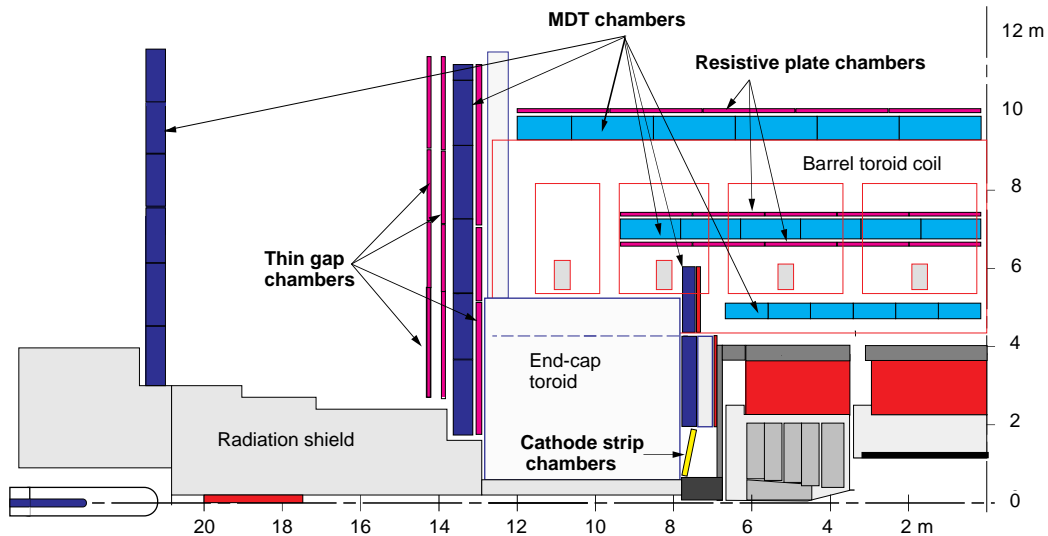


Figure 3.10: Cross-sectional view of the muon detectors of ATLAS in the $(y-z)$ -plane.

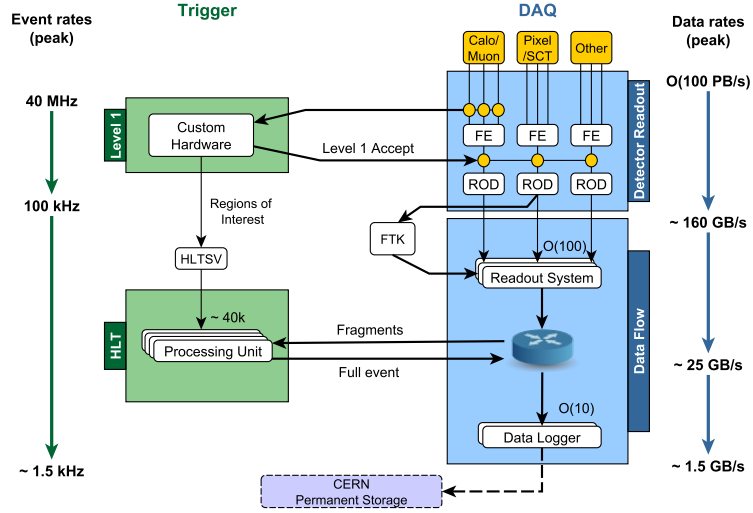


Figure 3.11: ATLAS TDAQ architecture.

901 custom triggering software. The HLT uses information from the hardware based
 902 L1 system to guide the retrieval of information from the Readout System (ROS)
 903 [37].

904 3.3.1 Hardware Trigger (L1)

905 The L1 trigger has access to raw data from the calorimeters and the muon system.
 906 The L1 calorimeter trigger (L1Calo) uses reduced-granularity information from
 907 7200 trigger towers of the calorimeters. These trigger towers are divided in a
 908 $\Delta\eta \times \Delta\phi$ space by 0.1×0.1 over most of the calorimeter, and larger in the forward
 909 region. A decision is made based on the multiplicities and E_T thresholds of
 910 the objects identified by the L1Calo algorithms: electromagnetic (EM) clusters,
 911 τ -leptons, jets, missing transverse energy, scalar sum E_T , and total transverse
 912 energy of the L1 jets. The L1 muon trigger (L1muon) uses measurements of the

913 trajectories of muons in the RPC and TGC trigger chambers, located in the barrel
 914 and end-cap regions of the muon spectrometer. The multiplicity of the various
 915 muon p_T thresholds is input to the trigger decision.

916 The central trigger processor (CTP) combines results from the L1Muon and
 917 L1Calo triggers to issue an overall L1 accept or reject decision. To facilitate
 918 this task, the CTP programs up to 256 configurations that consist of various
 919 combinations of E_T and p_T requirements, or thresholds. The CTP has the
 920 capability of implementing different isolation criteria to the different objects such
 921 as the L1 EM clusters. A trigger menu is implemented as a collection of L1 items,
 922 each containing a logical combination of one or more configured L1 thresholds.
 923 For example, the item L1_EM30i refers to an event requiring at least one isolated
 924 EM object with a transverse energy of $E_T > 30$ GeV. If the rates of a particular
 925 object is high, such as EM objects with low momentum, a prescale factor α is
 926 applied to the L1 item in the menu, where only 1 in α events is passed to the
 927 HLT. The L1 prescales are generally adjusted to maintain the optimal use of the
 928 allocated bandwidth for an L1 item during data-taking since the luminosity drops
 929 over the course of a run.

930 The L1 trigger has a 2.5 μ s latency where the data fragments are held in
 931 pipeline buffers located within detector-specific front-end electronics. Once the
 932 CTP issues an accept, the data is pushed to detector-specific Readout Drivers
 933 (RODs), then transferred to the Readout System (ROS). The rest of the chain is
 934 described next.

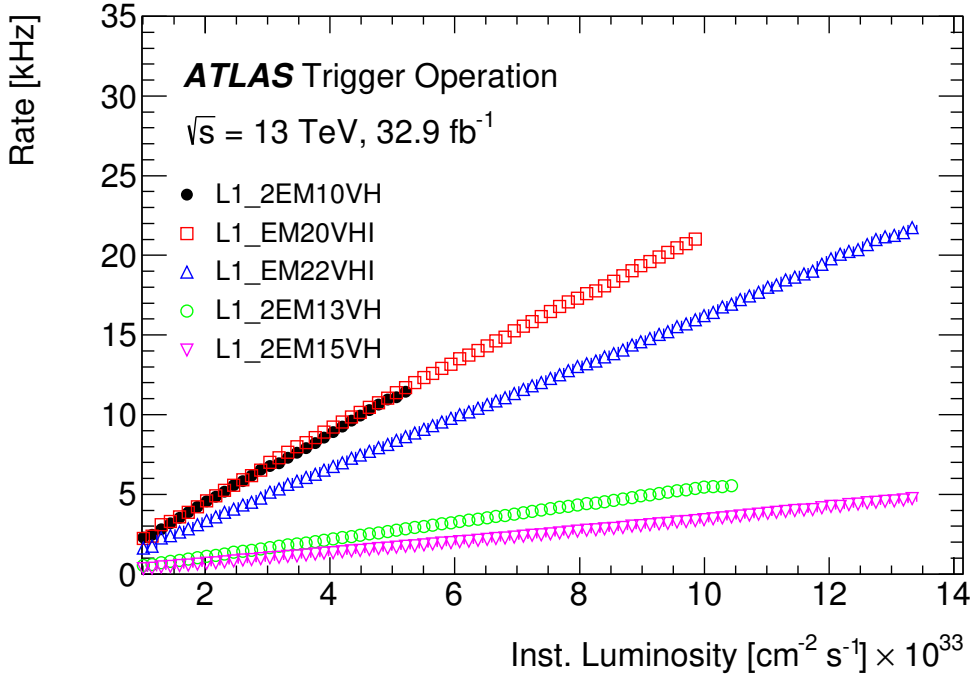


Figure 3.12: Output rates of Level-1 EM triggers as a function of the uncalibrated instantaneous luminosity measured online during the 2016 proton-proton data taking at a center-of-mass energy of 13 TeV. Rates are shown only for unprescaled triggers. All trigger rates show a linear dependency with instantaneous luminosity.

935 3.3.2 Dataflow Challenges in Run-2

936 The function of the DAQ system is to efficiently buffer, transport, and record the
 937 events that were selected by the trigger system. Its performance is affected by the
 938 instantaneous luminosity that leads to busy events with multiple proton-proton
 939 interactions occurring in each bunch crossing, referred to as pileup. The high
 940 pileup results in a higher data volume collected by the detector that needs to be
 941 processed at the required rate to avoid exerting back-pressure on the L1 system.
 942 In Run 2, the LHC has exceeded the designed instantaneous luminosity of

943 10^{34} cm $^{-2}$ s $^{-1}$ leading to pileup of $<\mu> = 30$ or more as shown in Figures 3.2a
 944 and 3.3b. The L1 accept rate has also increased from 75 kHz in Run 1 to 100 kHz
 945 in Run 2 and the average output rate of the data logger system has increased from
 946 400-600 Hz in Run 1 to about 3 kHz with 1.5 kHz for physics data. Moreover,
 947 there were new detectors that were added in Run 2 (Insertable B-layer (IBL),
 948 L1 topological trigger, Fast Tracker (FTK))[38] leading to an increase of 20% in
 949 the number of readout channels. To cope with these changes, the ATLAS TDAQ
 950 system was upgraded during Run-2 simplifying its architecture and increasing its
 951 flexibility. To be able to deliver more rate to the High Level Trigger (HLT), the
 952 upgrade also targeted the Readout System (ROS)[39]. For the same reason the
 953 two level of the HLT system were collapsed into a single level which made the
 954 system more flexible allowing for incremental data retrieval and analysis. The
 955 dataflow network system was re-designed to increase its capacity and simplify its
 956 architecture[40].

957 3.3.3 ATLAS Dataflow Design

958 In Run 1, the farm was subdivided into several slices, with each slice managed
 959 by a dedicated supervisor. This layout has been dropped in favor of global
 960 management by a single farm master operating at 100 kHz referred to as the HLT
 961 supervisor (HLTSV). The Region of Interest Builder (RoIB) that assembles the
 962 RoIs previously implemented on a VMEbus system is now integrated with the
 963 HLTSV and the RoI building done in software. Chapter 4 is dedicated to the work
 964 of the author in the RoIB evolution. The change in the HLT architecture from

965 two to one level required re-writing the HLT software and algorithms in such a
 966 way that each node in the farm can perform all processing steps. The handling of
 967 these processing steps is done by a single Data Collection Manager (DCM) process
 968 running on each HLT node to manage the L1 RoIs, the dataflow between the ROS
 969 and the HLT processing units (HLTPU), the event building processes, and the
 970 data logging. In the new architecture, the computing resources are managed more
 971 efficiently by balancing the utilization of all cluster nodes depending on the active
 972 HLT algorithms and by sharing the HLT code and services to reduce memory and
 973 resource usage.

974 The dataflow network shown in Figure 3.13 was simplified and upgraded to
 975 handle a larger data volume. A single network is used for ROI based access
 976 from the ROS, event building in the HLT processing nodes, and sending data
 977 for logging. A 10 GbE connectivity has been adopted throughout the dataflow
 978 system resulting in a factor of four increase in bandwidth between the data loggers
 979 and the permanent storage, and a 4×10 GbE output from each ROS PC to the
 980 core routers. The HLTSV and the HLT racks are all connected directly to each
 981 of the two core routers via 2×10 GbE connection. Each HLT rack is hosting up
 982 to 40 nodes connected by 2×1 GbE to the top-rack switches. The capacity of
 983 the routers can accommodate an increase in the number of HLT server racks and
 984 ROS PCs by a factor of two, which will be needed when the system scales as
 985 run conditions change. The core routers also provide load balancing and traffic
 986 shaping protocols [40] to distribute the data throughout the system more evenly.
 987 A duplication of core routers provide link redundancy at every level in case of link

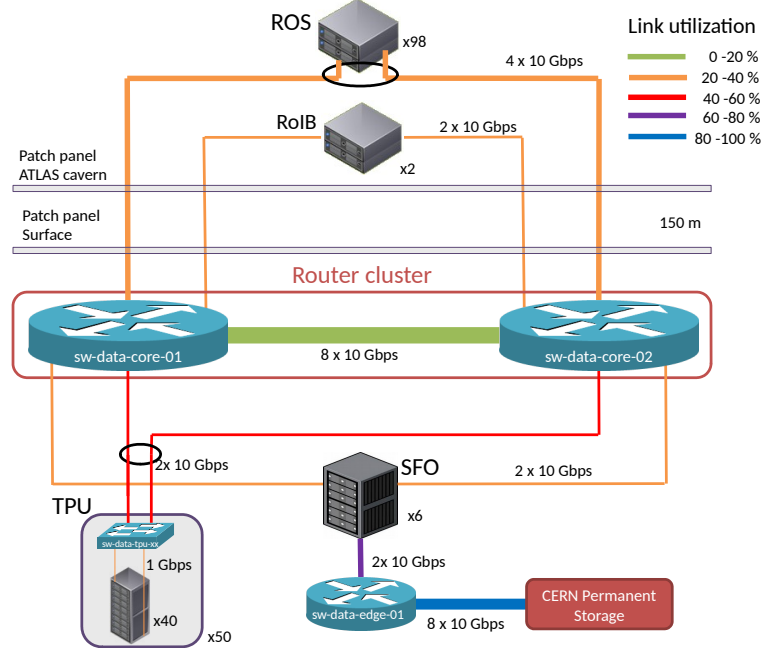


Figure 3.13: ATLAS Dataflow network

988 or switch failures.

989 To take advantage of multi-core architectures, the dataflow software is using
 990 multi-threaded software design for CPU consuming operations. The Input/Output
 991 of the dataflow is based on asynchronous communication using industry standard
 992 libraries such as the Boost::ASIO library. All the ATLAS software suite was
 993 switched to exclusively 64 bit operation in 2016.

994 In summary, the elements of the Run-2 ATLAS dataflow are:

- 995 • The Readout System (ROS) buffers front-end data from the detectors and
 996 provides a standard interface to the DAQ system.
- 997 • The Region of Interest Builder (RoIB) receives the L1 trigger information
 998 from the RoIs and combines the information for the HLT supervisor.

- 999 • The HLT Supervisor (HLTSV) can handle the input from the RoIB and
 1000 manage the HLT farm of about 2000 machines at over 100 kHz.

- 1001 • The Data Collection Manager (DCM) handles all Input/Output on the HLT
 1002 nodes, including RoI requests from the HLT and full event building.

- 1003 • The HLT processing units (HLTPU) run the actually HLT algorithms which
 1004 are forked from a single mother process to maximize memory sharing.

- 1005 • The Data loggers or SubFarm Output (SFO) are responsible for saving the
 1006 accepted events to disk, and sending the files to CERN permanent storage
 1007 infrastructure.

1008 3.4 ATLAS Operations

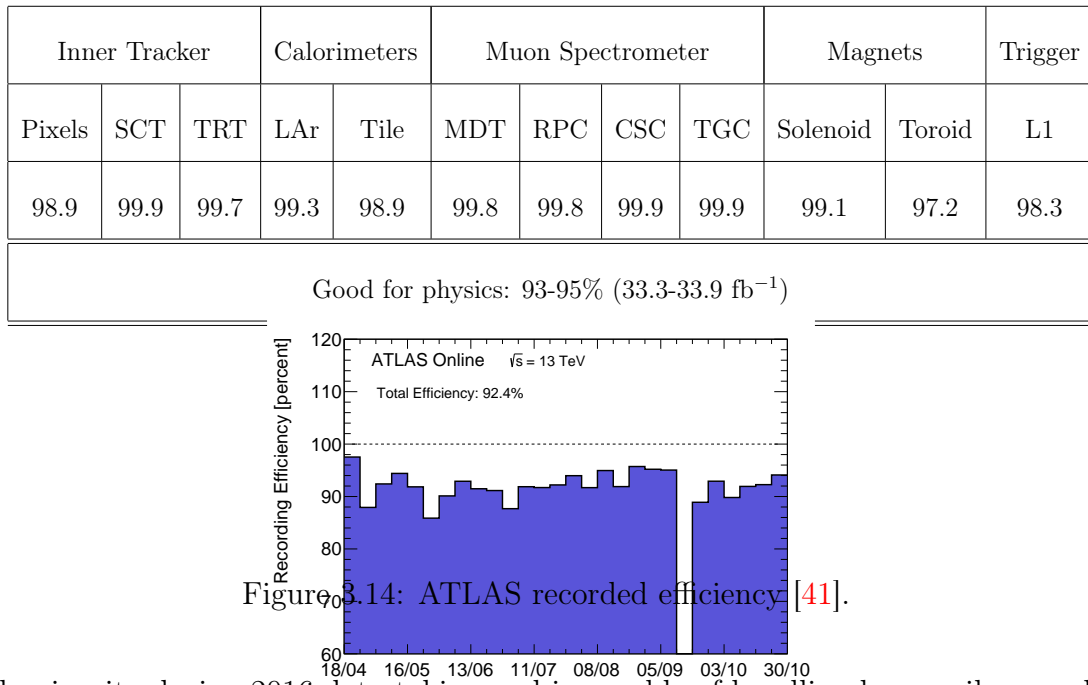
1009 3.4.1 ATLAS Operation

1010 The reliable operation of the different ATLAS systems directly impacts the
 1011 efficiency of the ATLAS experiment in recording the $p - p$ collisions delivered by
 1012 the LHC. As a result, high data-taking efficiency is crucial for the ATLAS physics
 1013 program.

1014 All the ATLAS subdetectors have operated with a very high efficiency (93–95%)
 1015 as shown in Table 3.1 for the 2016 data taking run.

1016 The ATLAS recorded efficiency in 2016 is over 90%, as shown in Figure 3.14
 1017 with a negligible fraction of data loss due to the ATLAS DAQ system. The
 1018 ATLAS dataflow architecture is scaling well with the increased instantaneous

Table 3.1: Luminosity weighted relative fraction of good quality data delivery efficiencies (%) by the various components of the ATLAS detector and trigger subsystems during LHC stable beams in pp collisions at $\sqrt{s} = 13$ TeV with 25 ns bunch spacing between April-October 2016, corresponding to a recorded integrated luminosity of 35.9 fb^{-1} . The toroid magnet was off for some runs, leading to a loss of 0.7 fb^{-1} .



1019 luminosity during 2016 data-taking and is capable of handling larger pileup and
 1020 thus larger event sizes. For illustration, Figure 3.15 shows the evolution of the
 1021 average processing time per event and the event size where there is relatively mild
 1022 increase as a function of pileup which is well within the system capacity.

1023 As a result of this excellent performance of all the subdetectors, ATLAS has
 1024 recorded almost 92% of the luminosity delivered by the LHC during 2015 and
 1025 2016 as illustrated in Figure 3.16. The total integrated luminosity used in this
 1026 analysis after applying a large number of checks amounts to 36.1 fb^{-1} divided

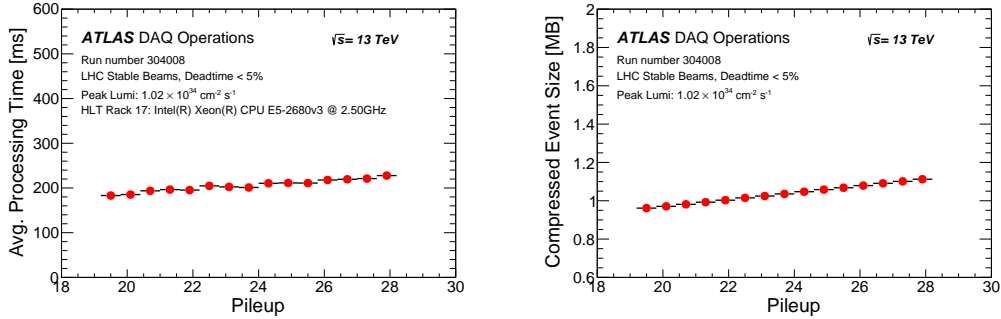


Figure 3.15: Performance in Run 2: Average processing time as a function of pileup (left), compressed event size as a function of pileup (right).

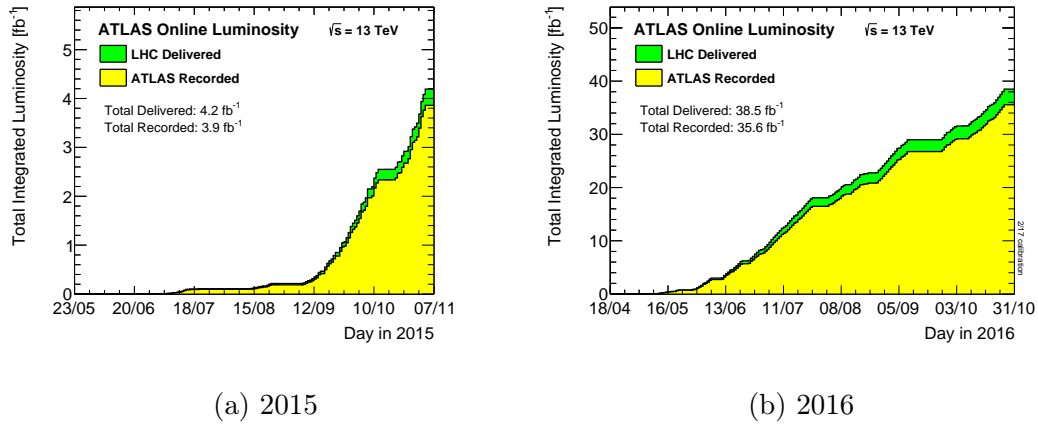


Figure 3.16: Cumulative luminosity versus time delivered to (green) and recorded by ATLAS (yellow) during stable beams for pp collisions at 13 TeV centre-of-mass energy in (a) 2015 and (b) 2016.

¹⁰²⁷ between 3.2 fb^{-1} in 2015 and 32.9 fb^{-1} in 2016.

¹⁰²⁸ 3.5 Event Simulation

¹⁰²⁹ In order to interpret the LHC data, it is essential to compare the observations
¹⁰³⁰ to the expected outcomes from a physical model, typically the standard model
¹⁰³¹ and a SUSY scenario. The event simulation starts from a proton proton collision

1032 leading to the process of interest all the way to the expected detector response.

1033 These steps are the following:

- 1034 • Event generation: The process of interest $pp \rightarrow X$ is generated by relying
1035 on random sampling using Monte Carlo (MC) techniques, which repeatedly
1036 draw samples that represent a possible outcome of a given process. The
1037 processes are generated using a software package, MADGRAPH [42] for
1038 example, which calculates the matrix element for each process to some
1039 order in QCD. Generators start from partons of a pp collision, using parton
1040 distribution functions, and calculate the processes up to leading order or
1041 next-to-leading order. For processes where the cross-section at a higher
1042 order is non-negligible a factor called the k -factor is applied to the expected
1043 cross-section. The partons from the hard interaction are coloured and radiate
1044 gluons described by a parton showering software, as PYTHIA [43]. The
1045 generators used in the analysis are given in Section 5.3. The raw output
1046 of such generators is an input to the next steps of simulation. They can
1047 also be used to perform generator level studies, also called “truth level”,
1048 undergoing minimal processing to evaluate the sensitivity and acceptance of
1049 the analysis (for example Table 5.7).

- 1050 • Detector simulation: The event generator gives particle momenta at the
1051 hadron level which are then processed by GEANT4 [44], which simulates
1052 the propagation of particles through the different materials comprising
1053 the detector. The simulation includes the best knowledge of the detector

1054 geometry, material budget and modeling of the particle interactions. The
 1055 full simulation of the detector is a slow process. For many applications,
 1056 such as the generation of SUSY signals, it is faster to use a parametrized
 1057 response of the calorimeters [45].

- 1058 ● Digitisation: The detector simulation records the interaction of particles
 1059 with the different components of the detector in the form of hits and energy
 1060 deposits in the detector. The latter are used as inputs to emulate the
 1061 response of the readout electronics of the detector. The output from this
 1062 step is identical to the data recorded by the detector.
- 1063 ● Reconstruction: At this stage, both the recorded events by the detector and
 1064 simulated events are used to identify objects associated with fundamental
 1065 particles, namely electrons, muons, photons, and jets. The energy deposits
 1066 not matched to physics objects are collected into a “soft terms” category
 1067 used in the computation of the missing transverse momentum.

1068 There are two other important elements of the simulation that are less un-
 1069 derstood. The simulated MC samples must handle the underlying event, which
 1070 is the remainder of the non-hard scattered partons of the original interacting
 1071 protons. Also, the MC generators must simulate the interactions between the
 1072 other particles in the beam crossing, also referred to as pileup. In practice, the
 1073 MC is generated with an expected pileup profile which is later corrected based on
 1074 the observed pileup profile.

1075 The final physics objects from the reconstruction step do not reflect all the
 1076 knowledge we have about the detector. For instance, the energies of the objects
 1077 must be calibrated or that certain parts of the detector may not always be working
 1078 with the desired specification. Once the reconstructed objects are defined and
 1079 calibrated, the data is ready for analysis. Typically, the size of the dataset is
 1080 reduced from petabytes to a size of few terabytes by only selecting the objects of
 1081 interest in the analysis. For instance, this analysis requires at least two leptons
 1082 applied to the samples used which significantly reduce the sample size.

1083 **3.6 Reconstruction and Identification Techniques**

1084 The identification and reconstruction step relies on the properties that particles
 1085 display when they interact with the different components of the detector described
 1086 in Section 3.2. Once the particle is identified, it is desirable to determine its
 1087 momentum and its origin among other properties. The important part for the
 1088 analysis is how well these objects are reconstructed which can be determined
 1089 by measuring the reconstruction and identification efficiencies as a function of
 1090 kinematic particles, usually p_T and η . In the next sections we briefly describe how
 1091 the main physics objects used in this analysis are identified and their efficiencies.

1092 **3.6.1 Basic Principle**

1093 In this section we describe the higher-level reconstruction of particles as they
 1094 interact with the different components of the detector. The schematic of Figure 3.17
 1095 summarizes the signatures of the different particles in the ATLAS detector.

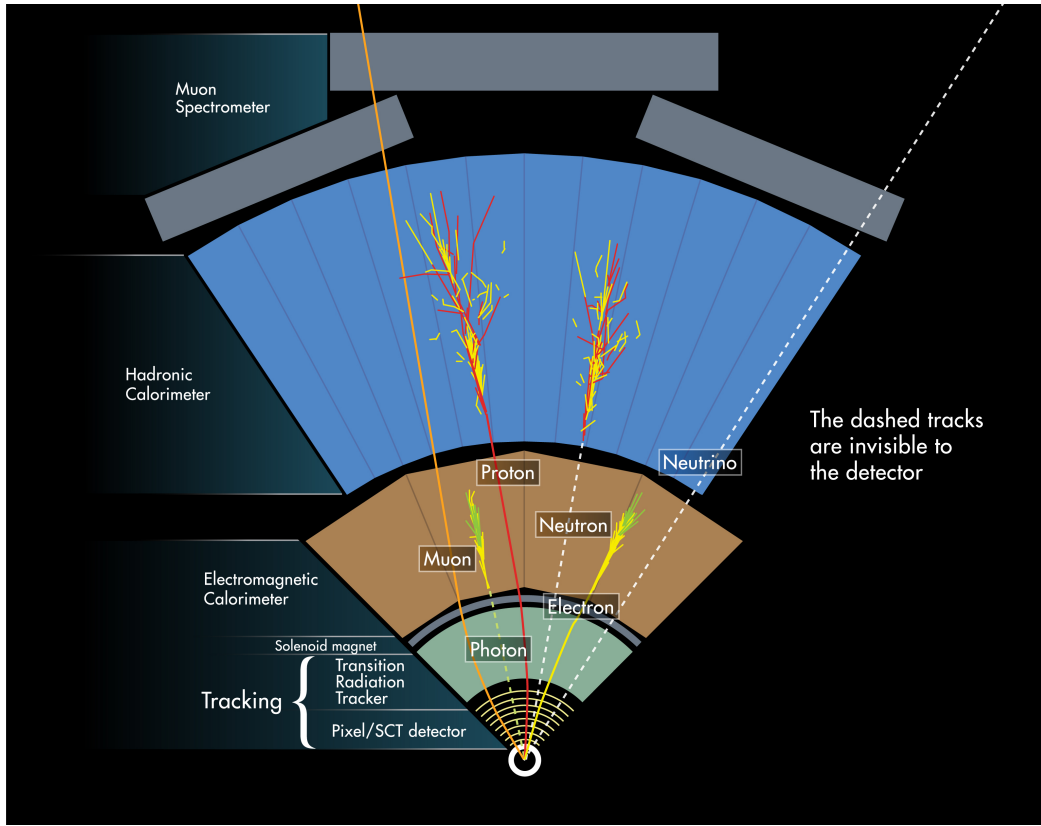


Figure 3.17: The different signatures of particles traversing the detector are shown in the transverse plane of the ATLAS detector.

1096 The most important reconstructed particles for the analysis presented in this
 1097 dissertation are charged leptons. Charged leptons come from electroweak processes
 1098 and provide clear signals which can be accurately reconstructed. In the remainder
 1099 of this dissertation, leptons will refer to only electrons or muons.

1100 Muons are the simplest to identify since they traverse the entire ATLAS
 1101 detector: all other interacting particles are stopped before reaching the muon
 1102 spectrometer. They are reconstructed as tracks in the inner detector matched to
 1103 tracks in the muon spectrometer, and leave little energy in the electromagnetic
 1104 and hadronic calorimeters. Muons are produced from decays of W and Z bosons

1105 with a relatively large momentum, above 15 GeV, and are produced in isolation
 1106 from surrounding detector activity, qualities that we will use in this analysis. The
 1107 latter is called “isolation” which requires the energy of the reconstructed tracks and
 1108 clusters near the reconstructed muon not exceed a certain value. This requirement
 1109 is effective at suppressing muons produced from background processes such as
 1110 meson decay in flight and heavy-flavor decay detailed in Chapter 6.

1111 Electrons are identified by a track in the inner detector that initiates an
 1112 electromagnetic shower in the electromagnetic calorimeter. Most of the time, all of
 1113 the energy of the electron is absorbed before reaching the hadronic calorimeter. The
 1114 electron is identified by matching reconstructed EM clusters to tracks reconstructed
 1115 in the inner detector. This signature suffers from Large backgrounds from other
 1116 types of charged particles can mimic this signature. For these reason, ATLAS
 1117 uses several tools to effectively distinguish between the desired electrons and
 1118 background. Similar to muons, isolation is one of these tools.

1119 Photons also produce an electromagnetic shower upon entering the calorimeter,
 1120 except that they leave no track in the inner detector since they are neutral. In
 1121 practice, photons might undergo a conversion to an e^+e^- pair in the detector
 1122 material before entering the calorimeter which will result in a track in the inner
 1123 detector. Photons of the former case are called un-converted, while the latter are
 1124 called converted photons. ATLAS has dedicated algorithms to identify photon
 1125 conversions from pairs of reconstructed tracks.

1126 Tau leptons are charged particles that decay to the other leptons (40% of
 1127 the time) or to hadrons (60 % of the time) before entering the detector. If

1128 they decay to electrons or muons and neutrinos, they are indistinguishable from
 1129 electrons or muons coming from W or Z bosons. The experimental signatures of
 1130 hadronically decaying taus are multiple hadronic showers matched to tracks in
 1131 the inner detector. The latter suffers from large backgrounds from other types of
 1132 particles that cannot be suppressed as efficiently as background from the leptonic
 1133 tau decay.

1134 Neutrinos only interact via the weak force and are thus not directly detected
 1135 by ATLAS. As shown in Figure 3.17, they pass through all the sub-detectors.
 1136 However, their presence is inferred from an overall transverse momentum imbalance
 1137 of the measured momenta in the event. Thus, the transverse momentum of the
 1138 neutrinos can be inferred. This type of signature is similar to potential new
 1139 particles that will not interact with our detector. Nevertheless, neutrinos are
 1140 very well understood and any potential contribution from them can be accurately
 1141 predicted.

1142 The reconstruction of jets is an essential part of the analysis presented in this
 1143 dissertation. Colored quark and gluons from the primary interaction undergo a
 1144 process referred to as hadronization, where they convert to sprays of colorless
 1145 hadrons. The collection of this spray of particles is referred to as a jet. The
 1146 reconstruction of a jet is based on regrouping of reconstructed clusters and tracks
 1147 into larger collections using various clustering algorithms as it will be described
 1148 next. By measuring the energy and direction of a jet, we can infer information
 1149 about the initial quarks or gluons that participated in the physics processes under
 1150 study. It can also be used to determine the energy of the initial parton in the

1151 hard interaction, a challenging aspect of jet reconstruction. The energy of the
 1152 jet must be calibrated by determining the Jet Energy Scale (JES) and the Jet
 1153 Energy Resolution (JER). The uncertainties associated with the JES and JER are
 1154 one of the largest experimental uncertainties in this analysis.

1155 The jet reconstruction algorithms cannot determine the type of parton that
 1156 initiated a given jet, except for b -quarks. Since b -quark hadron decay with sup-
 1157 pressed weak interactions, they are relatively long-lived travelling a few millimeters
 1158 before they decay. Given the fine tracking resolution of ATLAS, a millimeter
 1159 displacement from the interaction point is large enough to be resolved. It is thus
 1160 possible to identify jets containing b -hadrons in a process called “ b -tagging”. This
 1161 type of jets, called b -jets, are used in this analysis.

1162 More technical details about the reconstruction procedure and the efficiencies
 1163 of the reconstructed objects will be given next.

1164 3.6.2 Electrons

1165 Electrons are reconstructed and identified for $p_T > 5$ GeV and $|\eta| < 4.9$ [46].
 1166 The electrons are identified by a cluster in the electromagnetic calorimeter of
 1167 more than 2.5 GeV matched to a track in the inner detector. The electron
 1168 trajectory is determined using information from the inner detector. This involves
 1169 the measurement of the track associated parameters : the position in the transverse
 1170 (d_0) and longitudinal (z_0) planes of the perigee, the particle direction (ϕ, θ) and the
 1171 parameter which provides the inverse track momentum multiplied by the charge
 1172 (q/p). The track parameters and the associated uncertainties are obtained from

1173 the track fitting procedure performed with the ATLAS Global χ^2 Track Fitter.

1174 The goal is to improve the efficiency of identifying electrons while rejecting

1175 background electrons arising from hadronic jets mistaken for electrons, electrons

1176 from photon conversion, Dalitz decays and from semileptonic heavy-flavour hadron

1177 decays. To do so, three identification (ID) criteria, loose, medium, and tight

1178 are defined via likelihoods based on calorimetric cluster shower shapes, track

1179 and track-to-cluster matching variables. The tighter the ID criteria, the higher

1180 the rejection of background electrons but the lower the identification efficiency.

1181 Figure 3.18 shows the efficiencies in data and MC for three operating points

1182 that are based on a likelihood approach, Loose, Medium and Tight. The data

1183 efficiencies are obtained by applying data/MC efficiency ratios that were measured

1184 in $J/\psi \rightarrow e^+e^-$ and $Z \rightarrow e^+e^-$ events to MC simulation. The lower efficiency in

1185 data than in MC arises from the fact that the MC does not properly represent

1186 the 2016 TRT conditions, in addition to the known mis-modelling of calorimeter

1187 shower shapes in the GEANT4 detector simulation. The reconstruction efficiency

1188 of electrons is around 95% for low p_T and goes up to 99.9% for electron $p_T > 45$

1189 GeV.

1190 To study and compute the corrections needed to account for the detector

1191 geometry and material distribution two sets of MC samples are used. For the first

1192 set an ideal geometry (no mis-alignments) with the best knowledge of the dead

1193 material is implemented. For the second scenario, the dead material between the

1194 tracker and calorimeters is increased and the mis-alignments are included. The

1195 latter is used to assign the systematic uncertainties.

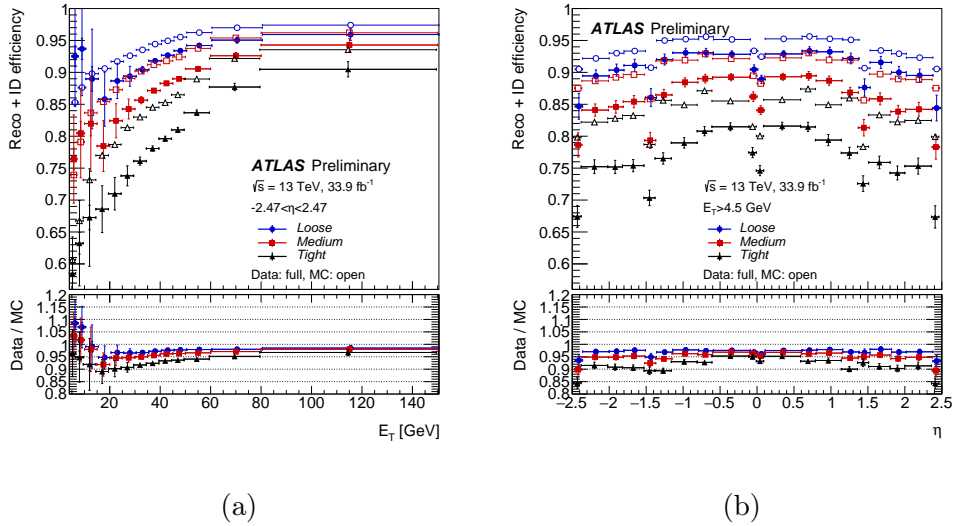


Figure 3.18: Electron reconstruction and identification efficiencies in $Z \rightarrow e^+e^-$ events as a function of (a) pseudo-rapidity η (b) transverse energy E_T . The total statistical and systematic uncertainty is displayed.

1196 3.6.3 Muons

The ATLAS detector has been designed to provide clean and efficient muon identification and precise muon momentum measurements over a wide range of energy and solid angle. The muon reconstruction starts in the inner detector where tracks are identified up to $|\eta| < 2.5$ in a solenoidal field of 2 Tesla. The muon spectrometer measures muons up to $|\eta| < 2.7$ providing momentum measurements with a design relative resolution of better than 3% over a wide p_T range and to 10% at TeV. Similar to electrons, four muon identification selections are defined in order to meet the specific needs of different physics analyses:

- loose muons: maximize efficiency: ideal for multilepton final states analysis
 - medium muons: minimize systematics uncertainties

- 1207 • tight muons: optimize purity
 1208 • high- p_T muons: maximize momentum resolution for high p_T tracks (> 100
 1209 GeV)

1210 Figure 3.19 shows the reconstruction efficiency of the muon for different selections
 1211 measured in $Z \rightarrow \mu\mu$ and $J/\psi \rightarrow \mu\mu$ events.

1212 The reconstruction efficiency is measured to be close to 99% over most of the
 1213 phase space relevant for the analysis. The isolation efficiency is between 93% and
 1214 100% based on the selection and muon momentum. The simulation reproduce
 1215 both efficiencies very well. The momentum resolution is measured to be as low as
 1216 1.7% and the momentum scale uncertainty is less than 0.05%.

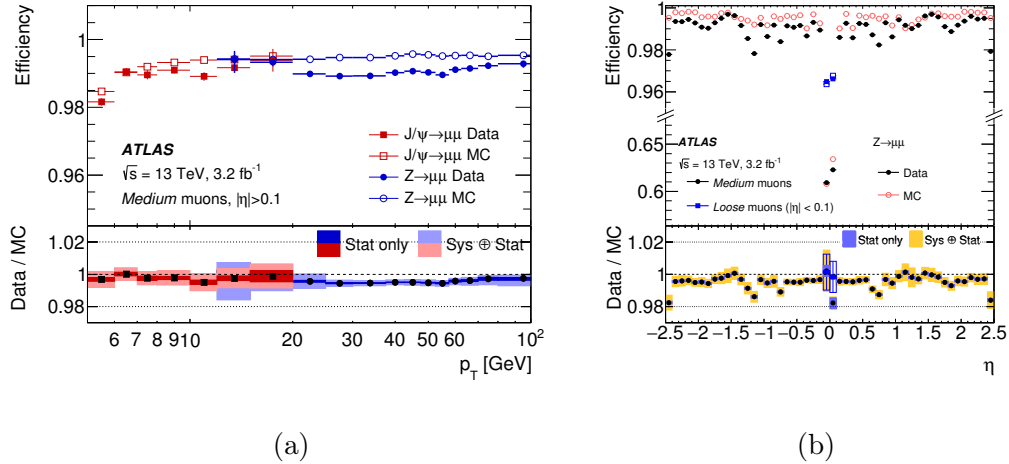


Figure 3.19: (a) Reconstruction efficiency for the medium muon selection as a function of (a) p_T (b) η of the muon. The error bars on the efficiencies indicate the statistical uncertainty. The panel at the bottom shows the ratio of the measured to predicted efficiencies, with statistical and systematic uncertainties.

1217 **3.6.4 Jets**

1218 Jets are reconstructed using the anti- k_t jet algorithm [47] with the distance
 1219 parameter R set to 0.4 and a three dimensional input of topological energy
 1220 clusters in the calorimeter [48]. The advantage of using the anti-kt algorithm is
 1221 that it is infrared and collinear safe.². It is also resilient to soft-QCD emissions,
 1222 a process that is common in the hadron colliders. The jets are constructed by
 1223 defining two distances:

- 1224 • $d_{ij} = \min((k_{kj}^{2p}, k_{kj}^{2p}) \frac{\Delta_{ij}^2}{R^2})$: the distance between two particles i and j.
 - 1225 • $d_{iB} = k_{ti}^{2p}$: the distance between a particle i and the beam B .
- 1226 where $\Delta_{ij}^2 = (y_i - y_j)^2 + (\phi_i - \phi_j)^2$ and k_{ti} , y_i , and ϕ_i are the transverse momentum,
 1227 rapidity, and azimuth of the particle i . The radius parameter R scales d_{ij} with
 1228 respect to d_{iB} such that any pair of final jets a and b are separated by at least
 1229 $R^2 = \Delta_{ab}^2$. The parameter p governs the relative power of energy with respect
 1230 to the geometrical scales, and is set to $p = -1$ for the anti- k_t algorithm.

1231 The energies of the jets are calibrated to account the necessary losses asso-
 1232 ciated with sampling calorimeter, the presence of dead material, energy loss in
 1233 non-instrumented regions, etc. This is performed using the local cluster weighting
 1234 (LCW) scheme [49], which uses calibrated topological clusters as input the anti- k_t
 1235 jet algorithm, and taking into account jet energy scale (JES) and jet energy reso-

²These two problems arise when defining a seed used as a starting point of an iterative process of re-clustering energy depositions in the calorimeter cells. If only particles above some momentum threshold are used as seeds then the procedure is collinear unsafe. On the other hand, if the addition of an infinitely soft particle leads to a new stable energy cone being found then the procedure is infrared unsafe.

lution (JER) calibrations. Both JES and JER can have an important contribution
 to the systematic uncertainties of this analysis. The fractional JES uncertainty in
 Figure 3.20 shows that jets with p_T below 50GeV can have a larger uncertainty.
 The choice was made to only require jets above 50 GeV in the analysis for this
 reason. The fractional JER is around 17% for jets with p_T of 30 GeV decreasing
 down to 5% for more energetic jets. An additional variable is used to suppress jets
 from pileup, called the jet vertex tagger (JVT). JVT is a multivariate combination
 of the fraction of the total momentum of tracks in the jet which is associated with
 the primary vertex and track-based variables to suppress pileup jets [50].

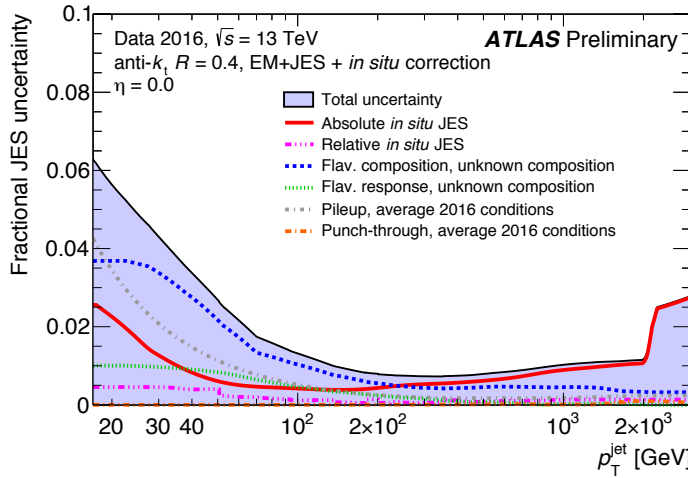


Figure 3.20: Fractional jet energy scale systematic uncertainty components as a function of p_T for anti- k_t jets at $\eta = 0.0$ with distance parameter of $R = 0.4$ after calibration. The total uncertainty (all components summed in quadrature) is shown as a filled blue region topped by a solid black line.

1245 **3.6.5 Heavy flavor**

1246 Jets containing b -hadrons (commonly referred to as b -tagging) is performed with
1247 the MV2 algorithm, a multivariate discriminant making use of track impact
1248 parameters and reconstructed secondary vertices [51, 52] to provide the best
1249 separation among the different jet flavour hypotheses. An example of the output
1250 of the multivariate discriminant is shown in Figure 3.21a where typically a cut
1251 must be applied on the score to identify an operating working point. Three MV2
1252 algorithms were released that correspond to MV2c00, MV2c10, and MV2c20.
1253 MV2c00 denotes the MV2 algorithm where no c-jet contribution was present
1254 in the training and MV2c10 (MV2c20) denote the MV2 outputs where a 7%
1255 (15%) c-jet fractions was present in the background sample. The performance
1256 of the optimized MV2c00, MV2c10 and MV2c20 b-tagging algorithms is shown
1257 in Figure 3.21b for the c-jet rejection as a function of the b-jet efficiency. The
1258 MV2c20 is the best performing algorithm leading to an optimal rejection of c-jets
1259 at a given b-tagging efficiency. As a result, it is the algorithm used in this analysis.

1260 **3.6.6 Missing transverse momentum**

1261 The missing transverse momentum is an important quantity in searching for new
1262 physics scenarios which expect a stable and non-electromagnetically interacting
1263 particle. Such particle does not interact with the detector and can only be identified
1264 through an imbalance of the momentum distribution between the particles of the
1265 event. Since the momentum of the colliding protons is almost along the beam,

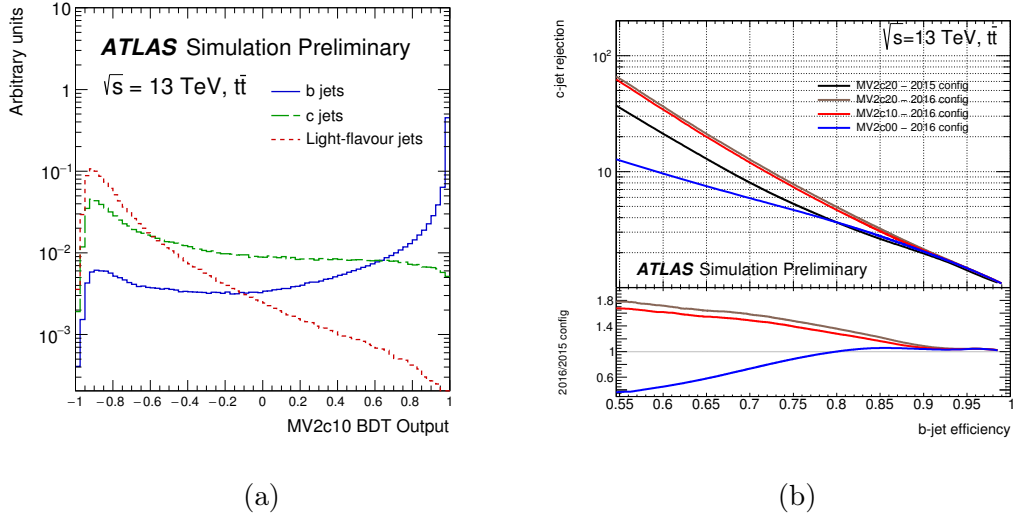


Figure 3.21: (a) MV2c10 BDT output for b- (solid blue), c- (dashed green) and light-flavour (dotted red) jets evaluated with $t\bar{t}$ events. (b) c-jet rejection versus b-jet efficiency for the 2015 and 2016 configurations of the algorithm. (for the 2016 configuration).

1266 longitudinal, the transverse component of the momenta of the scattered objects
 1267 should add up to zero. Based on the conservation of momentum, the sum of all
 1268 visible four momenta projected in the transverse plane should be close to zero if no
 1269 particles are missed. However, this quantity will be large if a particle, potentially
 1270 from new physics models, escaped detection. The missing transverse momentum
 1271 is defined as the negative vector sum of the transverse momenta of the visible
 1272 reconstructed objects in the event:

$$p_T^{\text{miss}} = - \sum_{\text{visible}} p_T \quad (3.5)$$

1273 where the visible objects include electrons, muons, jets, photons, taus, and a soft
 1274 term. In the rest of the dissertation, the magnitude of the missing transverse

₁₂₇₅ momentum vector is denoted by E_T^{miss} . The soft term is a fundamental quantity
₁₂₇₆ in the reconstruction of E_T^{miss} and be estimated by

- ₁₂₇₇ • Calorimeter based Soft Term (CST): accounts for both neutral and charged
₁₂₇₈ particle energies.
- ₁₂₇₉ • Track based Soft Term (TST): incorporates a natural pileup suppression by
₁₂₈₀ selecting only tracks from primary vertices.

₁₂₈₁ The E_T^{miss} performance depends on the event topology affected by the presence
₁₂₈₂ of true E_T^{miss} , from neutrinos for example, charged leptons, jet activity, and others.
₁₂₈₃ The E_T^{miss} performance is generally studied with processes with and without
₁₂₈₄ genuine E_T^{miss} , such as $W \rightarrow e\nu$ and $Z \rightarrow \mu\mu$ events. The scale and resolution
₁₂₈₅ for the reconstructed E_T^{miss} in these processes are indicative of the reconstruction
₁₂₈₆ quality. For illustration, results obtained with $Z \rightarrow \mu\mu$ events are shown in
₁₂₈₇ Figure 3.22. Generally, the E_T^{miss} has a resolution in the order of 10 to 20 GeV.

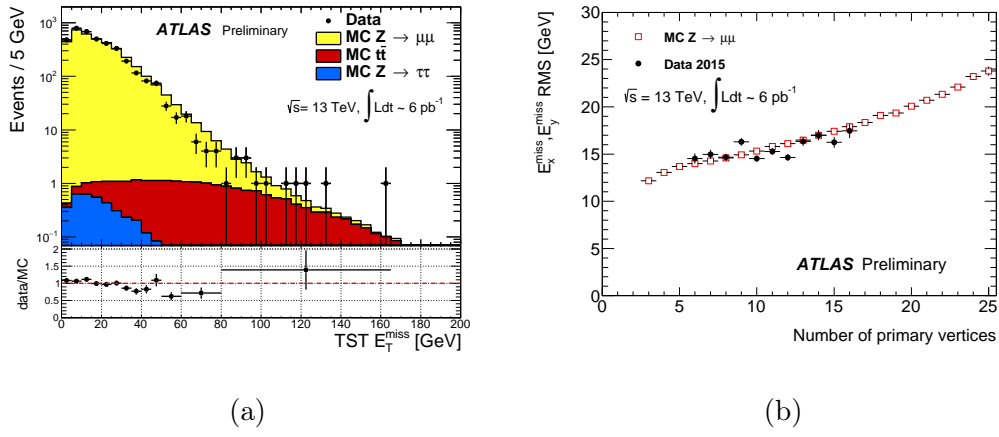


Figure 3.22: (a) E_T^{miss} distribution as measured in data with $Z \rightarrow \mu\mu$ events without pile-up suppression. (b) E_T^{miss} resolution as a function of the number of primary vertices in $Z \rightarrow \mu\mu$ events. The data (black circles) and MC simulation (red squares) are overlaid.

₁₂₈₈ **Chapter 4**

₁₂₈₉ **The Region of Interest Builder**

₁₂₉₀ **4.1 Overview**

₁₂₉₁ The TDAQ system reduces the proton interaction rate from 40 MHz to the
₁₂₉₂ ATLAS data storage capacity of about 1.5 kHz. A hardware First Level Trigger
₁₂₉₃ (L1) reduces the rate to 100 kHz and a software High Level Trigger (HLT)
₁₂₉₄ selects events for offline analysis. Jet, electromagnetic and tau clusters, missing
₁₂₉₅ transverse momentum (E_T^{miss}), $\sum E_T$, jet E_T , and muon candidate information
₁₂₉₆ from L1 determine detector Regions of Interest (RoIs) that seed HLT processing.
₁₂₉₇ These RoIs are provided to the HLT by a custom VMEbus based system, referred
₁₂₉₈ to as the Region of Interest Builder (RoIB) [53]. The RoIB collects data from L1
₁₂₉₉ trigger sources and assembles the data fragments into a complete record of L1 RoIs.
₁₃₀₀ These RoIs are made available to the HLT to initiate event processing. In order
₁₃₀₁ to improve maintainability and scalability, and to minimize the amount of custom
₁₃₀₂ hardware needing to be supported, the RoIB was implemented using commodity
₁₃₀₃ server hardware and an interface technology deployed within the ATLAS Trigger
₁₃₀₄ and Data Acquisition (TDAQ) system. The approach of implementing the RoIB
₁₃₀₅ functionality in software has been investigated in the past and the conclusion at
₁₃₀₆ that time was that a software based approach is possible but requires a card with a
₁₃₀₇ higher readout rate [54]. Since data readout cards operating at high rates became
₁₃₀₈ available and the capabilities of computers have improved with the increase in

1309 CPU clock speed and number of cores, it became possible to implement the RoIB
 1310 functionality using a PC based approach. The PC based RoIB must duplicate the
 1311 functionality of the VMEbus based RoIB, which means that the PC based solution
 1312 must receive and assemble the individual L1 fragments and pass them as a single
 1313 L1 result to the HLT. Modern computers have multicore CPU architectures with
 1314 the possibility of running multi-threaded application, a feature which is being
 1315 fully exploited in the RoIB software to achieve the desired performance of 100
 1316 kHz over 12 input links for fragment sizes of 400 bytes. This chapter describes
 1317 the work of the author in evolving the RoIB from the VMEbus based system to
 1318 the PC based system and gives details on the hardware, firmware, and software
 1319 designs used to achieve the full RoIB functionality.

1320 **4.2 VMEbus based RoIB**

1321 **4.2.1 Hardware implementation**

1322 The RoIB was implemented as a custom 9U VMEbus system that includes a
 1323 controller which configures and monitors the system along with custom cards that
 1324 receive and assemble the event fragments and send them to the HLT. Figure 4.1
 1325 shows a block of the RoIB and its connection to external systems.

1326 The RoIB contains four input cards and uses one builder card in the Run-2
 1327 configuration. Each input card accepts three inputs from L1 subsystems. The
 1328 builder card assembles the input data of the events and passes the results via
 1329 two optical links to another receiver card in a PC running the HLT supervisor

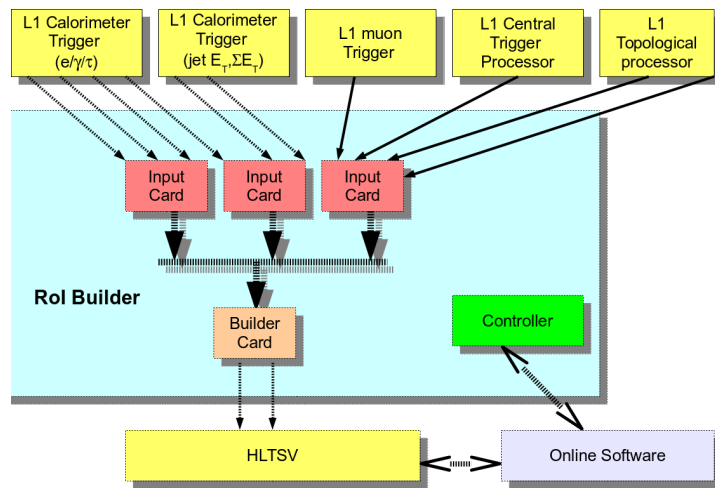


Figure 4.1: Block scheme of the RoI Builder and overview of connections to external systems. The custom input and builder cards and the controller, a commercially available single board computer, are installed in a single 9U VMEbus crate. The controller connects to the Control Network to interact with the rest of the data acquisition system.

1330 (HLTSV) application. The receiver card in the HLTSV is a TILAR card [55] that
 1331 implements four PCI-express Generation 1 (PCIe Gen1) with 8 lanes ¹ to interface
 1332 with the two optical links. The HLTSV manages the HLT processing farm by
 1333 using L1 results provided by the RoIB, retrieves events from the ROS, assigns
 1334 events to HLT farm nodes, and handles event bookkeeping including requesting
 1335 removal of data from ROS storage when no longer required.

1336 The fragments received by the RoIB are identified by a 32 bit identifier, the
 1337 extended L1 ID (L1ID). The RoIB input cards use the L1ID and the number of
 1338 outputs enabled to assign keys to the various fragments and send them to the
 1339 output channel in the builder card that was assigned that key value. The input
 1340 data is transferred over a custom J3 back-plane. The back-plane operates at 20
 1341 MHz and transfers 16 data bits per clock cycle simultaneously for up to 12 inputs.
 1342 The total maximum data throughput is therefore 480 MB/s, 40 MB/s per input.
 1343 The maximum size of any single fragment is limited to 512 bytes imposed by
 1344 resources available in the FPGA ² firmware. The current RoIB input links are
 1345 listed in Table 4.1.

1346 4.2.2 System Performance and Evolution

1347 The custom VMEbus based RoIB operated reliably during the first run of the
 1348 LHC, however, it is desirable to have a more flexible RoIB. In addition, the RoIB

¹PCI stands for Peripheral Component Interconnect which is a high-speed input/output (I/O) serial bus that can be installed on motherboard of a computer. It can transfer data at a speed of 250 megabytes per second per lane.

²FPGA stands for Field Programmable Gate Arrays which are semiconductor devices composed of configurable logic blocks that can be reprogrammed for a desired application.

Table 4.1: L1 input sources to the RoIB.

Source	Links
Central Trigger Processor (CTP)	1
L1 calorimeters ($e/\gamma, \tau, \text{jet}, \sum E_T$)	6
Muon Trigger to CTP Interface (MUCTPI)	1
Topological processor (L1Topo)	2
Spare	2

1349 is getting close to its design limitation, as seen in Figure 4.5. For fragments of
 1350 400 bytes and inputs from eight L1 systems, referred to as channels, the current
 1351 RoIB rate limit is 60 kHz which is below the required 100 kHz at L1. While the
 1352 current fragment size coming from L1 is around 160 bytes, the sizes are expected
 1353 to grow due to the increase of instantaneous luminosity and the complexity of
 1354 the L1 triggers. The current VMEbus system will be replaced by a PCI-express
 1355 card hosted in the HLTSV PC with the possibility to upgrade the commodity
 1356 hardware (e.g. ability to upgrade CPUs). The new configuration simplifies the
 1357 readout architecture of ATLAS. The targeted rate for event building is 100 kHz
 1358 over 12 input channels for fragment sizes on the order of 400 bytes.

1359 4.3 PC based RoIB

1360 A custom PCIe card developed by the ALICE collaboration, the Common ReadOut
 1361 Receiver Card (C-RORC) [56], was deployed as an upgraded detector readout

1362 interface within the ATLAS ROS with ATLAS specific firmware and software
 1363 called the RobinNP [57]. The new PC based RoIB uses the RobinNP firmware
 1364 and a dedicated program interface to facilitate the implementation of the RoIB
 1365 functionality on a commodity PC. In this section, we describe the C-RORC
 1366 hardware as well as the RobinNP firmware, API, and the event building software.

1367 **4.3.1 The Common Readout Receiver Card**

1368 The C-RORC implements 8 PCIe Gen1 lanes with 1.4 GB/s bandwidth to the
 1369 CPU fed via 12 optical links each running 200 MB/s on 3 QSFP³ transceivers. It
 1370 utilizes a single Xilinx Virtex-6 series FPGA that handles data input from the 12
 1371 links and buffers the data in two on-board DDR3 memories. It is also capable of
 1372 processing and initiating DMA transfer of event data from the on-board memory
 1373 to its host PC's memory. The major components of the C-RORC are annotated
 1374 in the picture shown in Figure 4.2.

1375 **4.3.2 Readout System Firmware and Software**

1376 The RobinNP firmware used for the RoIB is identical to that used in the ATLAS
 1377 ROS[37]. As shown in the schematic of Figure 4.3, the logic is divided into two
 1378 functional blocks, known as sub-ROBs, each servicing six input links and one
 1379 DDR3 memory module. Event data fragments arriving via a link are subjected to
 1380 a range of error checks before being stored in the memory module for the relevant
 1381 sub-ROB. At the same time a token representing the address of a region of the

³QSFP stands for a Quad Small Form-factor Pluggable which is a hot-pluggable transceiver used for data transfer.

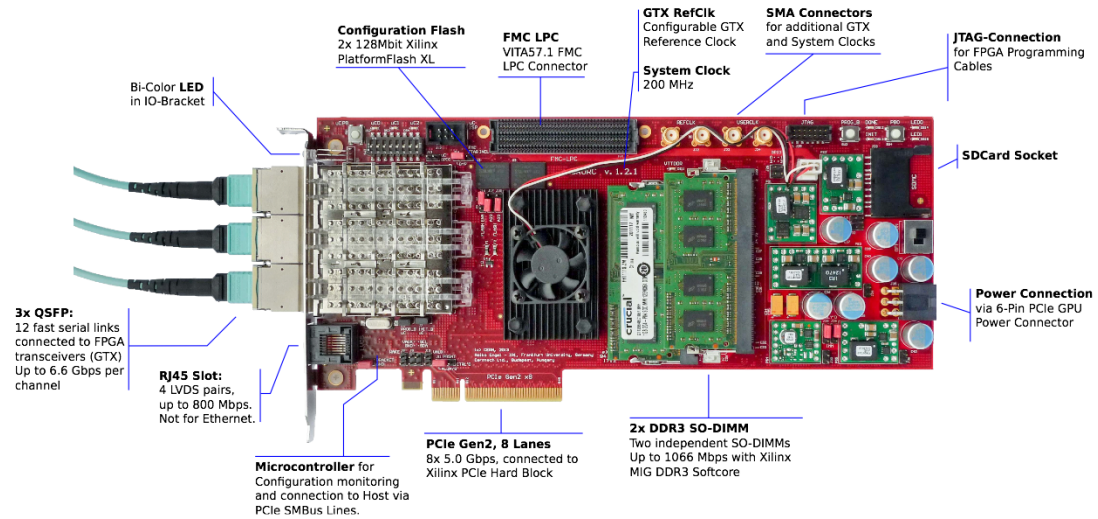


Figure 4.2: Photo of the C-RORC board with the major components and features annotated [57].

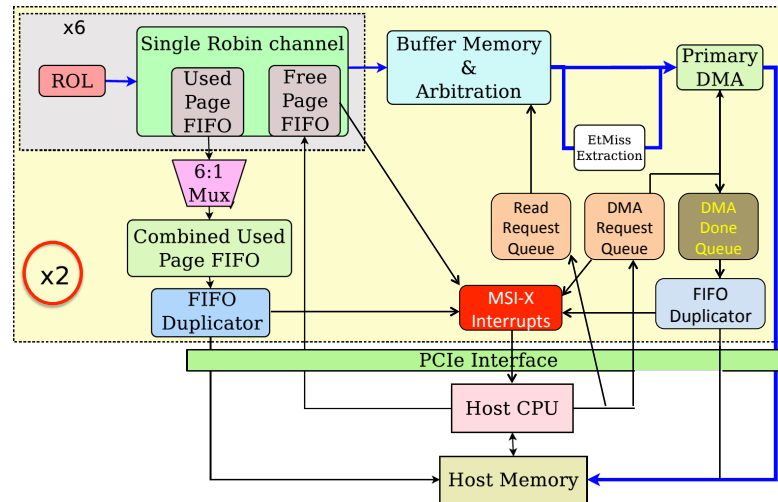


Figure 4.3: RobinNP firmware organization and flow of data from host CPU to the firmware (by means of programmed I/O) and from the firmware to the host memory (by means of DMA).

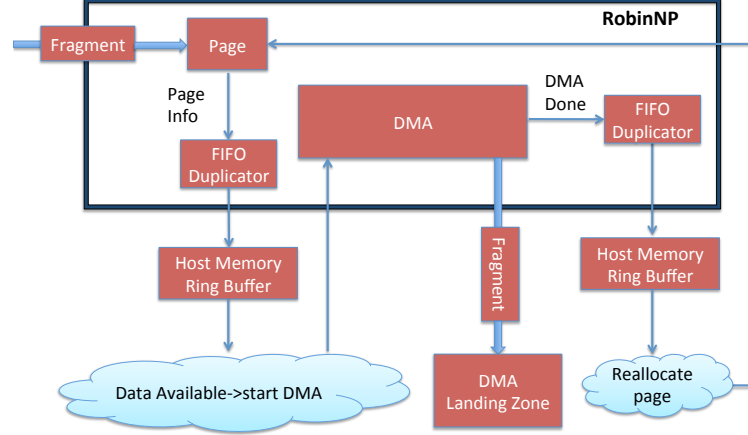


Figure 4.4: Layout of the readout system firmware and software specific to the RoIB.

memory, referred to as a page, is passed to a listening software process via a ‘FIFO duplicator’. To avoid a costly read across the PCIe bus, data is continuously streamed from firmware to software via a chain of firmware and software FIFOs.

Notification of new data arriving in the software FIFO is managed via coalesced interrupts to allow for efficient use of CPU resources. For the RoIB application, the receipt of page information immediately triggers a DMA of fragment data from the RobinNP memory into the host PC memory. The fragments are then passed via a queue (one per sub-ROB) to the RoIB process along with any relevant fragment error information. A schematic of this shortened dataflow path is presented in Figure 4.4. The API for the RoIB process consists of these queues, return queues for processed pages now available for re-use and a configuration interface. The software is implemented with multiple threads each handling specific tasks such as supply of free pages, receipt of used pages, DMA control and bulk receipt of fragment data.

¹³⁹⁶ **4.3.3 RoIB Software**

¹³⁹⁷ The HLTSV is a multi-threaded application that obtains a L1 result from a
¹³⁹⁸ variety of possible input sources and exchanges information with the rest of the
¹³⁹⁹ HLT computing farm. For the RoIB, the L1 source is a RobinNP interface that
¹⁴⁰⁰ performs fragment assembly and is used as a plug-in to the HLTSV application.

¹⁴⁰¹ The RobinNP plug-in has two receive threads, each thread services six channels by
¹⁴⁰² pulling fragments from the RobinNP on-board memories to the host PC. Fragments
¹⁴⁰³ with the same L1ID are copied to a contiguous memory space and a queue of
¹⁴⁰⁴ completed events is prepared. Upon request by the HLTSV, a pointer to the
¹⁴⁰⁵ contiguous memory space is passed back to the HLTSV process for further handling.

¹⁴⁰⁶ In order to optimize concurrent access to RoIB data structures, containers from
¹⁴⁰⁷ the Intel threading building block (TBB) library were used. These containers
¹⁴⁰⁸ allow multiple threads to concurrently access and update items in the container
¹⁴⁰⁹ while maintaining high performance.

¹⁴¹⁰ **4.4 Prototype Tests**

¹⁴¹¹ In order to understand the requirements for the underlying server PC, a validation
¹⁴¹² system based on Intel(R) Xeon(R) CPU E5-1650 v2 @ 3.5 GHz with six cores was
¹⁴¹³ used to perform tests of the PC based RoIB. The goal was to perform software
¹⁴¹⁴ based fragment assembly at a rate of 100 kHz over 12 channels for a typical
¹⁴¹⁵ fragment size of 400 bytes. The current system offers flexibility in terms of the
¹⁴¹⁶ fragment size allowed which was not the case in the VMEbus based RoIB. The

¹⁴¹⁷ initial tests were performed with a standalone application that implements a
¹⁴¹⁸ minimal interface for event building. Once the system was validated, the relevant
¹⁴¹⁹ code modules were integrated into an HLTSV process running within the full
¹⁴²⁰ ATLAS TDAQ software suite with appropriately scaled test hardware to represent
¹⁴²¹ the remaining elements of the system.

¹⁴²² **4.4.1 Standalone Tests**

¹⁴²³ The goal was to test input/output bandwidth limitations of the RobinNP and the
¹⁴²⁴ rate of event building. Initial performance testing used a standalone RobinNP
¹⁴²⁵ application and an external source that emulates the L1 trigger data in the form of
¹⁴²⁶ 32-bit word fragments with 12 channels. In this test, the host PC was running the
¹⁴²⁷ assembly routine with a single threaded application. Figure 4.5 shows the input
¹⁴²⁸ rate without event building as a function of fragment size. For 400 byte fragments
¹⁴²⁹ the input rate to the RobinNP is 215 kHz. The same figure shows the event
¹⁴³⁰ building rate which is 150 kHz. This performance shows that the event building
¹⁴³¹ at the required rate of 100 kHz with 12 channels is achievable in a standalone
¹⁴³² application.

¹⁴³³ **4.4.2 Full System Tests**

¹⁴³⁴ Since the HLTSV is performing tasks other than the event building, there is
¹⁴³⁵ overhead associated with additional operations that reduces the performance. For
¹⁴³⁶ this reason, we use the full ATLAS TDAQ software in a test environment that
¹⁴³⁷ emulates the major components of the ATLAS data acquisition system, shown

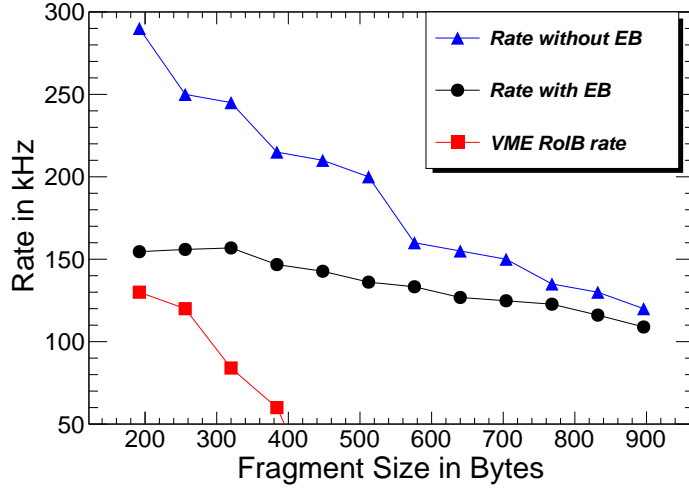


Figure 4.5: Rate as a function of the fragment size (in bytes) with an external source that emulates the L1 trigger input. The rates shown are for the input rate to the RobinNP without event building (EB) (triangle), rate with EB (circle), and for comparison, the current VMEbus RoIB rate is also shown (square).

¹⁴³⁸ in Figure 3.14. The setup includes an emulated input from L1 trigger sources,
¹⁴³⁹ the HLTSV and other PCs to simulate the HLT computing farm, and the ROS
¹⁴⁴⁰ that buffers the full event data. In this test setup, an external source sends data
¹⁴⁴¹ that emulates L1 RoIs via 12 links connected to the RobinNP hosted by the
¹⁴⁴² HLTSV. When the HLTSV requests a built RoI event, the software RoIB plug-in
¹⁴⁴³ provides the RoI event which will be used to seed requests for the event data to
¹⁴⁴⁴ be processed. Figure 4.6 shows an event building rate of 110 kHz measured with
¹⁴⁴⁵ 400 byte fragments with the HLTSV application in a setup close to the ATLAS
¹⁴⁴⁶ TDAQ system.

¹⁴⁴⁷ As shown in Figure 4.7, the performance of the PC-RoIB with realistic running
¹⁴⁴⁸ ATLAS conditions is improved over the VME-RoIB particularly at high RoI sizes

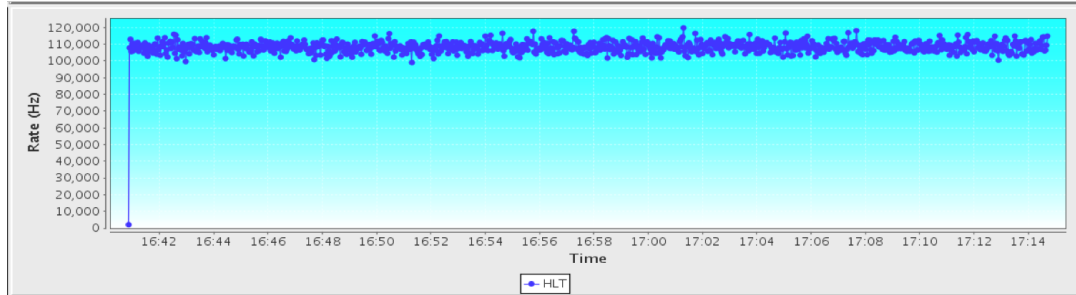


Figure 4.6: Screenshot of a monitoring tool which shows the HLTSV processing rate using the ATLAS TDAQ software.

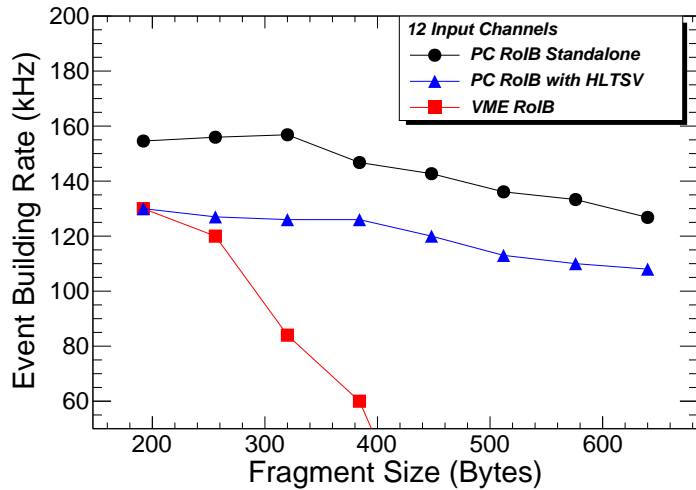


Figure 4.7: The event building rate as a function of the RoI record size in bytes.

The rates are shown for a standalone application that implements a minimal interface for event building, the integrated RoIB software into an HLTSV process running within the full ATLAS TDAQ software suite, and for comparison the VME-RoIB performance.

¹⁴⁴⁹ and maintains a rate of over 100 kHz with 12 channels.

¹⁴⁵⁰ The design specification of the ATLAS L1 trigger is to send data at 100 kHz. While the tests above showed that the PC RoIB meets the desired rate

1452 requirement in the case that an external source is sending data as fast as possible
 1453 (much more than 100 kHz), it is important to test that the PC RoIB will sustain
 1454 the 100 kHz rate if the external source sends data at exactly 100 kHz. Figure 4.8a
 1455 demonstrates that in the event that the incoming data to the PC RoIB is fixed
 1456 at 100 kHz, the event building in the PC RoIB still operates at this rate. The
 1457 other important variable that can affect the rate is the number of channels. In
 1458 particular, the ATLAS detector might decide to disable some of the channels
 1459 which should not affect the rate of operation of the PC RoIB. Figure 4.8b shows
 1460 that the PC RoIB will operate at even higher rates if the number of channels is
 1461 reduced.

1462 With these tests, the author validated the operation of the new PC RoIB
 1463 which deemed it ready to be deployed in the ATLAS system.

1464 **4.5 Online Performance in Run-2**

1465 The author deployed the new PC RoIB in the ATLAS trigger and data acquisition
 1466 system during the LHC winter shutdown in January 2016. Initially, the PC RoIB
 1467 was used as the main system with the VMEbus RoIB was used as a backup
 1468 system. Later, the VMEbus RoIB was removed completely and the PC RoIB
 1469 became the only system running in the ATLAS trigger. The PC RoIB operated
 1470 reliably since its installation without any problems and without deadtime for the
 1471 ATLAS data collection. Figure 4.9a shows that the RoIB event assembly does
 1472 not depend on pileup conditions and Figure 4.9b shows that the memory usage of

₁₄₇₃ the HLTSV is at the level of 5%. It has now participated in collecting a dataset
₁₄₇₄ of over 35 fb^{-1} exceeding the dataset collected by the VMEbus RoIB (22 fb^{-1}).
₁₄₇₅ The performance of the PC RoIB during the data taking of ATLAS has been very
₁₄₇₆ stable.

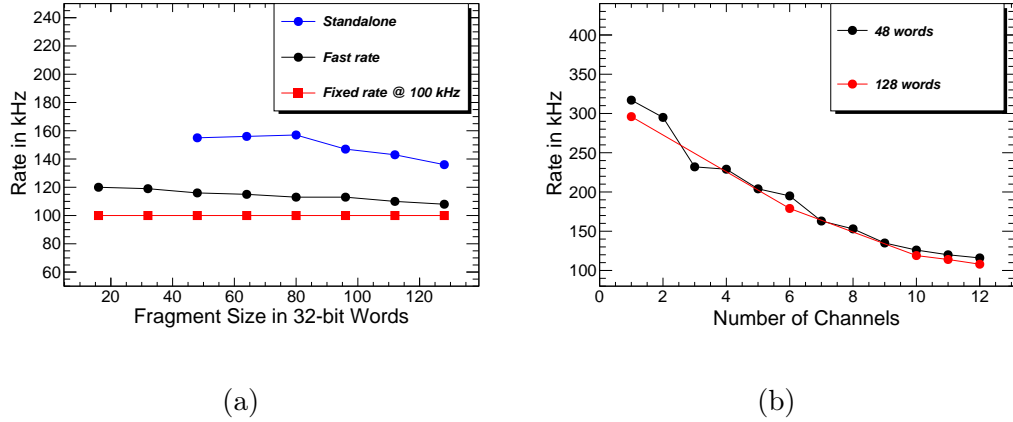


Figure 4.8: The event building rate as a function of (a) the fragment size (b) the number of channels. The rates are shown for a standalone application that implements a minimal interface for event building, the integrated RoIB software into an HLTSV process running within the full ATLAS TDAQ software suite.

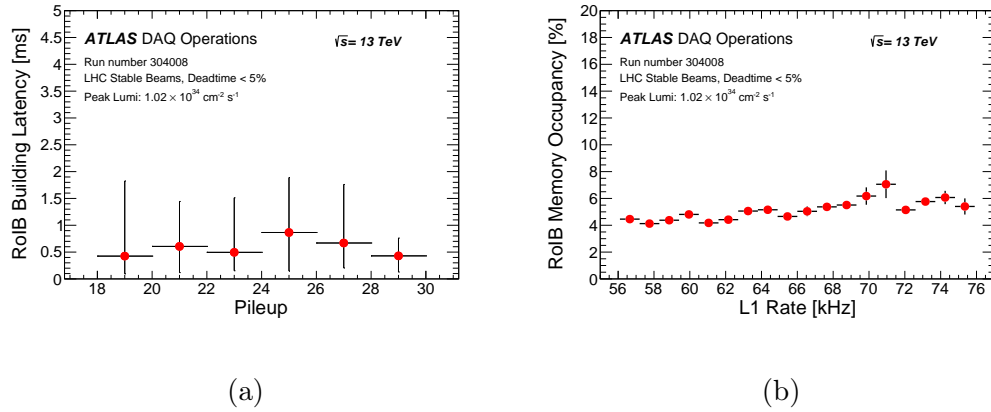


Figure 4.9: RoIB performance: RoIB building latency as a function of pileup (left), RoIB memory occupancy as a function of L1 rate (right).

₁₄₇₇ **Chapter 5**

₁₄₇₈ **Analysis Strategy**

₁₄₇₉ **5.1 Overview**

₁₄₈₀ The chapters thus far described supersymmetry as an extension of the standard
₁₄₈₁ model, motivated the need to search for it, and described the experimental
₁₄₈₂ apparatus used for this search, the LHC and ATLAS. At this stage, we are ready
₁₄₈₃ to discuss the search for supersymmetry that the author has performed.

₁₄₈₄ The main task in designing a search for new physics signatures is to ensure
₁₄₈₅ that the search regions, expected to have an enhancement of the signal (also
₁₄₈₆ referred to as the signal regions), have an acceptance for a wide range of new
₁₄₈₇ physics models that are well motivated. In addition, it is important to design
₁₄₈₈ the search in a way that minimizes the contamination from the known physics
₁₄₈₉ processes of the standard model. In other words, a typical signal region should
₁₄₉₀ have a maximum expected signal with a minimum expected background.

₁₄₉₁ The search for supersymmetry with leptons of the same-electric charge or more
₁₄₉₂ than three leptons meets both criteria. The search targets the strong production
₁₄₉₃ of supersymmetric particles which mainly involves gluino pair production. Since
₁₄₉₄ gluinos are Majorana fermions, they can decay to either a positive or negative
₁₄₉₅ lepton in each branch of the pair production. As a result, it is as likely to have two
₁₄₉₆ leptons of the same electric charge as it is to have two leptons of opposite electric
₁₄₉₇ charge. While the opposite-sign leptons is a common signature in the standard

1498 model, the same-sign leptons signature is very rare. Also, processes that involve
 1499 more than two leptons are also rare in the standard model. On one hand the
 1500 electroweak processes leading to W and Z bosons have a low cross sections. On
 1501 the other hand the low branching ratio to leptons lead to an extreme background
 1502 reduction. The requirement of three or more leptons allows the analysis to target
 1503 supersymmetric models with longer decay chains. The presence of a third softer
 1504 lepton also increases the sensitivity to scenarios with small mass difference between
 1505 the supersymmetric particles.

1506 The next important step in a search for new physics is to estimate the back-
 1507 grounds present in the signal regions. The standard model backgrounds with a
 1508 same-sign lepton pair or three or more leptons predominantly comes from the
 1509 associated production of a top quark pair and a vector boson ($t\bar{t} + W$, $t\bar{t} +$
 1510 Z), and multi-boson production (di-boson and tri-boson). These backgrounds
 1511 that lead to a signature with same-sign leptons or three or more leptons are
 1512 referred to as *irreducible backgrounds*. However, the high cross section processes
 1513 from the standard model such as $t\bar{t}$, might contribute to the signal regions via a
 1514 mis-reconstruction of this process by the detector. As a result, there are two very
 1515 important backgrounds that affect the analysis that are referred to as *reducible*
 1516 *backgrounds*. The top quark pair production ($t\bar{t}$) process may decay fully leptoni-
 1517 cally ($t\bar{t} \rightarrow (b\ell^+\bar{\nu})(\bar{b}\ell^-\nu)$) and contribute to the signal regions if the lepton charge
 1518 is mis-measured. In the case of a semi-leptonic decay of $t\bar{t}$ ($t\bar{t} \rightarrow (b\ell^+\bar{\nu})(\bar{b}q\bar{q}')$)
 1519 where the hadronic decay is mis-identified as a leptonic decay, the process will
 1520 contribute with a “fake” lepton in the signal regions. The background estimation

1521 methodology will aim at estimating both reducible and irreducible backgrounds
1522 with Monte Carlo simulation and data-driven methods.

1523 Finally, we assess the compatibility between the observed data and the pre-
1524 dicted background in one counting experiment for each signal region by doing a
1525 hypothesis test of the background-only or the background as well as the sought
1526 after signal hypotheses. If an excess is found in data, we proceed to evaluate
1527 if this excess can lead to reject the background-only hypothesis and we check
1528 the plausibility that the new signal can describe the data. Otherwise, we set
1529 exclusion limits for a certain region of the parameter space of a defined model or
1530 we set model-independent upper limits on the number of events from a beyond
1531 the standard model process.

1532 5.2 Benchmarking Models

1533 Final states with two same-sign leptons or three leptons and multiple jets can probe
1534 a variety of supersymmetric models represented by decays of heavy superpartners
1535 involving massive gauge bosons, sleptons or top quarks. The decays of the
1536 superpartners can lead to many experimental signatures that may lead to different
1537 lepton, jet, and b -tagged jet multiplicities. To exploit this wide range of possible
1538 signatures, the analysis uses six R -parity-conserving SUSY scenarios featuring
1539 gluino, bottom squark or top squark pair production. These scenarios were used
1540 as benchmarks to identify regions of the phase space where the analysis can bring
1541 particularly useful complementarity to other SUSY searches, and subsequently

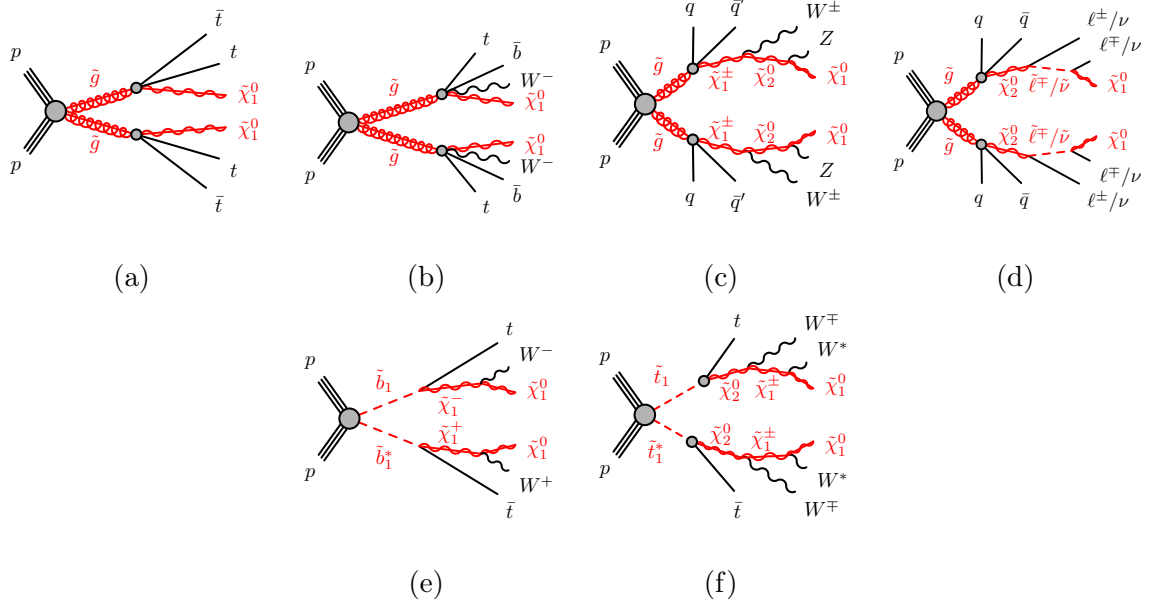


Figure 5.1: SUSY processes featuring gluino ((a), (b), (c), (d)) or third-generation squark ((e), (f)) pair production studied in this analysis. In Figure 5.1d, $\tilde{\ell} \equiv \tilde{e}, \tilde{\mu}, \tilde{\tau}$ and $\tilde{\nu} \equiv \tilde{\nu}_e, \tilde{\nu}_\mu, \tilde{\nu}_\tau$. In Figure 5.1f, the W^* labels indicate largely off-shell W bosons – the mass difference between $\tilde{\chi}_1^\pm$ and $\tilde{\chi}_1^0$ is around 1 GeV.

1542 define signal regions with a particular focus on these regions. In this section, the
1543 scenarios considered are presented with details about the assumed superpartner
1544 masses and decay modes. Exclusion limits obtained prior to the work of the
1545 author will also be shown to highlight the improvement in reach that this analysis
1546 brings.

1547 Gluino pair production with slepton-mediated two-step decay $\tilde{g} \rightarrow$

1548 $q\bar{q}\ell\bar{\ell}\tilde{\chi}_1^0$

This scenario (Fig. 5.1d) features gluino pair-production with two-step decays via neutralinos $\tilde{\chi}_2^0$ and sleptons, $\tilde{g} \rightarrow q\bar{q}'\tilde{\chi}_2^0 \rightarrow q\bar{q}'(\tilde{\ell}\ell/\tilde{\nu}\nu) \rightarrow q\bar{q}'(\ell\ell/\nu\nu)\tilde{\chi}_1^0$. The decays

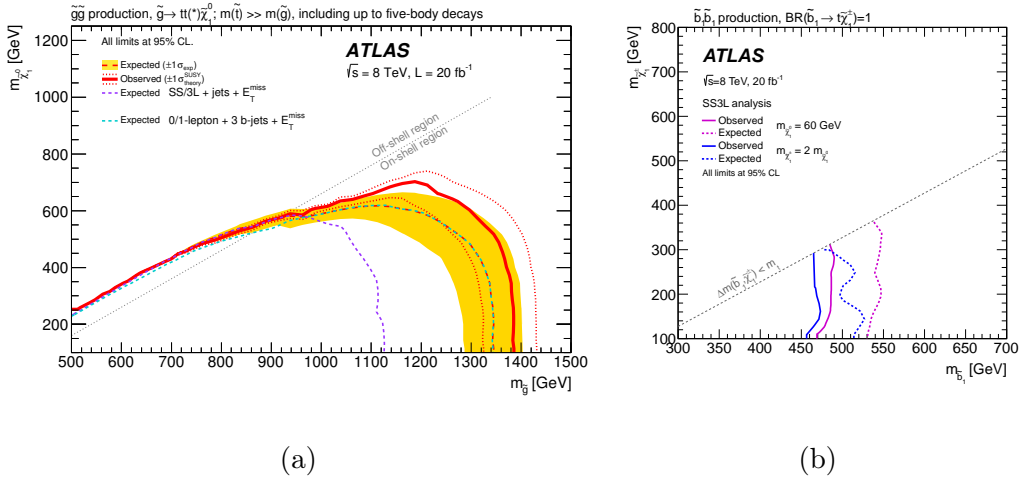


Figure 5.2: Exclusion limits on the gluino-stop offshell [58] (left) and direct sbottom [59] (right) scenarios set by ATLAS with the 2012 dataset prior to the author’s work.

are mediated by generic heavy squarks, therefore the b -jet multiplicity in this scenario is low. The final state is made of charged leptons, four additional jets and invisible particles (neutrinos and neutralinos). The average jet multiplicity per event is the smallest among the four scenarios; another characteristic is the large fraction of events with several leptons, unlike the other scenarios that have a rather low acceptance due to the branching ratios of $W \rightarrow \ell\nu$ or $Z \rightarrow \ell\ell$. The exclusion limits obtained in Run 1 (Fig. 5.3b) show again that the SS/3L+jets final state is very competitive to probe those models. This scenario is used as a benchmark to define the signal regions with ≥ 3 leptons and no b -jet.

The signal grid is built with variable gluino and $\tilde{\chi}_1^0$ masses; the $\tilde{\chi}_2^0$ mass is chosen half-way between the gluino and LSP masses, and the sleptons masses are also set equal and half-way between the $\tilde{\chi}_2^0$ and LSP masses. The $\tilde{\chi}_2^0$ may decay to

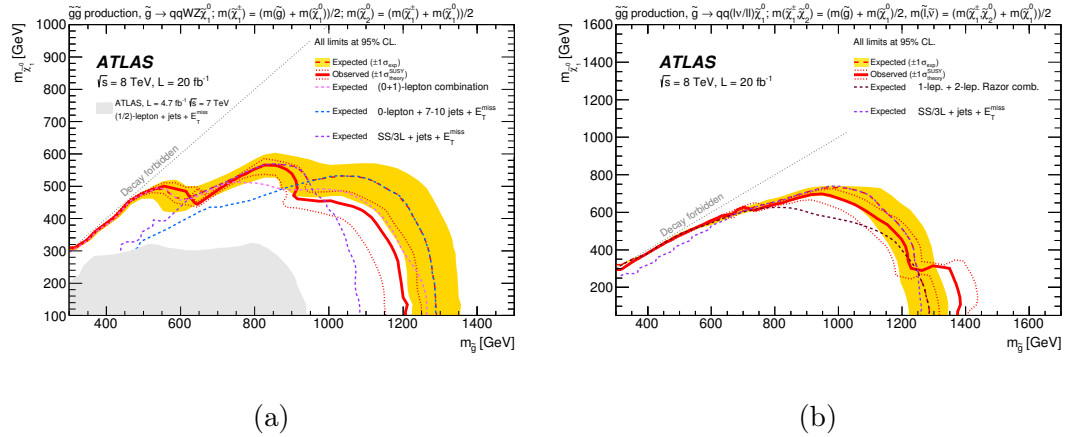


Figure 5.3: Exclusion limits on scenarios featuring gluino pair production followed by two-step decays via heavy gauge bosons or sleptons set by ATLAS with the 2012 dataset prior to the author’s work [58].

any of the six “left-handed” sleptons ($\tilde{\ell}, \tilde{\nu}$) with equal probability. “Right-handed” sleptons are assumed heavy and do not participate to the decay.

1565 Gluino pair production with gaugino-mediated two-step decay $\tilde{g} \rightarrow$

1566 $q\bar{q}'WZ\tilde{\chi}_1^0$

1567 This scenario (Fig. 5.1c) features gluino pair-production with two-step decays
 1568 via gauginos and W and Z bosons, $\tilde{g} \rightarrow q\bar{q}'\tilde{\chi}_1^\pm \rightarrow q\bar{q}'W\tilde{\chi}_2^0 \rightarrow q\bar{q}'WZ\tilde{\chi}_1^0$, mediated
 1569 by generic heavy squarks of the first and second generations. The final state is
 1570 made of two W and two Z bosons (possibly offshell), four additional jets and
 1571 invisible particles (neutrinos and neutralinos). This generally leads to events with
 1572 large jet multiplicities and a fair branching ratio for dileptonic final states. The
 1573 exclusion limits obtained in Run 1 indeed illustrate the competitiveness of the
 1574 SS/3L+jets search (Fig. 5.3a) particularly the heavy- $\tilde{\chi}_1^0$ region of the phase space.

1575 This scenario is used as a benchmark to define the signal regions with many jets
1576 but none tagged as a b -jet.

1577 The signal grid is built with variable gluino and $\tilde{\chi}_1^0$ masses, and the $\tilde{\chi}_1^\pm$ and
1578 $\tilde{\chi}_2^0$ masses are set such that the former lies half-way between the gluino and $\tilde{\chi}_1^0$
1579 masses, and the latter half-way between $\tilde{\chi}_1^\pm$ and $\tilde{\chi}_1^0$ masses.

1580 **Sbottom pair production with one-step decay $\tilde{b}_1 \rightarrow t\tilde{\chi}_1^\pm$**

1581 In this scenario (Fig. 5.1e), bottom squarks are rather light and assumed to
1582 decay in a top quark and a chargino $\tilde{\chi}_1^\pm$, with a subsequent $\tilde{\chi}_1^\pm \rightarrow W^\pm \tilde{\chi}_1^0$ decay,
1583 providing complementarity to the mainstream search [60] which focuses on the
1584 channel $\tilde{b}_1 \rightarrow b\tilde{\chi}_1^0$. The final state resulting from the production of a $\tilde{b}_1\tilde{b}_1^*$ pair
1585 contains two top quarks, two W bosons and two neutralinos. While this final
1586 state may lead to various experimental signatures, the model was considered in
1587 Run-1 [58] only by the same-sign leptons and jets search, leading to the exclusion
1588 limits presented in Fig. 5.2. Signal events typically contain one or two b -tagged
1589 jets, therefore this scenario is used as benchmark to define the signal regions with
1590 ≥ 1 b -jet.

1591 The model adopts a fixed chargino-neutralino mass difference of 100 GeV,
1592 therefore always allowing on-shell W bosons in the $\tilde{\chi}_1^\pm \rightarrow W\tilde{\chi}_1^0$ decay ¹ Only pair
1593 production of the lightest sbottom is considered, followed by an exclusive decay
1594 in the aforementioned channel.

¹A different chargino mass assumption is adopted in the current work compared to the Run 1 paper [58]. Fig. 5.2 is shown for illustration only. The reduced chargino-neutralino mass gap in the current analysis allows us to study signal scenarios with heavy neutralinos, which were not considered previously.

1595 **Gluino pair production with stop-mediated decay $\tilde{g} \rightarrow t\bar{t}\tilde{\chi}_1^0$**

1596 In this scenario inspired by naturalness arguments, gluinos are coupling prefer-
1597 entially to stops which are lighter than the other squarks. Gluinos are however
1598 considered lighter than stops, and decay directly into a $t\bar{t}\tilde{\chi}_1^0$ triplet via a virtual
1599 stop (Fig. 5.1a). The pair production of gluinos leads to a final state containing
1600 four top quarks and two neutralinos. This characteristic final state is accessible
1601 through various experimental signatures, which is why this model is commonly
1602 used as a benchmark to compare analyses sensitivities. The searches performed
1603 with Run-1 data [58], summarized in Fig. 5.2a, showed that the same-sign leptons
1604 final state is competitive only at large neutralino mass. This region of the phase
1605 space is consequently given a particular attention in the choice of signal regions de-
1606 scribed further on. For instance, the region of phase-space with $\Delta m(\tilde{g}, \tilde{\chi}_1^0) < 2m_t$,
1607 where gluinos decay via one or two offshell top quarks, is only accessible for
1608 this analysis. In the signal samples referenced in this document, the mass of
1609 the lightest stop is fixed to 10 TeV and is mostly a \tilde{t}_R state. Only gluino pair
1610 production is considered, followed by an exclusive decay in the aforementioned
1611 channel. Signal events typically contain many b -tagged jets, therefore this scenario
1612 is used as benchmark to define the signal regions with ≥ 2 b -jets.

1613 **$\tilde{t}_1\tilde{t}_1^*$ with “three-same-sign leptons” signature**

1614 Inspired by Ref. [61], a simplified model featuring a stop pair-production with
1615 two-step decays via a neutralino $\tilde{\chi}_2^0$ and a chargino $\tilde{\chi}_1^\pm$ is added in this version of

₁₆₁₆ the analysis, according to the decay illustrated on Fig. 5.1f:

$$\tilde{t}_1 \rightarrow t\tilde{\chi}_2^0 \rightarrow t\tilde{\chi}_1^\pm W^\mp \rightarrow tW^\pm W^\mp \tilde{\chi}_1^0.$$

₁₆₁₈ This simplified model is a well-motivated representation of a pMSSM model.

₁₆₁₉ The lightest stop (\tilde{t}_1) is right-handed and $\tilde{\chi}_2^0$ is bino-like which leads to a large

₁₆₂₀ branching ratio in the decay $\tilde{t}_1 \rightarrow t\tilde{\chi}_2^0$. Furthermore, the decay $\tilde{\chi}_2^0 \rightarrow \tilde{\chi}_1^\pm W^\mp$

₁₆₂₁ is also enhanced since $\tilde{\chi}_1^\pm$ is wino-like, as long as $\tilde{\chi}_1^\pm$ and $\tilde{\chi}_1^0$ are nearly mass

₁₆₂₂ degenerate and $m_{\tilde{\chi}_2^0} - m_{\tilde{\chi}_1^0} < m_H = 125$ GeV to suppress the decay $\tilde{\chi}_2^0 \rightarrow \tilde{\chi}_1^0 + H$

₁₆₂₃ (the decay $\tilde{\chi}_2^0 \rightarrow \tilde{\chi}_1^0 + Z$ is suppressed). By respecting these conditions and evading

₁₆₂₄ the bottom squark limit shown in Fig. 5.2b, we consider a one-dimensional grid

₁₆₂₅ with a \tilde{t}_1 mass varying between 550 GeV and 800 GeV with a 50 GeV gap², a

₁₆₂₆ two body decay to an on-shell top quark and a $\tilde{\chi}_2^0$ which has a 100 GeV mass

₁₆₂₇ difference from $\tilde{\chi}_1^0$. The mass difference between the $\tilde{\chi}_1^\pm$ and $\tilde{\chi}_1^0$ is taken to be

₁₆₂₈ 500 MeV which is not excluded by the disappearing track analysis. In fact, this

₁₆₂₉ mass gap could easily be increased by introducing a small amount of higgsino

₁₆₃₀ mixing [62].

₁₆₃₁ While the stop pair production is similar to the sbottom pair production

₁₆₃₂ in terms of kinematics, the stop pair production offers a unique topology that

₁₆₃₃ leads to three leptons of the same electric charge. This final state benefits from

₁₆₃₄ an extreme reduction of the SM background while maintaining a good signal

₁₆₃₅ acceptance which helps loosen the kinematic cuts to access a more compressed

₁₆₃₆ SUSY phase space. As a result, this scenario is complementary to the search for

₁₆₃₇ bottom squarks.

²Only the points at \tilde{t}_1 mass of 550 GeV are available at the moment.

1638 **Non-Universal Higgs Models**

1639 In references [63, 64, 65], theorists studied a complete two-extra-parameter non-

1640 universal Higgs model (NUHM2) that can have low fine tuning (natural) and

1641 predicts final state signatures that allow large background rejection while retaining

1642 high signal efficiency. The NUHM2 model allows the soft SUSY breaking masses of

1643 the Higgs multiplets, m_{H_u} and m_{H_d} , to be different from matter scalar masses (m_0)

1644 at the grand unification scale. The NUHM2 model is expected to form the effective

1645 theory for energies lower than m_{GUT} resulting from SU(5) or general SU(10) grand

1646 unified theories. The scalar mass m_0 , the soft SUSY breaking gaugino mass $m_{1/2}$,

1647 the pseudoscalar Higgs boson mass m_A , the trilinear SUSY breaking parameter

1648 A_0 , the weak scale ratio of Higgs field vacuum expectation values $\tan \beta$, and the

1649 superpotential Higgs mass μ are the free parameters. Both $m_{1/2}$ and μ are varied

1650 while the other parameters are fixed to $m_0 = 5$ TeV, $A_0 = -1.6m_0$, $\tan \beta = 15$,

1651 $m_A = 1$ TeV, and $\text{sign}(\mu) > 0$. These parameter choices lead directly to a Higgs

1652 mass of 125 GeV in accord with experiment. In this “radiatively-driven natural”

1653 SUSY approach, the higgsino is required to have a mass below 200-300 GeV, the

1654 stop to have a mass below ~ 3 TeV, and the gluino below ~ 4 TeV. The model

1655 mainly involves gluino pair production with gluinos decaying predominantly to

1656 $t\bar{t}\tilde{\chi}_1^0$ and $t b\tilde{\chi}_1^\pm$, giving rise to final states with two same-sign leptons and E_T^{miss} .

1657 Table 5.1 shows the branching ratios of the dominant gluino decay modes for

1658 $m_{1/2} = 400$ GeV. Simulated NUHM2 signal samples with mass ($m_{1/2}$) values from

1659 300-800 GeV and $\mu = 150$ GeV were generated where the gluino mass in this

Decay	BR	Decay	BR
$t\bar{t}\chi_1^0$	0.13	$tb\chi_1^\pm$	0.45
$t\bar{t}\chi_2^0$	0.21	$tb\chi_2^\pm$	0.04
$t\bar{t}\chi_3^0$	0.13	-	-
$t\bar{t}\chi_4^0$	0.02	-	-
$t\bar{t}\chi_i^0$	0.49	$tb\chi_i^\pm$	0.49

Table 5.1: The dominant gluino decay modes for $m_{1/2} = 400$ GeV for the NUHM2 model.

₁₆₆₀ model is approximately $2.5 \times m_{1/2}$.

₁₆₆₁ 5.3 Dataset and Simulated Event Samples

₁₆₆₂ 5.3.1 Collision Data

₁₆₆₃ The analysis uses pp -collisions data at $\sqrt{s} = 13$ TeV collected by the ATLAS
₁₆₆₄ detector during 2015 and 2016 with a peak instantaneous luminosity of $L =$
₁₆₆₅ $1.4 \times 10^{34} \text{ cm}^{-2}\text{s}^{-1}$. The total integrated luminosity considered corresponds to
₁₆₆₆ 36.1 fb^{-1} (3.2 fb^{-1} in 2015 and 32.9 fb^{-1} in 2016) recorded after applying beam,
₁₆₆₇ detector, and data-quality requirements. The combined luminosity uncertainty
₁₆₆₈ for 2015 and 2016 is 3.2%, assuming partially correlated uncertainties in 2015 and
₁₆₆₉ 2016. The integrated luminosity was established following the same methodology
₁₆₇₀ as that detailed in Ref. [66], from a preliminary calibration of the luminosity scale

1671 using a pair of x - y beam separation scans.

1672 **5.3.2 Simulated Event Samples**

1673 Monte Carlo (MC) simulated event samples are used to model the SUSY signal
1674 and SM backgrounds. The irreducible SM backgrounds refer to processes that
1675 lead to two same-sign and/or three “prompt” leptons where the prompt leptons are
1676 produced directly in the hard-scattering process, or in the subsequent decays of
1677 W, Z, H bosons or prompt τ leptons. The reducible backgrounds, mainly arising
1678 from $t\bar{t}$ and $V+jets$ production, are estimated either from data or from MC
1679 simulation as described in Section 6.

1680 Table 5.2 presents the event generator, parton shower, cross-section normaliza-
1681 tion, PDF set and the set of tuned parameters for the modelling of the parton
1682 shower, hadronization and underlying event. Apart from the MC samples produced
1683 by the SHERPA generator, all MC samples used the EVTGEN v1.2.0 program [67]
1684 to model the properties of bottom and charm hadron decays.

1685 The MC samples were processed through either a full ATLAS detector simula-
1686 tion [78] based on GEANT4 [44] or a fast simulation using a parameterization of
1687 the calorimeter response and GEANT4 for the inner detector and muon spectrom-
1688 eter [45], and are reconstructed in the same manner as the data. All simulated
1689 samples are generated with a range of minimum-bias interactions using PYTHIA
1690 8 [43] with the MSTW2008LO PDF set [79] and the A2 tune overlaid on the
1691 hard-scattering event to account for the multiple pp interactions in the same
1692 bunch crossing (in-time pileup) and neighbouring bunch crossing (out-of-time

Physics process	Event generator	Parton shower	Cross-section order	Cross-section value (fb)	PDF set	Set of tuned parameters
Signal	aMC@NLO 2.2.3 [42]	Pythia 8.186 [43]	NLO+NLL	See Table 5.4	NNPDF2.3LO [68]	A14 [69]
$t\bar{t} + X$						
$t\bar{t}W, t\bar{t}Z/\gamma^*$	aMC@NLO 2.2.2	Pythia 8.186	NLO [70]	600.8, 123.7	NNPDF2.3LO	A14
$t\bar{t}H$	aMC@NLO 2.3.2	Pythia 8.186	NLO [70]	507.1	NNPDF2.3LO	A14
$4t$	aMC@NLO 2.2.2	Pythia 8.186	NLO [42]	9.2	NNPDF2.3LO	A14
Diboson						
ZZ, WZ	SHERPA 2.2.1 [71]	SHERPA 2.2.1	NLO [72]	$1.3 \cdot 10^3, 4.5 \cdot 10^3$	NNPDF2.3LO	SHERPA default
inc. $W^\pm W^\pm$	SHERPA 2.1.1	SHERPA 2.1.1	NLO [72]	86	CT10 [73]	SHERPA default
Rare						
$t\bar{t}WW, t\bar{t}WZ$	aMC@NLO 2.2.2	Pythia 8.186	NLO [42]	9.9, 0.36	NNPDF2.3LO	A14
$tZ, tWZ, t\bar{t}\bar{t}$	aMC@NLO 2.2.2	Pythia 8.186	LO	240, 16, 1.6	NNPDF2.3LO	A14
WH, ZH	aMC@NLO 2.2.2	Pythia 8.186	NLO [74]	$1.4 \cdot 10^3, 868$	NNPDF2.3LO	A14
Triboson	SHERPA 2.1.1	SHERPA 2.1.1	NLO [72]	14.9	CT10	SHERPA default
Irreducible (Incl.)						
$W+Jets$	POWHEG-BOX	Pythia 8.186	NNLO	$2.0 \cdot 10^7$	CT10	AZNLO[75]
$Z+Jets$	POWHEG-BOX	Pythia 8.186	NNLO	$1.9 \cdot 10^7$	CT10	AZNLO[75]
$t\bar{t}$	POWHEG-BOX	Pythia 6.428	NNLO+NNLL [76]	$8.3 \cdot 10^5$	CT10	PERUGIA2012 (P2012) [77]

Table 5.2: Simulated signal and background event samples: the corresponding event generator, parton shower, cross-section normalization, PDF set and set of tuned parameters are shown for each sample. Because of their very small contribution to the signal-region background estimate, $t\bar{t}WW, t\bar{t}WZ, tZ, tWZ, t\bar{t}\bar{t}, WH, ZH$ and triboson are summed and labelled “rare”.

1693 pileup). The distribution of the average number of interactions per bunch crossing
 1694 $\langle\mu\rangle$ ranges from 0.5 to 39.5, with a profile set as an estimate of the combined
 1695 2015+2016 data $\langle\mu\rangle$ profile. With larger luminosity collected during this year and
 1696 the μ distribution in data being closer to that in the MC profile, the simulated
 1697 samples are re-weighted to reproduce the observed distribution of the average
 1698 number of collisions per bunch crossing (μ).

1699 **Background process simulation**

1700 The two dominant irreducible background processes are $t\bar{t}V$ (with V being a W
1701 or Z/γ^* boson) and diboson production with final states of four charged leptons
1702 ℓ ,³ three charged leptons and one neutrino, or two same-sign charged leptons and
1703 two neutrinos.

1704 The production of a $t\bar{t}V$ constitutes the main source of background with
1705 prompt same-sign leptons for event selections including b -jets. Simulated events
1706 for these processes were generated at NLO with AMC@NLO v2.2.2 [42] interfaced
1707 to PYTHIA 8, with up to two (ttW) or one ($ttZ^{(*)}$) extra parton included in the
1708 matrix elements [80]. The samples are normalised to the inclusive process NLO
1709 cross-section using appropriate k -factors [42].

1710 The production of multiple W, Z bosons decaying leptonically constitutes the
1711 main source of background with prompt same-sign leptons for event selections
1712 vetoing b -jets. Diboson processes with four charged leptons, three charged leptons
1713 and one neutrino, or two charged leptons and two neutrinos were simulated at
1714 NLO using the SHERPA 2.2.1 generator [71], as described in detail in Ref. [72].

1715 The main samples simulate $qq \rightarrow VV \rightarrow$ leptons production including the doubly
1716 resonant WZ and ZZ processes, non-resonant contributions as well as Higgs-
1717 mediated contributions, and their interferences; up to three extra partons were
1718 included (at LO) in the matrix elements. Simulated events for the $W^\pm W^\pm jj$
1719 process (including non-resonant contributions) were produced at LO with up

³All lepton flavours are included here and τ leptons subsequently decay leptonically or hadronically.

1720 to one extra parton, separately for QCD-induced ($\mathcal{O}(\alpha_{\text{em}}^4)$) and VBS-induced
 1721 ($\mathcal{O}(\alpha_{\text{em}}^6)$) production – the interferences being neglected. Additional samples for
 1722 VBS-induced $qq \rightarrow 3\ell\nu jj$ and $qq \rightarrow 4\ell$ and loop-induced $gg \rightarrow WZ^{(*)}/ZZ^{(*)}$
 1723 processes were also produced with the same configuration. The samples generated
 1724 at NLO are directly normalized to the cross-sections provided by the generator.

1725 Production of a Higgs boson in association with a $t\bar{t}$ pair is simulated using
 1726 AMC@NLO [42] (in MADGRAPH v2.2.2) interfaced to HERWIG 2.7.1 [81]. The
 1727 UEEE5 underlying-event tune is used together with the CTEQ6L1 [82] (matrix
 1728 element) and CT10 [73] (parton shower) PDF sets. Simulated samples of SM
 1729 Higgs boson production in association with a W or Z boson are produced with
 1730 PYTHIA 8.186, using the A14 tune and the NNPDF23LO PDF set. Events are
 1731 normalised with cross-sections calculated at NLO [74].

1732 MADGRAPH v2.2.2 [83] is used to simulate the $t\bar{t}WW$, tZ , $t\bar{t}t\bar{t}$ and $t\bar{t}t$ processes,
 1733 and the generator cross-section is used for tZ and $t\bar{t}t$. MADGRAPH interfaced to
 1734 PYTHIA 8 is used to generate $t\bar{t}WZ$ processes, and appropriate k -factors are taken
 1735 from [42]. AMC@NLO interfaced to PYTHIA 8 is used for the generation of the
 1736 tWZ process, with an alternative sample generated with AMC@NLO interfaced
 1737 to HERWIG used to evaluate the parton shower uncertainty. Fully leptonic triboson
 1738 processes (WWW , WWZ , WZZ and ZZZ) with up to six charged leptons are
 1739 simulated using SHERPA v2.1.1 and described in Ref. [72]. The 4ℓ and $2\ell + 2\nu$
 1740 processes are calculated at next-to-leading order (NLO) for up to one additional
 1741 parton; final states with two and three additional partons are calculated at leading
 1742 order (LO). The $WWZ \rightarrow 4\ell + 2\nu$ or $2\ell + 4\nu$ processes are calculated at LO with

1743 up to two additional partons. The $WWW/WZZ \rightarrow 3\ell + 3\nu$, $WZZ \rightarrow 5\ell + 1\nu$,
 1744 $ZZZ \rightarrow 6\ell + 0\nu$, $4\ell + 2\nu$ or $2\ell + 4\nu$ processes are calculated at NLO with up
 1745 to two extra partons at LO. The CT10 [73] parton distribution function (PDF)
 1746 set is used for all SHERPA samples in conjunction with a dedicated tuning of
 1747 the parton shower parameters developed by the SHERPA authors. The generator
 1748 cross-sections (at NLO for most of the processes) are used when normalising these
 1749 backgrounds.

1750 Double parton scattering (DPS) occurs when two partons interact simulta-
 1751 neously in a proton-proton collision leading to two hard scattering processes
 1752 overlapping in a detector event. Accordingly, two single W production processes
 1753 can lead to a $W^\pm + W^\pm$ final state via DPS. This background is expected to have
 1754 a negligible contribution to signal regions with high jet multiplicities. To estimate
 1755 a conservative upper bound on cross-section for WW events which might arise
 1756 from DPS, a standard ansatz is adopted: in this, for a collision in which a hard
 1757 process (X) occurs, the probability that an additional (distinguishable) process
 1758 (Y) occurs is parametrized as:

$$\sigma_{XY}^{DPS} = \sigma_X \sigma_Y / \sigma_{eff} \quad (5.1)$$

1759 where σ_X is the production cross section of the hard process X and σ_{eff} (effective
 1760 area parameter) parametrizes the double-parton interaction part of the production
 1761 cross section for the composite system (X+Y). A value of σ_{eff} is 10-20 mb is
 1762 assumed in this study (as obtained from 7 TeV measurements, and with no
 1763 observed dependence on \sqrt{s}), and it is independent on the processes involved. For

₁₇₆₄ the case of $W^\pm + W^\pm$ production:

$$\sigma_{W^\pm W^\pm}^{DPS} = \frac{\sigma_{W^+}\sigma_{W^+} + \sigma_{W^-}\sigma_{W^-} + 2\sigma_{W^+}\sigma_{W^-}}{\sigma_{eff}} \simeq 0.19 - 0.38 \text{ pb.} \quad (5.2)$$

₁₇₆₅ After the application of the SR criteria, only 4 raw MC events in the DPS

₁₇₆₆ $WW \rightarrow \ell\nu\ell\nu$ remain. Table 5.3 shows the expected contribution in the SRs where

₁₇₆₇ some MC event survives all the cuts. The ranges quoted in the tables reflect the

₁₇₆₈ range in the predicted $\sigma_{W^\pm W^\pm}^{DPS}$ cross-section above, as well as the combinatorics

₁₇₆₉ for scaling the jet multiplicity⁴. Due to the large uncertainties involved in these

₁₇₇₀ estimates, some of them difficult to quantify (such as the modelling of DPS by

₁₇₇₁ PYTHIA at LO), the contribution from this background is not included in the final

₁₇₇₂ SR background estimates. Note that the estimated DPS contribution is typically

₁₇₇₃ much smaller than the uncertainty on the total background for the SRs.

Table 5.3: Number of raw MC events and its equivalent for 36.1 fb^{-1} with and without the correction as a function of the jet multiplicity. Only the SRs where at least one MC event passes all the cuts are shown.

SR	Raw MC events	Without N_{jet} correction	With N_{jet} correction
Rpc2L0bS	2	0.016-0.033	0.09-0.38
Rpc2L0bH	1	0.006-0.012	0.05-0.17

Table 5.4: Signal cross-sections [pb] and related uncertainties [%] for scenarios featuring $\tilde{g}\tilde{g}$ (top table) or $\tilde{b}_1\tilde{b}_1^*$ (bottom table) production, as a function of the pair-produced superpartner mass, reproduced from Ref. [84].

Gluino mass (GeV)	500	550	600	650	700
Cross section (pb)	$27.4 \pm 14\%$	$15.6 \pm 14\%$	$9.20 \pm 14\%$	$5.60 \pm 14\%$	$3.53 \pm 14\%$
750	800	850	900	950	1000
$2.27 \pm 14\%$	$1.49 \pm 15\%$	$0.996 \pm 15\%$	$0.677 \pm 16\%$	$0.466 \pm 16\%$	$0.325 \pm 17\%$
1050	1100	1150	1200	1250	1300
$0.229 \pm 17\%$	$0.163 \pm 18\%$	$0.118 \pm 18\%$	$0.0856 \pm 18\%$	$0.0627 \pm 19\%$	$0.0461 \pm 20\%$
1350	1400	1450	1500	1550	1600
$0.0340 \pm 20\%$	$0.0253 \pm 21\%$	$0.0189 \pm 22\%$	$0.0142 \pm 23\%$	$0.0107 \pm 23\%$	$0.00810 \pm 24\%$

Sbottom mass (GeV)	400	450	500	550
Cross section (pb)	$1.84 \pm 14\%$	$0.948 \pm 13\%$	$0.518 \pm 13\%$	$0.296 \pm 13\%$
600	650	700	750	800
$0.175 \pm 13\%$	$0.107 \pm 13\%$	$0.0670 \pm 13\%$	$0.0431 \pm 14\%$	$0.0283 \pm 14\%$

1774 Signal cross-sections and simulations

1775 The signal processes are generated from leading order (LO) matrix elements with
 1776 up to two extra partons (only one for the grid featuring slepton-mediated gluino
 1777 decays), using the MADGRAPH V5.2.2.3 generator [42] interfaced to PYTHIA
 1778 8.186 [43] with the *ATLAS 14* tune [69] for the modelling of the SUSY decay
 1779 chain, parton showering, hadronization and the description of the underlying

⁴For instance, a DPS event with 6 jets can be due to the overlap of two events with 6+0 jets, or 5+1, 4+2 or 3+3 jets. All possible combinations are considered and the range quoted in the table shows the combinations leading to the smallest and largest correction factors.

1780 event. Parton luminosities are provided by the NNPDF23LO [85] set of parton
1781 distribution functions. Jet-parton matching is realized following the CKKW-L
1782 prescription [86], with a matching scale set to one quarter of the pair-produced
1783 superpartner mass.

1784 The signal samples are normalised to the next-to-next-to-leading order cross-
1785 section from Ref. [84] including the re-summation of soft gluon emission at
1786 next-to-next-to-leading-logarithmic accuracy (NLO+NLL), as detailed in Ref. [87];
1787 some of these cross-sections are shown for illustration in Table 5.4.

1788 Cross-section uncertainties are also taken from Ref. [84] as well, and include
1789 contributions from varied normalization and factorization scales, as well as PDF
1790 uncertainties. They typically vary between 15 and 25%. Uncertainties on the
1791 signal acceptance are not considered since these are generally smaller than the
1792 uncertainties on the inclusive production cross-section.

1793 5.4 Event Selection

1794 5.4.1 Pre-selection and event cleaning

1795 A sample of two same-sign or three leptons is selected applying the following
1796 criteria:

- 1797 • **Jet Cleaning:** Events are required to pass a set of cleaning requirements.
1798 An event is rejected if any pre-selected jets ($|\eta| < 4.9$, after jet-electron
1799 overlap removal) fails the jet quality criteria. The cleaning requirements
1800 are intended to remove events where significant energy was deposited in the

1801 calorimeters due to instrumental effects such as cosmic rays, beam-induced
 1802 (non-collision) particles, and noise. Around 0.5% of data events are lost
 1803 after applying this cut.

1804 • **Primary Vertex:** Events are required to have a reconstructed vertex [88]
 1805 with at least two associated tracks with $p_T > 400$ MeV. The vertex with the
 1806 largest Σp_T^2 of the associated tracks is chosen as the primary vertex of the
 1807 event. This cut is found to be 100% efficient.

1808 • **Bad Muon Veto:** Events containing at least one pre-selected muon sat-
 1809 isfying $\sigma(q/p)/|q/p| > 0.2$ before the overlap removal are rejected. Around
 1810 0.1% of data events are removed by this cut.

1811 • **Cosmic Muon Veto:** Events containing a cosmic muon candidate are
 1812 rejected. Cosmic muon candidates are looked for among pre-selected muons,
 1813 if they fail the requirements $|z_0| < 1.0$ mm and $|d_0| < 0.2$ mm, where the
 1814 longitudinal and transverse impact parameters z_0 and d_0 are calculated with
 1815 respect to the primary vertex. Up to 6% of data events are lost at this
 1816 cleaning cut.

1817 • **At least two leptons:** Events are required to contain at least two signal
 1818 leptons with $p_T > 20$ GeV for the two leading leptons. If the event contains a
 1819 third signal lepton with $p_T > 10$ GeV the event is regarded as a three-lepton
 1820 event, otherwise as a two-lepton event. The data sample obtained is then
 1821 divided into three channels depending on the flavor of the two leptons
 1822 forming a same-sign pair (ee , $\mu\mu$, $e\mu$). If more than one same-sign pairs

₁₈₂₃ can be built, the one involving the leading lepton will be considered for the
₁₈₂₄ channel selection.

- ₁₈₂₅ • **Same-sign:** if the event has exactly two leptons, then these two leptons
₁₈₂₆ have to be of identical electric charge (“same-sign”).

₁₈₂₇ The following event variables are also used in the definition of the signal and
₁₈₂₈ validation regions in the analysis:

- ₁₈₂₉ • The inclusive effective mass m_{eff} defined as the scalar sum of all the signal
₁₈₃₀ leptons p_T , all signal jets p_T and E_T^{miss} .

₁₈₃₁ 5.4.2 Trigger strategy

₁₈₃₂ Events are selected using a combination of dilepton and E_T^{miss} triggers, the latter
₁₈₃₃ being used only for events with $E_T^{\text{miss}} > 250\text{GeV}$. Since the trigger thresholds
₁₈₃₄ have been raised between 2015 and 2016 due to the continuous increase of the
₁₈₃₅ instantaneous luminosity, the dilepton triggers used for:

- ₁₈₃₆ • 2015 data: logical **or** of a trigger with two electrons of 12 GeV, with an
₁₈₃₇ electron of 17 GeV and a muon of 14 GeV, with two muons of 18 GeV and
₁₈₃₈ 8 GeV.

- ₁₈₃₉ • 2016 data: logical **or** of a trigger with two electrons of 17 GeV, with an
₁₈₄₀ electron of 17 GeV and a muon of 14 GeV, with two muons of 22 GeV and
₁₈₄₁ 8 GeV.

₁₈₄₂ The E_T^{miss} trigger was also raised from 70GeV to a 100 GeV and 110 GeV. The
₁₈₄₃ trigger-level requirements on E_T^{miss} and the leading and subleading lepton p_T are

₁₈₄₄ looser than those applied offline to ensure that trigger efficiencies are constant in
₁₈₄₅ the relevant phase space.

₁₈₄₆ **Trigger matching**

₁₈₄₇ For events exclusively selected via one or several of the dilepton triggers, we
₁₈₄₈ require a matching between the online and offline leptons with $p_T > 20\text{GeV}$. with
₁₈₄₉ the exception of the di-muon trigger for which muons with $p_T > 10\text{GeV}$ are also
₁₈₅₀ considered. In addition, for the di-muon trigger in the 2016 configuration, the p_T
₁₈₅₁ requirement of the leading matched muon is raised to 23 GeV to remain on the
₁₈₅₂ trigger efficiency plateau.

₁₈₅₃ **Trigger scale factors**

₁₈₅₄ The simulated events are corrected for any potential differences in the trigger
₁₈₅₅ efficiency between data and MC simulation. Assuming no correlation between the
₁₈₅₆ E_T^{miss} and dilepton triggers, trigger scale factors are applied to MC events which
₁₈₅₇ were not selected by the E_T^{miss} trigger. These scale factors are computed for each
₁₈₅₈ event, considering the combination of fired triggers, the number and flavours of
₁₈₅₉ the leptons,

₁₈₆₀ **5.4.3 Object definition**

₁₈₆₁ This section presents the definitions of the objects used in the analysis: jets,
₁₈₆₂ electrons, muons and E_T^{miss} (the taus are not considered).

1863 **Jets**

1864 The jets are kept only if they have $p_T > 20$ GeV and lie within $|\eta| < 2.8$. To
1865 mitigate the effects of pileup, the pile-up contribution is subtracted from the
1866 expected average energy contribution according to the jet area [89, 90]. In order
1867 to reduce the effects of pile-up, a significant fraction of the tracks in jets with
1868 $p_T < 60$ GeV and $|\eta| < 2.4$ must originate from the primary vertex, as defined by
1869 the jet vertex tagger (JVT) [91]. The jet calibration follows the prescription in
1870 Ref. [90].

1871 The 70% efficiency operating point of the MV2c10 algorithm was chosen which
1872 corresponds to the average efficiency for tagging b -jets in simulated $t\bar{t}$ events.
1873 This efficiency working point was favored by optimisation studies performed
1874 in simulated signal and background samples. The rejection factors for light-
1875 quark/gluon jets, c -quark jets and hadronically decaying τ leptons in simulated
1876 $t\bar{t}$ events are approximately 380, 12 and 54, respectively [52, 92]. Jets with
1877 $|\eta| < 2.5$ which satisfy the b -tagging and JVT requirements are identified as
1878 b -jets. Correction factors and uncertainties determined from data for the b -tagging
1879 efficiencies and mis-tag rates are applied to the simulated samples [52].

1880 For the data-driven background estimations, two categories of electrons and
1881 muons are used: “candidate” and “signal” with the latter being a subset of the
1882 “candidate” leptons satisfying tighter selection criteria.

1883 **Electrons**

1884 Electron candidates are reconstructed from energy depositions in the electromagnetic calorimeter and required to be matched to an inner detector track, to have
1885 $p_T > 10\text{GeV}$ and $|\eta| < 2.47$, and to pass the “Loose” likelihood-based electron
1886 identification requirement [46]. Electrons in the transition region between the
1887 barrel and endcap electromagnetic calorimeters ($1.37 < |\eta| < 1.52$) are rejected
1888 to reduce the contribution from fake/non-prompt electrons. The transverse im-
1889 pact parameter d_0 with respect to the reconstructed primary vertex must satisfy
1890 $|d_0/\sigma(d_0)| < 5$. This last requirement helps reduce the contribution from charge
1891 mis-identification.

1893 Signal electrons are additionally required to pass the “Medium” likelihood-
1894 based identification requirement [46]. Only signal electrons with $|\eta| < 2.0$ are
1895 considered, to reduce the level of charge-flip background. In addition, signal
1896 electrons that are likely to be reconstructed with an incorrect charge assignment
1897 are rejected using a few electron cluster and track properties: the track impact
1898 parameter, the track curvature significance, the cluster width and the quality of
1899 the matching between the cluster and its associated track, both in terms of energy
1900 and position. These variables, as well as the electron p_T and η , are combined into
1901 a single classifier using a boosted decision tree (BDT). A selection requirement on
1902 the BDT output is chosen such as to achieve a rejection factor between 7 and 8
1903 for electrons with a wrong charge assignment while selecting properly measured
1904 electrons with an efficiency of 97% (in $Z \rightarrow ee$ MC).

1905 A multiplicative event weight is applied for each signal electron in MC to the
1906 overall event weight in order to correct for differences in efficiency between data
1907 and MC.

1908 **Muons**

1909 Muons candidates are reconstructed from muon spectrometer tracks matched to
1910 the inner detector tracks in the region $|\eta| < 2.5$. Muon candidates must pass the
1911 “Medium” identification requirements [93] and have $p_T > 10\text{GeV}$ and $|\eta| < 2.4$.
1912 Signal muons are required to pass $|d_0|/\sigma(d_0) < 3$ and $|z_0 \cdot \sin(\theta)| < 0.5\text{mm}$.

1913 A multiplicative event weight is applied for each selected muon in MC to the
1914 overall event weight in order to correct for differences in efficiency between data
1915 and MC.

1916 **Overlap removal**

1917 According to the above definitions, one single final state object may fall in
1918 more than one category, being therefore effectively double-counted. For example,
1919 one isolated electron is typically reconstructed both as an electron and as a
1920 jet. A procedure to remove overlaps between final state objects was therefore
1921 put in place, and applied on pre-selected objects. Any jet within a distance
1922 $\Delta R_y \equiv \sqrt{(\Delta y)^2 + (\Delta\phi)^2} = 0.2$ of a lepton candidate is discarded, unless the jet is
1923 b -tagged,⁵ in which case the lepton is discarded since it probably originated from a
1924 semileptonic b -hadron decay. Any remaining lepton within $\Delta R_y \equiv \min\{0.4, 0.1 +$

5In this case the b -tagging operating point corresponding to an efficiency of 85% is used.

₁₉₂₅ $9.6\text{GeV}/p_T(\ell)\}$ of a jet is discarded. In the case of muons, the muon is retained
₁₉₂₆ and the jet is discarded if the jet has fewer than three associated tracks. This
₁₉₂₇ reduces inefficiencies for high-energy muons undergoing significant energy loss in
₁₉₂₈ the calorimeter.

₁₉₂₉ **Missing transverse energy**

₁₉₃₀ The missing transverse energy (E_T^{miss}) is computed as a negative vector sum of
₁₉₃₁ the transverse momenta of all identified candidate objects (electrons, photons [94],
₁₉₃₂ muons and jets) and an additional soft term. The soft term is constructed from
₁₉₃₃ all tracks associated with the primary vertex but not with any physics object. In
₁₉₃₄ this way, the E_T^{miss} is adjusted for the best calibration of the jets and the other
₁₉₃₅ identified physics objects listed above, while maintaining approximate pile-up
₁₉₃₆ independence in the soft term [95, 96].

₁₉₃₇ **5.4.4 Data-MC comparisons**

₁₉₃₈ In order to validate the various choices made regarding the object definitions
₁₉₃₉ and event selection, check their sensible behavior and their reasonable modelling
₁₉₄₀ in the simulations, we looked at the distributions of several kinematic variables
₁₉₄₁ obtained with the full available data set. Figures 5.4-5.6 show such selected
₁₉₄₂ distributions in data compared to MC. The background distributions are taken
₁₉₄₃ directly from MC with no data-driven estimation of the charge flip or non-prompt
₁₉₄₄ lepton backgrounds.

₁₉₄₅ Figure 5.4 shows the dilepton invariant mass distributions for both opposite-

¹⁹⁴⁶ sign (OS) and same-sign (SS) dilepton events, computed with the two leading
¹⁹⁴⁷ p_T leptons. A very good agreement with MC is observed in the OS channels,
¹⁹⁴⁸ with a clear Z -boson mass peak in the ee and $\mu\mu$ channels. In the SS channels,
¹⁹⁴⁹ the Z -boson mass peak is also observed in the ee channel due to electron charge
¹⁹⁵⁰ mis-identification, with MC overestimating data. An accumulation of events at the
¹⁹⁵¹ Z -boson mass is also observed in the SS $e\mu$ and $\mu\mu$ channels due to three-lepton
¹⁹⁵² events from either Z +jets with a fake lepton or from WZ production.

¹⁹⁵³ The transverse momentum distributions of the signal leptons used in the
¹⁹⁵⁴ analysis are shown in Figure 5.5, with a reasonable data-MC agreement except
¹⁹⁵⁵ at low lepton p_T where some discrepancies and accumulation of events involving
¹⁹⁵⁶ fake leptons (Z +jets, W +jets, $t\bar{t}$) are observed. Figure 5.6 shows the E_T^{miss} and
¹⁹⁵⁷ m_{eff} distributions.

¹⁹⁵⁸ The background estimation, in Chapter 6 and Chapter 7, will be dedicated to
¹⁹⁵⁹ improving the estimates of the background prediction using data-driven methods.

¹⁹⁶⁰ 5.5 Signal Regions

¹⁹⁶¹ In order to maximize the sensitivity to the signal models of Figure 5.1, 13 non-
¹⁹⁶² exclusive signal regions are defined in Table 5.6. The SRs are named in the form
¹⁹⁶³ $RPCNLMbX$, where N indicates the number of leptons required, M the number
¹⁹⁶⁴ of b -jets required, and X indicates the severity of the E_T^{miss} or m_{eff} requirements
¹⁹⁶⁵ (Soft, Medium or Hard). All signal regions allow any number of additional leptons
¹⁹⁶⁶ in addition to a $e^\pm e^\pm$, $e^\pm \mu^\pm$ or $\mu^\pm \mu^\pm$ pair. Signal regions with 3 leptons can be

¹⁹⁶⁷ either any charge combination or all three with the same charge (Rpc3LSS1b).

¹⁹⁶⁸ For each lepton/ b -jet multiplicity, two signal regions are defined targeting either

¹⁹⁶⁹ compressed spectra or large mass splittings.

¹⁹⁷⁰ The optimization of the definitions of signal regions relied on a brute-force

¹⁹⁷¹ scan of several discriminating variables in a loose classification of events in terms

¹⁹⁷² of number of b -jets and/or leptons in the final state, each being associated to the

¹⁹⁷³ signal scenario favouring this final state. The other main discriminant variables

¹⁹⁷⁴ (e.g number of jets above a certain p_T threshold, m_{eff} , E_T^{miss} , $E_T^{\text{miss}}/m_{\text{eff}}$ ratio) were

¹⁹⁷⁵ then allowed to vary, to determine for each point of the parameter space the best

¹⁹⁷⁶ configuration. The figure of merit used to rank configurations is the discovery

¹⁹⁷⁷ significance (Z_0) defined in Eq. 5.3 which represents a statistical test based on

¹⁹⁷⁸ a ratio of two Poisson means [97]:

$$Z_0 = \sqrt{2 \left((s + b) \ln \left(1 + \frac{s}{b} \right) - s \right)} \quad (5.3)$$

¹⁹⁷⁹ where s and b represent the expected number of signal and background events⁶.

¹⁹⁸⁰ A realistic systematic uncertainty of $\Delta b = 30\%$ on the expected background

¹⁹⁸¹ yield was included in the statistical test by replacing b with $b + \Delta b$ in Eq. 5.3.

¹⁹⁸² To preserve the discovery potential, only configurations leading to at least two

¹⁹⁸³ signal events were considered for a given signal point. The total number of

¹⁹⁸⁴ background events should not be smaller than 1; to model in a more realistic way

¹⁹⁸⁵ the effect of non-prompt and fake leptons and electron charge mis-identification

¹⁹⁸⁶ backgrounds, which are determined from data in the analysis, the MC predictions

⁶Note that Eq.5.3 simplifies to the commonly used figure of merit $\frac{s}{\sqrt{b}} + \mathcal{O}\left(\frac{s}{b}\right)$ if $\frac{s}{b} \ll 1$.

¹⁹⁸⁷ for those processes in $t\bar{t}$ and $Z+jets$ MC were scaled using the factors obtained
¹⁹⁸⁸ from the MC template method (Section 6.3.1), as shown in Table 5.5. Note that
¹⁹⁸⁹ different corrections are applied depending on the showering (Pythia or Sherpa)
¹⁹⁹⁰ used for each sample, and for the fake and non-prompt leptons originated from
¹⁹⁹¹ heavy-flavour (HF) and light-flavour (LF).

Table 5.5: Scaling factors applied to the electron charge-flip and non-prompt/fake lepton background in the SR optimization procedure.

	Charge mis-id	HF e	HF μ	LF e	LF μ
Pythia	0.96 ± 0.08	1.80 ± 0.45	2.10 ± 0.58	1.55 ± 0.14	0.74 ± 0.81
Sherpa	1.02 ± 0.09	2.72 ± 0.57	1.81 ± 0.75	1.16 ± 0.18	1.84 ± 1.16

¹⁹⁹² Since the signal regions defined out of the scanning procedure may not be
¹⁹⁹³ mutually exclusive, the results expressed in terms of exclusion limits will be
¹⁹⁹⁴ obtained by using for each signal point the SR giving the best expected sensitivity.
¹⁹⁹⁵ For the latter, only the signal regions that were defined aiming for that particular
¹⁹⁹⁶ signal model are considered, though.

¹⁹⁹⁷ Figures 5.7 and 5.8 show the performance of the SRs in the four RPC benchmark
¹⁹⁹⁸ models with top quarks considered. The discovery significance for each signal point
¹⁹⁹⁹ is shown, together with the contours corresponding to a 3σ discovery sensitivity,
²⁰⁰⁰ 1.64σ discovery sensitivity and 95% confidence level limits.

²⁰⁰¹ Dedicated new SRs have been optimized for the gluino pair production with
²⁰⁰² stop-mediated decay $\tilde{g} \rightarrow t\bar{t}\tilde{\chi}_1^0$ with off-shell tops.

Signal region	$N_{\text{leptons}}^{\text{signal}}$	$N_{b\text{-jets}}$	N_{jets}	p_T^{jet} [GeV]	E_T^{miss} [GeV]	m_{eff} [GeV]	$E_T^{\text{miss}}/m_{\text{eff}}$	Other	Targeted Signal
Rpc2L2bS	$\geq 2\text{SS}$	≥ 2	≥ 6	> 25	> 200	> 600	> 0.25	—	Fig. 5.1a
Rpc2L2bH	$\geq 2\text{SS}$	≥ 2	≥ 6	> 25	—	> 1800	> 0.15	—	Fig. 5.1a, NUHM2
Rpc2Lsoft1b	$\geq 2\text{SS}$	≥ 1	≥ 6	> 25	> 100	—	> 0.3	$20,10 < p_T^{\ell_1}, p_T^{\ell_2} < 100 \text{ GeV}$	Fig. 5.1b
Rpc2Lsoft2b	$\geq 2\text{SS}$	≥ 2	≥ 6	> 25	> 200	> 600	> 0.25	$20,10 < p_T^{\ell_1}, p_T^{\ell_2} < 100 \text{ GeV}$	Fig. 5.1b
Rpc2L0bS	$\geq 2\text{SS}$	$= 0$	≥ 6	> 25	> 150	—	> 0.25	—	Fig. 5.1c
Rpc2L0bH	$\geq 2\text{SS}$	$= 0$	≥ 6	> 40	> 250	> 900	—	—	Fig. 5.1c
Rpc3L0bS	≥ 3	$= 0$	≥ 4	> 40	> 200	> 600	—	—	Fig. 5.1d
Rpc3L0bH	≥ 3	$= 0$	≥ 4	> 40	> 200	> 1600	—	—	Fig. 5.1d
Rpc3L1bS	≥ 3	≥ 1	≥ 4	> 40	> 200	> 600	—	—	Other
Rpc3L1bH	≥ 3	≥ 1	≥ 4	> 40	> 200	> 1600	—	—	Other
Rpc2L1bS	$\geq 2\text{SS}$	≥ 1	≥ 6	> 25	> 150	> 600	> 0.25	—	Fig. 5.1e
Rpc2L1bH	$\geq 2\text{SS}$	≥ 1	≥ 6	> 25	> 250	—	> 0.2	—	Fig. 5.1e
Rpc3LSS1b	$\geq \ell^\pm \ell^\pm \ell^\pm$	≥ 1	—	—	—	—	—	veto $81 < m_{e^\pm e^\pm} < 101 \text{ GeV}$	Fig. 5.1f

Table 5.6: Summary of the signal region definitions. Unless explicitly stated in the table, at least two signal leptons with $p_T > 20 \text{ GeV}$ and same charge (SS) are required in each signal region. Requirements are placed on the number of signal leptons ($N_{\text{leptons}}^{\text{signal}}$), the number of b -jets with $p_T > 20 \text{ GeV}$ ($N_{b\text{-jets}}$), the number of jets (N_{jets}) above a certain p_T threshold (p_T^{jet}), E_T^{miss} , m_{eff} and/or $E_T^{\text{miss}}/m_{\text{eff}}$. The last column indicates the targeted signal model. The Rpc3L1b and Rpc3L1bH SRs are not motivated by a particular signal model and can be seen as a natural extension of the Rpc3L0b SRs with the same kinematic selections but requiring at least one b -jet.

²⁰⁰³ The $\tilde{g}\tilde{g}$ production with $\tilde{g} \rightarrow t\bar{t}\tilde{\chi}_1^0$ scenario at low LSP masses (where the multi- b analysis has a much better sensitivity [98]) is not the only motivation

2005 for Rpc2L2bH signal region, but also the NUHM2 model, which features large
 2006 branching ratios for the $\tilde{g} \rightarrow t\bar{t}\tilde{\chi}_{1,2,3}^0$ and $\tilde{g} \rightarrow t\bar{b}\tilde{\chi}_{1,2}^\pm$ decays. As shown in Figure 5.9,
 2007 with the Rpc2L2bH signal region, $m_{1/2}$ values of 600 GeV can be excluded at 95%
 2008 CL or observed with a 3σ significance. This SR will be then used for the first
 2009 interpretation in this model.

2010 In addition, the SS/3L analysis has the unique potential to explore the region
 2011 of phase space at high LSP masses with a more compressed spectra. This scenario
 2012 leads to softer decay products, in particular softer b -jets as seen in Figure 5.10,
 2013 which makes the multi- b analysis less sensitive. For this reason, two additional
 2014 signal regions were introduced with at least 1 b -jet (Rpc2Lsoft1b) or 2 b -jets
 2015 (Rpc2Lsoft2b) defined in Table 5.6. In addition, these signal regions are defined
 2016 with an upper cut on the leading lepton p_T . The sensitivity is degraded if this
 2017 upper cut is removed as shown in Figure 5.11.

2018 Motivated by the \tilde{t} production with $\tilde{t}_1 \rightarrow \tilde{\chi}_2^0 W$ model in Section 5.2, the
 2019 signature of three leptons with the same electric charge (3LSS) is explored for
 2020 the first time. As shown in Figure 5.12, after an inclusive 3LSS selection, the
 2021 background is dominated by dibosons and $Z+jets$ (with only one real lepton,
 2022 and the two other leptons with either an electron with charge mis-identified or a
 2023 fake lepton) both dominantly without b -jets. Once a b -jet requirement is applied,
 2024 the background is dominated by $t\bar{t}V$, with a clear peak at $m_{\ell\ell} \approx m_Z$ showing
 2025 that a large fraction of these events are originated from charge mis-identification
 2026 from events containing $Z \rightarrow ee$. After applying a $81 < m_{e^\pm e^\pm} < 101$ GeV veto,
 2027 the background is reduced to only 1.7 events for 36.5 fb^{-1} , almost removing the

2028 $Z + \text{jets}$ and diboson backgrounds completely. The final background is dominated
2029 by $t\bar{t} + H, Z, W$, with $\sim 60\%$ originating from charge flips and $\sim 40\%$ from fakes and
2030 non-prompt leptons. With these very generic selections (Rpc3LSS1b in Table 5.6),
2031 a significance of 3.7σ can be obtained for $m_{\tilde{t}} = 550$ GeV. Figure 5.13 shows some
2032 lepton distributions, including the number of electrons, where most of the charge
2033 flip background populates the bins with 2 or 3 electrons, although cutting away
2034 those bins would also have a large impact on the signal.

2035 Finally, since the SRs defined for the $\tilde{g}\tilde{g}$ production with $\tilde{g} \rightarrow q\bar{q}\ell\bar{\ell}\tilde{\chi}_1^0$ feature
2036 a b -jet veto (Rpc3L0bS and Rpc3L0bH), and to avoid leaving uncovered the 3
2037 lepton plus b -jets signature, SRs with the same kinematic cuts as Rpc3L0bS and
2038 Rpc3L0bH but with a ≥ 1 b -jet requirement are also proposed in Table 5.6 as
2039 Rpc3L1bS and Rpc3L1bH.

2040 5.6 Analysis Acceptance and Efficiency

2041 Based on the signal regions defined in Section 5.6, it is useful to evaluate the
2042 signal acceptance of the analysis using parton level MC simulation (truth study).
2043 The acceptance encodes all the kinematic cuts applied on the signal as well as
2044 the branching ratios of all the decay particles. This information will help us
2045 understand the sensitivity reach of the analysis and also allow theorists to use
2046 this information when comparing the simplified model results to their models.
2047 The signal acceptance is shown in Figure 5.14a with the rest of the signal regions
2048 shown in Appendix A.4. Table 5.7 shows an example of a detailed cut-flow for

²⁰⁴⁹ weighted signal MC events illustrating the impact of cuts from the Rpc2L0bH
²⁰⁵⁰ signal region on a signal model. More tables are shown in Appendix A.3.

Rpc2L0bH, $\tilde{g}\tilde{g}$ production, $\tilde{g} \rightarrow q\bar{q}' WZ\tilde{\chi}_1^0$ $m_{\tilde{g}} = 1.6\text{TeV}$, $(m_{\tilde{\chi}_1^\pm} - 750) = (m_{\tilde{\chi}_2^0} - 375) = m_{\tilde{\chi}_1^0} = 100\text{GeV}$	
MC events generated	20000
Expected for 36.1 fb^{-1}	2.9×10^2
≥ 2 SS leptons ($p_T > 20\text{GeV}$)	12.8 ± 0.5
Trigger	12.5 ± 0.5
no b -jet ($p_T > 20\text{GeV}$)	8.5 ± 0.4
≥ 6 jets ($p_T > 40\text{GeV}$)	7.12 ± 0.35
$E_T^{\text{miss}} > 250\text{GeV}$	5.13 ± 0.29
$m_{\text{eff}} > 0.9\text{TeV}$	5.13 ± 0.29

Table 5.7: Number of signal events at different stages of the Rpc2L0bH signal region selection. Only statistical uncertainties are shown.

²⁰⁵¹ Another quantity of interest, to experimentalists in particular, is the detector
²⁰⁵² efficiency that entails the reconstruction and identification efficiencies of the
²⁰⁵³ different particles used in the analysis. The efficiency ϵ can be obtained from the
²⁰⁵⁴ relation

$$S = L_{\text{int}} \cdot \sigma_{\text{prod}} \cdot A \cdot \epsilon \quad (5.4)$$

2055 Where S is the expected number of signal events, σ_{prod} is the production cross
2056 section of the signal process, L_{int} is the integrated luminosity, and A is the
2057 acceptance. Figure 5.14b shows

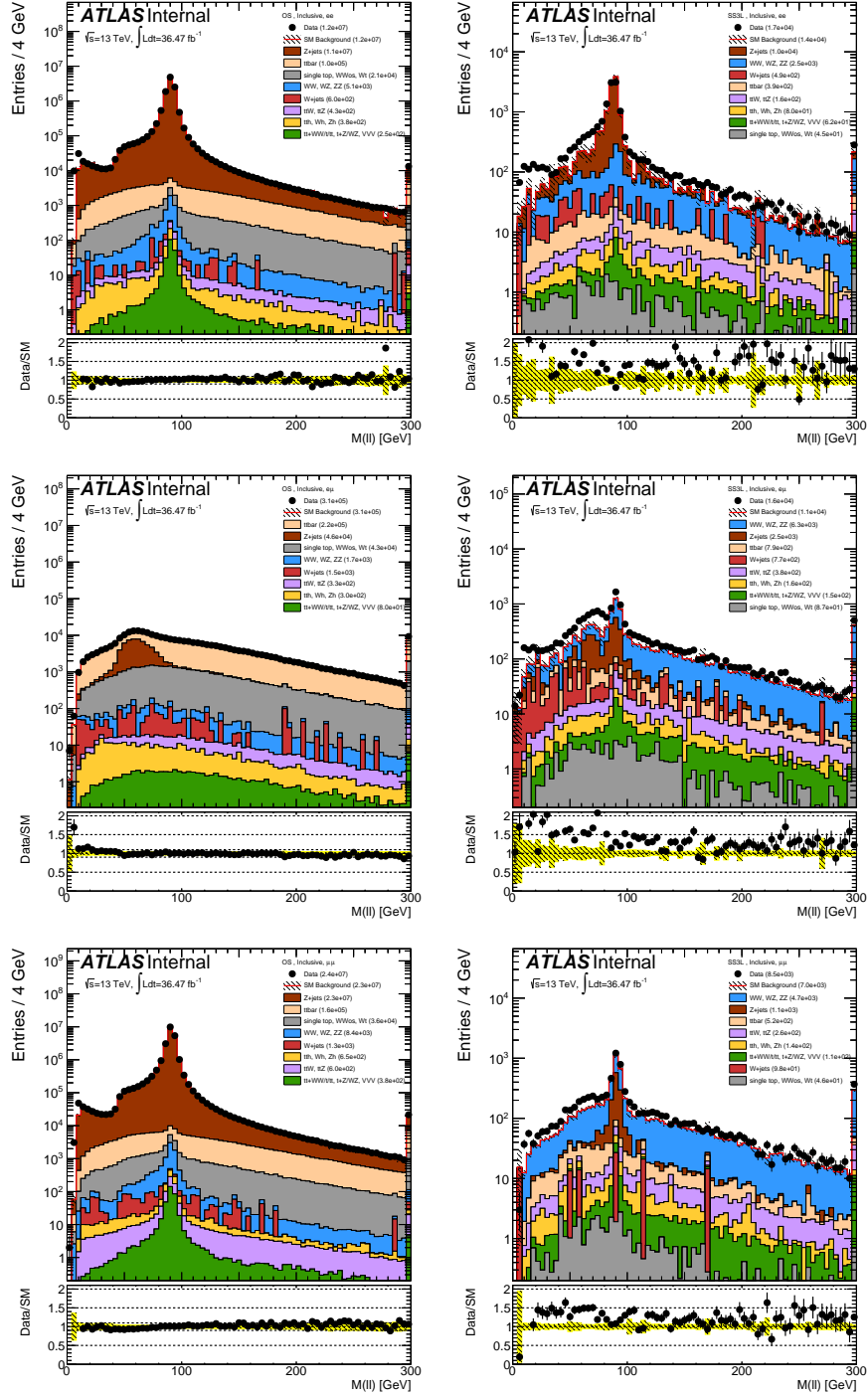


Figure 5.4: Dilepton invariant mass distributions for opposite-sign (left) and same-sign (right) pairs for events selected in the ee (top), $e\mu$ (center) and $\mu\mu$ (bottom) channels. No low-mass Drell-Yan sample is included. The prediction is taken from MC only. Only luminosity and MC statistical uncertainties are included.

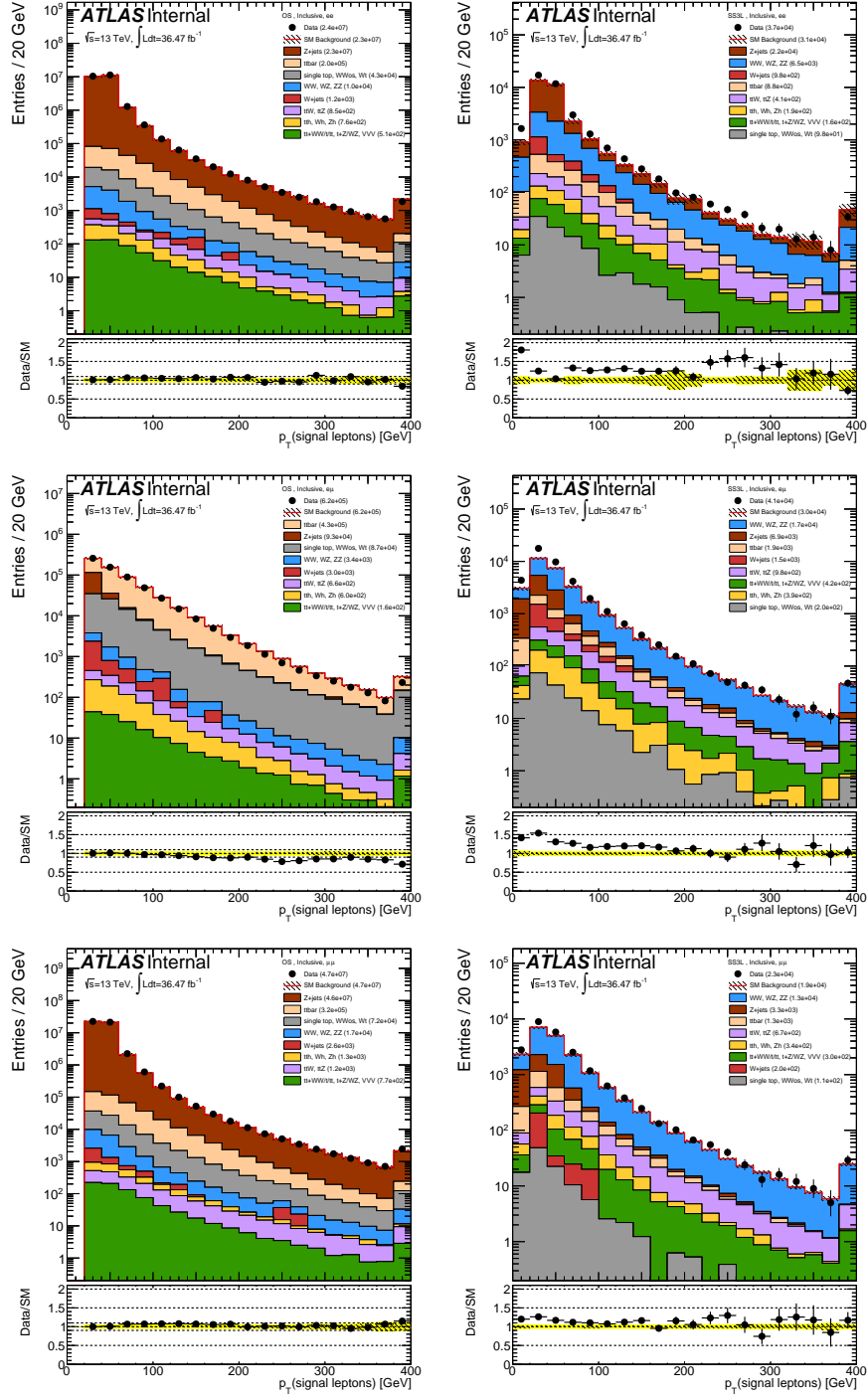


Figure 5.5: Signal lepton transverse momentum distributions for opposite-sign (left) and same-sign (right) pairs for events selected in the ee (top), $e\mu$ (center) and $\mu\bar{\mu}$ (bottom) channels. The prediction is taken from MC only. Only luminosity and MC statistical uncertainties are included.

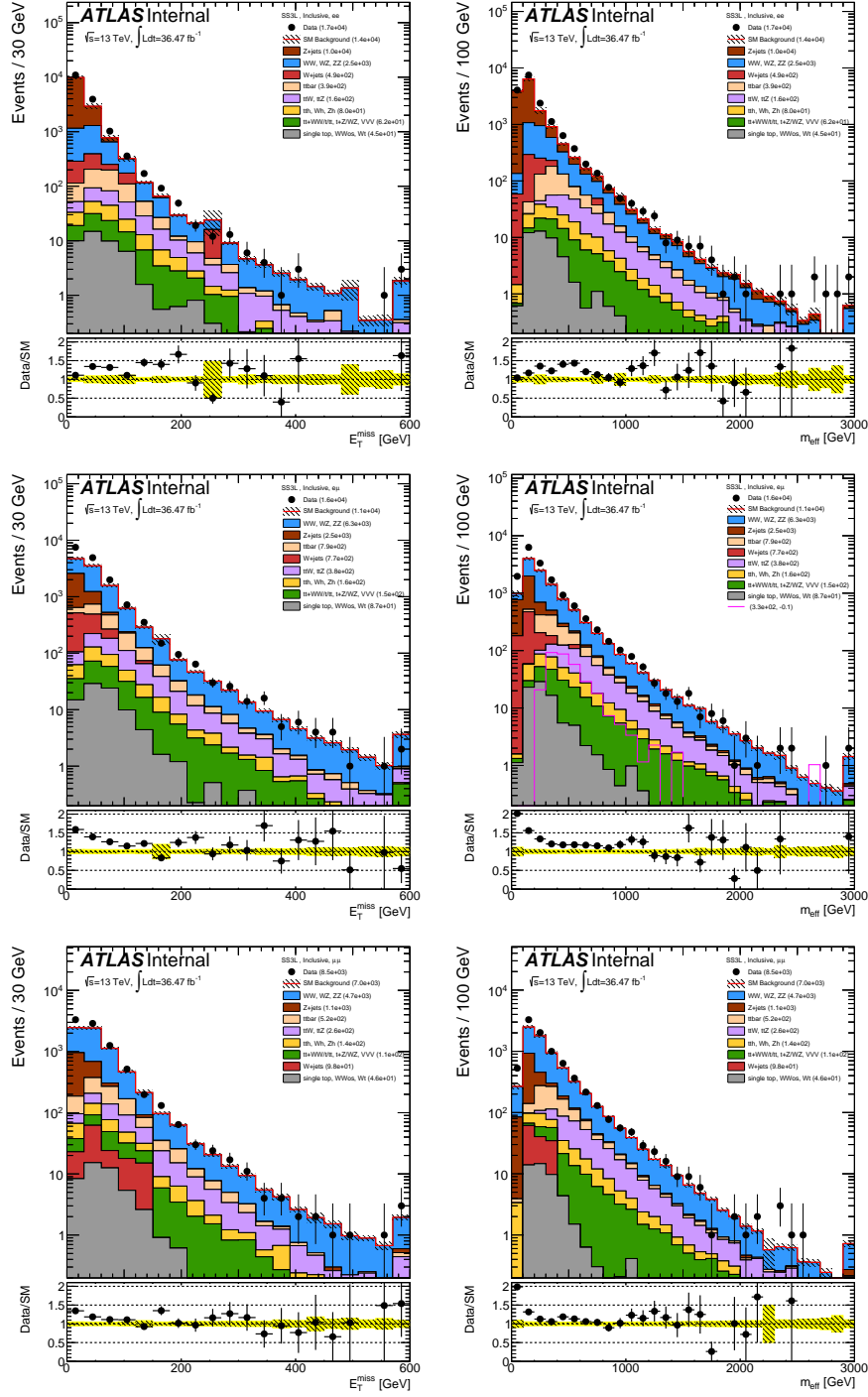


Figure 5.6: Distributions of the E_T^{miss} (left) and effective mass (right) for events selected in the ee (top), $e\mu$ (center) and $\mu\mu$ (bottom) channels. The prediction is taken from MC only. Only luminosity and MC statistical uncertainties are included.

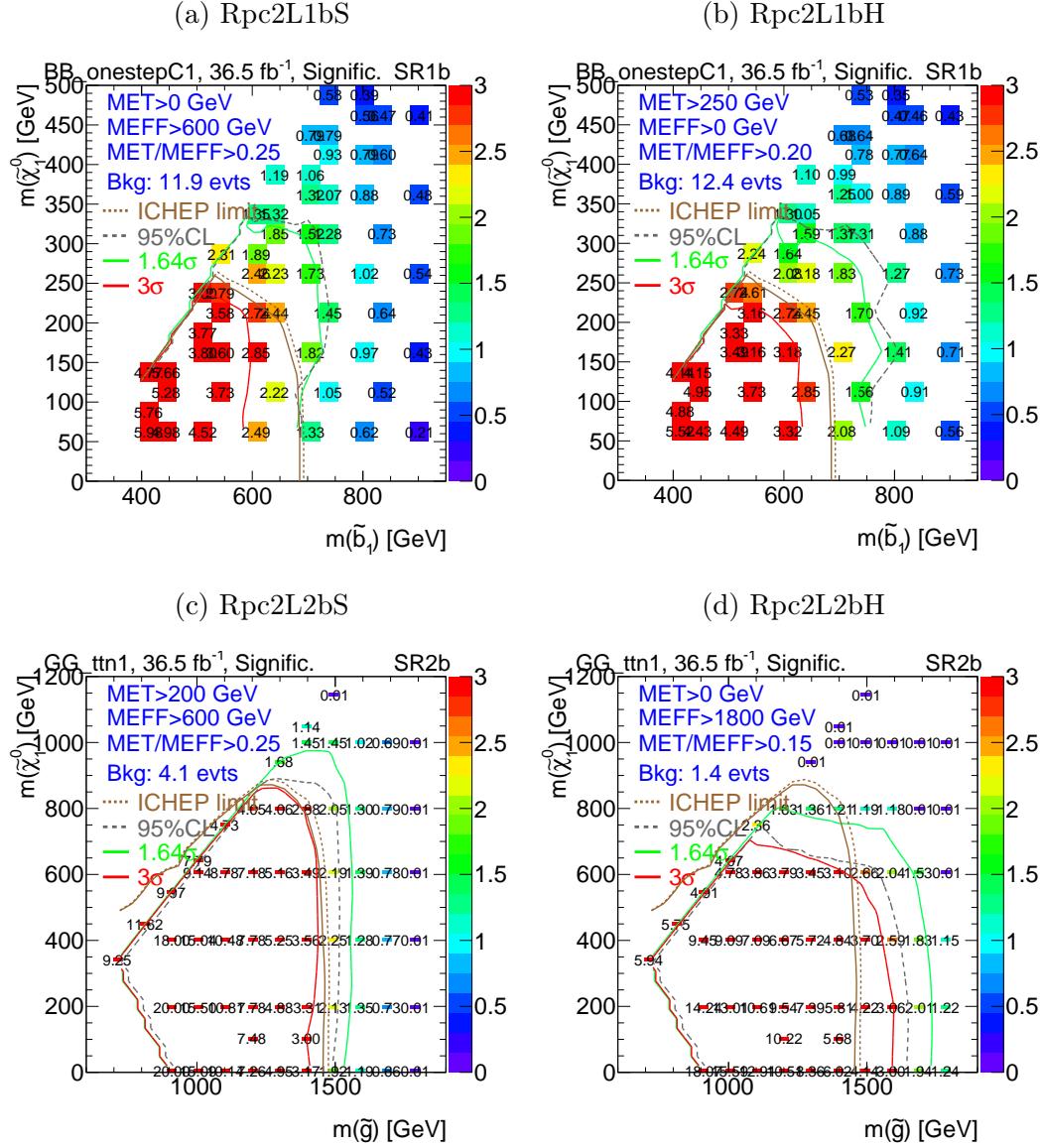
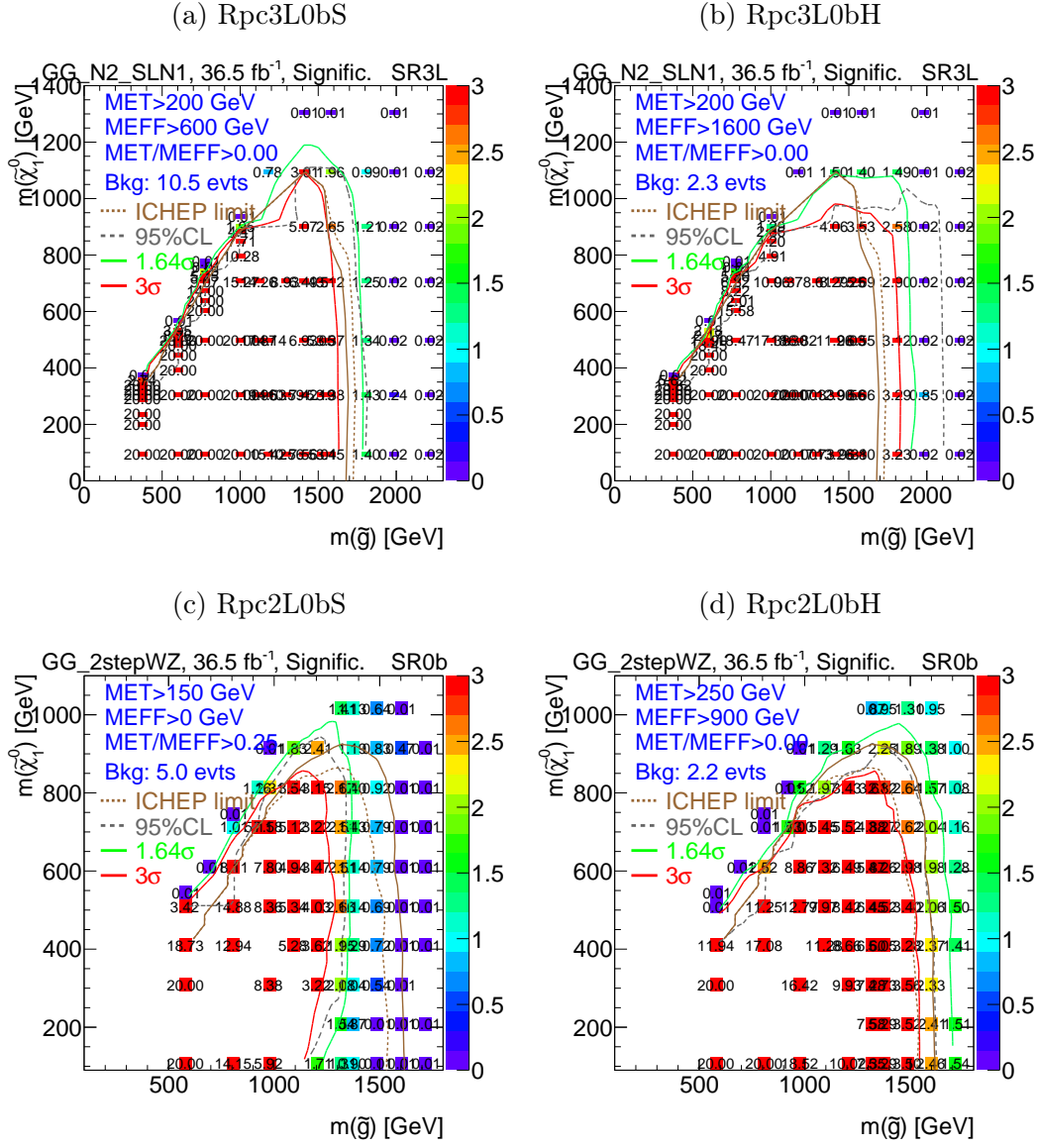


Figure 5.7: Discovery significance for the SRs with b -jets defined in Table 5.6 for 36.5 fb^{-1} : Rpc2L1bS and Rpc2L1bH in the $\tilde{b}_1 \tilde{b}_1^* \rightarrow t\bar{t} \tilde{\chi}_1^+ \tilde{\chi}_1^-$ grid (top), Rpc2L2bS and Rpc2L2bH in the $\tilde{g}\tilde{g} \rightarrow t\bar{t} t\bar{t} \tilde{\chi}_1^0 \tilde{\chi}_1^0$ grid (bottom). The 95% CL, 1.64σ , and 3σ discovery contours from the proposed signal regions are shown in grey, green, and red, respectively.

Figure 5.8: Discovery significance for the SRs without b -jets defined in Table 5.6

for 36.5 fb^{-1} : Rpc2L0bS and Rpc2L0bH in the $\tilde{g}\tilde{g}$ with $\tilde{g} \rightarrow q\bar{q}'WZ\tilde{\chi}_1^0$ grid (top)

and Rpc3L0bS and Rpc3L0bH in the $\tilde{g}\tilde{g}$ with $\tilde{g} \rightarrow q\bar{q}(\ell\ell/\ell\nu)\tilde{\chi}_1^0$ grid (bottom).

The 95% CL, 1.64σ , and 3σ discovery contours from the proposed signal regions are shown in grey, green, and red, respectively.

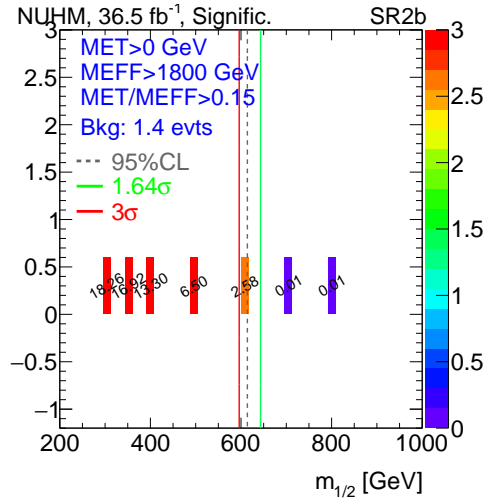


Figure 5.9: Discovery significance for Rpc2L2bH signal region for 36.5 fb^{-1} , NUHM2 model. The 95% CL, 1.64σ , and 3σ discovery contours from the proposed signal regions are shown in grey, green, and red, respectively.

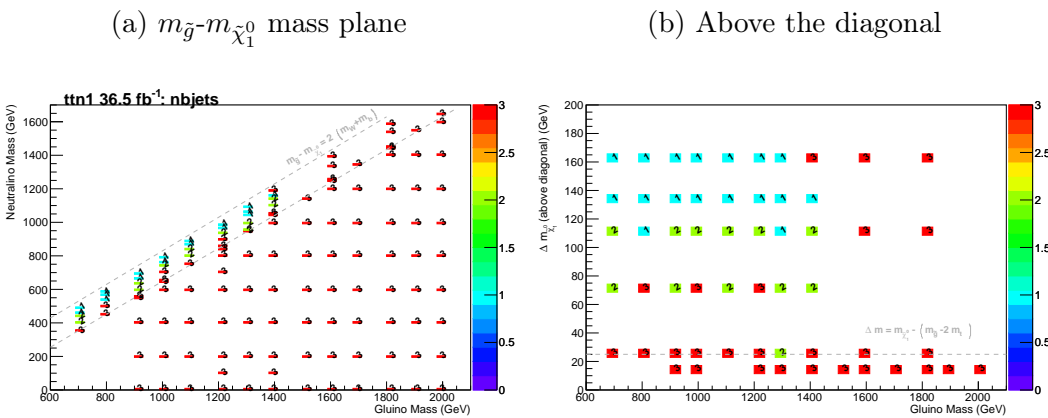


Figure 5.10: Optimal cut on the number of b -jets leading to the best discovery significance.

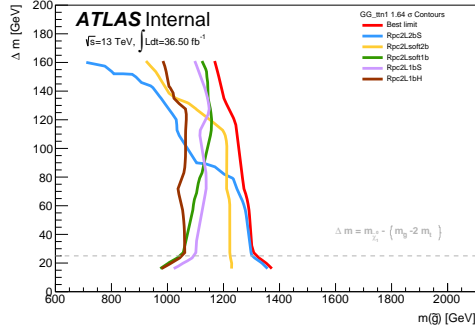
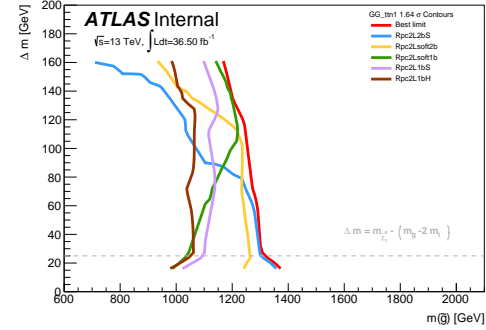
(a) Without $p_T^{\ell_1}$ uppercut(b) With $p_T^{\ell_1}$ uppercut

Figure 5.11: Comparison of significance contours at 1.64σ for 36.5 fb^{-1} between Rpc2Lsoft2b and Rpc2Lsoft1b and other signal regions in the off-diagonal region considering the option of an upper cut on the leading lepton p_T .

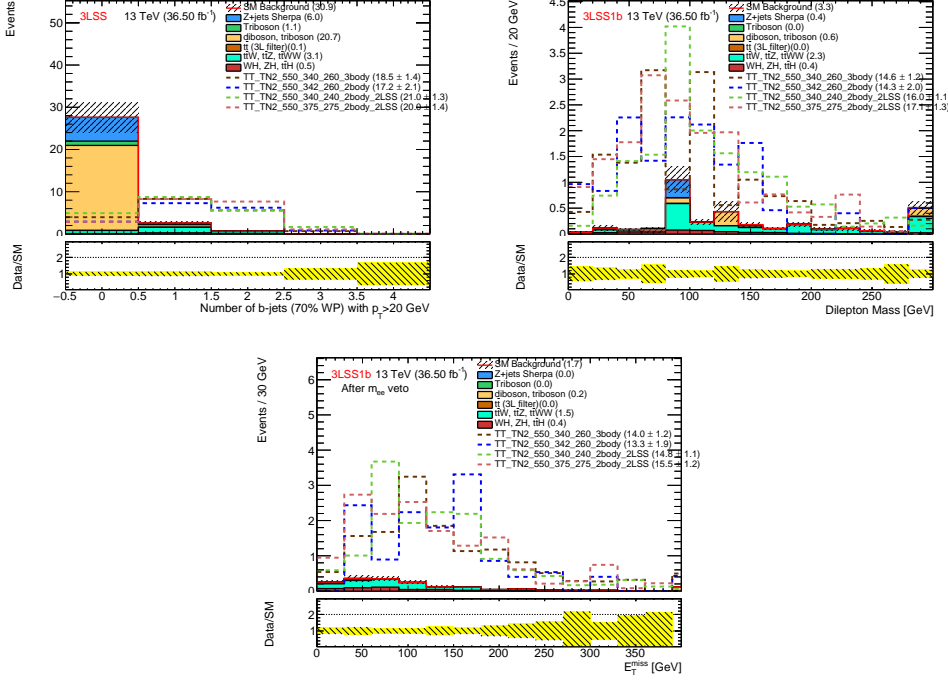


Figure 5.12: b -jet multiplicity after a 3LSS selection (top left), dilepton invariant mass distributions after a 3LSS plus ≥ 1 b -jet selection (top right), and E_T^{miss} distribution after a 3LSS, ≥ 1 b -jet and $81 < m_{e^\pm e^\pm} < 101$ GeV veto selection (bottom), all corresponding to 36.5 fb^{-1} . The background distributions are stacked, while the lines show the predictions for four signal points at \tilde{t} mass of 550 GeV.

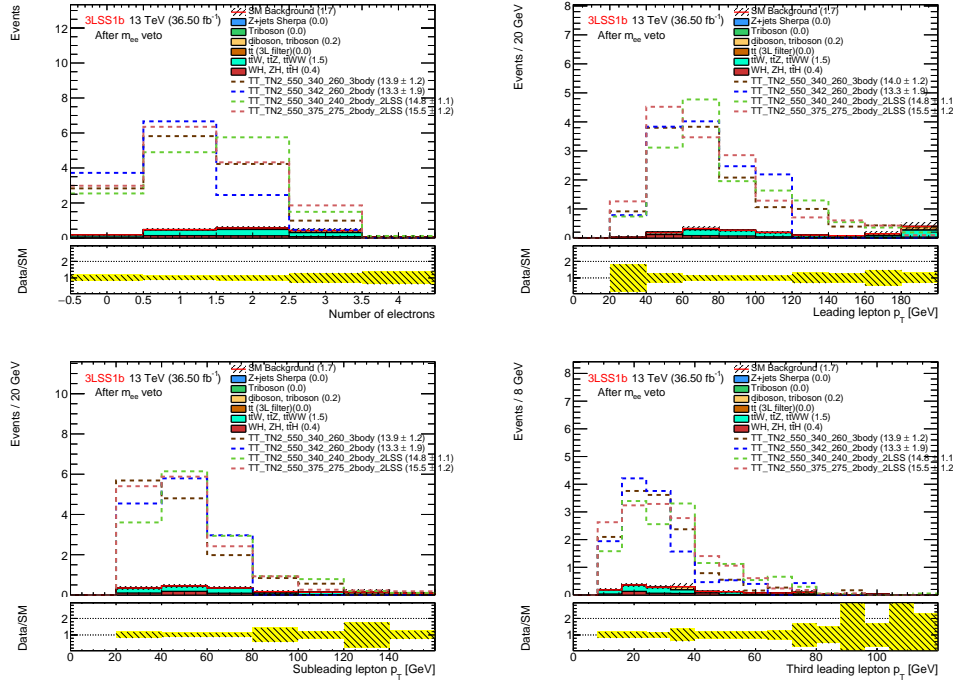


Figure 5.13: Number of electron (top left), and p_T of the leading (top right), subleading (bottom left) and third leading lepton (bottom right) after a 3LSS, ≥ 1 b -jet and $81 < m_{e^\pm e^\pm} < 101$ GeV veto selection (bottom), all corresponding to 36.5 fb^{-1} . The background distributions are stacked, while the lines show the predictions for four signal points at \tilde{t} mass of 550 GeV.

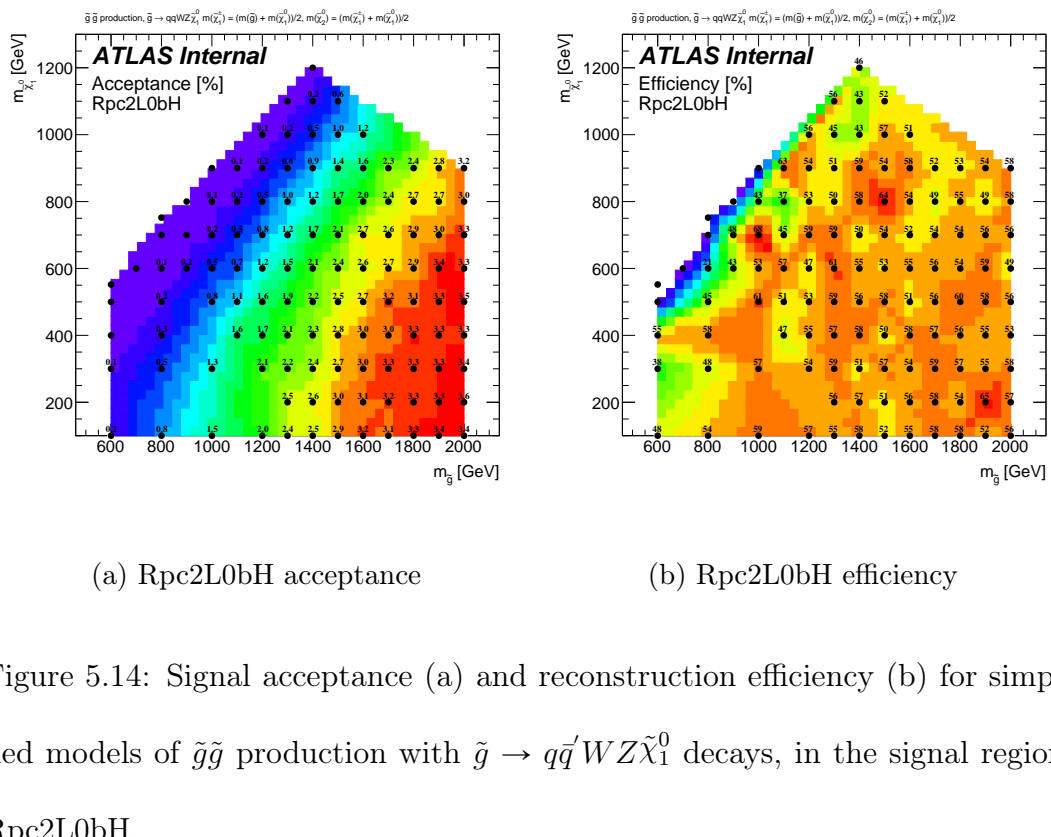


Figure 5.14: Signal acceptance (a) and reconstruction efficiency (b) for simplified models of $\tilde{g}\tilde{g}$ production with $\tilde{g} \rightarrow q\bar{q}'WZ\tilde{\chi}_1^0$ decays, in the signal regions Rpc2L0bH.

2058 **Chapter 6**

2059 **Data-driven Background Estimation Techniques**

2060 **6.1 The problem of fakes**

2061 The reconstructed objects (leptons, photons, b -jets, etc.) in a collision event are

2062 used to perform a wide range of SM measurements or searches for evidence of BSM

2063 physics. The assumption is that these objects are ‘real’ representing the desired

2064 particles in the final state used in the analysis. In practice, the reconstructed

2065 objects might not be always ‘real’. In fact, they may be something completely

2066 different that were mistakenly reconstructed as the desired object, called ‘fake’.

2067 For the purpose of the analysis presented in this thesis, the focus is on ‘fake’

2068 leptons. To illustrate the problem, a hadronic jet may deposit more energy in

2069 the electromagnetic calorimeter than the hadronic calorimeter, or that it leaves a

2070 narrow deposit of energy, leading the reconstruction algorithms to mistake this

2071 jet for an electron. From the analysis point of view, the ‘fake’ electron will pass

2072 all the selection criteria and will be indistinguishable from a ‘real’ electron. It is

2073 important for the analysis that requires a reconstructed electron to model the fake

2074 electron background to get a sound result. This example was given with electrons,

2075 but can be generalized to muons as well. In short, any analysis that uses leptons

2076 in the final state must account for the ‘fake’ lepton background. This background

2077 can be more or less important depending on the detector, the analysis selection,

2078 and the number of leptons required. To estimate this background it is important

2079 to first understand what type of processes lead to fake leptons.

2080 6.2 Common processes for faking leptons

2081 The reconstruction of ‘fake’ leptons can be an instrumental effect related to the
2082 inability to identify the object based on its measured properties by the detector.

2083 In this case, the reconstructed lepton is not a real lepton and the production
2084 process will be different for electrons and muons.

2085 The reconstruction of electrons relies on the observation of well aligned particle
2086 hits in the layers of the ID that are consistent with an energy deposition in the
2087 EM calorimeter. Photons can mimic this signature since they deposit energy in
2088 the EM calorimeter that happens to be aligned with a charged track. A jet for
2089 example containing charged and neutral pions can lead to such scenarios. It is
2090 possible for the jet to have one charged pion leaving a track similar to that of an
2091 electron. The decay of π^0 mesons to photons in this jet can deposit energy in the
2092 EM calorimeter leading to the required signature. Another mechanism that can
2093 lead to fake electrons is the emission of photons via Bremsstrahlung from high
2094 energy muons. The muon track can be mistaken for that of an electron and the
2095 photons interact with the EM calorimeter leading to a signature similar to that of
2096 electrons. An additional process is that of photon conversions into a e^+e^- .

2097 The reconstruction of muons relies on the observation of tracks from the ID
2098 matched to tracks from the muon spectrometer. It is possible for charged hadrons
2099 with long lifetime to traverse the calorimeter layers and leave hits in the muon

2100 spectrometer. These hits may coincide with other hits from the ID due to the
 2101 random activity in the event. As a result, a muon can get reconstructed. Another
 2102 instance may occur when pions or kaons decay in-flight to muons in the muon
 2103 spectrometer and happen to align with the primary vertex.

2104 The leptons that are used in the physics analyses must be coming from the
 2105 hard scatter, generally referred to as prompt leptons. There is another case where
 2106 the reconstructed lepton is a real lepton but is not a lepton coming from the
 2107 hard interaction, referred to as non-prompt leptons. Non-prompt leptons can be
 2108 produced from heavy flavor meson decays with a low energy activity around the
 2109 lepton which allows it to pass isolation requirements. A good example of this type
 2110 of process is the semi-leptonic decay of top quark pairs which contribute to final
 2111 states with two leptons.

2112 For the rest of the thesis, the fake leptons will be referred to as fake/non-prompt
 2113 (FNP) leptons. There are several methods used to perform the estimation of
 2114 FNP lepton backgrounds. A method that the author developed will be described
 2115 next along with a standard method for estimating this type of backgrounds. The
 2116 benefit of having two methods for estimating the FNP lepton background is to
 2117 have enough confidence in the final estimate. The two methods use different
 2118 assumptions which naturally leads to a more robust estimation of this difficult
 2119 background. Moreover, the final estimate of the FNP lepton background is taken
 2120 as a statistical combination of the estimates from the two methods leading to a
 2121 reduction of the systematic uncertainties on the estimate.

2122 6.3 The Monte Carlo Template Method

2123 6.3.1 Motivation

2124 The processes leading to FNP leptons depend on the selection applied in the
 2125 analysis. For instance, a selection with same-sign leptons will have contributions
 2126 from top quark pair production ($t\bar{t}$) or the associated production of a vector
 2127 boson and jets ($W+jets$ or $Z+jets$). These processes cannot give two leptons
 2128 of the same electric charge unless there is a charge mis-measurement (mainly
 2129 affecting electrons) or that a FNP lepton was produced. It is possible to generate
 2130 the processes that can contribute to a FNP lepton, such as $t\bar{t}$ or $V+jets$, with
 2131 Monte Carlo event generators processed through Geant4 detector simulation of the
 2132 ATLAS detector. This approach will yield an estimate, however it might not be
 2133 reliable. For instance, the detector simulation itself might not reproduce the true
 2134 behavior of the interaction of the physics objects with the detector, particularly
 2135 when looking at rare processes such as the production of FNP leptons. The second
 2136 limitation is in the generation of enough MC events to probe the region of the
 2137 phase space targeted by the analysis which affects the statistical uncertainties in
 2138 the estimates. The latter concern is addressed by ensuring that the simulations
 2139 for the major backgrounds ($t\bar{t}$ and $V+jets$) have much higher event count than
 2140 the corresponding number of events observed in the data sample. In fact, these
 2141 backgrounds have a large number of simulated events because they are important
 2142 for many analyses (including SM measurements and BSM searches). The rest of

²¹⁴³ the section will concentrate on addressing the former limitation.

²¹⁴⁴ 6.3.2 Description of the method

²¹⁴⁵ The MC template method relies on the correct modelling of FNP leptons kinematics
²¹⁴⁶ in MC simulation to extrapolate background predictions from control regions to
²¹⁴⁷ the signal regions. The method assumes that the kinematic shapes for each source
²¹⁴⁸ of FNP lepton is correctly modeled in the simulations, and the normalization for
²¹⁴⁹ each source is extracted in a combined fit to data control regions. The number
²¹⁵⁰ of normalization factors depend on the number of identified origins of the FNP
²¹⁵¹ lepton in the signal regions and the control regions are designed to constrain these
²¹⁵² factors in regions enriched with FNP leptons from the same origin.

²¹⁵³ To illustrate the approach, we describe the application of the method in the
²¹⁵⁴ SS/3L analysis later described in this thesis. The processes of interest that may
²¹⁵⁵ lead to a FNP lepton or a charge flip are $t\bar{t}$ and $V+jets$. FNP leptons are classified
²¹⁵⁶ using an algorithm that navigates the generator particle record to determine where
²¹⁵⁷ the FNP lepton is originating from. The lepton is classified as either an electron or
²¹⁵⁸ a muon that is prompt from decays of on-shell W and Z bosons, non-prompt from
²¹⁵⁹ a heavy flavor b decay (HF), or fake from mis-identification of a light flavor jet or
²¹⁶⁰ a photon (LF). In the case of an electron, we further classify the prompt electrons
²¹⁶¹ to prompt electrons with the correct charge or with a charge mis-measurement,
²¹⁶² commonly named charge flip. In total, five categories referred to as MC templates
²¹⁶³ are constructed following the classification illustrated in Figure 6.1.

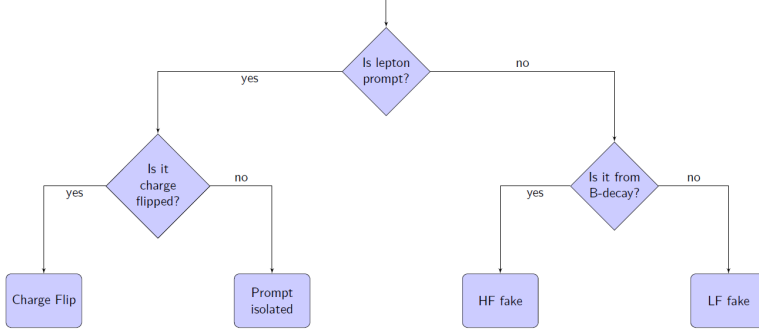


Figure 6.1: Lepton classification.

2164 6.3.3 Correction factors

2165 The FNP estimate relies on kinematic extrapolation using processes expected to
2166 contribute via FNP leptons from control regions with low jet multiplicity and
2167 E_T^{miss} , to the signal regions that require high jet multiplicity and E_T^{miss} . The
2168 control regions are chosen to separate FNP leptons from HF origins and FNP
2169 leptons from LF origins. For instance, a control sample characterized by the
2170 presence of a b -jet will be enriched in processes with one FNP lepton that is
2171 coming from a HF decay, while a sample characterized by the absence of a b -jet
2172 will have one FNP lepton from LF decay. The presence of one FNP lepton in the
2173 control sample allows the correction of the production rate of these FNP leptons
2174 by performing a fit to data.

2175 For example, if a $Z \rightarrow \mu\mu + \text{LF jet}$ event is reconstructed as a $\mu^+\mu^-e^+$ event,
2176 then the electron is fake. Therefore, a correction of $\text{LF jet} \rightarrow e$ ($\text{Fr}(\text{LF} \rightarrow e)$) is
2177 applied to the rate of $\mu\mu e$ events. The correction $\text{Fr}(\text{LF} \rightarrow e)$ is constrained by
2178 a fit to data in control regions dominated by LF jet $\rightarrow e$ type fakes. Similarly,
2179 three other corrections are defined as LF jet $\rightarrow \mu$ ($\text{Fr}(\text{LF} \rightarrow \mu)$), HF jet $\rightarrow e$

2180 ($\text{Fr}(\text{HF} \rightarrow e)$), HF jet $\rightarrow \mu$ ($\text{Fr}(\text{HF} \rightarrow \mu)$). An additional correction is applied to
 2181 correct the charge flip rate predicted by simulation. For example, a $Z \rightarrow e^+e^-$ event
 2182 is reconstructed as e^+e^+ or e^-e^- . The simulation takes into account the charge
 2183 flip rate but the fraction of time it occurs may be wrong. The charge flip ($\text{Cf}(e)$)
 2184 correction, derived from a data fit, is expected to recover this mis-modeling. The
 2185 charge flip rate only concern electrons as the muon charge flip rate is negligible.

2186 A likelihood fit is defined as the product of the Poisson probabilities describing
 2187 the observed events in the binned distributions from the expected number of
 2188 events rescaled by the five multipliers which are left free to float in the fit. These
 2189 multipliers are applied to the MC predictions in the signal regions to obtain an
 2190 estimation of the charge flip and FNP backgrounds.

2191 6.3.4 Control regions

2192 The corrections depend on the simulated sample, the reconstructed final state,
 2193 and the flavor of the leptons. As a result, care must be taken when designing the
 2194 control regions used to perform the fit of the FNP leptons and electron charge flip
 2195 templates. For instance, each template needs to be constrained in a selection that
 2196 is representative of the processes leading to FNP leptons and charge flip electrons
 2197 present in the kinematic region targeted by the search for BSM physics.

2198 In the SS/3L analysis discussed in this dissertation, the control regions are
 2199 defined with at least two same-sign leptons, $E_T^{\text{miss}} > 40$ GeV, and two or more jets.
 2200 This pre-selection ensures that the FNP leptons are not from fakes originating
 2201 from QCD like event topologies. They are further split in regions with or without

2202 *b*-jets to constrain the HF and LF leptons respectively. In addition, they are also
 2203 split with different flavours of the same-sign lepton pair ee, e μ , and $\mu\mu$, giving a
 2204 total of six control regions. Any event entering the signal region is vetoed. The
 2205 ee channel will constrain the charge flip correction factor, fake leptons from LF
 2206 decays in the selection without *b*-jets, and non-prompt decay from HF in the
 2207 selection with *b*-jets. The $\mu\mu$ channel will constrain the muon fake rates in the
 2208 LF and HF decays for the selection without or with *b*-jets, respectively. The e μ
 2209 channel will constrain both the electron and muon fakes for events containing
 2210 both lepton flavors.

2211 The six distributions are chosen for variables that provide the best separation
 2212 between processes with prompt leptons and processes with FNP leptons and
 2213 charge flip and are shown before and after the fit in Figures 6.2-6.4 and Figures
 2214 6.3-6.5, respectively.

2215 The minimization of the negative log likelihood using the MINUIT package leads
 2216 to the multipliers shown in Tables 6.1 and 6.2. The tables represent the multipliers
 2217 obtained from the fit upon using two different parton showers, POWHEG-Box
 2218 +Pythia and SHERPA for the processes that lead to FNP leptons and charge flips.
 2219 The systematic uncertainty is obtained by varying the generator from POWHEG-
 2220 Box +Pythia to SHERPA and evaluating the impact on the expected background
 2221 from FNP and charge flip leptons. This is found to be the dominant contribution
 2222 to the systematic uncertainty of the method (up to 80%). The uncertainties in the
 2223 multipliers themselves correspond to how much the parameter needs to be varied
 2224 for a one standard deviation change in the likelihood function. This uncertainty

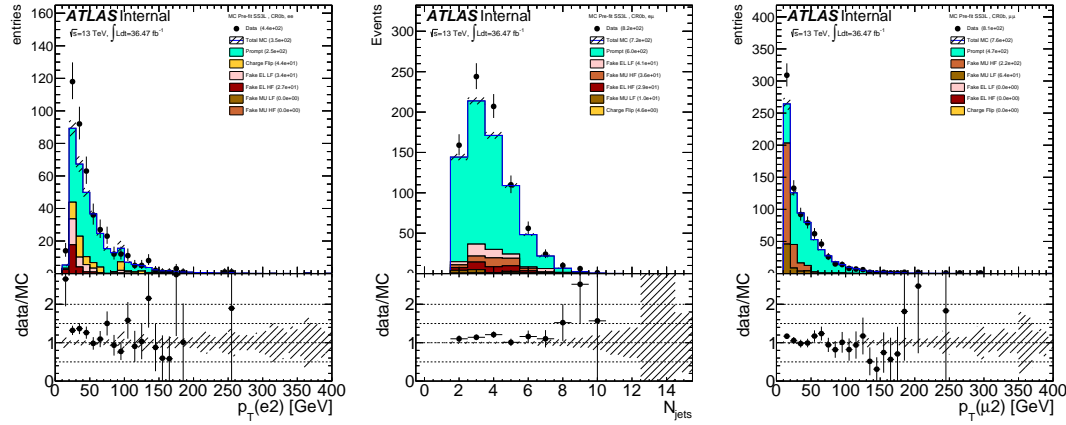


Figure 6.2: Pre-fit distributions for ee channel (left), for $e\mu$ channel (middle), and for $\mu\mu$ channel (right) from CR0b that were used in the fit to extract the FNP lepton and charge flip multipliers. The generator used in these plots is POWHEG-Box +Pythia. The hashed band represents the sum of systematic uncertainties on the predictions.

2225 takes into account the limited number of simulated events and is included as a
 2226 systematic uncertainty on the expected number of background events.

2227 6.4 Matrix Method

2228 The FNP leptons do not often pass one of the lepton selection criteria but have
 2229 non-zero impact parameter, and are often not well-isolated. These selection
 2230 requirements are key ingredients to control the FNP leptons. The number of
 2231 events with at least one FNP lepton is estimated using two classes of leptons:
 2232 a real-enriched class of “tight” leptons corresponding to signal leptons and a
 2233 fake-enriched class of “loose” leptons corresponding to candidate leptons with

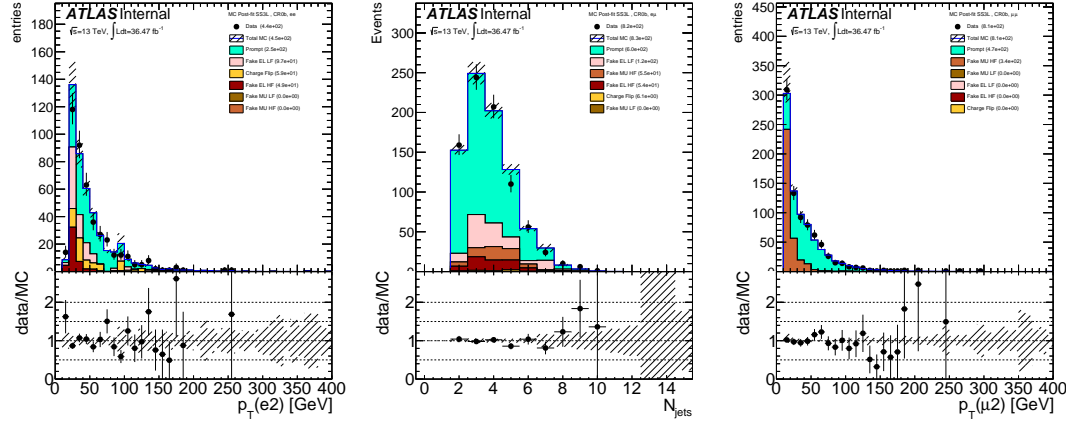


Figure 6.3: Post-fit distributions for ee channel (left), for $e\mu$ channel (middle), and for $\mu\mu$ channel (right) from CR0b that were used in the fit to extract the FNP lepton and charge flip multipliers. The generator used in these plots is POWHEG-Box +Pythia . The hashed band represents the sum of systematic uncertainties on the predictions.

Table 6.1: The FNP and charge flip multipliers obtained after minimizing the likelihood function using POWHEG-Box +Pythia. The uncertainty in the multipliers takes into account the limited statistics of simulated events.

Category	Multiplier	Uncertainty
chFlip	1.49	0.58
HF EL	2.80	0.98
LF EL	2.89	0.88
HF MU	1.59	0.31
LF MU	1.00	1.34

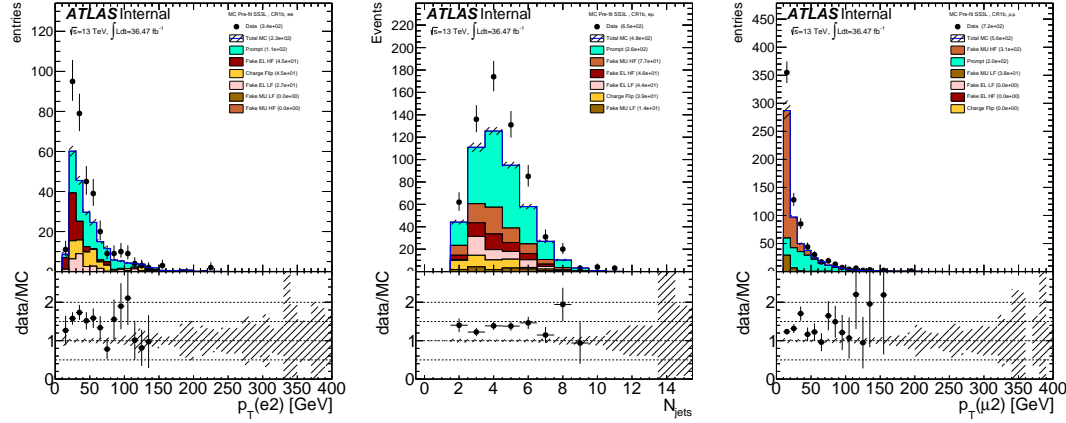


Figure 6.4: Pre-fit distributions for ee channel (left), for $e\mu$ channel (middle), and for $\mu\mu$ channel (right) from CR1b that were used in the fit to extract the FNP lepton and charge flip multipliers. The generator used in these plots is POWHEG-Box + Pythia. The hashed band represents the sum of systematic uncertainties on the predictions.

Table 6.2: The FNP and charge flip multipliers obtained after minimizing the likelihood function using SHERPA. The uncertainty in the multipliers takes into account the limited statistics of simulated events.

Category	Multiplier	Uncertainty
chFlip	1.34	0.58
HF EL	2.40	0.85
LF EL	1.83	1.04
HF MU	1.17	0.16
LF MU	2.40	0.81

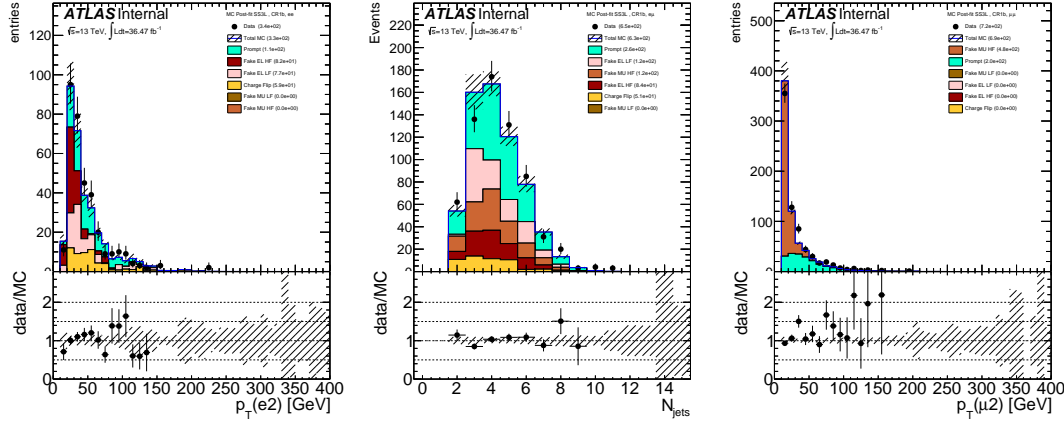


Figure 6.5: Post-fit distributions for ee channel (left), for $e\mu$ channel (middle), and for $\mu\mu$ channel (right) from CR1b that were used in the fit to extract the FNP lepton and charge flip multipliers. The generator used in these plots is POWHEG-Box + Pythia. The hashed band represents the sum of systematic uncertainties on the predictions.

2234 relaxed identification criteria¹. In the next sections, a description of the simplest
 2235 form of the matrix method will be given with events containing one object. Then a
 2236 generalized treatment that can handle events with an arbitrary number of leptons
 2237 in the final states will be discussed.

2238 6.4.1 Events with one object

2239 Given the probabilities ε/ζ for a real/FNP candidate lepton to satisfy the signal
 2240 lepton criteria, one can relate the number of events with one candidate lepton
 2241 passing/failing signal requirements ($n_{\text{pass}}/n_{\text{fail}}$) to the number of events with one
 2242 real/FNP signal leptons ($n_{\text{real}}/n_{\text{FNP}}$):

¹Signal leptons are leptons satisfying the signal lepton definition, while the candidate leptons are leptons satisfying some pre-selection cuts and usually passing the overlap removal requirements as discussed in the analysis Section 5.4.3.

$$\begin{pmatrix} n_{\text{pass}} \\ n_{\text{fail}} \end{pmatrix} = \begin{pmatrix} \varepsilon & \zeta \\ 1 - \varepsilon & 1 - \zeta \end{pmatrix} \begin{pmatrix} n_{\text{real}} \\ n_{\text{FNP}} \end{pmatrix}; \quad (6.1)$$

2243 allowing to determine the unknown number of events n_{FNP} from the observed
2244 n_{pass} and n_{fail} given measurements of the probabilities ε/ζ .

2245 The predictive power of the matrix method comes from the fact that the
2246 real and FNP leptons have different composition in the two collections of tight
2247 and loose objects leading to $\varepsilon \neq \zeta$. In fact, the tight lepton collection will be
2248 dominated by real objects while the loose region will be dominated by fake objects.

2249 As a result, the inequality $\varepsilon >> \zeta$ will always hold true which guarantees that
2250 the matrix in Eq. 6.1 is invertible and gives positive estimates.

2251 The next step is to invert the relation in Eq. 6.1 to obtain

$$\begin{pmatrix} n_{\text{real}} \\ n_{\text{FNP}} \end{pmatrix} = \frac{1}{\varepsilon - \zeta} \begin{pmatrix} \bar{\zeta} & -\zeta \\ -\bar{\varepsilon} & \varepsilon \end{pmatrix} \begin{pmatrix} n_{\text{pass}} \\ n_{\text{fail}} \end{pmatrix}; \quad (6.2)$$

2252 where $\bar{\varepsilon} = 1 - \varepsilon$ and $\bar{\zeta} = 1 - \zeta$. The FNP lepton component is:

$$n_{\text{FNP}} = \frac{1}{\varepsilon - \zeta} ((\varepsilon - 1) n_{\text{pass}} + n_{\text{fail}}). \quad (6.3)$$

2253 However, the quantity of interest is the expected FNP lepton background that
2254 passes the tight selection criteria: $n_{\text{pass}} \cap \text{FNP} = \zeta n_{\text{FNP}}$. To obtain this quantity,
2255 the identity from Eq. 6.1 is used to get:

$$n_{\text{FNP}} = \frac{\zeta}{\varepsilon - \zeta} ((\varepsilon - 1) n_{\text{pass}} + n_{\text{fail}}). \quad (6.4)$$

2256 The linearity of Eq. 6.4 with respect to n_{pass} and n_{fail} allows the method to
 2257 be applied on an event-by-event, effectively resulting into a weight being assigned
 2258 to each event. By defining

$$n_{\text{pass}} = \sum_{\text{all events}} \mathbb{1}_{\text{pass}}, \quad n_{\text{fail}} = \sum_{\text{all events}} \mathbb{1}_{\text{fail}}, \quad \mathbb{1}_{\text{fail}} = 1 - \mathbb{1}_{\text{pass}},$$

2259 where $\mathbb{1}_{\text{pass(fail)}} = 1$ if the object passes (fails) the tight selection requirement and
 2260 $\mathbb{1}_{\text{pass(fail)}} = 0$ otherwise. Eq. 6.4 can be written as

$$n_{\text{FNP}} = \sum_{\text{all events}} \left\{ \frac{\zeta}{\varepsilon - \zeta} (\varepsilon - \mathbb{1}_{\text{pass}}) \right\} = \sum_{\text{all events}} \omega$$

2261 where

$$\omega = \frac{\zeta}{\varepsilon - \zeta} (\varepsilon - \mathbb{1}_{\text{pass}}) \tag{6.5}$$

2262 is the weight to be assigned to each event in the case of one FNP lepton in the
 2263 event. The generalization of this formalism to higher dimensions with multiple
 2264 objects will be covered next.

2265 6.4.2 Dynamic matrix method

2266 The one lepton case readily generalizes to events with more than one lepton in
 2267 a formalism that can handle an arbitrary number of leptons in the event. The
 2268 method should be applied event-by-event, effectively resulting into a weight being
 2269 assigned to each event. The predicted yield of events with FNP leptons is simply
 2270 the sum of weights. A general formula will be derived starting from the two

²²⁷¹ objects case, then specific examples will be given to illustrate the application of
²²⁷² the method.

²²⁷³ If two objects are present in the event, the probabilities ε/ζ will depend on
²²⁷⁴ the kinematic properties of these objects. Typically the probability will vary as
²²⁷⁵ a function of p_T and $|\eta|$. For this reason, the probabilities will be different and
²²⁷⁶ will have an index to identify the object under study: ε_i/ζ_i where $i = 1, 2, \dots$. An
²²⁷⁷ identity similar to Eq. 6.1 can be formed for two objects with a change in notation
²²⁷⁸ for simplicity:

$$\begin{pmatrix} N_{TT} \\ N_{TL} \\ N_{LT} \\ N_{LL} \end{pmatrix} = \Lambda \times \begin{pmatrix} N_{RR} \\ N_{RF} \\ N_{FR} \\ N_{FF} \end{pmatrix}, \quad (6.6)$$

²²⁷⁹ where $(N_{RR}, N_{RF}, N_{FR}, N_{FF})$ are the number of events with respectively two real,
²²⁸⁰ one real plus one FNP (two terms), and two FNP leptons before applying tight
²²⁸¹ cuts, respectively, and $(N_{TT}, N_{TL}, N_{LT}, N_{LL})$ are the observed number of events
²²⁸² for which respectively both lepton pass the tight cut, only one of them (two terms),
²²⁸³ or both fail the tight cut, respectively.

²²⁸⁴ Λ is given by:

$$\Lambda = \begin{pmatrix} \varepsilon_1 \varepsilon_2 & \varepsilon_1 \zeta_2 & \zeta_1 \varepsilon_2 & \zeta_1 \zeta_2 \\ \varepsilon_1 (1 - \varepsilon_2) & \varepsilon_1 (1 - \zeta_2) & \zeta_1 (1 - \varepsilon_2) & \zeta_1 (1 - \zeta_2) \\ (1 - \varepsilon_1) \varepsilon_2 & (1 - \varepsilon_1) \zeta_2 & (1 - \zeta_1) \varepsilon_2 & (1 - \zeta_1) \zeta_2 \\ (1 - \varepsilon_1) (1 - \varepsilon_2) & (1 - \varepsilon_1) (1 - \zeta_2) & (1 - \zeta_1) (1 - \varepsilon_2) & (1 - \zeta_1) (1 - \zeta_2) \end{pmatrix}$$

which can also be written in terms of a Kronecker product in Eq. 6.6 to obtain:

$$\begin{pmatrix} N_{TT} \\ N_{TL} \\ N_{LT} \\ N_{LL} \end{pmatrix} = \begin{pmatrix} \varepsilon_1 & \zeta_1 \\ \bar{\varepsilon}_1 & \bar{\zeta}_1 \end{pmatrix} \otimes \begin{pmatrix} \varepsilon_2 & \zeta_2 \\ \bar{\varepsilon}_2 & \bar{\zeta}_2 \end{pmatrix} \begin{pmatrix} N_{RR} \\ N_{RF} \\ N_{FR} \\ N_{FF} \end{pmatrix} \quad (6.7)$$

To make the notation more compact, the set of 4 numbers $(N_{TT}, N_{TL}, N_{LT}, N_{LL})$ can be represented by a rank 2 tensor $\mathcal{T}_{\alpha_1 \alpha_2}$ where α_i corresponds to one object that is either tight (T) or loose (L). Similarly the numbers $(N_{RR}, N_{RF}, N_{FR}, N_{FF})$ can be represented by $\mathcal{R}_{\alpha_1 \alpha_2}$ where α_i corresponds to one object that is either real (R) or FNP (F). With this convention, the Kronecker product of Eq. 6.7 can be obtained by contracting each index α_i of the tensors \mathcal{T} or \mathcal{R} by the 2×2 matrix $\phi_{i \beta_i}^{\alpha_i}$:

$$\mathcal{T}_{\beta_1 \beta_2} = \phi_{1 \beta_1}^{\alpha_1} \phi_{2 \beta_2}^{\alpha_2} \mathcal{R}_{\alpha_1 \alpha_2}, \quad \phi_i = \begin{pmatrix} \varepsilon_i & \zeta_i \\ \bar{\varepsilon}_i & \bar{\zeta}_i \end{pmatrix} \quad (6.8)$$

Following the same procedure as in the one object case, the matrix inversion of the $4 \times 4 \Lambda$ matrix is simplified to a matrix inversion of the $2 \times 2 \phi$ matrices. The quantity of interest is the FNP lepton background that passes the tight selection criteria as in Eq. 6.4 which can be compactly written in the two objects case as:

$$\mathcal{T}_{\nu_1 \nu_2}^{\text{FNP}} = \phi_{\nu_1}^{\mu_1} \phi_{\nu_2}^{\mu_2} \xi^{\beta_1 \beta_2}_{\mu_1 \mu_2} \phi^{-1}_{\beta_1}{}^{\alpha_1} \phi^{-1}_{\beta_2}{}^{\alpha_2} \mathcal{T}_{\alpha_1 \alpha_2}. \quad (6.9)$$

The tensor ξ encodes the component of tight and FNP lepton background. In the two objects case, ξ needs to select the total background with at least one fake

²²⁹⁸ lepton $N_F = N_{RF} + N_{FR} + N_{FF}$ that are also passing the tight selection criteria
²²⁹⁹ corresponding to the region with signal leptons. As a result, ξ takes the form:

$$\xi = \begin{pmatrix} 0 & 0 & 0 & 0 \\ 0 & 1 & 0 & 0 \\ 0 & 0 & 1 & 0 \\ 0 & 0 & 0 & 1 \end{pmatrix}$$

²³⁰⁰ To further illustrate, Eq. 6.9 can be written explicitly in the notation of Eq.
²³⁰¹ 6.6 as:

$$N_{\text{FNP}}^{\text{signal}} = \begin{pmatrix} 0 & \varepsilon_1 \zeta_2 & \zeta_1 \varepsilon_2 & \zeta_1 \zeta_2 \end{pmatrix} \Lambda^{-1} \begin{pmatrix} N_{TT} \\ N_{TL} \\ N_{LT} \\ N_{LL} \end{pmatrix}$$

²³⁰² The generalization of Eq. 6.9 from the two objects case to m number of objects
²³⁰³ in the final state is straightforward:

$$\mathcal{T}_{\nu_1 \dots \nu_m}^{\text{FNP}} = \phi_{\nu_1}^{\mu_1} \dots \phi_{\nu_m}^{\mu_m} \xi_{\mu_1 \dots \mu_m}^{\beta_1 \dots \beta_m} \phi_{\beta_1}^{-1} \dots \phi_{\beta_m}^{-1} \mathcal{T}_{\alpha_1 \dots \alpha_m}. \quad (6.10)$$

²³⁰⁴ The tensor ξ is of the general form

$$\xi_{\mu_1 \dots \mu_m}^{\beta_1 \dots \beta_m} = \delta_{\mu_1}^{\beta_1} \dots \delta_{\mu_m}^{\beta_m} h(\beta_1, \dots, \beta_m, \nu_1, \dots, \nu_m)$$

²³⁰⁵ where the function h can take values 0 or 1 based on the tight or loose configuration
²³⁰⁶ being computed which is encoded in the dependence on the indices ν_i .

2307 The application of the matrix method to multilepton final states comes with
 2308 two important remarks. Firstly, contributions of events with charge-flip electrons
 2309 would bias a straightforward matrix method estimate (in particular for a final
 2310 state formed by two leptons with the same electric charge). This happens because
 2311 the candidate-to-signal efficiency for such electrons is typically lower than for
 2312 real electrons having a correctly-assigned charge. One therefore needs to subtract
 2313 from n_{pass} and n_{fail} the estimated contributions from charge-flip. This can be
 2314 performed by including events with pairs of opposite-sign candidate leptons in the
 2315 matrix method estimate, but assigning them an extra weight corresponding to
 2316 the charge-flip weight. Thanks (again) to the linearity of the matrix method with
 2317 respect to n_{pass} and n_{fail} , this weight-based procedure is completely equivalent
 2318 (but more practical) to the aforementioned subtraction.

2319 Secondly, the analytic expression of the matrix method event weight depends
 2320 on the lepton multiplicity of the final state. This concerns events with three or
 2321 more candidate leptons: one such event takes part both in the evaluation of the
 2322 FNP lepton background for a selection with two signal leptons or a selection with
 2323 three signal leptons, but with different weights². Therefore, for a given event
 2324 used as input to the matrix method, one should consider all possible leptons
 2325 combinations, each with its own weight and its own set of kinematic variables.
 2326 For example, a $e^+e^-\mu^+$ event is used in the background estimate both as an $e^+\mu^+$
 2327 event (with a weight w_1) and as an $e^+e^-\mu^+$ event (with a weight $w_2 \neq w_1$).

²This can appear for inclusive selections: for example an event with two signal leptons may or not contain additional candidate leptons, in a transparent way

2328 6.4.3 Propagation of uncertainties

2329 The two parameters (ε and ζ respectively) can be measured in data, and depend
2330 on the flavor and kinematics of the involved leptons. Systematic uncertainties
2331 resulting from the measurement of these two parameters, and their extrapolation
2332 to the signal regions, can be propagated to uncertainties on the event weight
2333 through standard first-order approximations. The different sources of uncertainties
2334 should be tracked separately so that correlations of uncertainties across different
2335 events can be accounted for correctly. The resulting set of uncertainties on the
2336 cumulated event weights can be then added in quadrature to form the systematic
2337 uncertainty on the predicted FNP lepton background yield. The corresponding
2338 statistical uncertainty can be taken as the RMS of the event weights.

²³³⁹ **Chapter 7**

²³⁴⁰ **Background Estimation**

²³⁴¹ **7.1 Overview**

²³⁴² In this analysis, two types of backgrounds can be distinguished. The first category
²³⁴³ is the irreducible background from events with two same-sign prompt leptons or
²³⁴⁴ at least three prompt leptons and is estimated using the MC simulation samples
²³⁴⁵ (Section 7.2). Since diboson and $t\bar{t}V$ events are the main backgrounds in the signal
²³⁴⁶ regions, dedicated validation regions with an enhanced contribution from these
²³⁴⁷ processes, and small signal contamination, are defined to verify the background
²³⁴⁸ predictions from the simulation (Section 7.3). The second category is the reducible
²³⁴⁹ background, which includes events containing electrons with mis-measured charge,
²³⁵⁰ mainly from the production of top quark pairs, and events containing at least one
²³⁵¹ fake or non-prompt (FNP) lepton. The application of the data-driven methods of
²³⁵² Chapter 6 is presented in Section 7.2).

²³⁵³ **7.2 Irreducible Backgrounds**

²³⁵⁴ **7.2.1 Expected yields in the signal regions**

²³⁵⁵ The predicted event yields in the signal regions are presented in Table 7.1, while
²³⁵⁶ the contributions of particular rare processes to the signal regions, relative to the
²³⁵⁷ summed contributions of all these processes, are shown in Table 7.2.

Table 7.1: Expected yields for background processes with prompt leptons, in the SRs proposed in Section 5.6, for 36.1 fb^{-1} . Quoted uncertainties include statistical sources only. Rare category includes $t\bar{t}WW$, $t\bar{t}WZ$, $3t$, tZ , tWZ , WH , ZH and VVV , and detailed contributions of these processes can be found in Table 7.2.

	$t\bar{t}V$	VV	$t\bar{t}H$	$t\bar{t}t\bar{t}$	rare
Rpc2L0bH	0.20 ± 0.05	1.14 ± 0.23	0.08 ± 0.04	0.02 ± 0.01	0.17 ± 0.04
Rpc2L0bS	0.82 ± 0.10	3.13 ± 0.21	0.26 ± 0.05	0.01 ± 0.00	0.20 ± 0.04
Rpc2L1bH	3.86 ± 0.20	0.61 ± 0.06	1.01 ± 0.10	0.53 ± 0.03	0.97 ± 0.12
Rpc2L1bS	3.94 ± 0.20	0.48 ± 0.05	1.28 ± 0.10	0.33 ± 0.03	0.87 ± 0.12
Rpc2L2bH	0.41 ± 0.05	0.04 ± 0.01	0.10 ± 0.03	0.17 ± 0.02	0.14 ± 0.04
Rpc2L2bS	1.57 ± 0.12	0.10 ± 0.03	0.44 ± 0.06	0.25 ± 0.02	0.32 ± 0.05
Rpc2Lsoft1b	1.24 ± 0.11	0.14 ± 0.02	0.44 ± 0.06	0.09 ± 0.01	0.18 ± 0.04
Rpc2Lsoft2b	1.15 ± 0.10	0.05 ± 0.02	0.37 ± 0.06	0.20 ± 0.02	0.17 ± 0.03
Rpc3L0bH	0.18 ± 0.04	2.64 ± 0.12	0.03 ± 0.02	0.01 ± 0.00	0.29 ± 0.04
Rpc3L0bS	0.99 ± 0.09	8.95 ± 0.21	0.12 ± 0.04	0.02 ± 0.01	0.75 ± 0.07
Rpc3L1bH	1.52 ± 0.11	0.48 ± 0.05	0.25 ± 0.06	0.28 ± 0.03	0.87 ± 0.12
Rpc3L1bS	7.02 ± 0.23	1.44 ± 0.10	1.36 ± 0.10	0.69 ± 0.04	2.51 ± 0.22
Rpc3LSS1b	0.00 ± 0.00	0.00 ± 0.00	0.21 ± 0.04	0.00 ± 0.00	0.09 ± 0.01

2358 7.2.2 Validation regions

2359 Dedicated validation regions are defined to verify the estimate of the $W^\pm W^\pm jj$,
 2360 the $WZjjjj(j)$, the $t\bar{t}W$ and $t\bar{t}Z$ processes in the signal regions. For a better
 2361 validation of WZ processes in association with a large jet multiplicity, two VRs
 2362 are proposed : $WZ4j$ and $WZ5j$, with 4 and respectively 5 reconstructed jets in

Table 7.2: Contributions of particular rare processes to the signal regions, relative to the summed contributions of all these processes.

	VVV	VH	$3t$	tZ	$t\bar{t}WW$	tWZ	$t\bar{t}WZ$
Rpc2L0bH	23%	0%	2%	3%	25%	43%	1%
Rpc2L0bS	50%	0%	3%	15%	14%	16%	0%
Rpc2L1bH	2%	0%	7%	4%	41%	41%	2%
Rpc2L1bS	2%	0%	6%	3%	34%	50%	2%
Rpc2L2bH	3%	0%	15%	4%	47%	27%	1%
Rpc2L2bS	2%	0%	13%	2%	42%	36%	2%
Rpc2Lsoft1b	3%	0%	9%	0%	76%	7%	2%
Rpc2Lsoft2b	2%	0%	17%	4%	54%	19%	2%
Rpc3L0bH	52%	0%	0%	3%	1%	40%	1%
Rpc3L0bS	50%	0%	0%	4%	2%	39%	1%
Rpc3L1bH	3%	0%	3%	3%	17%	70%	1%
Rpc3L1bS	2%	0%	3%	7%	18%	64%	2%
Rpc3LSS1b	25%	0%	0%	0%	0%	0%	74%

²³⁶³ the event. The corresponding selections are summarized in Table 7.3.

²³⁶⁴ $W^\pm W^\pm + \text{jets validation region}$

²³⁶⁵ The $W^\pm W^\pm + \text{jets}$ processes contribute mainly in the signal regions with no

²³⁶⁶ b -tagged jet requirement and two same-sign leptons. This validation region,

²³⁶⁷ $W^\pm W^\pm$ -VR, has exactly one SS pair (and no additional baseline leptons), zero

²³⁶⁸ b -jets and at least two jets with p_T above 50 GeV. Additional requirements on

²³⁶⁹ E_T^{miss} and m_{eff} help to decrease the amount of detector background as shown in

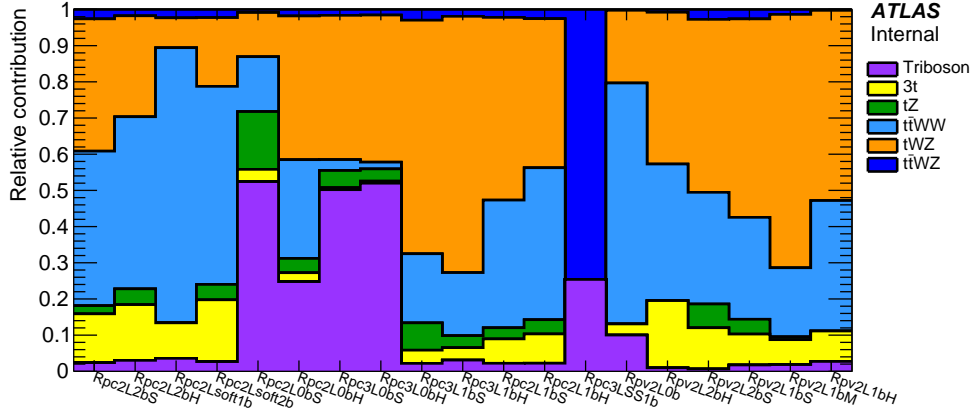


Figure 7.1: Relative contribution in each signal region from the processes in the category labelled as rare in the paper ($t\bar{t}WW$, $t\bar{t}WZ$, tZ , tWZ , $tt\bar{t}$, WH , ZH and triboson production).

2370 Figure 7.2 (left and middle). To further improve the purity, the sub-leading lepton
 2371 p_T is increased to 30 GeV, and cuts on minimum angular separation between
 2372 the leptons and jets, and between the two leptons (Figure 7.2, right) are placed
 2373 as detailed in Table 7.3. The purity is around 34% with this definition of the
 2374 validation region. Signal contamination (highly reduced by applying a veto of all
 2375 SRs) it is found to be at most 5% when looking at $\tilde{g} \rightarrow q\bar{q}(\tilde{\ell}\ell/\tilde{\nu}\nu)$ scenarios.

2376 **$WZ + \text{jets validation region}$**

2377 Contributions from $WZ+\text{jets}$ processes can be significant in regions vetoing the
 2378 presence of b -jets and requiring three leptons. Given the large data sample
 2379 collected, it is possible to design validation regions that require at least four
 2380 and even at least five jets with $p_T > 25$ GeV in the event. Thus, two validation
 2381 regions, $WZ4j\text{-VR}$ and $WZ5j\text{-VR}$, are proposed to better probe the modelling
 2382 of the jet multiplicity in WZ processes. Both regions are defined with exactly

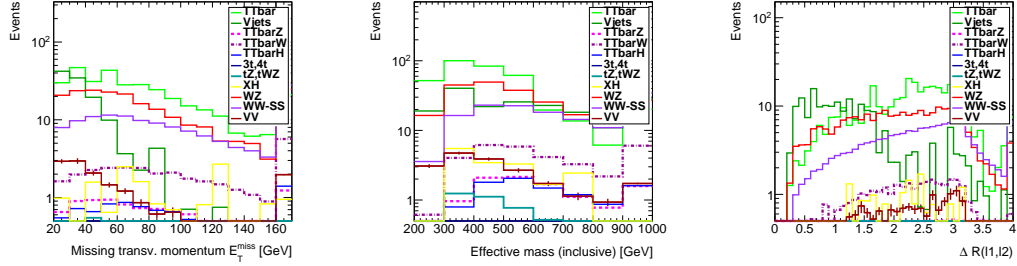


Figure 7.2: E_T^{miss} (left), m_{eff} (middle) and $\min \Delta R(\ell_1, \ell_2)$ (right) after lepton and jet selection of the $W^\pm W^\pm$ -VR (and no additional requirements). Signal regions are vetoed. All MC samples are normalized to a luminosity of 36.1 fb^{-1} . The last bin includes overflow.

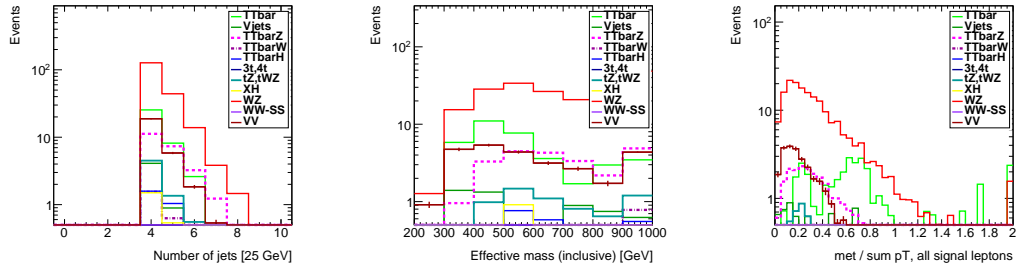


Figure 7.3: Number of jets with $p_T > 25 \text{ GeV}$ (left), m_{eff} (middle) and ratio between the E_T^{miss} in the event and the sum of all lepton p_T (right) after lepton and four jet selection of the WZ -VR (and no additional requirements). Signal regions are vetoed as detailed in Table 7.3. All MC samples are normalized to a luminosity of 36.1 fb^{-1} . The last bin includes overflow.

2383 three signal leptons and no fourth baseline lepton, to reduce the ZZ background
 2384 contamination. The m_{eff} , and the upper cut on the ratio between the E_T^{miss} in the
 2385 event and the sum of all lepton p_T are great discriminants against the reducible
 2386 backgrounds. Some kinematic distributions after lepton and four jet selection are
 2387 shown in Figure 7.3.

2388 Purity in $WZ4j$ -VR ($WZ5j$ -VR) is around 67% (64%). When looking at
 2389 $\tilde{g} \rightarrow q\bar{q}(\tilde{\ell}\ell/\tilde{\nu}\nu)$ scenarios, the signal contamination is below 5% in most of the
 2390 non-excluded phase space, except for small $\Delta M(\tilde{g}, \tilde{\chi}_1^0)$ where it can go up to
 2391 30% (15%). Signal contamination is found to be much lower for $\tilde{g} \rightarrow q\bar{q}WZ\tilde{\chi}_1^0$
 2392 scenarios.

2393 $t\bar{t} + W$ background validation

2394 A $t\bar{t} + W$ validation region ($t\bar{t}W$ -VR) is defined with exactly one SS lepton pair
 2395 and at least one b -jet. At least four jets are required in the ee and $e\mu$ channels,
 2396 while in the $\mu\mu$ channel the selection is relaxed to at least three jets (less reducible
 2397 background); also the jet p_T thresholds are different between these two cases
 2398 (same motivation). As shown in Figure 7.4, the amount of $t\bar{t}$ background after
 2399 this pre-selection is still very large and additional requirements on E_T^{miss} , m_{eff} and
 2400 on the ratio between the sum of p_T of all b -jets and the sum of p_T of all jets are
 2401 placed as mentioned in Table 7.3. With this definition the achieved purity in
 2402 $t\bar{t}W$ -VR is 33%. Signal contamination is around 20% when looking at $b\bar{b}$ SUSY
 2403 models.

2404 $t\bar{t} + Z$ background validation

2405 A $t\bar{t} + Z$ enriched validation region (ttZ -VR) is defined with at least one SFOS
 2406 lepton pair and at least one b -jet. At least three jets are required in the event
 2407 regardless of the lepton channel. Some kinematic distributions after this pre-
 2408 selection are shown in Figure 7.5 (left and middle). To increase the purity, the
 2409 invariant mass of the SFOS lepton pair is selected to be inside the [81, 101]
 2410 GeV interval and the m_{eff} in the event should be greater than 450 GeV. With

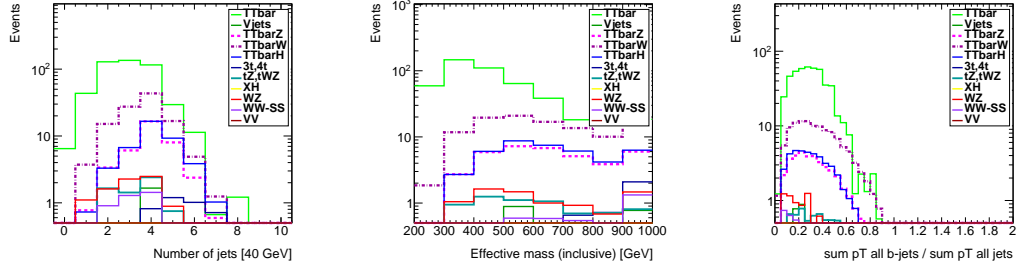


Figure 7.4: Number of jets with $p_T > 40$ GeV (left), m_{eff} (middle) and ratio between the sum of all b -jets p_T and the sum of all jets p_T (right) after lepton and jet selection of the $t\bar{t}W$ -VR (and no additional requirements). Signal regions are vetoed as detailed in Table 7.3. All MC samples are normalized to a luminosity of 36.1 fb^{-1} . The last bin includes overflow.

2411 this selection, the purity is 58%. One can increase it even further (by $\sim 10\%$) if at
 2412 least two b -jets are required in the event. However, with such a cut the statistics
 2413 will be highly reduced (up to a factor 2 lower as illustrated in Figure 7.5, right),
 2414 so it is not pursued. The signal contamination is found to be around 5% for $\tilde{b}_1\tilde{b}_1^*$
 2415 pair production.

2416 7.2.3 Validation of irreducible background estimates

2417 The observed yields, compared with the background predictions and uncertainties,
 2418 can be seen in Table 7.4. There is good agreement between data and the estimated
 2419 background in all the validation regions.

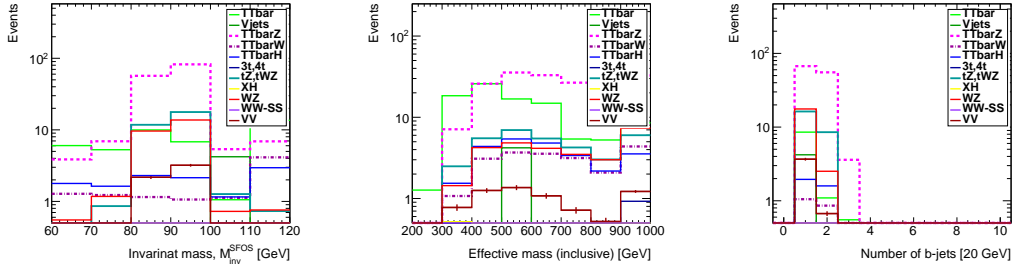


Figure 7.5: Invariant mass of the SFOS lepton pair (left) and m_{eff} (middle) after lepton and jet selection of the $t\bar{t}Z$ -VR (and no additional requirements). Number of b -jets with $p_T > 20$ GeV after the $t\bar{t}Z$ -VR selection. Signal regions are vetoed as detailed in Table 7.3. All MC samples are normalized to a luminosity of 36.1 fb^{-1} . The last bin includes overflow.

2420 7.3 Reducible Backgrounds

2421 The reducible backgrounds consist of the charge-flip background and the FNP
 2422 lepton background. The charge flip background is obtained by re-weighting
 2423 opposite-sign lepton pairs data with the measured charge-flip probability and
 2424 cross checked with the estimate obtained with the MC template method. Two
 2425 data-driven methods are used to estimate the FNP lepton background, the matrix
 2426 method and the MC template method, which are combined to obtain the final
 2427 estimate. These methods were discussed in detail in Chapter 6. This section
 2428 describes the application of these methods in the context of the SS/3L analysis
 2429 and the validation of the reducible background estimates.

²⁴³⁰ **7.3.1 Charge-flip Background**

²⁴³¹ The lepton charge mis-measurement commonly referred to as “charge flip”, is
²⁴³² an experimental background strongly associated to analyses relying on same-
²⁴³³ sign leptons final states. In those events, the electric charge of one of the two
²⁴³⁴ leptons forming an opposite-sign (OS) pair, coming from an abundant SM process
²⁴³⁵ ($pp \rightarrow Z, t\bar{t}, W^+W^- \dots$), is mis-identified leading to a much rarer same-sign (SS)
²⁴³⁶ pair event. In most cases, the source of such a mis-identification is the creation
²⁴³⁷ of additional close-by tracks $e^\pm \rightarrow e^\pm\gamma \rightarrow e^\pm e^\pm e^\mp$ via Bremsstrahlung of the
²⁴³⁸ original electron when interacting with the material of the inner tracker. If one of
²⁴³⁹ the secondary electron tracks is subsequently preferred to the original track in the
²⁴⁴⁰ reconstruction of the electron candidate, the charge assigned to the electron might
²⁴⁴¹ be incorrect, leading to a charge-flip event. Errors on the track charge assignment
²⁴⁴² itself may occur as well, but they are much rarer. In the case of muons, charge-flip
²⁴⁴³ is essentially negligible due to the much smaller interaction cross-section with
²⁴⁴⁴ matter, and the requirement of identical charges to be measured for the inner
²⁴⁴⁵ tracker and muon spectrometer tracks.

²⁴⁴⁶ A purely data-driven method is used to estimate event yields for the electron
²⁴⁴⁷ charge-flip background. Assuming that the electron charge flip rates $\xi(\eta, p_T)$
²⁴⁴⁸ are known, a simple way to predict these yields is to select events with pairs of
²⁴⁴⁹ opposite-sign leptons in data and assign them a weight:

$$w_{\text{flip}} = \xi_1(1 - \xi_2) + (1 - \xi_1)\xi_2 \quad (7.1)$$

2450 where $\xi_{(i)} = 0$ for muons.

2451 The advantages of this method are a good statistical precision since the charge
2452 flip rate is quite small, and the absence of dependency to the simulation and
2453 related uncertainties. Obviously, it requires a precise measurement of the rates,
2454 which is described in this section. An inconvenience of this approach is that the
2455 reconstructed momentum for charge-flipped electrons tends to be negatively biased
2456 (too low by a few GeV), since such important Bremsstrahlung topologies represent
2457 only a very small fraction of the cases used to tune electron energy calibration.
2458 Simply re-weighting electrons from opposite-sign lepton pairs therefore does not
2459 predict correctly the charge-flip background shape for variables very sensitive to
2460 the electron momentum, for example the m_{ee} line-shape. However, the kinematic
2461 range and variables used in the analysis are not sensitive to this effect and can
2462 safely be neglected.

2463 For the nominal (tight) estimate of the charge-flip background contributions,
2464 only events with exactly two OS signal electrons are considered. Corrections in the
2465 fake lepton estimate however require estimating as well charge-flip contributions for
2466 selections involving baseline electrons failing signal requirements; for that reason,
2467 the charge-flip (loose) rate is measured for these two categories of electrons.

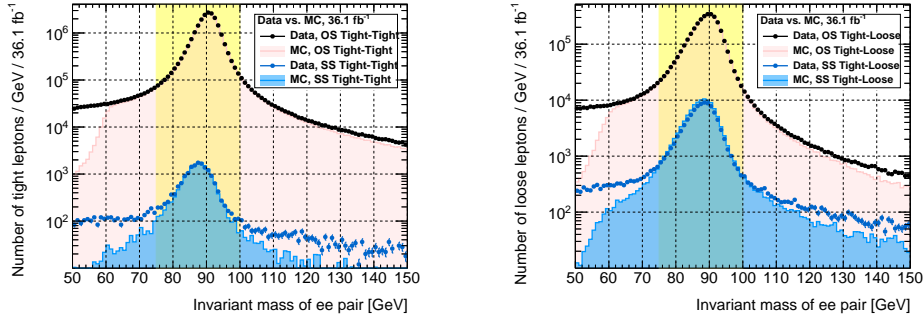


Figure 7.6: Invariant mass of opposite- and same-sign electron pairs, when both electrons satisfy signal requirements (left) or one of them fails them (right). Drell-Yan MC samples are not included, thus the drop in the MC distributions (light magenta filled area).

2468 Methodology

2469 Charge-flip rates are measured in data relying on a clean $Z \rightarrow ee$ sample ($75 <$
 2470 $m_{ee} < 100$ GeV), in which the rates can be determined from the relative proportions
 2471 of OS and SS electron pairs. Figure 7.6 illustrates this event selection. The rates are
 2472 measured as function of η and p_T , to follow their dependency to the distribution
 2473 of material in the detector, the Bremsstrahlung emission rate, and the track
 2474 curvature. Because of this binned measurements, and that the two electrons
 2475 in a given pair generally have different kinematic properties, it has been found
 2476 that the most efficient and less biased use of the available statistics is obtained
 2477 by simultaneously extracting the rates in all bins via the maximization of the

²⁴⁷⁸ likelihood function describing the Poisson-expected yields of SS pairs:

$$\begin{aligned} L(\{N_{\varpi}^{\text{SS,obs}}\} | \{\xi(\eta, p_T)\}) = \\ \prod_{\varpi} \mathcal{P}(N_{\varpi}^{\text{SS,obs}} | w_{\text{flip}}(\xi(\eta_1, p_{T,1}), \xi(\eta_2, p_{T,2})) \times N_{\varpi}^{\text{OS+SS,obs}}) \end{aligned} \quad (7.2)$$

²⁴⁷⁹ with $\varpi = (\eta_1, p_{T,1}, \eta_2, p_{T,2})$ indexing bins, where (arbitrarily) $p_{T,1} > p_{T,2}$; the
²⁴⁸⁰ expression of w_{flip} is given by (7.1). Statistical uncertainties on the extracted
²⁴⁸¹ charge-flip rates are obtained (in a standard way) from the likelihood's numerically-
²⁴⁸² computed Hessian matrix.

²⁴⁸³ In the nominal charge-flip measurement, the two electrons are required to
²⁴⁸⁴ satisfy signal requirements. To measure charge-flip rates for baseline electrons
²⁴⁸⁵ failing signal (noted $\bar{\xi}$ below), pairs with only one signal electron are used; this
²⁴⁸⁶ provides larger statistics than applying (7.2) to electrons pairs where both fail
²⁴⁸⁷ the signal cuts. However, the expression of the likelihood has to be adapted due
²⁴⁸⁸ to the induced asymmetry between the two electrons forming the pair:

$$\begin{aligned} L(\{N_{\varpi}^{\text{SS,obs}}\} | \{\xi(\eta_1, p_{T,1}), \bar{\xi}(\eta_2, p_{T,2})\}) = \\ \prod_{\varpi} \mathcal{P}(N_{\varpi}^{\text{SS,obs}} | w_{\text{flip}}(\xi(\eta_1, p_{T,1}), \bar{\xi}(\eta_2, p_{T,2})) \times N_{\varpi}^{\text{OS+SS,obs}}) \end{aligned} \quad (7.3)$$

²⁴⁸⁹ where this time $(\eta_1, p_{T,1})$ corresponds to the signal electron. Using the same
²⁴⁹⁰ η and p_T binning for both measurements, the number of free variables in the
²⁴⁹¹ maximization of (7.3) – as well as the number of terms in the product forming
²⁴⁹² L – is twice larger than for the nominal case (7.2). In fact, a by-product of the
²⁴⁹³ maximization of (7.3) is another determination of the charge-flip rates for signal
²⁴⁹⁴ electrons, although with a more limited precision than obtained in the nominal
²⁴⁹⁵ measurement (7.2).

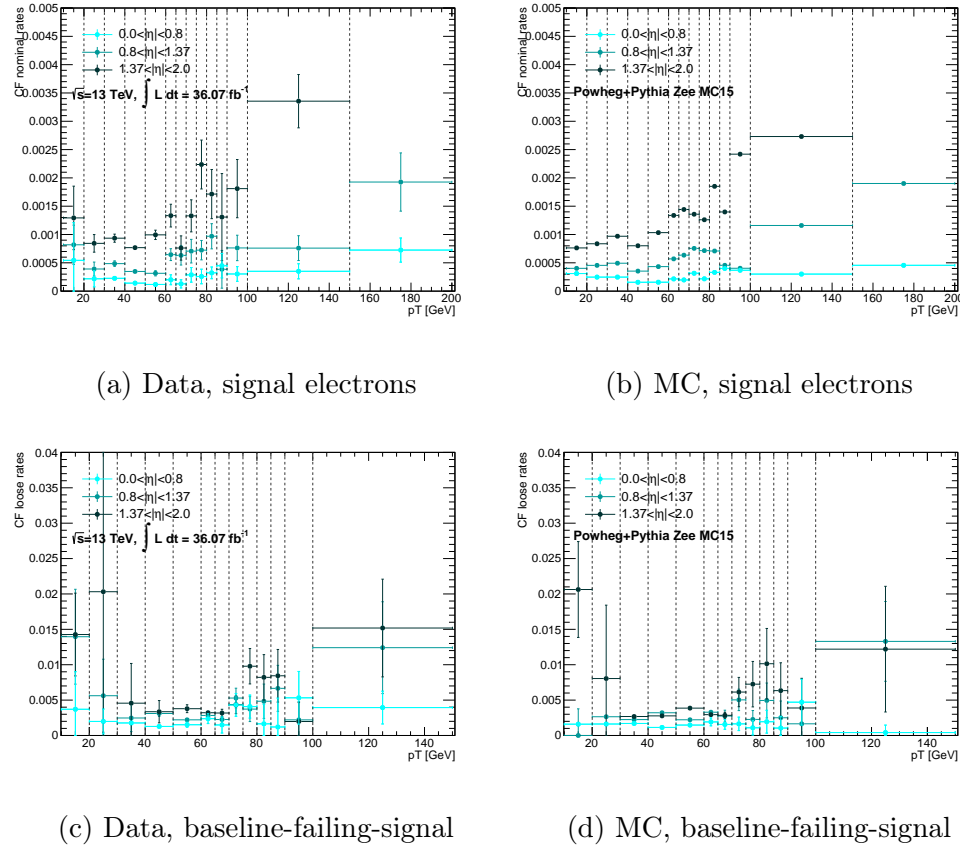


Figure 7.7: Charge-flip rate as measured in data (left) and MC (right). Only the statistical uncertainty is displayed. The last p_T bin is inclusive.

Background subtraction is performed through a simple linear extrapolation of the invariant mass distribution sidebands; it matters mostly for low p_T in the nominal measurement, and for the additional measurement with baseline electrons failing signal requirements, where the level of background is larger.

Measured rates

The charge-flip rates measured in data and MC are shown on Figure 7.7. In data, the nominal rates (Fig. 7.7a) go up to $\sim 0.1\%$ in the barrel region ($|\eta| < 1.37$),

2503 while it increases up to $\sim 0.2\%$ in the end-cap region ($|\eta| > 1.37$). For baseline
 2504 electrons failing signal requirements (Fig. 7.7c), the rates are in general greater
 2505 than the nominal ones in every bin, as expected. The charge-flip rates for these
 2506 electrons go up to $\sim 0.5\%$ in the barrel region and up 1% in the end-cap region.
 2507 Compared to the rates used in the previous version of the analysis [99], the
 2508 central values are much lower now. After suppressing the charge flip events with
 2509 the charge-flip electron BDT classifier described in Section 5.4.3, the charge flip
 2510 rates are strongly reduced for both signal and baseline-failing-signal electrons (up
 2511 to a factor 20 in some bins). Figure 7.8 illustrates the charge flip background
 reduction in a loose selection. Below 30 GeV the statistics is very low for the

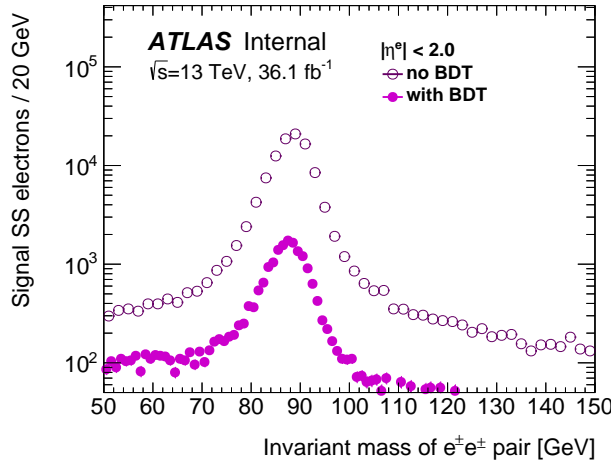


Figure 7.8: Invariant mass of the signal $e^\pm e^\pm$ pair distribution with (full markers)
 and without (open markers) charge-flip electron BDT selection applied.

2512
 2513 loose measurement; however, these results are used only to measure the electron
 2514 fake rate and, as illustrated in Figure 7.13, in this p_T interval the charge flip
 2515 background is negligible.

2516 The charge-flip rates in MC (Figs. 7.7b, 7.7d) are obtained by applying the same
 2517 methodology as in data. Generally, the rates are not very far from data, validating
 2518 the use of MC to predict charge-flip background in several of the optimization
 2519 studies presented in this document. In addition, a closure test is performed on
 2520 $t\bar{t}$ MC, checking that weighted OS events can reproduce the distribution of SS
 2521 charge-flip events (identified by truth-matching). A good overall agreement is
 2522 found, largely within the assigned uncertainties as shown in Figure 7.9.

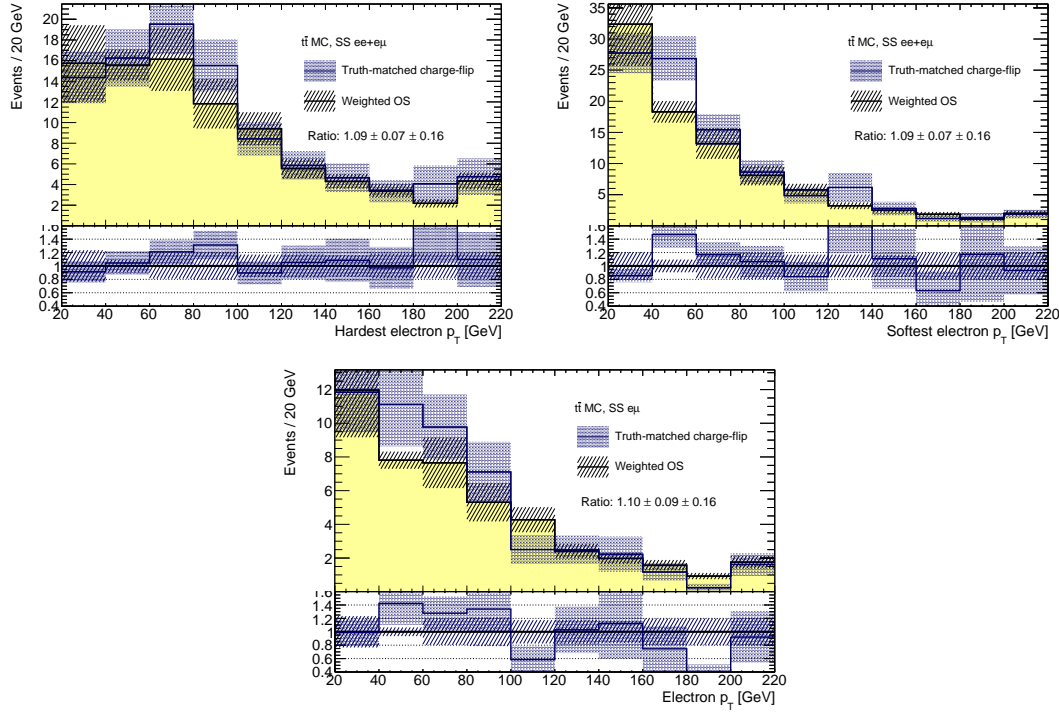


Figure 7.9: Closure test for the charge-flip background prediction, for simulated $t\bar{t}$ events using charge-flip rates measured in $Z \rightarrow ee$ MC (with the systematic uncertainties from the data measurements, though). Events are selected in the $e\mu$ and ee channels, using signal leptons only, and charge-flipped electrons are identified by truth-matching.

2523 **Systematic uncertainties**

2524 The main uncertainties on the measured charge-flip rates come from the presence
 2525 of background and the way it is estimated. To assess them, variations of the
 2526 selection and background estimation are considered:

- 2527 1) $75 < m_{ee} < 100$ GeV, no background subtraction;
- 2528 2) $75 < m_{ee} < 100$ GeV, sidebands of 20 GeV;
- 2529 3) $75 < m_{ee} < 100$ GeV, sidebands of 25 GeV (nominal measurement);
- 2530 4) $75 < m_{ee} < 100$ GeV, sidebands of 30 GeV;
- 2531 5) $80 < m_{ee} < 100$ GeV, sidebands of 20 GeV.

2532 The effect of applying the background subtraction itself is evaluated by com-
 2533 paring configurations 1 and 3. The impact of the width of the m_{ee} chosen for the
 2534 measurement is by comparing configurations 3 and 5, while the sideband width
 2535 effects are evaluated by comparing configuration 3 and 2, or 3 and 4. The largest
 2536 deviation in each bin is taken as the systematic uncertainty on the charge-flip
 2537 rate.

2538 For the signal electrons charge-flip rates the systematic uncertainties vary
 2539 in general between 2% and 20% (increasing up to $> 50\%$ in the region with
 2540 $p_T < 10$ GeV), whereas for baseline-failing-signal electrons they vary between 3%
 2541 and 30% (increasing up to $> 50\%$ in the region with $p_T < 10$ GeV). Part of these
 2542 large values, at low p_T and in the [80,90] GeV p_T interval, can be explained by
 2543 large statistical fluctuations between the different configurations.

2544 **7.3.2 Matrix Method**

2545 The matrix method relates the number of events containing prompt or FNP
2546 leptons to the number of observed events with tight or loose-not-tight leptons
2547 using the probability for loose prompt or FNP leptons to satisfy the tight criteria.

2548 The formalism for this method has been discussed in Section 6.4. The next
2549 sections will concentrate on the measurement of the two input variables needed
2550 for the matrix method: the probability for loose FNP leptons to satisfy the tight
2551 selection criteria (ζ) and the probability for loose prompt leptons to satisfy the
2552 tight selection criteria (ε).

2553 **Baseline-to-signal efficiency for fake muons**

2554 Baseline-to-signal efficiency for fake leptons (further called “fake rate”, (ζ)) is
2555 measured in a sample enriched in fake leptons from $t\bar{t}$ processes. The MC
2556 simulations indicate that this background has the largest contribution to FNP
2557 lepton background in the signal regions, even those with b -jet vetoes, due to the
2558 requirements on jet multiplicity and E_T^{miss} . The events used for the measurements
2559 require exactly two same-sign muons (and no extra baseline lepton), at least one
2560 b -jet, and at least 3 jets that were acquired by di-muon triggers. One of the muons
2561 in the event (referred to as “tag”) is required to satisfy signal requirements, verify
2562 $p_T > 25$ GeV, and trigger the event recording. The measurement may then be
2563 performed on the other lepton (“probe”), likely to be the fake lepton of the pair.

2564 Figure 7.10a shows the number of signal muon probes available after this

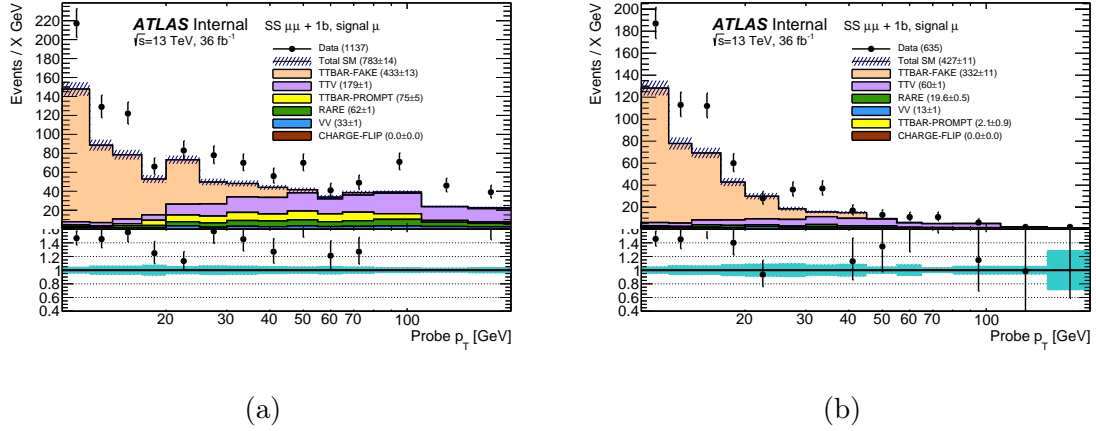


Figure 7.10: Signal probe muon p_T distribution in data and MC, after pre-selection (left) or further tightening of the tag muon requirements (right). The yellow area indicates $t\bar{t}$ events in which the tag muon is fake and the probe real, leading to a measurement bias.

2565 pre-selection. It is clear that at this stage, measurements above 25 GeV would
 2566 be very affected by the important fraction of events in which the tag muon is
 2567 fake and the probe muon is real. To overcome this issue, two alternatives are
 2568 considered:

- 2569 ● tighten the p_T and isolation requirements of the tag muon beyond the “signal”
 2570 requirements, to reduce its probability of being a fake muon
- 2571 ● use an identical selection for tag and probe muons, and require them to be
 2572 in the same (p_T, η) bin for the measurement; after subtraction of estimated
 2573 contributions from processes with two prompt muons, all events have one
 2574 real and one fake muon, and the symmetry in the muon selection can be

taken advantage of to obtain an unbiased measurement of the fake rate:

$$\zeta = \frac{\varepsilon n_2}{\varepsilon n_1 + (2\varepsilon - 1)n_2}$$

2571 with n_1, n_2 the number of events with 1 or 2 signal muons, and ε the efficiency
 2572 for prompt muons.

2573 This method is limited to measurements in inclusive or wide bins. It also
 2574 cannot be used at too low p_T , due to contributions from processes with two
 2575 fake muons (e.g. from $B\bar{B}$ meson production).

2576 Comparisons made with $t\bar{t}$ MC indicated that when using a very tight isolation
 2577 requirement on the tag muon ($\max(E_T^{\text{topo}, \text{cone } 40}, p_T^{\text{cone } 40}) < 0.02 \times p_T)$, the level
 2578 of bias is always largely inferior to the statistical uncertainty in the measurement,
 2579 which itself is smaller than for the other two methods.

2580 Figure 7.10b shows the number of signal muon probes when applying those rein-
 2581 forced isolation criteria to the tag muon, as well as requiring $p_T^{\text{tag}} > \max(40, p_T^{\text{probe}} +$
 2582 10) GeV. As expected, the number of pairs with a fake tag muons is down to a
 2583 minor level, at least according to the simulation.

2584 Muon fake rates as predicted by the simulation ($t\bar{t}$, inclusive selection of leptons
 2585 via truth-matching) are shown on Fig. 7.11 as function of p_T and $|\eta|$. One can
 2586 expect a moderate dependency of the fake rates to the transverse momentum,
 2587 with the strongest evolution at low p_T and a slight increase toward higher p_T .
 2588 The fake rates are also essentially independent of the pseudorapidity, except at
 2589 the edge ($|\eta| > 2.3$) where there is a strongly pronounced increase of the rates.
 2590 This motivates measurements in data as function of p_T in two $|\eta|$ bins.

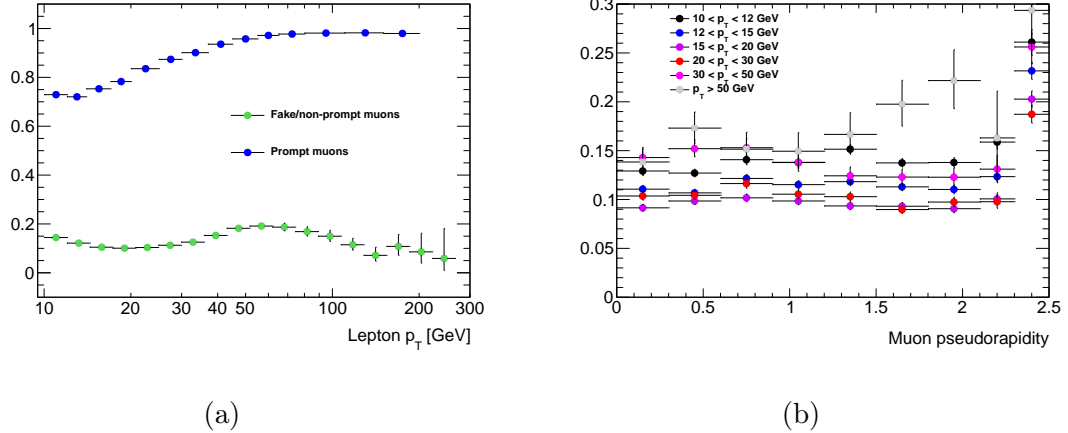


Figure 7.11: Muon fake rates in $t\bar{t}$ MC with an inclusive selection, as a function of p_T (left, green markers) or $|\eta|$ in different momentum ranges (right).

2591 Observations in data seem to indicate that the rejection of fake tag muons
 2592 by the reinforced isolation criteria is quite less important than in the simulation,
 2593 or that the amount of fake muons at high p_T is larger than in the simulation, or
 2594 both. This leads to an unknown level of bias in measurements performed with
 2595 the straightforward tag-and-probe selection at high p_T . For that reason, the final
 2596 rates measured in data are provided by the tag-and-probe method below 25 GeV,
 2597 and by the symmetric selection for $p_T > 25$ GeV. The former are obtained with

$$\zeta = \frac{n_{\text{signal}}^{\text{data}} - n_{\text{signal}}^{\text{MC}}}{n_{\text{baseline}}^{\text{data}} - n_{\text{baseline}}^{\text{MC}}} \quad (7.4)$$

with $\Delta\zeta_{\text{stat}} = \frac{\sqrt{(1 - 2\zeta)n_{\text{signal}}^{\text{data}} + \zeta^2 n_{\text{baseline}}^{\text{data}}}}{n_{\text{baseline}}^{\text{data}} - n_{\text{baseline}}^{\text{MC}}}$

while the latter are obtained with:

$$\zeta = \frac{\varepsilon(n_{\text{both signal}}^{\text{data}} - n_{\text{both signal}}^{\text{MC}})}{\varepsilon(n_{\text{only 1 signal}}^{\text{data}} - n_{\text{only 1 signal}}^{\text{MC}}) + (2\varepsilon - 1)(n_{\text{both signal}}^{\text{data}} - n_{\text{both signal}}^{\text{MC}})} \quad (7.5)$$

with $\Delta\zeta_{\text{stat}} = \frac{\zeta}{n_{\text{both signal}}^{\text{data}} - n_{\text{both signal}}^{\text{MC}}} \sqrt{\zeta^2 n_{\text{only 1 signal}} + \left(1 - \frac{2\varepsilon - 1}{\varepsilon}\zeta\right)^2 n_{\text{both signal}}}$

2598 the efficiency for prompt muons ε is assigned values compatible with section 7.3.2.

2599 The measured rates are presented in Table 7.5. The central values are shown
 2600 together with the associated statistical uncertainty, as well as the propagation
 2601 of the uncertainty on the subtracted backgrounds normalization, which is taken
 2602 as a global $\Delta B/B = 20\%$. The rates are of the order of 10% up to 30 GeV,
 2603 beyond which they increase. Overall these values are not very different from those
 2604 predicted by the simulation.

2605 Some of the validation and signal regions require events with 2 or more b -
 2606 tagged jets, which reduces the fraction of non-prompt muons coming from B
 2607 meson decays. Figure 7.12 illustrates how this impacts the fake rates. Given the
 2608 good agreement between data and simulation for the measured values, a correction
 2609 is applied to the measured rates for events with ≥ 2 b -jets, taken directly from
 2610 simulated $t\bar{t}$ events. This correction factor varies between 1 and 2 with p_T , and
 2611 the whole size of the correction is assigned as an additional systematic uncertainty
 2612 (see Table 7.6).

2613 Systematic uncertainties

2614 To cover potential differences in the fake rates between the measurement regions
 2615 and the signal regions, that could be due to different origins or kinematic properties
 2616 of the fake leptons, uncertainties are set based on the extent of those differences

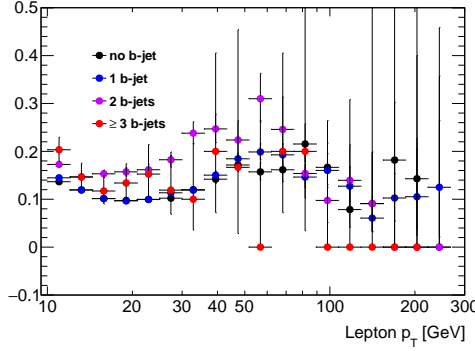


Figure 7.12: Muon fake rates in $t\bar{t}$ MC with an inclusive selection, as function of p_T and split according to the number of b -tagged jets in the event.

2617 predicted by the simulation. The largest effect is the decrease of the fake rates
2618 with H_T (especially for high- p_T muons), which likely correlates to a harder jet at
2619 the origin of the non-prompt muon, hence a reduced likelihood to satisfy isolation
2620 requirements. Table 7.6 summarizes the additional systematic uncertainties
2621 applied to the muon fake rates. They vary from 30% at low p_T , to up to 85% for
2622 $p_T > 40$ GeV; in that range, the uncertainties are made H_T -dependent.

2623 As already shown, Fig. 7.12 shows the variation of the fake rate in $t\bar{t}$ MC as a
2624 function of the number of b -tagged jets in the event. Unsurprisingly, the rates
2625 are very similar for $0b$ and $\geq 1b$ final states, justifying the use of the fake rates
2626 measured in this section (i.e. in a $\geq 1b$ region) to predict fake muon background
2627 in all signal regions.

2628 Baseline-to-signal efficiency for fake electrons

2629 Electron fake rates are measured with a similar methodology, but the $e^\pm e^\pm$ channel
2630 is unusable due to the presence of a large charge-flip background. This is overcome

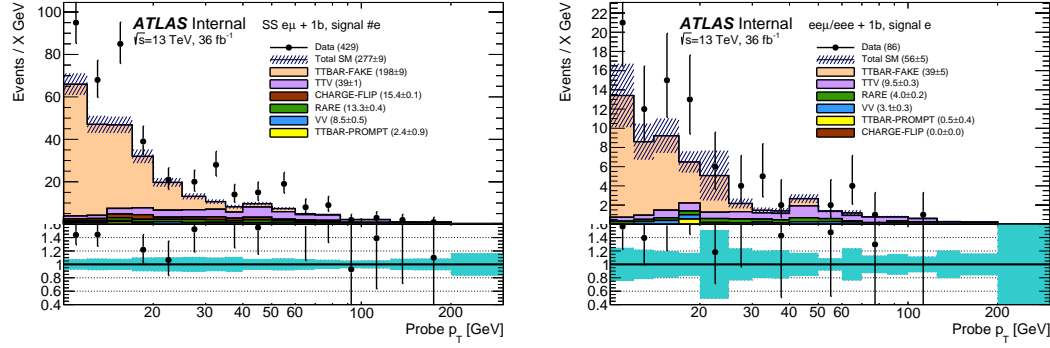


Figure 7.13: Signal probe electron p_T distribution in data and MC, for $e^\pm\mu^\pm$ pairs (left, with probe electrons satisfying a reinforced tag muon selection) or $\ell^\pm e^\mp e^\mp$ pairs (right, with reinforced tag electron selection), as described in section 7.3.2. The yellow area indicates $t\bar{t}$ events in which the tag lepton is fake and the probe electron real, leading to a measurement bias.

2631 by working with $e^\pm\mu^\pm$ pairs instead (with a tag muon), but mixing leptons
 2632 of different flavours brings additional complications (for example, the unbiased
 2633 measurement cannot be employed to measure muon fake rates at higher p_T , as
 2634 there is no symmetry between the leptons). To improve confidence, measurements
 2635 are performed in four different ways, which complement each other:

- 2636 • straightforward tag-and-probe with $e\mu$ pairs, with the same tag muon
 2637 selection as in the previous section.
- 2638 • same selection, but subtracting from the numerator the number of pairs
 2639 with one fake tag muon and one prompt probe electron, itself estimated from
 2640 the number of observed $e\mu$ events with a muon failing signal requirements,
 2641 scaled by an efficiency correction factor $e\mu/\mu\mu$ taken from $t\bar{t}$ MC (only for

2642 pairs with one fake muon). This only works if the two muons satisfy the
 2643 same kinematic requirements, therefore can be used only for measurements
 2644 in wide or inclusive bins.

- 2645 • selecting $\ell^\mp e^\pm e^\pm + \geq 1b$ events, with a Z veto on SFOS pairs. This selection
 2646 entirely suppresses contributions from charge-flip, or events with fake muons.

2647 One of the electron, with standard signal requirements, is required to
 2648 satisfy the same reinforced p_T and isolation requirements as for the muon
 2649 measurement, and the measurement can be performed on the other electron.

- 2650 • same selection, using the symmetry between the two same-sign electrons to
 2651 measure the rates in an unbiased way, similarly to the muon case.

2652 Events are acquired with the combination of single-muon (as in previous section)
 2653 and $e\mu$ triggers.

2654 Figure 7.13 shows the number of signal probe electrons selected in the $e\mu$
 2655 and ℓee channels. There are significantly fewer events selected in the trilepton
 2656 channel. Figure 7.14 shows the electron fake rate as a function of p_T or η in $t\bar{t}$
 2657 MC. The variations of the rates as function of the pseudorapidity are not very
 2658 large, therefore measurements are only performed as a function of p_T . The low
 2659 p_T range is dominated by non-prompt electrons from heavy flavour decays, while
 2660 beyond 30 GeV, electron fakes mostly come from conversions of photons produced
 2661 inside jets, such as $\pi^0 \rightarrow \gamma\gamma$ decays.

2662 Based on the estimated levels of bias, and achievable statistical precision of
 2663 the different methods, the electron fake rate is measured with the tag-and-probe

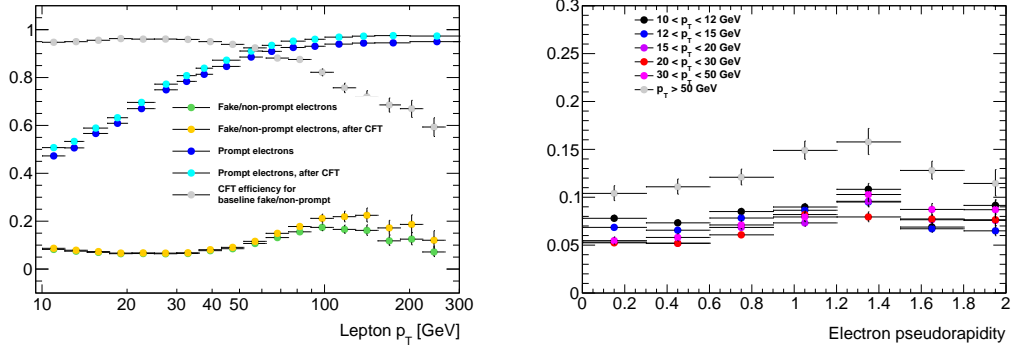


Figure 7.14: Electron fake rates in $t\bar{t}$ MC with an inclusive selection, as function of p_T (left, yellow/green markers = with/without CFT cut applied) or $|\eta|$ in different momentum ranges (right).

²⁶⁶⁴ $e\mu$ selection up to 30 GeV, and by combining “unbiased” evaluations in both $e\mu$
²⁶⁶⁵ and ℓee channels beyond. The measured rates are presented in Table 7.7, together
²⁶⁶⁶ with the associated statistical and background-subtraction uncertainties. The
²⁶⁶⁷ rates are of the order of 10% up to 30 GeV, beyond which they increase up to
²⁶⁶⁸ 25%.

²⁶⁶⁹ Unlike muons, MC-based correction factors are not applied for final states
²⁶⁷⁰ with ≥ 2 b -tagged jets. This is because there is less good agreement between the
²⁶⁷¹ measured rates and the simulation; in particular the former take larger values in
²⁶⁷² the medium- p_T range.

²⁶⁷³ Systematic uncertainties

²⁶⁷⁴
²⁶⁷⁵ Similarly to the muon case, systematic uncertainties are assigned to cover for
²⁶⁷⁶ difference in the rates in the measurement regions and in the signal regions that
²⁶⁷⁷ would be due to different sources of fake leptons, or different kinematic properties

2678 of these sources. Unlike muons, there is much less of a dependency to H_T . The
 2679 dominant source of potential differences is therefore the origin of the fake electron
 2680 (see Fig. 7.15); for $p_T < 20$ GeV, non-prompt electrons from heavy-flavor hadron
 2681 decays dominate, which is confirmed by the good agreement between MC fake
 2682 rates and those measured in data. In that range, an uncertainty of 30% is assigned
 2683 to the fake rates (inflated to 50% for final states with $\geq 2b$ -tagged jets). The
 2684 rates measured in data are larger than those predicted by the simulation, and
 2685 would for example be consistent with a larger amount of electrons from photon
 2686 conversions than predicted. In that range, an uncertainty of 50% is assigned to
 2687 cover any arbitrary variation of the relative contributions of each source.

2688 Finally, Figure 7.15 shows the variation of the fake rate in $t\bar{t}$ MC as function of
 2689 the number of b -tagged jets in the event. As expected, the rates are very similar
 2690 for $0b$ and $\geq 1b$ final states, justifying the use of the fake rates measured in this
 2691 section (i.e. in a $\geq 1b$ region) to predict fake electron background in all signal
 2692 regions.

2693 Baseline-to-signal efficiency for real leptons

2694 Baseline-to-signal efficiency for real leptons is measured in a high purity data
 2695 sample of opposite-sign same-flavor leptons with the standard Z tag-and-probe
 2696 method. Events are selected by a single lepton trigger. The tag lepton, required
 2697 to have triggered the event recording, also satisfies signal requirements and verifies
 2698 $p_T > 25$ GeV. The probe lepton used for the efficiency measurement satisfies
 2699 baseline requirements. All possible tag-and-probe combinations are considered

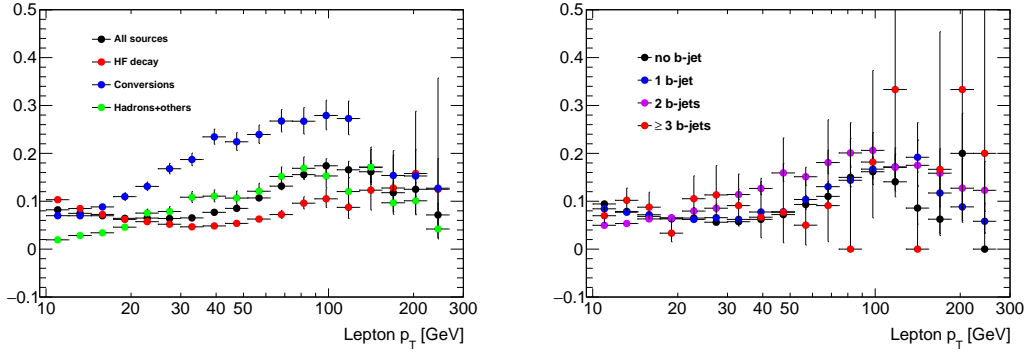


Figure 7.15: Electron fake rates in $t\bar{t}$ MC with an inclusive selection, as a function of p_T and split according to the source of the fake electron (left). The relative contributions of each source (for signal electrons) are indicated on the right-hand-side.

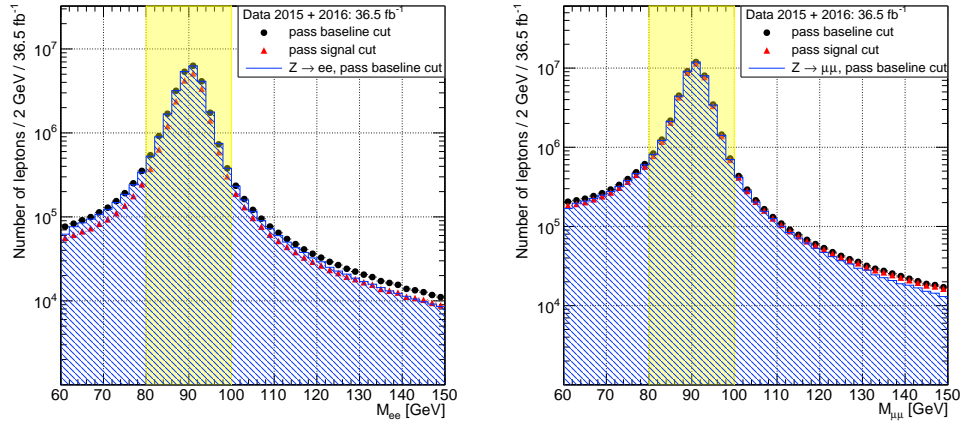


Figure 7.16: Invariant mass of opposite-sign same-flavor electrons (left) and muons (right), after the tag selection, where the probe satisfies the baseline requirements or the signal requirements.

2700 in an event (including permutation of the tag and probe leptons), as long as the
 2701 invariant mass of the pair is comprised between 80 and 100 GeV. Figure 7.16
 2702 illustrates this event selection.

2703 A non-negligible background contamination in the electron channel affects
 2704 measurements below $p_T = 20$ GeV. This contamination is taken into account in the
 2705 measurement using a background template method inspired by the method used
 2706 to measure reconstruction, identification, and isolation efficiencies documented
 2707 in [100]. This template is built from the tag-and-probe invariant mass distribution
 2708 for baseline-level probe electrons that fail both tight identification and isolation
 2709 requirements, smoothed by assuming an exponential shape whose parameters are
 2710 determined by a fit in the interval $60 < m_{ee} < 120$ GeV excluding the $80 < m_{ee} <$
 2711 100 GeV region. The background template is then normalized to the main tag-
 2712 and-probe distribution in the background-dominated tail $120 < m_{ee} < 150$ GeV.
 2713 The estimated level of background goes up to 4%, reached for probe electrons
 2714 with $p_T < 15$ GeV and $|\eta| < 0.8$.

2715 The efficiency is measured as a function of p_T and η , and the results are
 2716 presented in Fig 7.17 for electrons and muons. The background subtraction is
 2717 applied on the electron channel only. The following systematic uncertainties are
 2718 assigned to the measured efficiencies:

- 2719 • Background contamination: 27 variations of the tag-and-probe method
 2720 are considered to assess the electron measurement systematics. Three
 2721 m_{ee} windows and 9 variations of the background subtraction methods are
 2722 considered. The largest contribution to the systematics arises from the m_{ee}
 2723 window variation. This is expected as the proportion of electrons affected
 2724 by Bremsstrahlung depends on m_{ee} . The resulting relative systematics

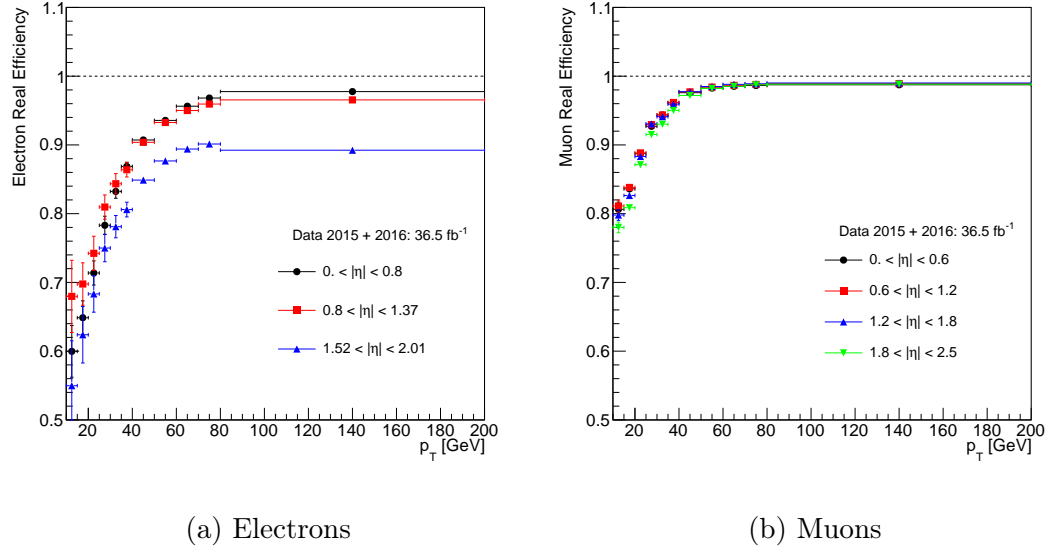


Figure 7.17: Baseline-to-signal efficiencies as a function of p_T and $|\eta|$ for real electrons (left) and muons (right), measured in 2015+2016 data. The $|\eta|$ binning used in the electron case corresponds to the geometry of the electromagnetic calorimeter. For muons a homogeneous $|\eta|$ binning is considered. The error bars corresponds to the quadratic sum of the statistical and tag-and-probe measurement systematic uncertainties.

2725 vary from 6% \sim 12% in the $10 < p_T < 15$ GeV region, 3% to 6% in
 2726 the $15 < p_T < 20$ GeV region, 1% to 3% in the $20 < p_T < 40$ GeV
 2727 region, and less than 1% for $p_T > 40$ GeV. The systematic uncertainties
 2728 associated to the muon efficiencies measurement vary from 1% to 1.3% in
 2729 the $10 < p_T < 15$ GeV region and less than 1% for $p_T > 15$ GeV.

- 2730 • Trigger: a systematic uncertainty accounting for a potential bias at trigger
 2731 level is considered and it varies between 0 and 4%, depending on the p_T

2732 range.

- 2733 • Extrapolation to busy environments: efficiencies are typically lower in such
- 2734 environments due to the proximity of jets and leptons; an uncertainty is
- 2735 assigned by comparing efficiencies in simulated $Z \rightarrow \ell\ell$ and $\tilde{g} \rightarrow t\bar{t}\tilde{\chi}_1^0$ events,
- 2736 for $\Delta m(\tilde{g}, \tilde{\chi}_1^0) > 1$ TeV which represents an extreme case of final states
- 2737 with highly boosted top quarks. The uncertainty, taken as the difference
- 2738 in efficiencies, is parametrized as a function of p_T and ΔR (the angular
- 2739 distance between the lepton and the closest jet).

2740 The resulting systematic uncertainties are summarized in Table 7.8 and Table 7.9.

2741

2742

2743 7.3.3 MC Template Method

2744 As discussed in Section 6.3.1, the MC template method is a simulation-based

2745 method that provides an alternative estimate of the reducible backgrounds affecting

2746 the analysis. It relies on the correct modelling of FNP leptons and charge-flipped

2747 electron kinematics in $t\bar{t}$ and $V+jets$. FNP leptons are classified in four categories,

2748 namely electrons and muons coming from b and light-quark jets. Normalisation

2749 factors for each of the five sources (including photon conversions) are computed to

2750 match the observed data in dedicated control regions. The fifth category is events

2751 with prompt electrons that have a charge mis-measurement (charge flip, EL HF,

2752 MU HF, EL LF, MU LF). Six non-overlapping control regions are defined by the
 2753 presence of b -jets and by the flavors of the same sign lepton pair in the event:

- 2754 • CR0b: events without b -jets in ee , $e\mu$, and $\mu\mu$ channels.
 - 2755 • CR1b: events with at least one b -jet in ee , $e\mu$, and $\mu\mu$ channels.
- 2756 All the selected events contain two or more same-sign signal leptons and
 2757 $E_T^{\text{miss}} > 40$ GeV and 2 or more jets. Events satisfying the signal regions require-
 2758 ments are excluded from the control regions. The purpose of the E_T^{miss} requirement
 2759 is to remove multi-jet events that have two or more FNP leptons and tend to
 2760 have low E_T^{miss} . The six distributions are chosen for variables that provide the
 2761 best separation between processes with prompt leptons and processes with fake
 2762 leptons and charge flip and are shown before and after the fit in Figures 6.2-6.4
 2763 and Figures 6.3-6.5, respectively. The multipliers obtained after the minimiza-
 2764 tion of the negative log likelihood were given in Tables 6.1 and 6.2. The tables
 2765 represent the correction factors obtained from the fit upon using two different
 2766 parton showers, POWHEG-Box +Pythia and SHERPA for the processes that lead
 2767 to non-prompt leptons and charge flips. The goal of varying the parton shower is
 2768 to access the dependence of the fake and charge flip estimates on the choice of
 2769 the parton shower.

2770 The MC template method is validated by looking at the agreement between
 2771 observed data and prediction as shown in Figure 7.21 and Figure 7.21. In the
 2772 MC template method, the systematic uncertainty is obtained by changing the
 2773 generator from POWHEG-Box +Pythia to SHERPA and propagating uncertainties

2774 from the control region fit to the global normalization scale factors applied to the
 2775 MC samples. The uncertainties in these scale factors are in the range 75–80%,
 2776 depending on the SRs. In practice, only $t\bar{t}$ contributes to the SRs and the final
 2777 yields with systematic uncertainties from fit uncertainty, theory uncertainties
 2778 on $t\bar{t}$, and comparison of different showers (Pythia and Sherpa) are shown in
 2779 Table 7.10. This table also shows a global correction factor derived by taking the
 2780 ratio of the weighted $t\bar{t}$ to raw MC $t\bar{t}$ with a global uncertainty that includes all
 2781 systematic uncertainties used to obtain the final estimate.

2782 **7.3.4 Reducible Background Validation**

2783 The reducible backgrounds estimated with the methods described in the previous
 2784 sections are validated by comparing observed data to predicted background after
 2785 various kinematic requirements. The next sections will validate the MC template
 2786 method used to estimate the charge flip and the FNP lepton background, and the
 2787 matrix method used to estimate the FNP lepton background.

2788 **Data/MC comparisons**

2789 The overall level of agreement obtained by the matrix method can be seen in
 2790 different channels in Fig 7.18. The distributions of several variables are shown on
 2791 Fig 7.19 for an inclusive same-sign leptons selection after various requirements
 2792 on the number of jets and b -jets. These distributions illustrate that the data are
 2793 described by the prediction within uncertainties. The apparent disagreement for
 2794 m_{eff} above 1 TeV in Figure 7.19d is covered by the large theory uncertainty for

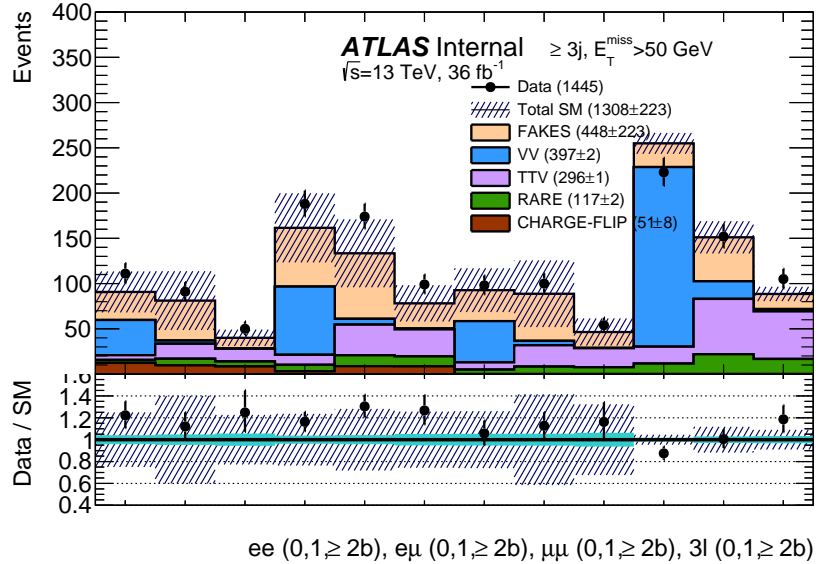


Figure 7.18: Summarized level of agreement between observed data (2015+2016, 36.5 fb^{-1}) and expected SM+detector backgrounds for events with ≥ 2 same-sign leptons ($p_T > 20 \text{ GeV}$), $E_T^{\text{miss}} > 50 \text{ GeV}$ and ≥ 3 jets ($p_T > 40 \text{ GeV}$), split as function of the lepton flavours and the number of b -tagged jets. Uncertainties include statistical sources, as well as systematic uncertainties for the data-driven backgrounds; for illustration, statistical uncertainties alone are shown in the light-coloured error bands in the ratio plots. Events belonging to any of the signal regions are rejected, both in data and MC.

2795 the diboson background, which is not shown but amounts to about 30% for m_{eff}
 2796 above 1 TeV. To avoid the presence of signal in the tails of these distributions,
 2797 events belonging to any of the signal regions are vetoed both in data and for the
 2798 predicted backgrounds.

2799 Figure 7.20 shows a comparison between the estimates of the MC template
 2800 method and the matrix method in a loose selection. Other E_T^{miss} distributions
 2801 with events satisfying the signal region requirements except the E_T^{miss} cut are

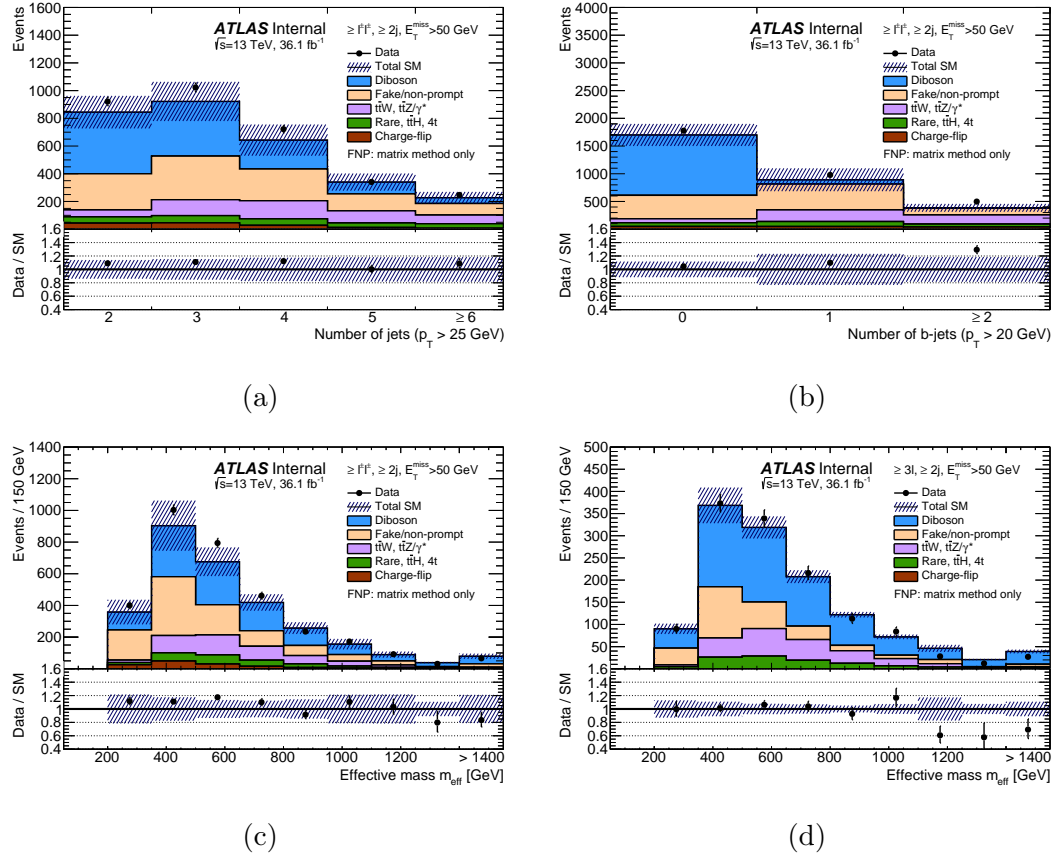


Figure 7.19: Distributions of (a) the number of jets, (b) the number of b -tagged jets and (c), (d) the effective mass. The distributions are made after requiring at least two jets ($p_T > 40 \text{ GeV}$) and $E_T^{\text{miss}} > 50 \text{ GeV}$, as well as at least two same-sign leptons ((a), (b), (c)) or three leptons (d). The uncertainty bands include the statistical uncertainties for the background prediction as well as the systematic uncertainties for fake- or non-prompt-lepton backgrounds (using the matrix method) and charge-flip electrons. Not included are theoretical uncertainties in the irreducible background contributions. The rare category is defined in the text.

2802 shown in Figure 7.21 comparing the two methods.

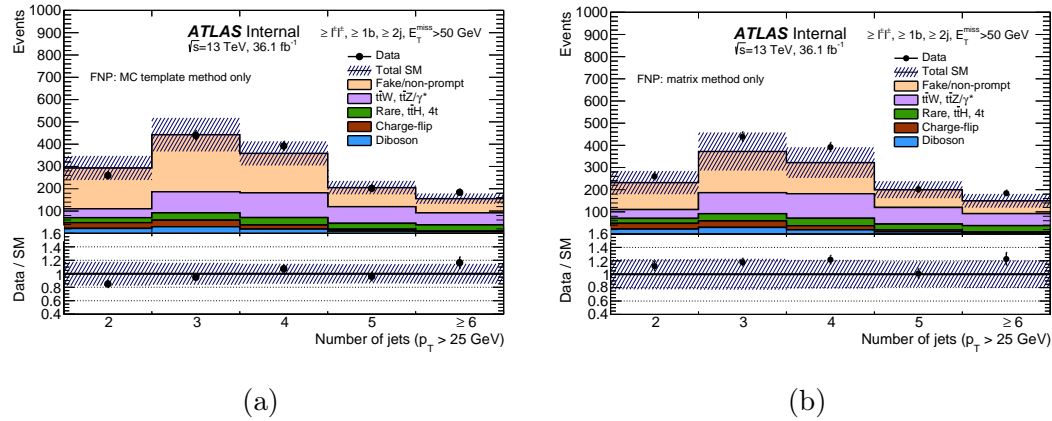


Figure 7.20: Distributions of the number of jets after requiring at least two jets ($p_T > 40\text{GeV}$) and $E_T^{\text{miss}} > 50\text{GeV}$, as well as at least two same-sign leptons. The fake or non-prompt leptons backgrounds are estimated alternatively with the MC template method (7.20b) or the matrix method (7.20a). The uncertainty band includes the statistical uncertainties for the background prediction as well as the full systematic uncertainties for fake or non-prompt leptons backgrounds or charge-flip electrons. The rare category is defined in the text. In both figures, the last bin contains the overflow.

2803 Reducible background estimates

The expected yield for processes with FNP leptons and charge-flip electrons, estimated with the matrix method, likelihood method (charge-flip), and the MC template method are presented in Table 7.11 and Table 7.12 for the signal regions and Table 7.13 for the validation regions. Since the predictions from the MC template and matrix methods in the signal and validation regions are consistent with each other, the final numbers retained for the FNP lepton background estimate (also shown in the tables) are taken as the weighted-average of the predictions from the matrix method and the MC template; the weights are based

2812 on the statistical component, and the systematic uncertainties are propagated
 2813 assuming conservatively a full correlation between the two methods (although
 2814 they are in fact largely independent!). The central value and statistical/systematic
 2815 uncertainties are therefore:

$$(w\zeta_1 + (1-w)\zeta_2) \pm \sqrt{w^2 (\Delta\zeta_1^{(\text{stat})})^2 + (1-w)^2 (\Delta\zeta_2^{(\text{stat})})^2} \quad (7.6)$$

$$\pm (w\Delta\zeta_1^{(\text{syst})} + (1-w)\Delta\zeta_2^{(\text{syst})})$$

$$\text{with } w = \frac{(\Delta\zeta_2^{(\text{stat})})^2}{(\Delta\zeta_1^{(\text{stat})})^2 + (\Delta\zeta_2^{(\text{stat})})^2}$$

2816 When the estimated value is too small(below 0.15), the expected yield is set
 2817 to 0.15 ± 0.15 , to cover for possibilities of an under-fluctuation of the number of
 2818 baseline-not-signal leptons when applying the matrix method, as well as lack of
 2819 statistics in the MC samples for the other method.

2820 The charge flip background is not combined between the MC template method
 2821 and the likelihood method due to the very large uncertainty in the MC template
 2822 estimate. The OS data has a much larger number of events which makes a precise
 2823 prediction of this background. The MC template result is used as a cross check.

2824 7.4 Systematic uncertainties

2825 The systematic uncertainties related to the estimated background from same-sign
 2826 prompt leptons arise from the experimental uncertainties as well as theoretical
 2827 modelling and theoretical cross-section uncertainties. The statistical uncertainty
 2828 of the simulated event samples is also taken into account.

2829 7.4.1 Theoretical Uncertainties

2830 The cross-sections used to normalize the MC samples are varied according to the
 2831 uncertainty in the cross-section calculation, which is 13% for $t\bar{t}W$, 12% for $t\bar{t}Z$
 2832 production [70], 6% for diboson production [72], 8% for $t\bar{t}H$ [70] and 30% for
 2833 $4t$ [42]. Additional uncertainties are assigned to some of these backgrounds to
 2834 account for the theoretical modelling of the kinematic distributions in the MC
 2835 simulation.

2836 Associate $t\bar{t} + W/Z$ production

2837 The theoretical uncertainties on the $t\bar{t}W$ and $t\bar{t}Z^{(*)}$ processes are evaluated by
 2838 several variations added in quadrature:

- 2839 ● Normalization and factorization scales varied independently up and down
 2840 by a factor of two from the central scale $\mu_0 = H_T/2$ as detailed in Ref. [80].
 2841 The largest deviation with respect to the nominal is used as the symmetric
 2842 uncertainty.
- 2843 ● Variation of the PDF used. The standard deviation of the yields obtained
 2844 using different PDF sets was used as the absolute uncertainty due to PDF.
 2845 The relative uncertainty is then computed by dividing the standard deviation
 2846 by the mean yield.
- 2847 ● Comparison of the nominal AMC@NLO MC samples to alternative SHERPA
 2848 (v2.2) samples produced at leading-order with one extra parton in the matrix
 2849 element for $t\bar{t}W$ and 2 extra partons for $t\bar{t}Z$ [80]. The yield comparison for

2850 all SRs is shown in Table 7.14, with negligible differences in some SRs and
 2851 up to 28% in the worst case.

2852 As a result of these studies, the total theory uncertainty for these processes is at
 2853 the level of 15-35% in the signal and validation regions used in the analysis.

2854 **Diboson $WZ, ZZ, W^\pm W^\pm$ production**

2855 The theoretical uncertainties on the WZ and ZZ processes are evaluated by
 2856 several variations added in quadrature:

2857 • Normalization and factorization scales varied independently up and down
 2858 by a factor of two from the central scale choice. The largest deviation with
 2859 respect to the nominal is used as the symmetric uncertainty.

2860 • The standard deviation of the yields obtained using different PDF sets was
 2861 used as the absolute uncertainty due to PDF. The relative uncertainty is
 2862 then computed by dividing the standard deviation by the mean yield.

2863 • Re-summation scale varied up and down by a factor of two from the nominal
 2864 value.

2865 • The scale for calculating the overlap between jets from the matrix element
 2866 and the parton shower is varied from the nominal value of 20 GeV down to
 2867 15 GeV and up to 30 GeV. The largest deviation with respect to the nominal
 2868 is used as the symmetric uncertainty due to matrix element matching.

2869 • An alternative recoil scheme is considered to estimate the uncertainty
 2870 associated with mis-modeling of jet multiplicities larger than three.

2871 Based on these studies and the cross-section uncertainties, the total theory
2872 uncertainty for these processes is at the level of 25-40% in the signal and validation
2873 regions used in the analysis.

2874 No theoretical uncertainties have been evaluated specifically for the $W^\pm W^\pm jj$
2875 process, to which we assign the same uncertainties as for WZ , by lack of a better
2876 choice. But it should be noted that contributions from this process are minor in
2877 the SRs and typically smaller than those from WZ and ZZ .

2878 **Other rare processes**

2879 A conservative 50% uncertainty is assigned on the summed contributions of all
2880 these processes ($t\bar{t}H$, tZ , tWZ , $t\bar{t}t\bar{t}$, $t\bar{t}WW$, $t\bar{t}WZ$, WH , ZH , VVV), which
2881 is generally quite larger than the uncertainties on their inclusive production
2882 cross-sections, and assumes a similar level of mis-modelling as for diboson or $t\bar{t}V$
2883 processes.

2884 **7.4.2 Experimental Uncertainties**

2885 Uncertainties associated with the measurement and reconstruction of the physics
2886 objects used in the analysis (leptons, jets, etc.) must be accounted for when
2887 interpreting the results. The systematic uncertainties from the data-driven method
2888 have already been discussed in Section 7.3. In fact, these data-driven backgrounds
2889 are affected by the same systematic uncertainty as in data to which they are
2890 being compared to. As a result, only systematic uncertainties on backgrounds
2891 estimated with MC simulation and detector simulation needs to be considered.

2892 The uncertainties considered for the analysis and recommended by the ATLAS
 2893 SUSY group are: **Jet energy scale (JES)**
 2894 In order to account for inefficiencies in the calorimeter cells and the varying
 2895 response to charged and neutral particles passing through them, the energies of
 2896 the jets used in this analysis were corrected. The calibration procedure uses a
 2897 combination of simulation and test beam and in situ data [90] with an uncertainty
 2898 correlated between all events. As a result, all distributions used in the final result
 2899 are produced with the nominal calibration as well as an up and down variation
 2900 of the jet energy scale (in a fully correlated way) by the $\pm 1\sigma$ uncertainty
 2901 of each nuisance parameter. A combined version of several independent sources
 2902 contributing to the calibration was used in the analysis to reduce the number of
 2903 nuisance variables in the fitting procedure.

2904 **Jet energy resolution (JER)**

2905 An extra p_T smearing is added to the jets based on their p_T and η to account for
 2906 a possible underestimate of the jet energy resolution in the MC simulation. A
 2907 systematic uncertainty is considered to account for this defect on the final result.
 2908 The JER in data has previously been estimated by ATLAS in dijet events.

2909 **Jet vertex tagger** The uncertainties account for the residual contamination
 2910 from pile-up jets after pile-up suppression and the MC generator choice [91].

2911 **Flavor tagging** The MC simulation does not reproduce correctly the b -
 2912 tagging, charm identification, and light jet reject efficiencies of the detector. A $t\bar{t}$
 2913 MC simulation and di-jet measurements are used to derive correction factors to
 2914 be applied to MC simulation [52, 92]. These correction factors are then varied

2915 within their uncertainties to produce up and down variations.

2916 **Lepton energy scale, resolution, and Identification efficiencies** Similar
2917 to the case of jets, electrons and muons also have corresponding energy scale
2918 and resolution systematic uncertainties. Corrections are also applied to take
2919 into account any variations in the identification efficiency in the detector and its
2920 simulation [46, 93, 46].

2921 **E_T^{miss} soft term uncertainties** The main effect come from the hard object
2922 uncertainties (most notably JES and JER) that are propagated to the E_T^{miss} .

2923 **Pileup re-weighting** This uncertainty is obtained by re-scaling the μ value
2924 in data by 1.00 and 1/1.18, covering the full difference between applying and
2925 not-applying the nominal μ correction of 1/1.09, as well as effects resulting from
2926 uncertainties on the luminosity measurements, which are expected to dominate.

2927 **Luminosity** The integrated luminosities in data corresponds to 3.2 fb^{-1} and
2928 32.9 fb^{-1} for 2015 and 2016 respectively. The combined luminosity error for 2015
2929 and 2016 is 3.2%, assuming partially correlated uncertainties in 2015 and 2016.

2930 **Trigger** To account for any differences between the trigger efficiency in simu-
2931 lation and data, corrections factors are derived to correct for them. Uncertainties
2932 on the correction factors as well as inefficiencies related to the plateau of the
2933 trigger are propagated to the final result.

2934 The uncertainty on the beam energy is neglected. All the experimental
2935 uncertainties are applied also on the signal samples when computing exclusion
2936 limits on SUSY scenarios.

2937 All of these uncertainties are fed into the fitting and limit setting machinery

²⁹³⁸ by treating them as uncorrelated uncertainties, and thus treated independently.

Validation Region	$N_{\text{leptons}}^{\text{signal}}$	$N_{b\text{-jets}}$	N_{jets}	p_T^{jet} [GeV]	E_T^{miss} [GeV]	m_{eff} [GeV]	Other
$t\bar{t}W$	= 2SS	≥ 1	≥ 4 ($e^\pm e^\pm, e^\pm \mu^\pm$) ≥ 3 ($\mu^\pm \mu^\pm$)	> 40 > 25	> 45	> 550	$p_T^{\ell_2} > 40$ GeV $\sum p_T^{\text{b-jet}} / \sum p_T^{\text{jet}} > 0.25$
$t\bar{Z}$	≥ 3 ≥ 1 SFOS pair	≥ 1	≥ 3	> 35	–	> 450	$81 < m_{\text{SFOS}} < 101$ GeV
$WZ4j$	= 3	= 0	≥ 4	> 25	–	> 450	$E_T^{\text{miss}} / \sum p_T^\ell < 0.7$
$WZ5j$	= 3	= 0	≥ 5	> 25	–	> 450	$E_T^{\text{miss}} / \sum p_T^\ell < 0.7$
$W^\pm W^\pm jj$	= 2SS	= 0	≥ 2	> 50	> 55	> 650	veto $81 < m_{e^\pm e^\pm} < 101$ GeV $p_T^{\ell_2} > 30$ GeV $\Delta R_\eta(\ell_{1,2}, j) > 0.7$ $\Delta R_\eta(\ell_1, \ell_2) > 1.3$
All VRs	Veto events belonging to any SR						

Table 7.3: Summary of the event selection in the validation regions (VRs). Requirements are placed on the number of signal leptons ($N_{\text{leptons}}^{\text{signal}}$), the number of b -jets with $p_T > 20$ GeV ($N_{b\text{-jets}}$) or the number of jets (N_{jets}) above a certain p_T threshold (p_T^{jet}). The two leading- p_T leptons are referred to as $\ell_{1,2}$ with decreasing p_T . Additional requirements are set on E_T^{miss} , m_{eff} , the invariant mass of the two leading electrons $m_{e^\pm e^\pm}$, the presence of SS leptons or a pair of same-flavour opposite-sign leptons (SFOS) and its invariant mass m_{SFOS} . A minimum angular separation between the leptons and the jets ($\Delta R_\eta(\ell_{1,2}, j)$) and between the two leptons ($\Delta R_\eta(\ell_1, \ell_2)$) is imposed in the $W^\pm W^\pm jj$ VR. For the two WZ VRs the selection also relies on the ratio of the E_T^{miss} in the event to the sum of p_T of all signal leptons p_T ($E_T^{\text{miss}} / \sum p_T^\ell$). The ratio of the scalar sum of the p_T of all b -jets to that of all jets in the event ($\sum p_T^{\text{b-jet}} / \sum p_T^{\text{jet}}$) is used in the $t\bar{t}W$ VR selection.

Validation Region	$t\bar{t}W$	$t\bar{t}Z$	$WZ4j$	$WZ5j$	$W^\pm W^\pm jj$
$t\bar{t}Z/\gamma^*$	6.2 ± 0.9	123 ± 17	17.8 ± 3.5	10.1 ± 2.3	1.06 ± 0.22
$t\bar{t}W$	19.0 ± 2.9	1.71 ± 0.27	1.30 ± 0.32	0.45 ± 0.14	4.1 ± 0.8
$t\bar{t}H$	5.8 ± 1.2	3.6 ± 1.8	1.8 ± 0.6	0.96 ± 0.34	0.69 ± 0.14
$4t$	1.02 ± 0.22	0.27 ± 0.14	0.04 ± 0.02	0.03 ± 0.02	0.03 ± 0.02
$W^\pm W^\pm$	0.5 ± 0.4	—	—	—	26 ± 14
WZ	1.4 ± 0.8	29 ± 17	200 ± 110	70 ± 40	27 ± 14
ZZ	0.04 ± 0.03	5.5 ± 3.1	22 ± 12	9 ± 5	0.53 ± 0.30
Rare	2.2 ± 0.5	26 ± 13	7.3 ± 2.1	3.0 ± 1.0	1.8 ± 0.5
Fake/non-prompt leptons	18 ± 16	22 ± 14	49 ± 31	17 ± 12	13 ± 10
Charge-flip	3.4 ± 0.5	—	—	—	1.74 ± 0.22
Total SM background	57 ± 16	212 ± 35	300 ± 130	110 ± 50	77 ± 31
Observed	71	209	257	106	99

Table 7.4: The numbers of observed data and expected background events in the validation regions. The rare category is defined in the text. Background categories with yields shown as “—” do not contribute to a given region (e.g. charge flips in three-lepton regions) or their estimates are below 0.01 events. The displayed yields include all statistical and systematic uncertainties.

Table 7.5: Muon fake rate measured in data and the associated statistical uncertainty. The systematic uncertainty originating from the subtraction of “backgrounds” with only prompt leptons is also displayed.

$10 < p_T < 12 \text{ GeV}$		$12 < p_T < 14$	
$ \eta < 2.3$	$ \eta > 2.3$	$ \eta < 2.3$	$ \eta > 2.3$
$0.14 \pm 0.01 \pm 0.00$	$0.22 \pm 0.05 \pm 0.00$	$0.11 \pm 0.01 \pm 0.00$	$0.24 \pm 0.06 \pm 0.00$
$14 < p_T < 17$		$17 < p_T < 20 \text{ GeV}$	
$ \eta < 2.3$	$ \eta > 2.3$	$ \eta < 2.3$	$ \eta > 2.3$
$0.12 \pm 0.01 \pm 0.00$	$0.09 \pm 0.05 \pm 0.00$	$0.09 \pm 0.01 \pm 0.00$	$0.21 \pm 0.07 \pm 0.00$
$20 < p_T < 30$	$30 < p_T < 40$	$40 < p_T < 60$	$p_T > 60$
$0.07 \pm 0.02 \pm 0.00$	$0.12 \pm 0.05 \pm 0.01$	$0.16 \pm 0.09 \pm 0.04$	$0.49 \pm 0.10 \pm 0.07$

Table 7.6: Additional systematic uncertainty on the muon fake rates, to address variations of the latter in different environments. The table also shows the correction factors and uncertainties applied to final states with $\geq 2 b$ -tagged jets.

p_T	< 14	$14 - 20$	$20 - 30$	$30 - 40$	$40 - 60$	> 60
$\Delta\zeta^{(\text{syst})}$	30%	30%	30%	50%	50% for $H_T < 600$ 70% for $600 < H_T < 1200$ 85% for $H_T > 1200$	
$\frac{\zeta_{\geq 2b}}{\zeta}$	1.2 ± 0.2	1.5 ± 0.5	1.7 ± 0.7	2.0 ± 1.0	1.5 ± 0.5	—

Table 7.7: Electron fake rate measured in data and the associated statistical uncertainty. The systematic uncertainty originating from the subtraction of “backgrounds” with only prompt leptons is also displayed.

$10 < p_T < 12$	$12 < p_T < 14$	$14 < p_T < 17$	$17 < p_T < 20$
$0.10 \pm 0.01 \pm 0.00$	$0.10 \pm 0.01 \pm 0.01$	$0.12 \pm 0.01 \pm 0.01$	$0.08 \pm 0.02 \pm 0.00$
$20 < p_T < 25$	$25 < p_T < 30$	$30 < p_T < 40$	$40 > p_T$
$0.07 \pm 0.02 \pm 0.01$	$0.11 \pm 0.03 \pm 0.01$	$0.20 \pm 0.07 \pm 0.03$	$0.25 \pm 0.10 \pm 0.05$

	Electrons			Muons			
	$0 < \eta < 0.8$	$0.8 < \eta < 1.37$	$1.52 < \eta < 2.01$	$0 < \eta < 0.6$	$0.6 < \eta < 1.2$	$1.2 < \eta < 1.8$	$1.8 < \eta < 2.5$
$10 \text{ GeV} < p_T < 15 \text{ GeV}$	0.047	0.063	0.089	0.014	0.010	0.008	0.011
$15 \text{ GeV} < p_T < 20 \text{ GeV}$	0.027	0.042	0.062	0.005	0.006	0.008	0.011
$20 \text{ GeV} < p_T < 25 \text{ GeV}$	0.018	0.031	0.041	0.003	0.006	0.010	0.010
$25 \text{ GeV} < p_T < 30 \text{ GeV}$	0.029	0.024	0.027	0.011	0.015	0.022	0.019
$30 \text{ GeV} < p_T < 35 \text{ GeV}$	0.023	0.021	0.023	0.007	0.009	0.014	0.011
$35 \text{ GeV} < p_T < 40 \text{ GeV}$	0.014	0.018	0.018	0.004	0.004	0.006	0.006
$40 \text{ GeV} < p_T < 50 \text{ GeV}$	0.007	0.010	0.010	0.002	0.001	0.002	0.001
$50 \text{ GeV} < p_T < 60 \text{ GeV}$	0.008	0.010	0.010	0.001	0.001	0.001	0.001
$60 \text{ GeV} < p_T < 70 \text{ GeV}$	0.007	0.010	0.010	0.001	0.001	0.001	0.002
$70 \text{ GeV} < p_T < 80 \text{ GeV}$	0.008	0.011	0.012	0.002	0.001	0.001	0.002
$80 \text{ GeV} < p_T < 120 \text{ GeV}$	0.010	0.010	0.011	0.004	0.002	0.002	0.002
$120 \text{ GeV} < p_T < 150 \text{ GeV}$	0.005	0.005	0.011	0.006	0.005	0.005	0.005
$150 \text{ GeV} < p_T < 200 \text{ GeV}$	0.005	0.002	0.019	0.005	0.005	0.005	0.006

Table 7.8: Systematic uncertainties on the measured real lepton efficiency, separating sources affecting the measurement itself (background subtraction, trigger bias, and different methods).

electrons (busy environments)								
$\Delta R(e, jet)$	[0, 0.1]	[0.1, 0.15]	[0.15, 0.2]	[0.2, 0.3]	[0.3, 0.35]	[0.35, 0.4]	[0.4, 0.6]	[0.6, 4]
10 GeV < p_T < 20 GeV	-	-	-	-	-	-	25.31%	6.5%
20 GeV < p_T < 30 GeV	-	-	-	-	-	73.37%	10.21%	0.37%
30 GeV < p_T < 40 GeV	-	-	-	97.71%	48.22%	15.54%	7.29%	0.58%
40 GeV < p_T < 50 GeV	-	-	-	52.81%	22.80%	16.73%	7.68%	1.10%
50 GeV < p_T < 60 GeV	-	-	-	29.96%	21.49%	20.23%	6.99%	2.78%
60 GeV < p_T < 80 GeV	-	-	55.89%	24.31%	17.40%	24.77%	6.20%	2.87%
80 GeV < p_T < 150 GeV	-	57.52%	30.24%	16.45%	12.73%	20.92%	4.44%	2.73%
150 GeV < p_T < 200 GeV	88.54%	40.16%	19.34%	8.45%	14.66%	16.57%	2.57%	1.90%

muons (busy environments)								
$\Delta R(\mu, jet)$	[0, 0.1]	[0.1, 0.15]	[0.15, 0.2]	[0.2, 0.3]	[0.3, 0.35]	[0.35, 0.4]	[0.4, 0.6]	[0.6, 4]
10 GeV < p_T < 20 GeV	-	-	-	-	-	-	33.59%	5.18%
20 GeV < p_T < 30 GeV	-	-	-	-	-	82.34%	22.27%	3.39%
30 GeV < p_T < 40 GeV	-	-	-	98.54%	56.36%	31.89%	14.22%	2.24%
40 GeV < p_T < 50 GeV	-	-	-	53.10%	21.33%	13.90%	6.81%	1.45%
50 GeV < p_T < 60 GeV	-	-	-	24.98%	13.72%	9.62%	3.83%	0.79%
60 GeV < p_T < 80 GeV	-	-	44.41%	13.75%	6.14%	4.76%	2.04%	0.15%
80 GeV < p_T < 150 GeV	-	29.94%	7.14%	3.16%	1.30%	1.04%	0.07%	0.57%
150 GeV < p_T < 200 GeV	82.26%	4.14%	1.02%	0.17%	0.29%	0.62%	1.02%	1.13%

Table 7.9: Systematic uncertainties on the measured real lepton efficiency, due to the extrapolation to busy environments using $\tilde{g} \rightarrow t\bar{t}\tilde{\chi}_1^0$ events.

Table 7.10: Expected yields for background processes with fake leptons, in the signal regions with a global correction factor that represents the ratio of weighted $t\bar{t}$ to raw MC $t\bar{t}$ with a global uncertainty that includes: fit uncertainty, theory uncertainties on $t\bar{t}$, comparison of different showers. The fraction of the systematic uncertainty from the comparison between two showers (Pythia and Sherpa) is also shown.

Region	MC Template method	Global correction	Shower systematic
Rpc2L0bH	$1.00 \pm 0.96 \pm 0.81$	2.80 ± 2.10	74%
Rpc2L0bS	$1.68 \pm 1.02 \pm 1.26$	2.89 ± 1.97	65%
Rpc2L1bH	$2.07 \pm 0.63 \pm 1.56$	1.22 ± 1.14	34%
Rpc2L1bS	$2.33 \pm 1.17 \pm 2.10$	1.83 ± 1.42	81%
Rpc2L2bH	< 0.5	0 ± 0	0%
Rpc2L2bS	$0.41 \pm 0.33 \pm 0.45$	1.47 ± 1.12	73%
Rpc2Lsoft1b	$2.48 \pm 1.32 \pm 1.86$	1.59 ± 1.31	68%
Rpc2Lsoft2b	$1.66 \pm 0.66 \pm 1.28$	1.72 ± 1.29	54%
Rpc3L0bH	< 0.5	0 ± 0	0%
Rpc3L0bS	$0.21 \pm 0.15 \pm 0.16$	2.90 ± 2.20	71%
Rpc3L1bH	$0.42 \pm 0.29 \pm 0.32$	1.59 ± 1.25	59%
Rpc3L1bS	$3.55 \pm 1.80 \pm 2.76$	1.76 ± 1.32	67%
Rpc3LSS1b	$0.90 \pm 0.14 \pm 0.69$	2.34 ± 1.44	56%

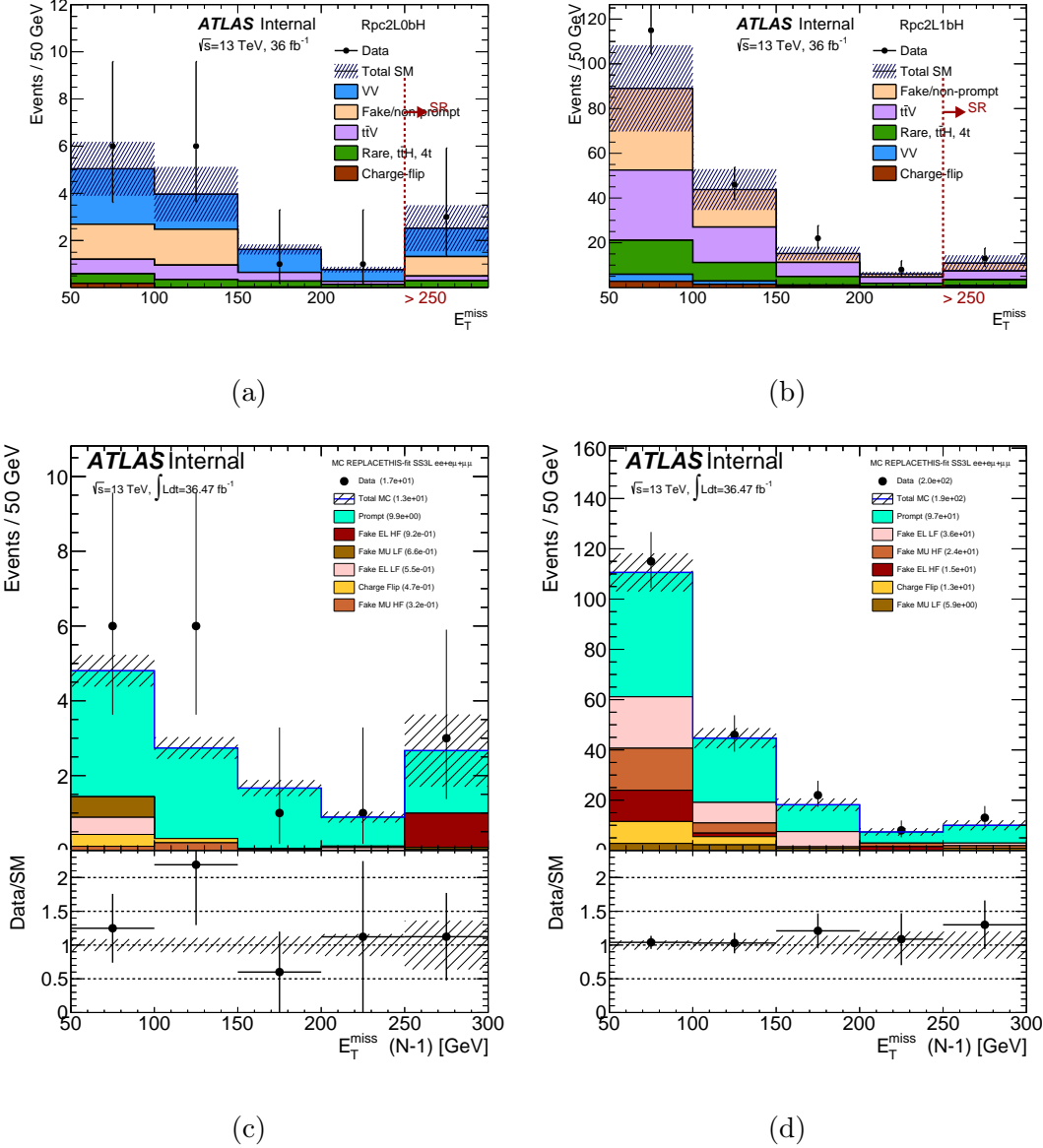


Figure 7.21: Missing transverse momentum distributions after (7.21a–7.21c) Rpc2L0bH and (7.21b–7.21d) Rpc2L1bH selection, except the E_T^{miss} requirement. Estimates with the matrix method are in the upper plots (7.21a–7.21a) while estimates with the MC template method are in the lower plots (7.21c–7.21c). The results in the signal regions are shown in the last (inclusive) bin of each plot. The statistical uncertainties in the background prediction are included in the uncertainty band, as well as the full systematic uncertainties for backgrounds with fake or non-prompt leptons, or charge-flip.

Table 7.11: Expected yields for background processes with fake leptons, in the signal regions shown for 36 fb^{-1} . Estimates from the matrix method and the MC template method are shown along with the retained estimates. Uncertainties include all statistical and systematic sources for the nominal estimate.

Region	Matrix method	Template method	Retained estimate
Rpc2L0bH	$0.83 \pm 0.56 \pm 0.74$	$1.00 \pm 0.96 \pm 0.81$	$0.87 \pm 0.48 \pm 0.76$
Rpc2L0bS	$1.51 \pm 0.60 \pm 0.66$	$1.68 \pm 1.02 \pm 1.26$	$1.55 \pm 0.52 \pm 0.81$
Rpc2L1bH	$3.54 \pm 1.62 \pm 3.12$	$2.07 \pm 0.63 \pm 1.56$	$2.26 \pm 0.59 \pm 1.76$
Rpc2L1bS	$2.65 \pm 1.21 \pm 1.89$	$02.33 \pm 01.17 \pm 02.10$	$2.48 \pm 0.84 \pm 2.00$
Rpc2L2bH	$-0.11 \pm 0.11 \pm 0.18$	< 0.5	$0.15 \pm 0.15 \pm 0.00$
Rpc2L2bS	$1.31 \pm 1.07 \pm 1.65$	$0.41 \pm 0.33 \pm 0.45$	$0.49 \pm 0.32 \pm 0.55$
Rpc2Lsoft1b	$4.75 \pm 1.42 \pm 2.64$	$2.48 \pm 1.32 \pm 1.86$	$3.53 \pm 0.97 \pm 2.22$
Rpc2Lsoft2b	$1.91 \pm 1.18 \pm 1.63$	$1.66 \pm 0.66 \pm 1.28$	$1.72 \pm 0.58 \pm 1.36$
Rpc3L0bH	$-0.01 \pm 0.11 \pm 0.10$	< 0.5	$0.15 \pm 0.15 \pm 0.00$
Rpc3L0bS	$2.31 \pm 1.50 \pm 2.63$	$0.21 \pm 0.15 \pm 0.16$	$0.23 \pm 0.15 \pm 0.18$
Rpc3L1bH	$0.57 \pm 0.43 \pm 0.50$	$0.42 \pm 0.29 \pm 0.32$	$0.47 \pm 0.24 \pm 0.38$
Rpc3L1bS	$4.94 \pm 1.83 \pm 2.96$	$3.55 \pm 1.80 \pm 2.76$	$4.23 \pm 1.28 \pm 2.86$
Rpc3LSS1b	$-0.18 \pm 1.24 \pm 2.85$	$0.90 \pm 0.14 \pm 0.69$	$0.89 \pm 0.14 \pm 0.72$

Table 7.12: Expected yields for background processes with charge-flipped electrons, in the signal regions shown for 36 fb^{-1} . Estimates from the likelihood method and the MC template method are shown. Uncertainties include all statistical and systematic sources. Charge-flip processes do not contribute to signal regions which require ≥ 3 leptons.

Region	Weighted OS data	Template method
Rpc2L0bH	$0.01 \pm 0.00 \pm 0.00$	< 0.4
Rpc2L0bS	$0.05 \pm 0.01 \pm 0.01$	$00.02 \pm 00.02 \pm 00.00$
Rpc2L1bH	$0.25 \pm 0.03 \pm 0.04$	$00.21 \pm 00.32 \pm 00.16$
Rpc2L1bS	$0.25 \pm 0.02 \pm 0.04$	$00.35 \pm 00.37 \pm 00.26$
Rpc2L2bH	$0.02 \pm 0.01 \pm 0.00$	< 0.4
Rpc2L2bS	$0.10 \pm 0.01 \pm 0.02$	< 0.4
Rpc2Lsoft1b	$0.08 \pm 0.01 \pm 0.02$	< 0.4
Rpc2Lsoft2b	$0.08 \pm 0.01 \pm 0.02$	< 0.4
Rpc3LSS1b	$0.39 \pm 0.03 \pm 0.07$	$00.81 \pm 00.53 \pm 00.34$

Table 7.13: Comparison of expected yields for background processes with fake leptons, in the validation regions, shown for 36 fb^{-1} between the data driven (DD) estimates and the MC template method (MC) estimates.

	VR- $t\bar{t}W$	VR- $t\bar{t}Z$	VR- $WZ4j$	VR- $WZ5j$	VR- $W^\pm W^\pm$
Fakes DD	$23 \pm 5 \pm 24$	$30 \pm 4 \pm 14$	$53 \pm 6 \pm 27$	$21 \pm 4 \pm 10$	$14 \pm 3 \pm 10$
Fakes MC	$14 \pm 4 \pm 10$	$18 \pm 3 \pm 13$	$46 \pm 5 \pm 34$	$16 \pm 2 \pm 12$	$13 \pm 2 \pm 10$
Combined	$18 \pm 3 \pm 15$	$22 \pm 2 \pm 13$	$49 \pm 4 \pm 30$	$17 \pm 2 \pm 12$	$13 \pm 2 \pm 10$
Charge-flip DD	$3.4 \pm 0.1 \pm 0.5$	–	–	–	$1.7 \pm 0.1 \pm 0.2$
Charge-flip MC	$3.8 \pm 1.0 \pm 1.9$	–	–	–	$1.0 \pm 0.3 \pm 0.2$

Table 7.14: Comparison of the event yields for the $t\bar{t}V$ background processes between AMC@NLO (default generator) and SHERPA in the SRs, as well as their relative difference.

SR	SHERPA	aMCATNLO	Relative diff.
Rpc2L0bH	0.25 ± 0.03	0.20 ± 0.05	25%
Rpc2L0bS	0.60 ± 0.06	0.82 ± 0.10	-26%
Rpc2L1bH	3.84 ± 0.14	3.86 ± 0.20	<1%
Rpc2L1bS	3.55 ± 0.13	3.94 ± 0.20	-9%
Rpc2L2bH	0.35 ± 0.04	0.41 ± 0.05	-14%
Rpc2L2bS	1.57 ± 0.08	1.57 ± 0.12	<1%
Rpc2Lsoft1b	1.01 ± 0.07	1.24 ± 0.11	-18%
Rpc2Lsoft2b	1.13 ± 0.07	1.15 ± 0.10	-1%
Rpc3L0bH	0.23 ± 0.02	0.18 ± 0.04	27%
Rpc3L0bS	0.90 ± 0.05	0.99 ± 0.09	-9%
Rpc3L1bH	1.54 ± 0.08	1.52 ± 0.11	1%
Rpc3L1bS	6.95 ± 0.16	7.02 ± 0.23	<1%
Rpc3LSS1b	0.00 ± 0.00	0.00 ± 0.00	-

2939 **Chapter 8**

2940 **Statistical Treatment**

2941 The goal of the analysis is to maximize the information that can be extracted from
2942 comparing the observed data to the background prediction in the signal regions
2943 designed to search for new physics topologies. Statistical tools are essential to
2944 tell in the most powerful way and to the best of our knowledge if there is a new
2945 physics signal beyond what is already known in the observed data. At the same
2946 time, it is important to properly treat the systematic uncertainties associated
2947 with the complexity of the experimental apparatus (ATLAS detector) and the
2948 background predictions when presenting an interpretation of the results. This
2949 chapter describes the statistical methodology employed to test the compatibility
2950 between data and prediction while taking into account the systematic uncertainties.

2951 The analysis' possible outcomes are represented by a likelihood function that
2952 combines observations, predictions, and associated uncertainties. At which point
2953 the hypothesis testing is performed with the corresponding one-sided profile
2954 likelihood ratio [101], and upper limits are provided as one-sided 95% confidence
2955 level intervals in the CL_s formalism [102]. The statistical tool used to perform the
2956 quantification of the significance of hypothetical excesses seen in data or upper
2957 limits setting on new physics contributions as implemented in this analysis will
2958 be described in this chapter.

2959 8.1 Likelihood Function

2960 The likelihood for a set of parameters $(\mu, \boldsymbol{\theta})$ given all the data that might have
 2961 been observed \mathbf{X} is the probability of observing the data given the parameters

$$\mathcal{L}(\mu, \boldsymbol{\theta} | \mathbf{X}) = \Pr(\mathbf{X} | \mu, \boldsymbol{\theta}). \quad (8.1)$$

2962 The data \mathbf{X} includes observation in the signal regions as well as other auxiliary
 2963 experiments such as control regions used to constrain backgrounds. In this analysis,
 2964 hypothesis tests are performed on one signal region at the time, single-binned, and
 2965 without control regions. As a result, the observed data \mathbf{X} has a one-dimensional
 2966 component with value X representing the count of events in the signal region.

2967 The first parameter of interest represents the ‘strength’ of the signal process $\mu > 0$
 2968 that will increase the number of expected events in the signal region given that the
 2969 signal of the new physics model tested is present. In practice, the signal strength
 2970 μ is used to scale the nominal expected cross section for the signal process, or the
 2971 number of expected signal events s . Thus, the predicted background will be of
 2972 the form $\mu s + \sum_i b_i$ where b_i represents the standard model background processes
 2973 expected to contribute to the signal region. The parameter $\boldsymbol{\theta}$ refers to the nuisance
 2974 parameters used to parametrize the systematic uncertainties (luminosity, JES,
 2975 JER, etc.) ¹. Thus, the likelihood is built as the product of a Poisson probability
 2976 density function describing the observed number of events in the signal region and
 2977 Gaussian distributions for each of the sources of systematic uncertainties. The

¹The parameters represented by $\boldsymbol{\theta}$ are called nuisance parameters since the aim is not to set a limit on them.

2978 likelihood takes the simple form

$$\Pr(X, \boldsymbol{\theta}^0 | \mu, \boldsymbol{\theta}) = \mathcal{P}\left(X \mid \mu s(\boldsymbol{\theta}) + \sum_i b_i(\boldsymbol{\theta})\right) \times \prod_j \mathcal{G}(\theta^0 | \theta_j) \quad (8.2)$$

2979 where $\mathcal{P}(X | \nu) = e^{-\nu} \nu^X / X!$ and $\mathcal{G}(\theta) = \frac{1}{\sqrt{2\pi\sigma_\theta^2}} e^{-\frac{(\theta-\theta^0)^2}{2\sigma_\theta^2}}$ are the Poisson and
2980 Gaussian probability density functions. Both signal and backgrounds depend on
2981 the nuisance parameter $\boldsymbol{\theta}$ which controls all independent sources of uncertainty and
2982 will be *profiled* (or constrained) in the CL_s procedure described next. Correlations
2983 of a given nuisance parameter between the different sources of backgrounds and the
2984 signal are taken into account when relevant. To give an example, the luminosity
2985 uncertainty will have a mean as the luminosity central value $\theta_{\text{lumi}}^{(0)}$ and the width as
2986 an experimentally determined uncertainty $\sigma_{\theta_{\text{lumi}}}$. When evaluating the effect of the
2987 luminosity uncertainty on the likelihood function, all terms involving the nuisance
2988 parameter θ_{lumi} will be scaled in the same way since luminosity is correlated across
2989 all backgrounds and signal.

2990 The likelihood function described in this section is used in a fit to data by the
2991 maximum likelihood method that aims at finding the value of the signal strength
2992 μ that makes the likelihood a maximum. The procedure relies on an iterative
2993 minimization algorithm implemented in MINUIT [103] and accessed by *RooFit*
2994 [104] within ROOT, a high energy physics data analysis framework [105]. The
2995 final uncertainties on the nuisance parameters in $\boldsymbol{\theta}$, constrained by the fit, are
2996 obtained from the covariance matrix of these parameters.

2997 8.2 Limit Setting Procedure

2998 8.2.1 Profile Likelihood Ratio

2999 The procedure for setting exclusion limits using the likelihood function (Eq.8.2)
 3000 relies on a profile-likelihood-ratio test [101]. The null hypothesis considered is
 3001 that of background only with $\mu = 0$ and the alternate hypothesis is the presence
 3002 of a signal with strength $\mu > 0$. According to the Neyman-Pearson Lemma [106],
 3003 the most powerful test when performing a hypothesis test between two simple
 3004 hypotheses, $\mu = 0$ and $\mu > 0$, is the profile-likelihood-ratio test, which rejects
 3005 $\mu = 0$ in favor of $\mu > 0$. The profile-likelihood-ratio test q_μ is defined to be

$$q_\mu(\mathbf{X}) = \begin{cases} -2 \ln \left(\frac{\mathcal{L}(\mu, \hat{\boldsymbol{\theta}}(\mu) | \mathbf{X})}{\mathcal{L}(\hat{\mu}, \hat{\boldsymbol{\theta}} | \mathbf{X})} \right), & \text{if } \mu > \hat{\mu} \\ 0, & \text{otherwise} \end{cases} \quad (8.3)$$

3006 For a given observation \mathbf{X} , the parameters $\hat{\mu}$ and $\boldsymbol{\theta}$ are obtained from maximizing
 3007 the likelihood. If the value of μ is also fixed, the set of values $\hat{\boldsymbol{\theta}}$ corresponds
 3008 to the set of values that maximize the likelihood for that particular value of μ .
 3009 The variable q_μ is always positive ($q_\mu \geq 0$). Qualitatively, small values of q_μ
 3010 correspond to a better compatibility between the observed data and the tested
 3011 hypothesis with a signal strength μ , while large values indicate a very improbable
 3012 signal hypothesis. The condition on the sign of $\mu - \hat{\mu}$ is necessary in order not to
 3013 interpret an upward fluctuation of data ($X > \mu s + b$) as incompatible with the
 3014 tested hypothesis. The form of q_μ is motivated by Wald and Wilk's [107, 108]
 3015 approximation formulas in the large sample limit where the distributions of q_μ also

³⁰¹⁶ become independent of nuisance parameters as it will be discussed next. The test
³⁰¹⁷ statistic for discovery will try to reject the background only hypothesis ($\mu = 0$).
³⁰¹⁸ Thus Eq.8.3 becomes

$$q_0(\mathbf{X}) = \begin{cases} -2 \ln \left(\frac{\mathcal{L}(0, \hat{\theta}(0) | \mathbf{X})}{\mathcal{L}(\hat{\mu}, \hat{\theta} | \mathbf{X})} \right), & \text{if } \hat{\mu} < 0 \\ 0, & \text{otherwise} \end{cases} \quad (8.4)$$

³⁰¹⁹ 8.2.2 The *p*-value

³⁰²⁰ At this stage, a test statistic q_μ has been constructed to distinguish between
³⁰²¹ the hypothesis that the data contains signal and background $\mu > 0$ and that of
³⁰²² background only $\mu = 0$. To illustrate the limit setting procedure, we consider
³⁰²³ distributions of the test statistic under each hypothesis: $f(q_\mu | \mu)$ for $\mu > 0$ and
³⁰²⁴ $f(q_0 | 0)$ for $\mu = 0$. These distributions are shown in Figure 8.1a and details on
³⁰²⁵ how to obtain their functional forms will be discussed later.

³⁰²⁶ Given that the actual observed data leads to a test variable $q_\mu^{(\text{obs})}$, it is possible
³⁰²⁷ to quantify the level of discrepancy between the observed data and the tested
³⁰²⁸ hypothesis ($\mu > 0$ or $\mu = 0$) using a *p*-value. The *p*-value of the signal hypothesis
³⁰²⁹ ($\mu > 0$) is then defined as the probability, under assumption of the signal hypothesis,
³⁰³⁰ to find a value of q_μ with equal or lesser compatibility with the signal model
³⁰³¹ considered relative to what is found with $q_\mu^{(\text{obs})}$. In other words, higher values of
³⁰³² q_μ indicate an increasing disagreement between data and the signal model. The
³⁰³³ mathematical expression of the *p*-value with $\mu > 0$ is taken as the probability to

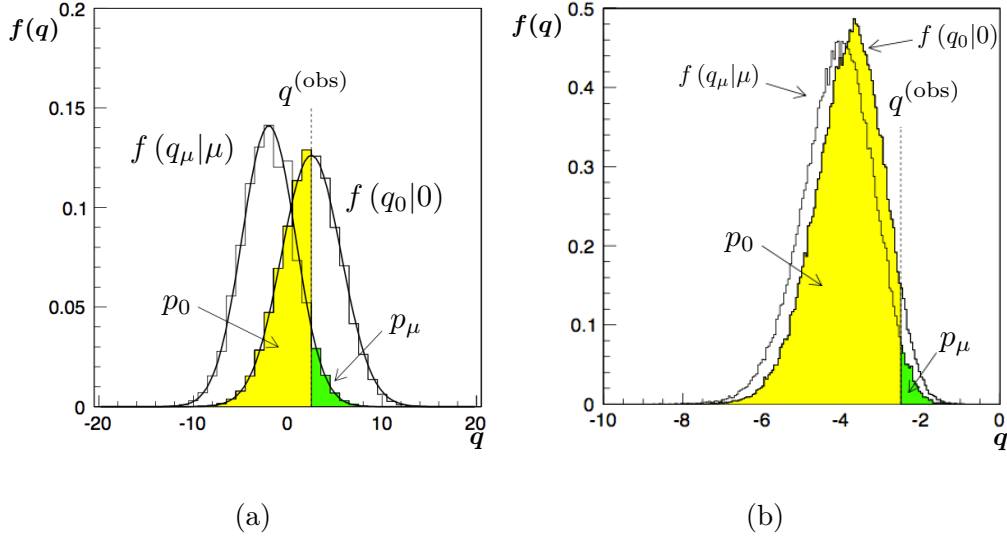


Figure 8.1: Distributions of the test variable q_μ under the $\mu > 0$ and $\mu = 0$ hypotheses: (a) typical case, (b) case where there is very little sensitivity to the signal model

3034 find q_μ greater than or equal $q_\mu^{(\text{obs})}$, under the signal hypothesis² is given by

$$p_\mu = \Pr(q_\mu \geq q_\mu^{(\text{obs})} | \mu) = \int_{q_\mu^{(\text{obs})}}^{\infty} f(q_\mu | \mu) dq_\mu \quad (8.5)$$

3035 where $q_\mu^{(\text{obs})}$ is the value of the statistic test observed in data and the function f

3036 denotes the probability distribution function of q_μ under the signal hypothesis.

3037 Similarly, the p -value of the background-only hypothesis with $\mu = 0$ takes the

3038 form of

$$p_0 = \Pr(q_0 \geq q_0^{(\text{obs})} | 0) = \int_{-\infty}^{q_0^{(\text{obs})}} f(q_0 | 0) dq_0 \quad (8.6)$$

3039 and can be interpreted as the probability of the observation to be consistent with

3040 the background only hypothesis: the smaller the p_0 value is, the less compatible

3041 data is with the background only hypothesis. In order to claim a discovery in

²Note that the background-only distribution $f(q_0 | 0)$ in the example given in Figure 8.1a is shifted to the right.

3042 particle physics, the background-only hypothesis must be rejected using the p_0 -
 3043 value. However, there is an ambiguity related to how small the p_0 -value needs to
 3044 be, before declaring a discovery. The problem can also be formulated in terms of
 3045 significance. Assuming a Gaussian distributed variable, how many Z standard
 3046 deviations σ above the mean are required to cover an upper-tail probability equal
 3047 to p expressed as

$$Z = \Phi^{-1} (1 - p) \quad (8.7)$$

3048 where Φ is the Gaussian cumulative distribution. The particle physics community
 3049 considers a discovery if $Z = 5$, commonly used “five sigma excess” statement,
 3050 which corresponds to $p_0 = 2.87 \times 10^{-7}$ or one in 3.5 million probability for the
 3051 background to be as extreme as the observation. In order to announce evidence
 3052 for a new particle, a significance of $Z = 3$ or $p_0 = 1.35 \times 10^{-3}$ is required.

3053 8.2.3 The CL_s Prescription

3054 The next step is to define a confidence interval (CI) that includes the parameter
 3055 μ at a specified confidence level (CL). In other words, instead of estimating the
 3056 parameter μ by a single value, an interval CI likely to include the parameter μ is
 3057 given. The CL provides a quantitative statement on how likely the interval CI is
 3058 to contain the parameter μ . Given the measurement of a parameter μ_{meas} , we
 3059 deduce that there is a 95% CI $[\mu_1, \mu_2]$. The statement means that in an ensemble
 3060 of experiments 95% of the obtained CIs will contain the true value of μ ³. The
 3061 upper limit is simply the case where the 95% CI is $[0, \mu_{up}]$: In an ensemble of

³The statement **does not** mean that there is a 95% probability that the interval $[\mu_1, \mu_2]$ contains the true value of the parameter μ .

3062 experiments 95% of the obtained *CIs* will contain the true value of μ , including
 3063 $\mu = 0$. The conclusion is that $\mu < \mu_{up}$ at the 95% *CL* or that μ_{up} is an upper
 3064 limit.

3065 Applying this concept to the problem at hand where we want to place an
 3066 upper limit on the expected number of signal events S ($S = \mu s$, s being the
 3067 expected number of signal events for $\mu = 1$) in one or more signal regions. The
 3068 *CL* is obtained from a standard statistical test of the signal model ($\mu > 0$) which
 3069 can establish the exclusion of the signal model at confidence level $1 - \alpha = 95\%$ if

$$CL_{s+b} = p_\mu < \alpha \quad (8.8)$$

3070 where $\alpha = 0.05$. Since the result section will present *CL* values in terms of the
 3071 expected number of signal events from beyond the standard model processes, we
 3072 continue this discussion of estimating an upper limit on S rather than μ . Thus, a
 3073 *CI* at confidence level $CL = 1 - \alpha$ for the expected number of signal events S can
 3074 be constructed from those values of S (or μ) that are not excluded, and the upper
 3075 limit $S_{up}^{1-\alpha}$ is the largest value of S not excluded. By construction, the interval
 3076 $[0, S_{up}^{95}]$ will cover the expected number of signal events S with a probability of at
 3077 least 95%, regardless of the value of S .

3078 An anomaly arises with the CL_{s+b} prescription when the number of expected
 3079 signal events is much less than that of the background and the data observation
 3080 had a downward fluctuation below the expected background. The procedure will
 3081 lead to excluding, with probability close to α , hypotheses to which the experiment
 3082 has no sensitivity. For $\alpha = 5\%$, it means that one out of twenty tests for different

3083 signal models where one has no sensitivity will result in exclusion. In fact, the
 3084 desired behavior of the exclusion probability in this case is to approach zero rather
 3085 than α . This scenario is illustrated in Figure 8.1b where the distribution of q_μ
 3086 under both the signal and background-only hypotheses are almost similar. To
 3087 remedy this problem, a different procedure is used where a model is regarded as
 3088 excluded if

$$CL_s = \frac{p_\mu}{1 - p_0} < \alpha. \quad (8.9)$$

3089 In this form, the p -value is penalized by dividing by $1 - p_0$. If the distribution of
 3090 q_μ under a signal or a background-only hypotheses are widely separated, then the
 3091 quantity $1 - p_0$ is close to unity which recovers the CL_{s+b} value. However, if the
 3092 distributions of both hypotheses are similar, due to the lack of sensitivity, $1 - p_0$
 3093 becomes smaller and the CL_{s+b} value is increased more leading to a weaker upper
 3094 limit. Similar to the case of CL_{s+b} , the upper limit on S_{up}^{95} is taken as the largest
 3095 value of the parameter S not excluded.

3096 8.2.4 Approximate Sampling Distributions

3097 The remaining task is to determine the sampling distributions $f(q_0|0)$ and $f(q_\mu|\mu)$
 3098 needed to compute the p -values used in the case of discovery and setting upper
 3099 limits, respectively. These distributions do not have an analytic form but can be
 3100 obtained from pseudo-experiments or asymptotic approximations. The pseudo-
 3101 experiments are more accurate than the asymptotic approximations since a large
 3102 number of datasets are generated which are drawn from a distribution that is
 3103 consistent with those observed. However, for a complex likelihood function where

3104 the procedure of generating pseudo-datasets needs to be repeated many times for
 3105 each parameter point of each model being considered, the pseudo-data set method
 3106 is computing intensive and not practical. For this reason, the current analysis
 3107 uses asymptotic formulae to approximate q_μ and shown to be valid in the large
 3108 sample size limit [101]. The approximation is based on an important result by
 3109 Wilks [107] and Wald [108] who showed that for a single parameter of interest,

$$q_\mu = \begin{cases} \frac{(\mu - \bar{\mu})^2}{\sigma^2} + \mathcal{O}\left(\frac{1}{\sqrt{N}}\right), & \text{if } \mu > \hat{\mu} \\ 0, & \text{otherwise.} \end{cases} \quad (8.10)$$

3110 where μ is a Gaussian distribution with a mean $\bar{\mu}$ and standard deviation σ ,
 3111 and a sample size N . In the case where $\mu = \hat{\mu}$, the test statistic q_μ follows a χ^2
 3112 distribution with one degree of freedom. The variance σ^2 is obtained from an
 3113 artificial data set called the “Asimov data set” ⁴ that verifies $X_A = \bar{\mu}s + b$. From
 3114 Eq.8.10, the variance is then $\sigma^2 = (\mu - \bar{\mu})^2/q_{\mu,A}$, where $q_{\mu,A}$ is evaluated from the
 3115 exact expression of q_μ using the Asimov data set.

3116 The results obtained from the asymptotic approximations have been compared
 3117 to exclusion limits obtained with a limited number of pseudo-experiments. A
 3118 reasonable agreement has been observed which validated the use of the asymptotic
 3119 formalism to obtain the exclusion limits on the different models.

⁴Inspired from the short story *Franchise*[109] by Isaac Asimov that entails replacing a single voter that represents the entire electorate population in an election. Similarly, an ensemble of pseudo-experiments can be replaced by a single representative data set.

3120 8.3 Statistical Implementation

3121 The statistical interpretations of the observations are performed with the **HistFitter**
 3122 framework [110], commonly in use within the SUSY ATLAS working group. It
 3123 consists of a user-friendly abstraction layer to the **HistFactory** and **RooFit**
 3124 frameworks [111, 112], to which it delegates the tasks of building a probabilistic
 3125 representation of the analysis, and performing hypothesis tests. **HistFitter** also
 3126 provides several related utilities, such as the creation of summary tables of yields
 3127 and uncertainties, or the creation of exclusion plots such as those presented in
 3128 Chapter 9.

3129 The likelihood function implemented in **HistFitter** is built as the product of
 3130 a Poisson probability density function describing the observed number of events
 3131 in the signal region and, to constrain the nuisance parameters associated with
 3132 the systematic uncertainties, Gaussian distributions whose widths correspond to
 3133 the sizes of these uncertainties; Poisson distributions are used instead for MC
 3134 simulation statistical uncertainties. Correlations of a given nuisance parameter
 3135 between the backgrounds and the signal are taken into account when relevant.
 3136 The hypothesis tests are performed for each of the signal regions independently.

³¹³⁷ **Chapter 9**

³¹³⁸ **Results and Interpretation**

³¹³⁹ **9.1 Predictions and Observations**

³¹⁴⁰ Observed data (36.1 fb^{-1}) and predicted SM backgrounds event yields are com-
³¹⁴¹ pared in Fig. 9.2 for signal regions addressing R -parity-conserving signal scenarios,
³¹⁴² for events satisfying the SR requirements except the E_T^{miss} cut. Adjustments to
³¹⁴³ the selections are made:

- SRs involving an effective mass cut: it is relaxed together with the E_T^{miss} cut to avoid indirectly tightening requirements on the visible leptonic and hadronic contributions to m_{eff} for low values of E_T^{miss} ; the m_{eff} requirement is therefore changed to:

$$m_{\text{eff}} > (m_{\text{eff}}^{\text{SR cut}}) - \max \left[(E_T^{\text{miss, SR cut}}) - E_T^{\text{miss}}, 0 \right]$$

- SRs involving a cut on the $E_T^{\text{miss}}/m_{\text{eff}}$ ratio: it is relaxed together with the E_T^{miss} cut to allow populating the low E_T^{miss} tail of the distributions:

$$\frac{E_T^{\text{miss}}}{m_{\text{eff}}} > \left(\frac{E_T^{\text{miss}}}{m_{\text{eff}}} \right)^{\text{SR cut}} \times \frac{E_T^{\text{miss}}}{\left(E_T^{\text{miss, SR cut}} \right)^{\text{SR cut}}}$$

³¹⁴⁴ in addition, an upper cut on m_{eff} is added.

³¹⁴⁵ Figure 9.3 shows the event yields for data and the expected background
³¹⁴⁶ contributions in all signal regions. Detailed information about the yields can be
³¹⁴⁷ found in Table 9.1. In all 13 SRs the number of observed data events is consistent
³¹⁴⁸ with the expected background within the uncertainties. The contributions listed

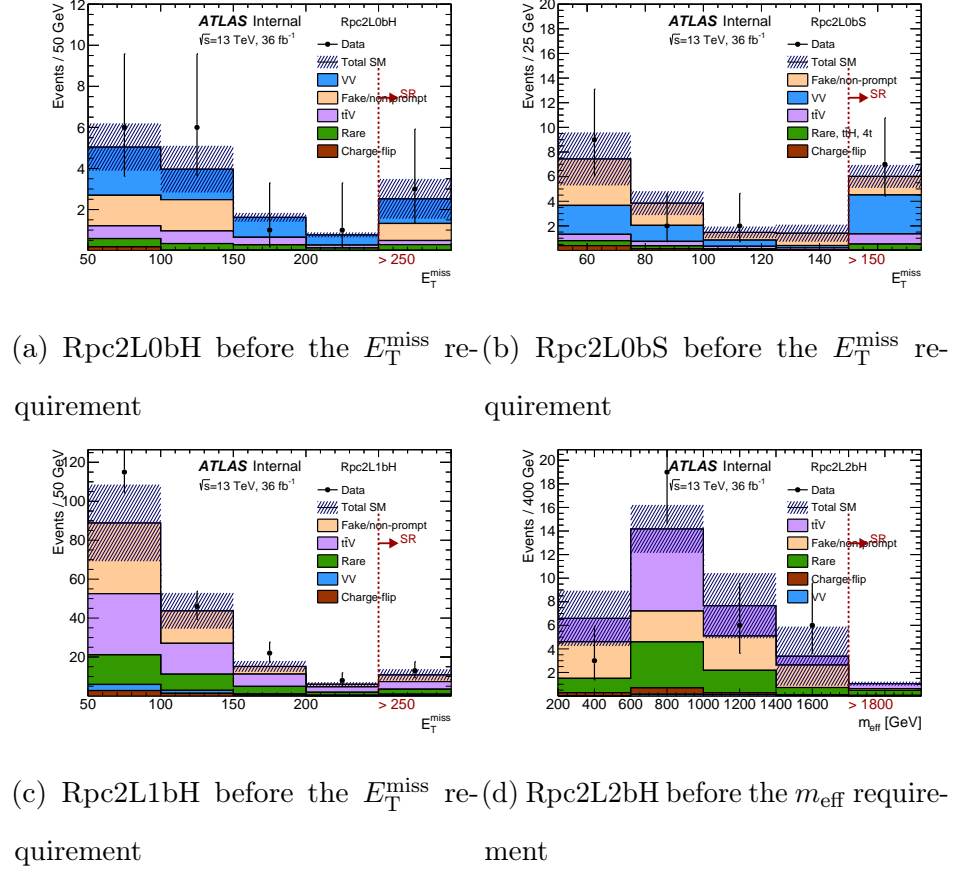


Figure 9.1: Missing transverse momentum distributions for observed data and predicted backgrounds with all the signal regions requirements, before the final E_T^{miss} . The effective mass and/or $E_T^{\text{miss}}/m_{\text{eff}}$ ratio cuts are also relaxed for E_T^{miss} values below the SR threshold (see text for details). The signal regions correspond to the last (inclusive) bins of the figures. The shaded area represents uncertainties on the total SM background estimate, which include all sources of statistical uncertainties, as well as the systematic uncertainties for fake lepton and charge-flip backgrounds.

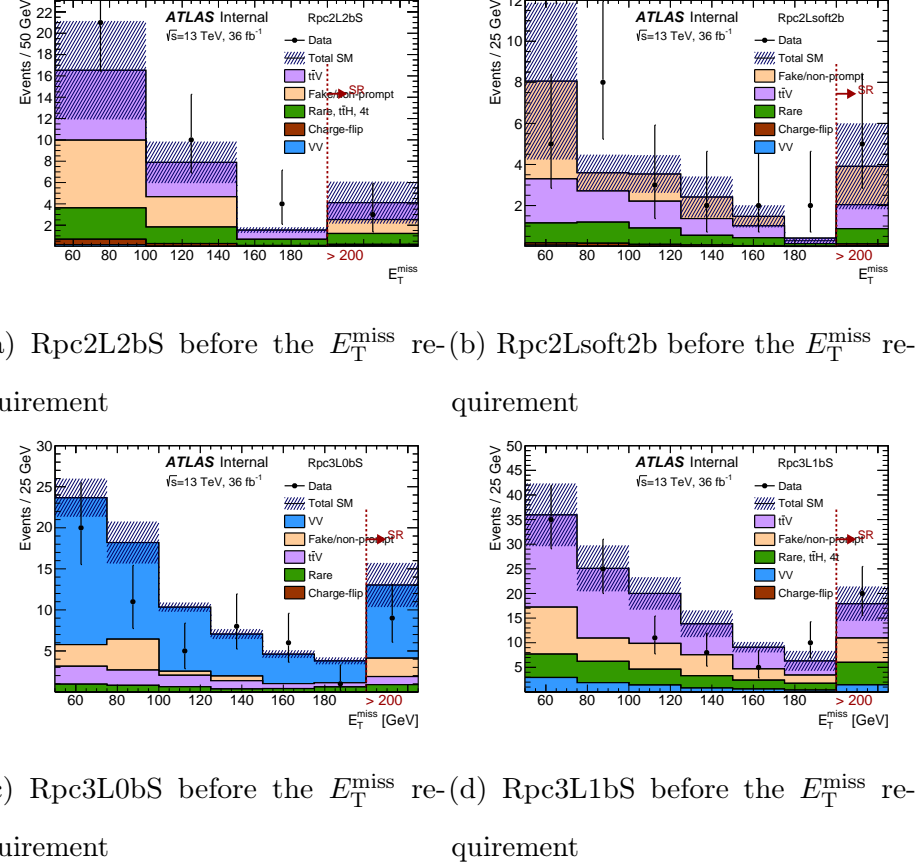


Figure 9.2: Missing transverse momentum distributions for observed data and predicted backgrounds with all the signal regions requirements, before the final E_T^{miss} . The effective mass and/or $E_T^{\text{miss}}/m_{\text{eff}}$ ratio cuts are also relaxed for E_T^{miss} values below the SR threshold (see text for details). The signal regions correspond to the last (inclusive) bins of the figures. The shaded area represents uncertainties on the total SM background estimate, which include all sources of statistical uncertainties, as well as the systematic uncertainties for fake lepton and charge-flip backgrounds.

3149 in the rare category are dominated by triboson, tWZ and $t\bar{t}WW$ production. The
 3150 triboson processes generally dominate in the SRs with no b -jets, while tWZ and
 3151 $t\bar{t}WW$ dominate in the SRs with one and two b -jets, respectively. Contributions
 3152 from WH , ZH , tZ and $t\bar{t}t$ production never represent more than 20% of the rare
 3153 background.

3154 Figure 9.3b summarizes the contributions from the different sources of sys-
 3155 tematic uncertainty to the total SM background predictions in the signal regions.
 3156 The uncertainties amount to 25–45% of the total background depending on the
 3157 signal region, dominated by systematic uncertainties coming from the reducible
 3158 background or the theory. The breakdown of the systematic uncertainties for each
 3159 signal region is given in Table 9.2

3160 9.2 Statistical Interpretation

3161 In the absence of any significant deviation from the standard model predictions,
 3162 the results will be interpreted to establish 95% confidence intervals using the
 3163 CL_s prescription [113] based on a profile-likelihood-ratio test [101] described in
 3164 Chapter 8. The interpretation will include upper limits on possible beyond the
 3165 standard model contributions to the signal regions in a model independent way,
 3166 as well as exclusion limits on the masses of SUSY particles in the benchmark
 3167 scenarios of Figure 5.1.

Signal Region	Rpc2L2bS	Rpc2L2bH	Rpc2Lsoft1b	Rpc2Lsoft2b	Rpc2L0bS	Rpc2L0bH
$t\bar{t}W, t\bar{t}Z\gamma^*$	1.6 ± 0.4	0.44 ± 0.14	1.3 ± 0.4	1.21 ± 0.33	0.82 ± 0.31	0.20 ± 0.10
$t\bar{t}H$	0.43 ± 0.25	0.10 ± 0.06	0.45 ± 0.24	0.36 ± 0.21	0.27 ± 0.15	0.08 ± 0.07
$4t$	0.26 ± 0.13	0.18 ± 0.09	0.09 ± 0.05	0.21 ± 0.11	0.01 ± 0.01	0.02 ± 0.02
Diboson	0.10 ± 0.10	0.04 ± 0.02	0.17 ± 0.09	0.05 ± 0.03	3.1 ± 1.4	1.0 ± 0.5
Rare	0.33 ± 0.18	0.15 ± 0.09	0.18 ± 0.10	0.17 ± 0.10	0.19 ± 0.11	0.17 ± 0.10
Fake/non-prompt leptons	0.5 ± 0.6	0.15 ± 0.15	3.5 ± 2.4	1.7 ± 1.5	1.6 ± 1.0	0.9 ± 0.9
Charge-flip	0.10 ± 0.01	0.02 ± 0.01	0.08 ± 0.02	0.08 ± 0.02	0.05 ± 0.01	0.01 ± 0.01
Total Background	3.3 ± 1.0	1.08 ± 0.32	5.8 ± 2.5	3.8 ± 1.6	6.0 ± 1.8	2.4 ± 1.0
Observed	3	0	4	5	7	3
S_{obs}^{95}	5.5	3.6	6.3	7.7	8.3	6.1
S_{exp}^{95}	$5.6^{+2.2}_{-1.5}$	$3.9^{+1.4}_{-0.4}$	$7.1^{+2.5}_{-1.5}$	$6.2^{+2.6}_{-1.5}$	$7.5^{+2.6}_{-1.8}$	$5.3^{+2.1}_{-1.3}$
$\sigma_{\text{vis}} [\text{fb}]$	0.15	0.10	0.17	0.21	0.23	0.17
$p_0 (Z)$	0.71 (-)	0.91 (-)	0.69 (-)	0.30 (0.5σ)	0.36 (0.4σ)	0.35 (0.4σ)

Signal Region	Rpc3L0bS	Rpc3L0bH	Rpc3L1bS	Rpc3L1bH	Rpc2L1bS	Rpc2L1bH	Rpc3LSS1b
$t\bar{t}W, t\bar{t}Z\gamma^*$	0.98 ± 0.25	0.18 ± 0.08	7.1 ± 1.1	1.54 ± 0.28	4.0 ± 1.0	4.0 ± 0.9	–
$t\bar{t}H$	0.12 ± 0.08	0.03 ± 0.02	1.4 ± 0.7	0.25 ± 0.14	1.3 ± 0.7	1.0 ± 0.6	0.22 ± 0.12
$4t$	0.02 ± 0.01	0.01 ± 0.01	0.7 ± 0.4	0.28 ± 0.15	0.34 ± 0.17	0.54 ± 0.28	–
Diboson	8.9 ± 2.9	2.6 ± 0.8	1.4 ± 0.5	0.48 ± 0.17	0.5 ± 0.3	0.7 ± 0.3	–
Rare	0.7 ± 0.4	0.29 ± 0.16	2.5 ± 1.3	0.9 ± 0.5	0.9 ± 0.5	1.0 ± 0.6	0.12 ± 0.07
Fake/non-prompt leptons	0.23 ± 0.23	0.15 ± 0.15	4.2 ± 3.1	0.5 ± 0.5	2.5 ± 2.2	2.3 ± 1.9	0.9 ± 0.7
Charge-flip	–	–	–	–	0.25 ± 0.04	0.25 ± 0.05	0.39 ± 0.08
Total Background	11.0 ± 3.0	3.3 ± 0.8	17 ± 4	3.9 ± 0.9	9.8 ± 2.9	9.8 ± 2.6	1.6 ± 0.8
Observed	9	3	20	4	14	13	1
S_{obs}^{95}	8.3	5.4	14.7	6.1	13.7	12.4	3.9
S_{exp}^{95}	$9.3^{+3.1}_{-2.3}$	$5.5^{+2.2}_{-1.5}$	$12.6^{+5.1}_{-3.4}$	$5.9^{+2.2}_{-1.8}$	$10.0^{+3.7}_{-2.6}$	$9.7^{+3.4}_{-2.6}$	$4.0^{+1.8}_{-0.3}$
$\sigma_{\text{vis}} [\text{fb}]$	0.23	0.15	0.41	0.17	0.38	0.34	0.11
$p_0 (Z)$	0.72 (-)	0.85 (-)	0.32 (0.5σ)	0.46 (0.1σ)	0.17 (1.0σ)	0.21 (0.8σ)	0.56 (-)

Table 9.1: Numbers of events observed in the signal regions compared with the expected backgrounds. The rare category is defined in the text. Background categories with yields shown as a “–” do not contribute to a given region (e.g. charge flips in three-lepton regions) or their estimates are below 0.01. The 95% confidence level (CL) upper limits are shown on the observed and expected numbers of BSM events, S_{obs}^{95} and S_{exp}^{95} (as well as the $\pm 1\sigma$ excursions from the expected limit), respectively. The 95% CL upper limits on the visible cross-section (σ_{vis}) are also given. Finally the p -values (p_0) give the probabilities of the observations being consistent with the estimated backgrounds. The number of equivalent Gaussian standard deviations (Z) is also shown when $p_0 < 0.5$.

Signal Region	Rpc2L2bS	Rpc2L2bH	Rpc2Lsoft1b	Rpc2Lsoft2b	Rpc2L0bS	Rpc2L0bH
Total background expectation	3.35	1.08	5.78	3.80	6.02	2.35
Total statistical	10.56%	15.67%	16.93%	15.61%	9.08%	20.87%
Total background systematic	30.41%	29.97%	43.10%	41.79%	30.51%	42.39%
Fake/non-prompt	15.46%	0.00%	38.39%	35.75%	13.46%	32.31%
Charge-flip	0.06%	0.00%	0.35%	0.53%	0.17%	0.00%
Jet Energy Scale	15.19%	11.37%	5.27%	9.28%	17.28%	8.11%
Other Jet Unc.	2.09%	2.71%	0.80%	0.99%	2.31%	3.42%
Flavor Tagging	6.27%	5.55%	0.81%	3.96%	3.33%	3.27%
Electrons	1.20%	1.72%	0.51%	0.51%	0.76%	0.74%
Muons	0.90%	1.39%	0.35%	0.51%	0.83%	0.93%
Missing transverse momentum	2.24%	1.68%	0.85%	1.50%	0.65%	0.54%
Diboson Th. Unc.	1.07%	1.39%	1.07%	0.50%	17.68%	13.54%
ttV Th. Unc.	7.33%	8.86%	5.01%	4.48%	4.06%	2.44%
Rare Th. Unc.	15.18%	19.67%	6.28%	9.75%	3.89%	5.87%
PDF	0.00%	0.00%	0.00%	0.00%	0.00%	0.00%

Signal Region	Rpc3L0bS	Rpc3L0bH	Rpc3L1bS	Rpc3L1bH	Rpc2L1bS	Rpc2L1bH	Rpc3LSS1b
Total background expectation	11.02	3.31	17.33	3.90	9.88	9.75	1.62
Total statistical	2.57%	6.05%	7.66%	7.70%	9.59%	6.65%	9.15%
Total background systematic	27.37%	25.40%	24.22%	24.02%	29.19%	26.52%	46.79%
Fake/non-prompt	1.63%	0.00%	16.50%	9.73%	19.93%	18.05%	44.45%
Charge-flip	0.00%	0.00%	0.00%	0.00%	0.40%	0.41%	4.32%
Jet Energy Scale	9.78%	8.98%	5.54%	4.20%	11.71%	10.40%	0.02%
Other Jet Unc.	3.41%	2.55%	0.70%	2.30%	1.42%	1.46%	0.20%
Flavor Tagging	2.79%	2.93%	2.22%	2.82%	1.32%	1.38%	0.32%
Electrons	1.78%	2.16%	1.66%	2.47%	0.67%	0.89%	0.41%
Muons	1.73%	2.12%	1.25%	1.79%	0.80%	0.92%	0.41%
Missing transverse momentum	0.78%	0.53%	0.38%	0.59%	1.70%	1.06%	0.00%
Diboson Th. Unc.	24.28%	21.58%	2.57%	3.78%	1.87%	2.50%	0.00%
ttV Th. Unc.	1.49%	1.76%	5.34%	5.56%	6.96%	5.72%	0.00%
Rare Th. Unc.	4.02%	5.02%	13.19%	18.11%	12.68%	13.16%	10.49%
PDF	0.00%	0.00%	0.00%	0.00%	0.00%	0.00%	0.00%

Table 9.2: Breakdown of the dominant systematic uncertainties on background estimates in the various signal regions. Note that the individual uncertainties can be correlated, and do not necessarily add up quadratically to the total background uncertainty. The percentages show the size of the uncertainty relative to the total expected background.

3168 9.2.1 Model independent discovery and upper limits

3169 Table 9.1 presents 95% confidence level (CL) observed (expected) model-independent
 3170 upper limits on the number of BSM events, S_{obs}^{95} (S_{exp}^{95}), that may contribute to
 3171 the signal regions. Normalizing these by the integrated luminosity L of the data
 3172 sample, they can be interpreted as upper limits on the visible BSM cross-section
 3173 (σ_{vis}), defined as $\sigma_{\text{vis}} = \sigma_{\text{prod}} \times A \times \epsilon = S_{\text{obs}}^{95}/L$, where σ_{prod} is the production
 3174 cross-section, A the acceptance and ϵ the reconstruction efficiency. The largest
 3175 deviation of the data from the background prediction corresponds to an excess of
 3176 1.0 standard deviation in the Rpc2L1bS SR.

3177 9.2.2 Model dependent exclusion limits

3178 Exclusion limits at 95% CL are set on the masses of the superpartners involved
 3179 in the SUSY benchmark scenarios considered. Apart from the NUHM2 model,
 3180 simplified models are used, corresponding to a single production mode and with
 3181 100% branching ratio to a specific decay chain, with the masses of the SUSY
 3182 particles not involved in the process set to very high values.

3183 In order to determine which signal region is used to set an exclusion limit on
 3184 a particular model, the expected CL_s value is computed for each signal region at
 3185 a given point in the signal parameter space. The signal region with the smallest
 3186 expected CL_s value (more disagreement with data under the signal hypothesis) is
 3187 used to set an exclusion limit on the model. An example on what signal region is
 3188 performing best at a given model using the decay is shown in Figure 9.4.

3189 Figures 9.6 and 9.8 show the exclusion limits in all the models considered
 3190 in Figure 5.1 and the NUHM2 model. The assumptions about the decay chain
 3191 considered for the different SUSY particles are stated above each figure. For each
 3192 region of the signal parameter space, the SR with the best expected sensitivity is
 3193 chosen.

3194 Each one of the Figures 9.6 contain:

- 3195 • Observed limit (thick solid red line): all uncertainties are included in the
 3196 fit as nuisance parameters, with the exception of the theoretical signal
 3197 uncertainties (PDF, scales) on the inclusive cross section.
- 3198 • Expected limit (less thick long-dashed black line): all uncertainties are in-
 3199 cluded in the fit as nuisance parameters, with the exception of the theoretical
 3200 signal uncertainties (PDF, scales) on the inclusive cross section.
- 3201 • $\pm 1\sigma$ lines around the observed limit (thin dark-red dotted): re-run limit
 3202 calculation while increasing or decreasing the signal cross section by the
 3203 theoretical signal uncertainties (PDF, scales).
- 3204 • $\pm 1\sigma$ band around expected limit (yellow band): represents the $\pm 1\sigma$ uncer-
 3205 tainty from the fit.

3206 The limits set are compared with the existing limits set by other ATLAS
 3207 SUSY searches [116, 117]. For the models shown in Figure 9.6, the mass limits on
 3208 gluinos and bottom squarks are up to 400GeV higher than the previous limits,
 3209 reflecting the improvements in the signal region definitions as well as the increase

3210 in integrated luminosity. Gluinos with masses up to 1.75 TeV are excluded in
 3211 scenarios with a light $\tilde{\chi}_1^0$ in Figure 9.5a. This limit is extended to 1.87 TeV when
 3212 $\tilde{\chi}_2^0$ and slepton masses are in between the gluino and the $\tilde{\chi}_1^0$ masses (Figure 9.6b).
 3213 More generally, gluino masses below 1.57 TeV and bottom squarks with masses
 3214 below 700 GeV are excluded in models with a massless LSP. The “compressed”
 3215 regions, where SUSY particle masses are close to each other, are also better
 3216 covered and LSP masses up to 1200 and 250 GeV are excluded in the gluino and
 3217 bottom squark pair-production models, respectively. Of particular interest is the
 3218 observed exclusion of models producing gluino pairs with an off-shell top quark in
 3219 the decay (Figure 5.1b), see Figure 9.5a. In this case, models are excluded for
 3220 mass differences between the gluino and neutralino of 205 GeV (only 35 GeV
 3221 larger than the minimum mass difference for decays into two on-shell W bosons
 3222 and two b -quarks) for a gluino mass below 0.9 TeV. The Rpc3LSS1b SR allows
 3223 the exclusion of top squarks with masses below 700 GeV when the top squark
 3224 decays to a top quark and a cascade of electroweakinos $\tilde{\chi}_2^0 \rightarrow \tilde{\chi}_1^\pm W^\mp \rightarrow W^* W^\mp \tilde{\chi}_1^0$
 3225 (see Figure 9.7b for the conditions on the sparticle masses).

3226 Finally, in the NUHM2 model with low fine-tuning, values of the param-
 3227 eter $m_{1/2}$ below 615 GeV are excluded, corresponding to gluino masses below
 3228 1500 GeV (Figure 9.8).

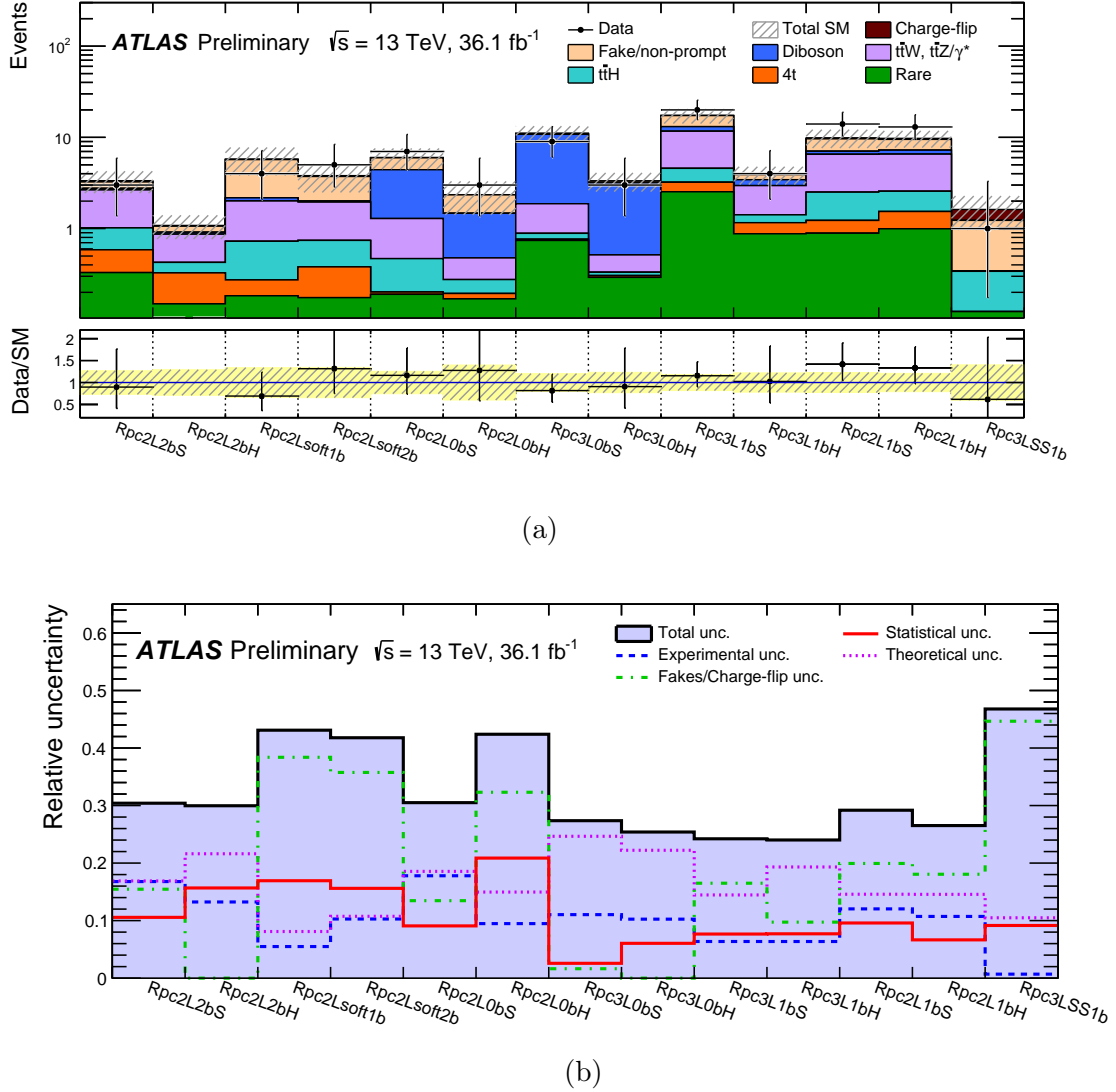


Figure 9.3: Comparison of (a) the observed and expected event yields in each signal region and (b) the relative uncertainties in the total background yield estimate. For the latter, “statistical uncertainty” corresponds to reducible and irreducible background statistical uncertainties. The background predictions correspond to those presented in Table 9.1 and the rare category is explained in the text.

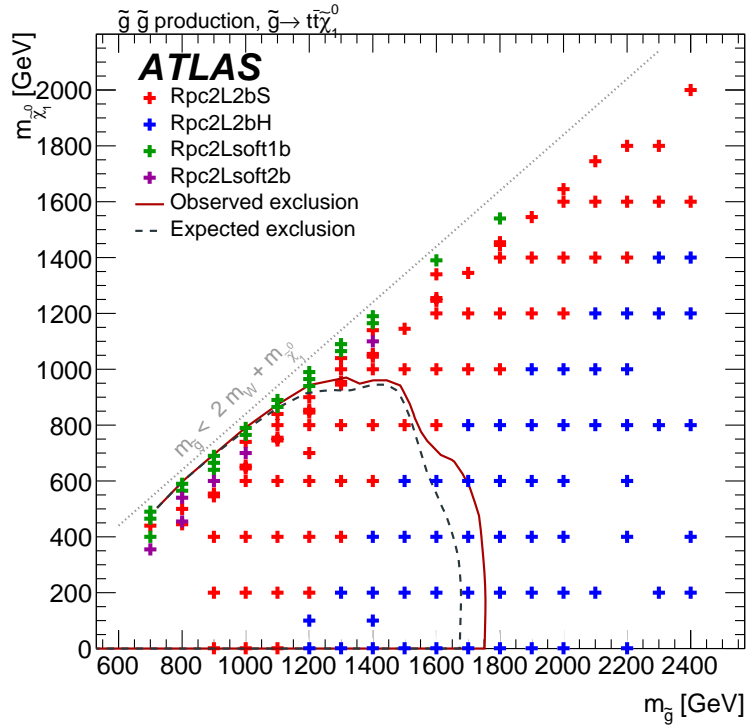


Figure 9.4: Illustration of the best expected signal region per signal grid point for the $\tilde{g} \rightarrow t\bar{t}\tilde{\chi}_1^0$ (Fig. 5.1a) model. This mapping is used for the final combined exclusion limits.

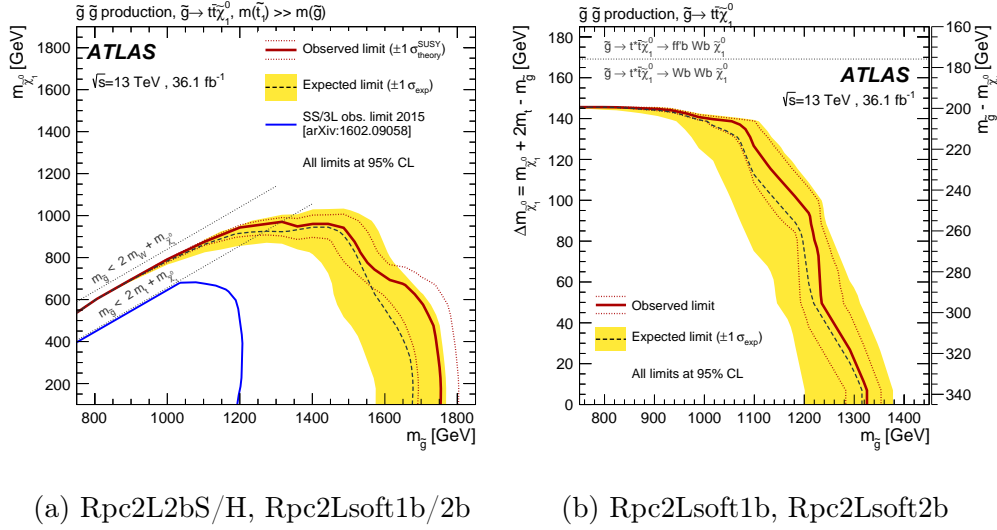


Figure 9.5: Observed and expected exclusion limits on the \tilde{g} and $\tilde{\chi}_1^0$ masses for (a) the model in Figure 5.1a and (b) the model in Figure 5.1b. Figure (b) is a zoomed version of Figure (a) in the mass-parameter space where there is at least one top-quark off-shell decay. All limits are computed at 95% CL. The dotted lines around the observed limit illustrate the change in the observed limit as the nominal signal cross-section is scaled up and down by the theoretical uncertainty. The contours of the band around the expected limit are the $\pm 1\sigma$ results, including all uncertainties except the theoretical ones in the signal cross-section.

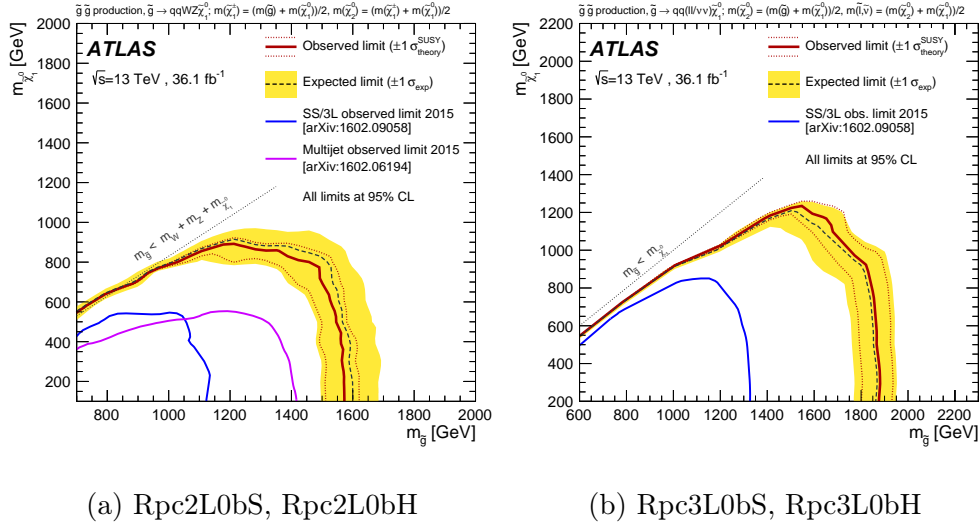
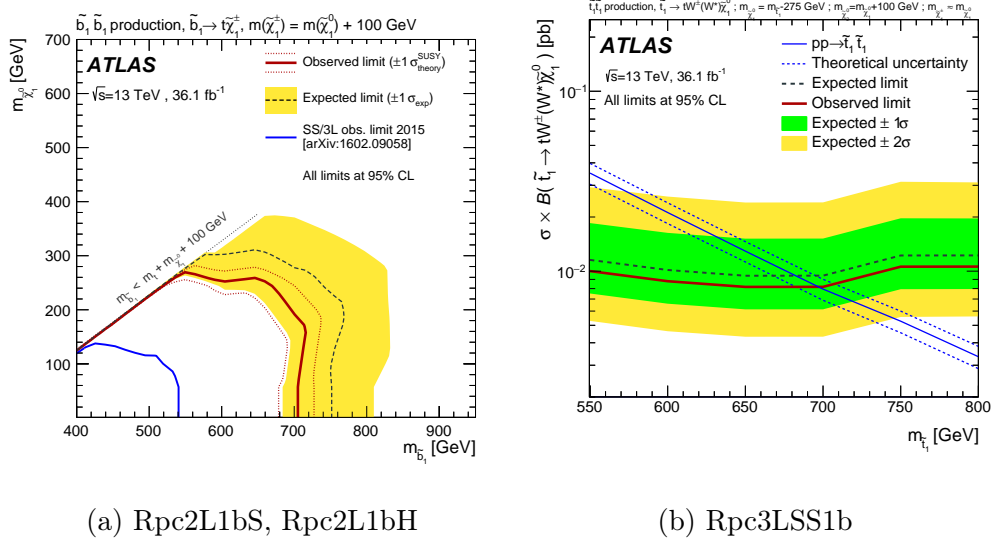


Figure 9.6: Observed and expected exclusion limits on the \tilde{g} and $\tilde{\chi}_1^0$ masses for (a) the model in Figure 5.1c and (b) the model in Figure 5.1d. All limits are computed at 95% CL. The dotted lines around the observed limit illustrate the change in the observed limit as the nominal signal cross-section is scaled up and down by the theoretical uncertainty. The contours of the band around the expected limit are the $\pm 1\sigma$ results, including all uncertainties except the theoretical ones in the signal cross-section.



(a) Rpc2L1bS, Rpc2L1bH

(b) Rpc3LSS1b

Figure 9.7: Observed and expected exclusion limits on the \tilde{b}_1 , \tilde{t}_1 , and $\tilde{\chi}_1^0$ masses for (a) the model in Figure 5.1e and (b) the model in Figure 5.1f. The two models are complementary where the one-dimensional change in stop masses (b) is along the grayed diagonal in the sbottom plot (b). All limits are computed at 95% CL. The dotted lines around the observed limit illustrate the change in the observed limit as the nominal signal cross-section is scaled up and down by the theoretical uncertainty. The contours of the band around the expected limit are the $\pm 1\sigma$ results ($\pm 2\sigma$ is also considered in (b)), including all uncertainties except the theoretical ones in the signal cross-section.

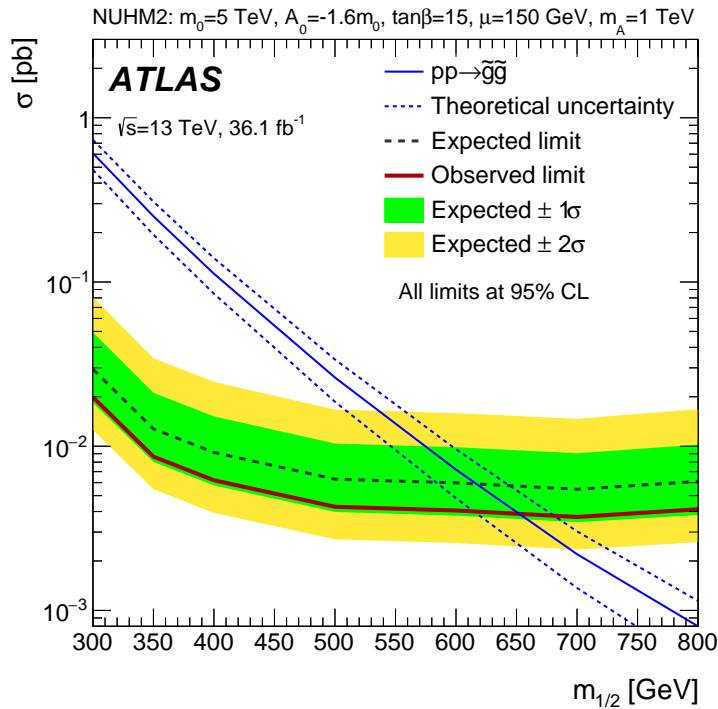


Figure 9.8: Observed and expected exclusion limits as a function of $m_{1/2}$ in the NUHM2 model [114, 115]. The signal region Rpc2L2bH is used to obtain the limits. The contours of the green (yellow) band around the expected limit are the $\pm 1\sigma$ ($\pm 2\sigma$) results, including all uncertainties. The limits are computed at 95% CL.

³²²⁹ **Chapter 10**

³²³⁰ **Conclusions**

³²³¹ A search for supersymmetry in events with two same-sign leptons or at least
³²³² three leptons, multiple jets, b -jets and large E_T^{miss} and/or large m_{eff} is presented.
³²³³ The analysis is performed with proton–proton collision data at $\sqrt{s} = 13\text{TeV}$
³²³⁴ collected in 2015 and 2016 with the ATLAS detector at the Large Hadron Collider
³²³⁵ corresponding to an integrated luminosity of 36.1 fb^{-1} . With no significant
³²³⁶ excess over the Standard Model prediction observed, results are interpreted in
³²³⁷ the framework of simplified models featuring gluino and squark production in
³²³⁸ R -parity-conserving scenarios. Lower limits on particle masses are derived at 95%
³²³⁹ confidence level. In the $\tilde{g}\tilde{g}$ simplified RPC models considered, gluinos with masses
³²⁴⁰ up to 1.87 TeV are excluded in scenarios with a light $\tilde{\chi}_1^0$. RPC models with bottom
³²⁴¹ squark masses below 700 GeV are also excluded in a $\tilde{b}_1\tilde{b}_1^*$ simplified model with
³²⁴² $\tilde{b}_1 \rightarrow tW^-\tilde{\chi}_1^0$ and a light $\tilde{\chi}_1^0$. All models with gluino masses below 1.3 TeV are
³²⁴³ excluded, greatly extending the previous exclusion limits. Model-independent
³²⁴⁴ limits on the cross-section of a possible signal contribution to the signal regions
³²⁴⁵ are set.

³²⁴⁶ **Appendix A**

³²⁴⁷ **Auxiliary material**

³²⁴⁸ **A.1 Signal region with best exclusion**

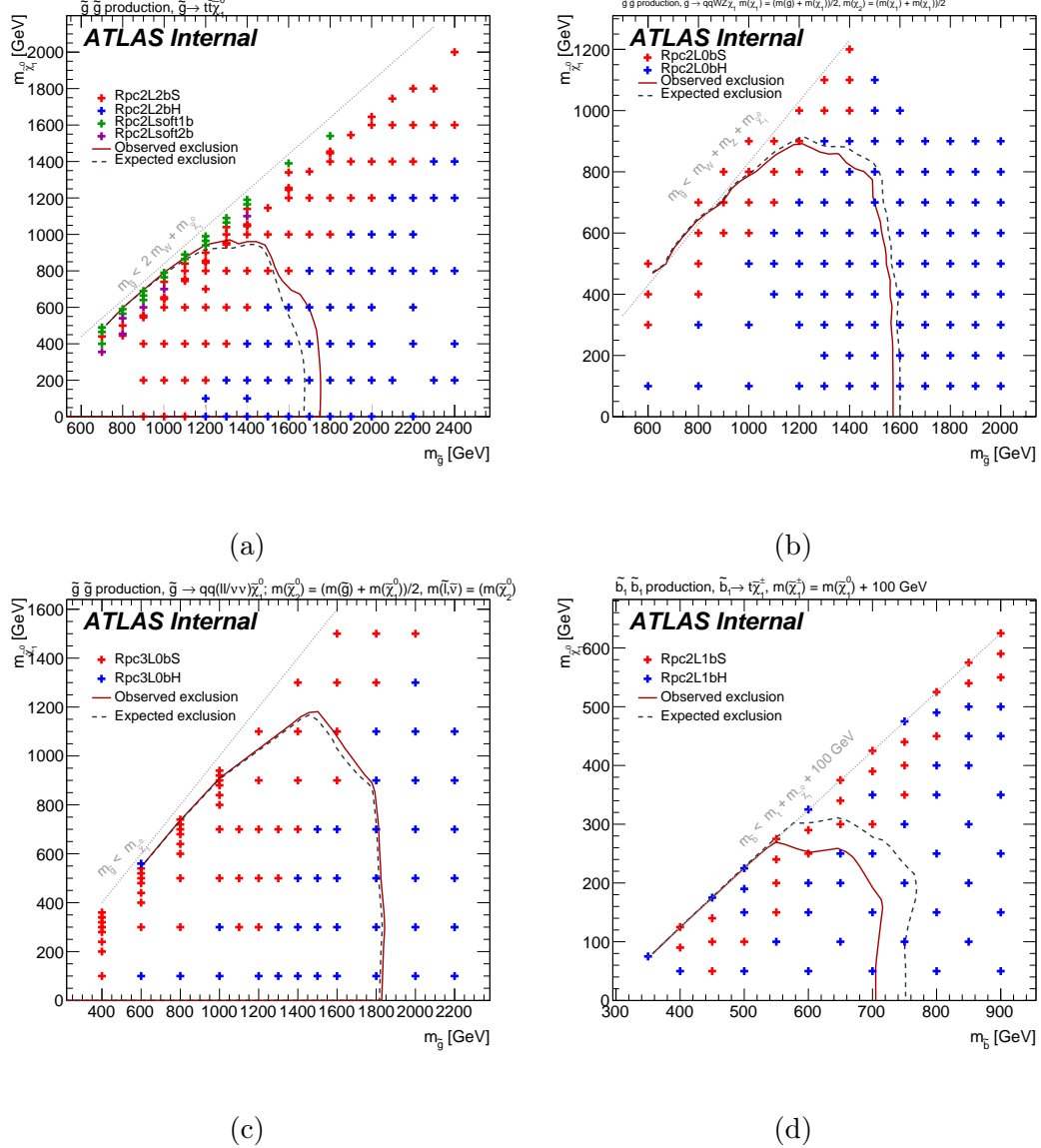


Figure A.1: Illustration of the best expected signal region per signal grid point for the $\tilde{g} \rightarrow q\bar{q}(\ell\ell/\nu\nu)\tilde{\chi}_1^0$ (Fig. 5.1a), $\tilde{g} \rightarrow q\bar{q}'WZ\tilde{\chi}_1^0$ (Fig. 5.1c), $\tilde{g} \rightarrow q\bar{q}'\ell/\nu\ell/\nu\tilde{\chi}_1^0$ (Fig. 5.1d), $\tilde{b} \rightarrow tW\tilde{\chi}_1^0$ (Fig. 5.1e) models. This mapping is used for the final combined exclusion limits.

3249 A.2 Upper limit on cross section

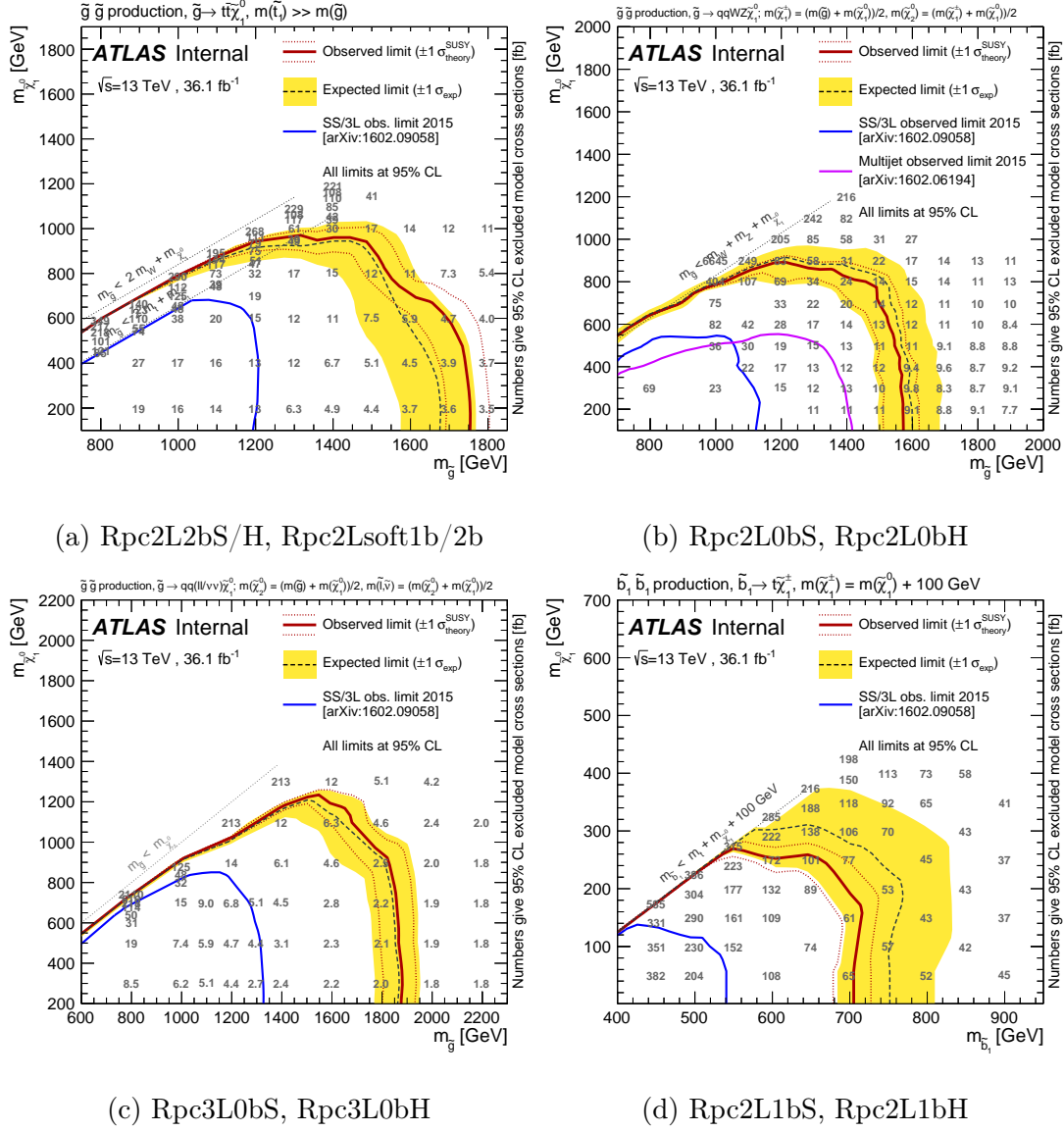


Figure A.2: Observed and expected exclusion limits on the \tilde{g} , \tilde{b}_1 , and $\tilde{\chi}_1^0$ masses in the context of RPC SUSY scenarios with simplified mass spectra. The signal regions used to obtain the limits are specified in the subtitle of each scenario. All limits are computed at 95% CL. The grey numbers show 95% CL upper limits on production cross-sections (in fb) obtained using the signal efficiency and acceptance specific to each model.

3250 **A.3 Signal region cutflow**

Rpc2L2bS, $\tilde{g}\tilde{g}$ production, $\tilde{g} \rightarrow t\bar{t}\tilde{\chi}_1^0$ $m_{\tilde{g}} = 1.5\text{TeV}$, $m_{\tilde{\chi}_1^0} = 800\text{GeV}$	
MC events generated	98000
Expected for 36.1 fb^{-1}	5.1×10^2
≥ 2 SS leptons ($p_T > 20\text{GeV}$)	19.96 ± 0.35
Trigger	19.17 ± 0.35
≥ 2 b -jets ($p_T > 20\text{GeV}$)	16.10 ± 0.32
≥ 6 jets ($p_T > 25\text{GeV}$)	13.11 ± 0.28
$E_T^{\text{miss}} > 200\text{GeV}$	10.17 ± 0.26
$m_{\text{eff}} > 0.6\text{TeV}$	10.17 ± 0.26
$E_T^{\text{miss}} > 0.25 \times m_{\text{eff}}$	5.94 ± 0.20

Table A.1: Number of signal events at different stages of the Rpc2L2bS signal region selection. Only statistical uncertainties are shown.

3251 **A.4 Acceptance and Efficiency**

Rpc2L2bH, $\tilde{g}\tilde{g}$ production, $\tilde{g} \rightarrow t\bar{t}\tilde{\chi}_1^0$ $m_{\tilde{g}} = 1.7\text{TeV}$, $m_{\tilde{\chi}_1^0} = 200\text{GeV}$	
MC events generated	98000
Expected for 36.1 fb^{-1}	1.7×10^2
≥ 2 SS leptons ($p_T > 20\text{GeV}$)	7.32 ± 0.13
Trigger	7.19 ± 0.13
≥ 2 b -jets ($p_T > 20\text{GeV}$)	5.81 ± 0.11
≥ 6 jets ($p_T > 40\text{GeV}$)	4.92 ± 0.11
$m_{\text{eff}} > 1.8\text{TeV}$	3.93 ± 0.09
$E_T^{\text{miss}} > 0.15 \times m_{\text{eff}}$	3.12 ± 0.08

Table A.2: Number of signal events at different stages of the Rpc2L2bH signal region selection. Only statistical uncertainties are shown.

Rpc2Lsoft1b, $\tilde{g}\tilde{g}$ production, $\tilde{g} \rightarrow tWb\tilde{\chi}_1^0$	
$m_{\tilde{g}} = 1.2\text{TeV}, m_{\tilde{\chi}_1^0} = 940\text{GeV}$	
MC events generated	50000
Expected for 36.1 fb^{-1}	3.1×10^3
≥ 2 SS leptons ($100 > p_T > 20, 10 \text{ GeV}$)	101.9 ± 2.7
Trigger	89.3 ± 2.5
≥ 1 b -jet ($p_T > 20\text{GeV}$)	75.1 ± 2.3
≥ 6 jets ($p_T > 25\text{GeV}$)	31.5 ± 1.5
$E_T^{\text{miss}} > 100\text{GeV}$	23.0 ± 1.3
$E_T^{\text{miss}} > 0.3 \times m_{\text{eff}}$	6.5 ± 0.7

Table A.3: Number of signal events at different stages of the Rpc2Lsoft1b signal region selection. Only statistical uncertainties are shown.

Rpc2Lsoft2b, $\tilde{g}\tilde{g}$ production, $\tilde{g} \rightarrow tWb\tilde{\chi}_1^0$ $m_{\tilde{g}} = 1.2\text{TeV}$, $m_{\tilde{\chi}_1^0} = 900\text{GeV}$	
MC events generated	50000
Expected for 36.1 fb^{-1}	3.1×10^3
≥ 2 SS leptons ($100 > p_T > 20, 10 \text{ GeV}$)	91.8 ± 2.6
Trigger	79.7 ± 2.4
≥ 2 b -jets ($p_T > 20\text{GeV}$)	41.3 ± 1.7
≥ 6 jets ($p_T > 25\text{GeV}$)	21.4 ± 1.2
$E_T^{\text{miss}} > 200\text{GeV}$	8.7 ± 0.7
$m_{\text{eff}} > 0.6\text{TeV}$	8.7 ± 0.7
$E_T^{\text{miss}} > 0.25 \times m_{\text{eff}}$	6.7 ± 0.6

Table A.4: Number of signal events at different stages of the Rpc2Lsoft2b signal region selection. Only statistical uncertainties are shown.

Rpc2L0bS, $\tilde{g}\tilde{g}$ production, $\tilde{g} \rightarrow q\bar{q}'WZ\tilde{\chi}_1^0$ $m_{\tilde{g}} = 1.2\text{TeV}$, $(m_{\tilde{\chi}_1^\pm} - 150) = (m_{\tilde{\chi}_2^0} - 75) = m_{\tilde{\chi}_1^0} = 900\text{GeV}$	
MC events generated	19000
Expected for 36.1 fb^{-1}	3.1×10^3
≥ 2 SS leptons ($p_T > 20\text{GeV}$)	64 ± 4
Trigger	58.6 ± 3.3
no b -jet ($p_T > 20\text{GeV}$)	46.3 ± 3.0
≥ 6 jets ($p_T > 25\text{GeV}$)	26.6 ± 2.4
$E_T^{\text{miss}} > 150\text{GeV}$	16.3 ± 2.0
$E_T^{\text{miss}} > 0.25 \times m_{\text{eff}}$	9.0 ± 1.3

Table A.5: Number of signal events at different stages of the Rpc2L0bS signal region selection. Only statistical uncertainties are shown.

Rpc2L0bH, $\tilde{g}\tilde{g}$ production, $\tilde{g} \rightarrow q\bar{q}'WZ\tilde{\chi}_1^0$ $m_{\tilde{g}} = 1.6\text{TeV}$, $(m_{\tilde{\chi}_1^\pm} - 750) = (m_{\tilde{\chi}_2^0} - 375) = m_{\tilde{\chi}_1^0} = 100\text{GeV}$	
MC events generated	20000
Expected for 36.1 fb^{-1}	2.9×10^2
≥ 2 SS leptons ($p_T > 20\text{GeV}$)	12.8 ± 0.5
Trigger	12.5 ± 0.5
no b -jet ($p_T > 20\text{GeV}$)	8.5 ± 0.4
≥ 6 jets ($p_T > 40\text{GeV}$)	7.12 ± 0.35
$E_T^{\text{miss}} > 250\text{GeV}$	5.13 ± 0.29
$m_{\text{eff}} > 0.9\text{TeV}$	5.13 ± 0.29

Table A.6: Number of signal events at different stages of the Rpc2L0bH signal region selection. Only statistical uncertainties are shown.

Rpc3L0bS, $\tilde{g}\tilde{g}$ production, $\tilde{g} \rightarrow q\bar{q}(\tilde{\ell}\ell/\tilde{\nu}\nu)$ $m_{\tilde{g}} = 1.4\text{TeV}$, $(m_{\tilde{\chi}_2^0} - 150) = (m_{\tilde{\ell},\tilde{\nu}} - 75) = m_{\tilde{\chi}_1^0} = 1100\text{GeV}$	
MC events generated	20000
Expected for 36.1 fb^{-1}	9.1×10^2
≥ 3 leptons ($p_T > 20, 20, 10$ GeV)	76.9 ± 2.1
Trigger	76.0 ± 2.0
no b -jet ($p_T > 20\text{GeV}$)	67.5 ± 1.9
≥ 4 jets ($p_T > 40\text{GeV}$)	31.6 ± 1.3
$E_T^{\text{miss}} > 200\text{GeV}$	17.1 ± 1.0
$m_{\text{eff}} > 0.6\text{TeV}$	17.1 ± 1.0

Table A.7: Number of signal events at different stages of the Rpc3L0bS signal region selection. Only statistical uncertainties are shown.

Rpc3L0bH, $\tilde{g}\tilde{g}$ production, $\tilde{g} \rightarrow q\bar{q}(\tilde{\ell}\ell/\tilde{\nu}\nu)$ $m_{\tilde{g}} = 1.8\text{TeV}$, $(m_{\tilde{\chi}_2^0} - 850) = (m_{\tilde{\ell},\tilde{\nu}} - 375) = m_{\tilde{\chi}_1^0} = 100\text{GeV}$	
MC events generated	20000
Expected for 36.1 fb^{-1}	1.0×10^2
≥ 3 leptons ($p_T > 20, 20, 10\text{ GeV}$)	9.98 ± 0.25
Trigger	9.94 ± 0.25
no b -jet ($p_T > 20\text{GeV}$)	8.44 ± 0.23
≥ 4 jets ($p_T > 40\text{GeV}$)	7.79 ± 0.22
$E_T^{\text{miss}} > 200\text{GeV}$	6.58 ± 0.21
$m_{\text{eff}} > 1.6\text{TeV}$	6.56 ± 0.21

Table A.8: Number of signal events at different stages of the Rpc3L0bH signal region selection. Only statistical uncertainties are shown.

Rpc2L1bS, $\tilde{b}_1 \tilde{b}_1^*$ production, $\tilde{b}_1 \rightarrow t \tilde{\chi}_1^- \rightarrow tW^- \tilde{\chi}_1^0$ $m_{\tilde{b}_1} = 600\text{GeV}$, $m_{\tilde{\chi}_1^\pm} = 350\text{GeV}$, $m_{\tilde{\chi}_1^0} = 250\text{GeV}$	
MC events generated	10000
Expected for 36.1 fb^{-1}	6.3×10^3
≥ 2 SS leptons ($p_T > 20\text{GeV}$)	221 ± 4
Trigger	201 ± 4
≥ 1 b -jet ($p_T > 20\text{GeV}$)	173 ± 4
≥ 6 jets ($p_T > 25\text{GeV}$)	66.3 ± 2.2
$E_T^{\text{miss}} > 150\text{GeV}$	36.5 ± 1.7
$m_{\text{eff}} > 0.6\text{TeV}$	36.1 ± 1.7
$E_T^{\text{miss}} > 0.25 \times m_{\text{eff}}$	15.1 ± 1.1

Table A.9: Number of signal events at different stages of the Rpc2L1bS signal region selection. Only statistical uncertainties are shown.

Rpc2L1bH, $\tilde{b}_1 \tilde{b}_1^*$ production, $\tilde{b}_1 \rightarrow t \tilde{\chi}_1^-$	
$m_{\tilde{b}_1} = 750\text{GeV}$, $m_{\tilde{\chi}_1^\pm} = 200\text{GeV}$, $m_{\tilde{\chi}_1^0} = 100\text{GeV}$	
MC events generated	10000
Expected for 36.1 fb^{-1}	1.6×10^3
≥ 2 SS leptons ($p_T > 20\text{GeV}$)	71.1 ± 1.2
Trigger	66.4 ± 1.2
≥ 1 b -jet ($p_T > 20\text{GeV}$)	56.6 ± 1.1
≥ 6 jets ($p_T > 25\text{GeV}$)	27.7 ± 0.7
$E_T^{\text{miss}} > 250\text{GeV}$	12.5 ± 0.5
$E_T^{\text{miss}} > 0.2 \times m_{\text{eff}}$	9.5 ± 0.4

Table A.10: Number of signal events at different stages of the Rpc2L1bH signal region selection. Only statistical uncertainties are shown.

Rpc3LSS1b, $\tilde{t}_1 \tilde{t}_1^*$ production, $\tilde{t}_1 \rightarrow t \tilde{\chi}_2^0 \rightarrow \tilde{t} W^\pm \tilde{\chi}_1^\mp$	
$m_{\tilde{t}_1} = 700\text{GeV}$, $m_{\tilde{\chi}_2^0} = 525\text{GeV}$, $m_{\tilde{\chi}_1^\pm} \approx m_{\tilde{\chi}_1^0} = 425\text{GeV}$	
MC events generated	5000
Expected for 36.1 fb^{-1}	2.4×10^3
≥ 3 SS leptons ($p_T > 20, 20, 10 \text{ GeV}$), $Z \rightarrow e^\pm e^\pm$ veto	4.6 ± 0.5
Trigger	4.5 ± 0.5
≥ 1 b -jet ($p_T > 20\text{GeV}$)	3.6 ± 0.4

Table A.11: Number of signal events at different stages of the Rpc3LSS1b signal region selection. Only statistical uncertainties are shown.

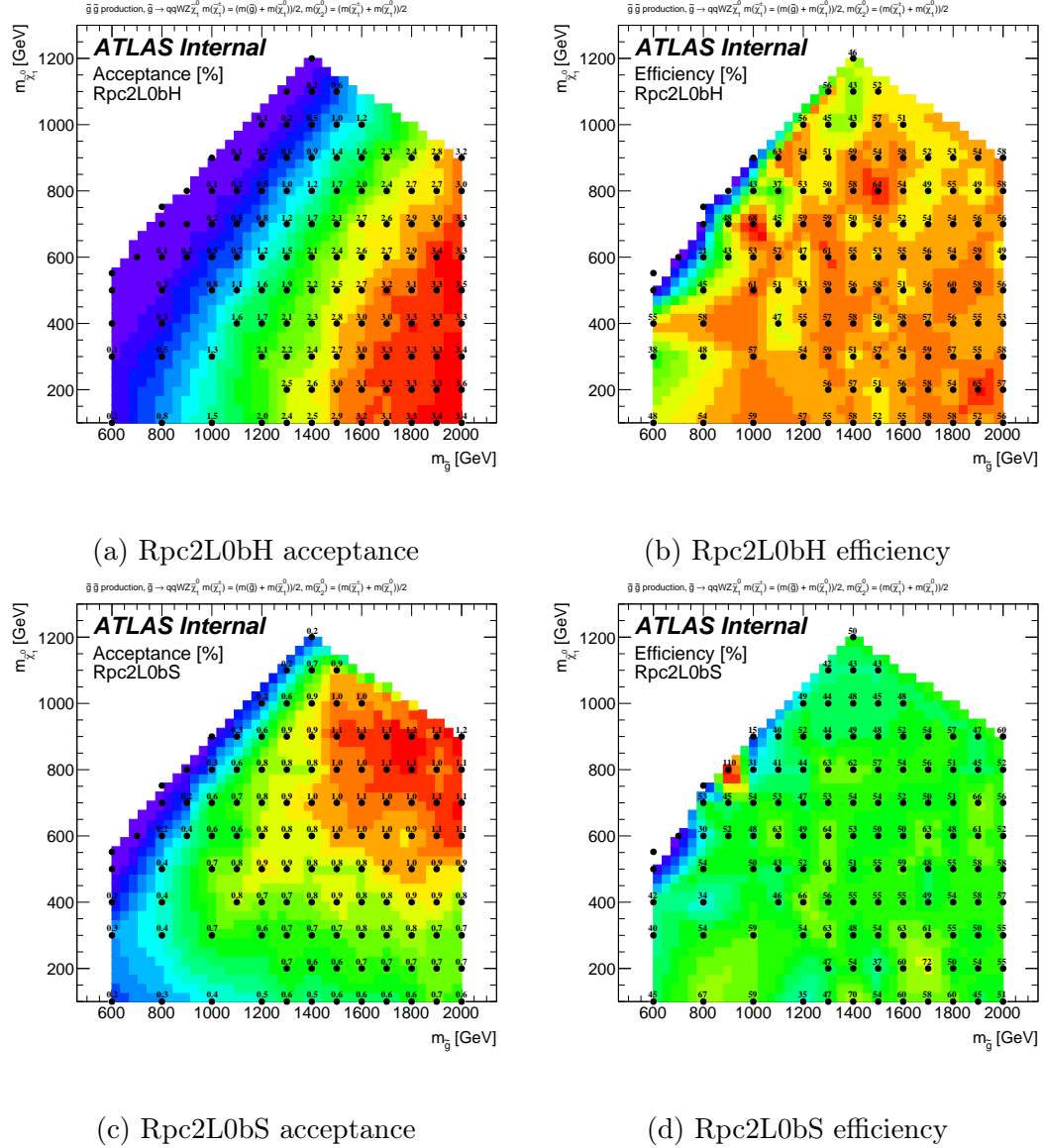


Figure A.3: Signal acceptance (a,c) and reconstruction efficiency (b,d) for simplified models of $\tilde{g}\tilde{g}$ production with $\tilde{g} \rightarrow q\bar{q}'WZ\tilde{\chi}_1^0$ decays, in the signal regions Rpc2L0bH (a,b) and Rpc2L0bS (c,d).

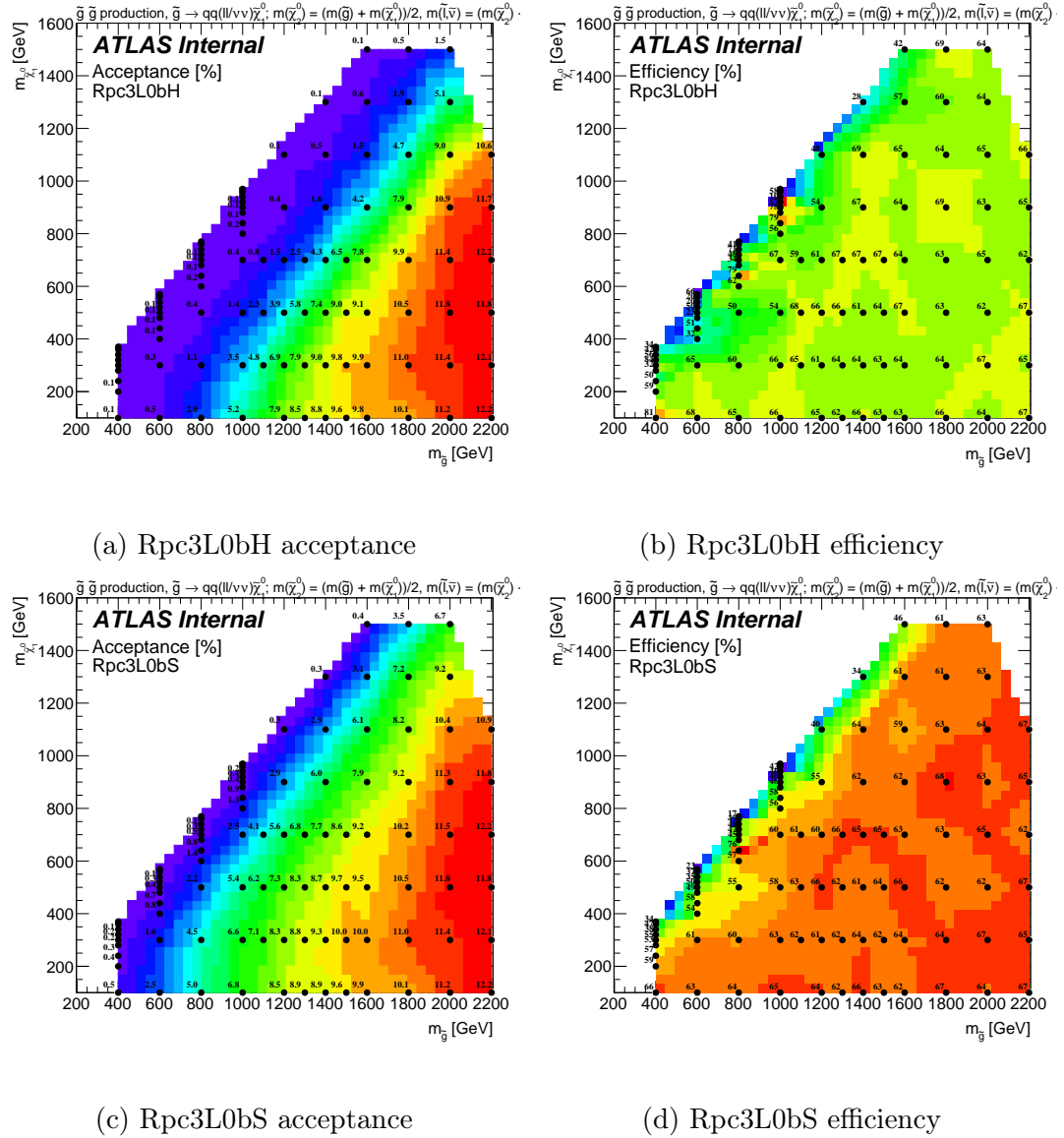


Figure A.4: Signal acceptance (a,c) and reconstruction efficiency (b,d) for simplified models of $\tilde{g}\tilde{g}$ production with $\tilde{g} \rightarrow q\bar{q}(\ell\ell/\nu\nu)\tilde{\chi}_1^0$ decays, in the signal regions Rpc3L0bH (a,b) and Rpc3L0bS (c,d).

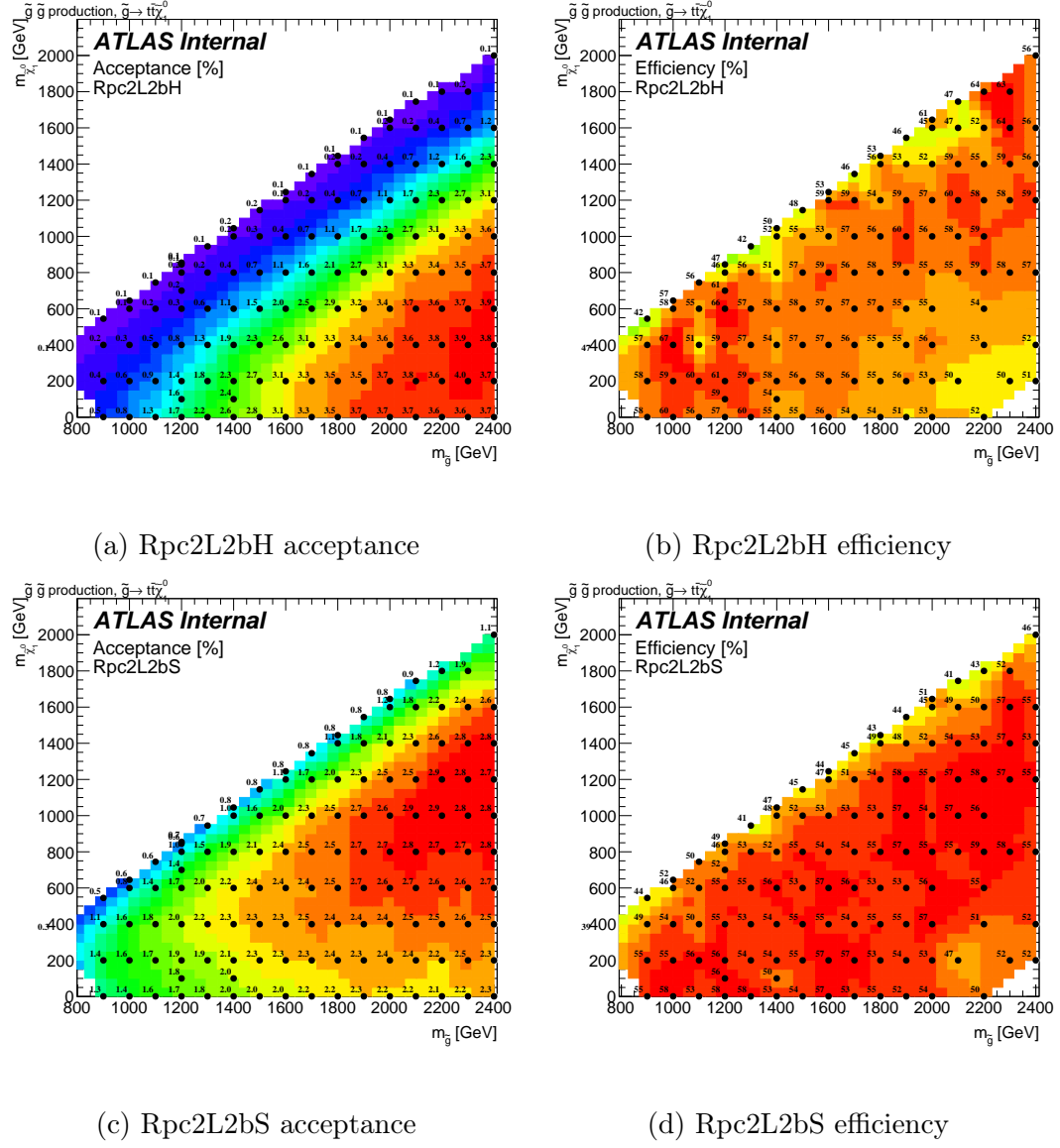


Figure A.5: Signal acceptance (a,c) and reconstruction efficiency (b,d) for simplified models of $\tilde{g}\tilde{g}$ production with $\tilde{g} \rightarrow t\bar{t}\tilde{\chi}_1^0$ decays, in the signal regions Rpc2L2bH (a,b) and Rpc2L2bS (c,d).

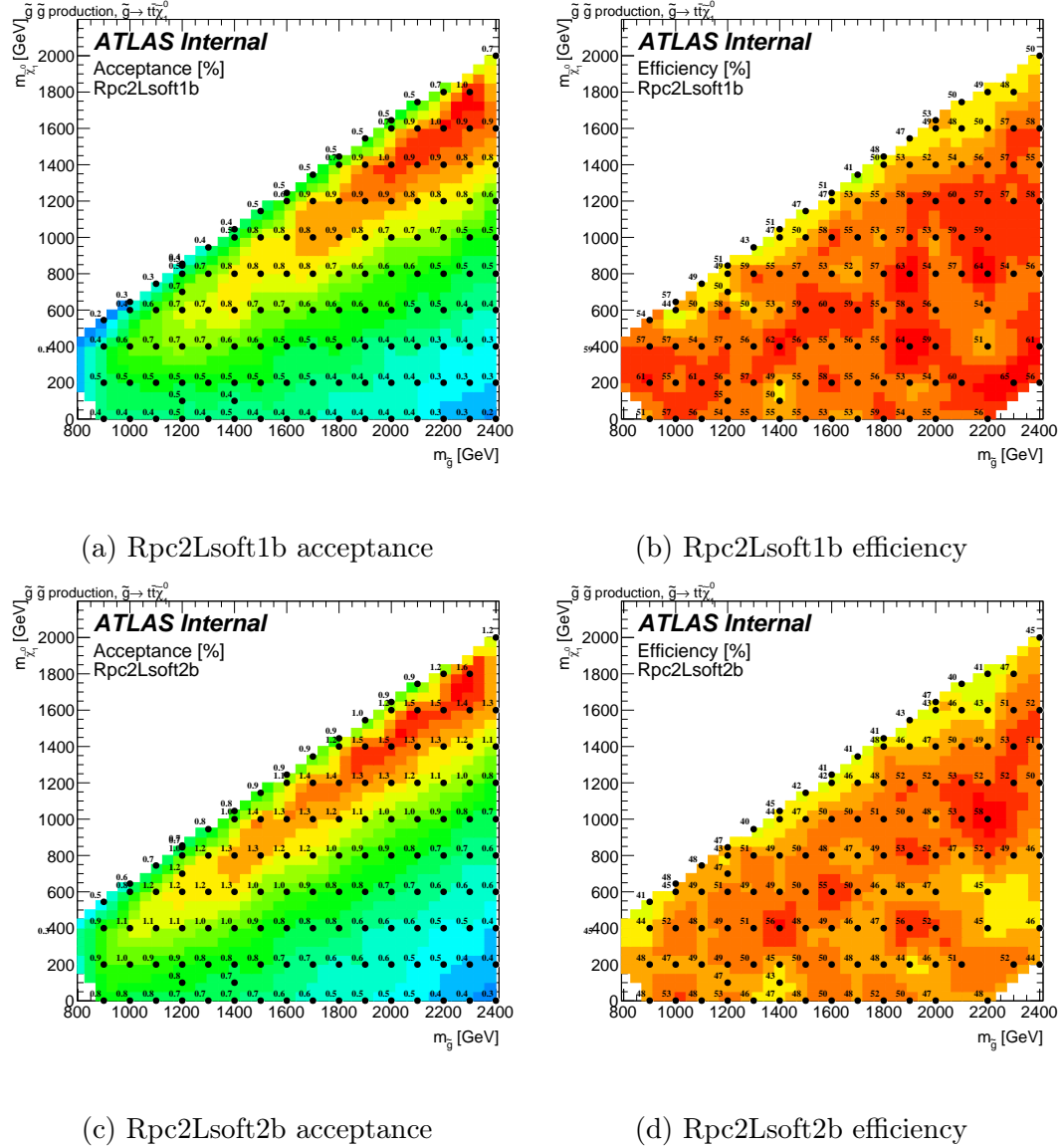


Figure A.6: Signal acceptance (a,c) and reconstruction efficiency (b,d) for simplified models of $\tilde{g}\tilde{g}$ production with $\tilde{g} \rightarrow t\bar{t}\tilde{\chi}_1^0$ decays, in the signal regions Rpc2Lsoft1b (a,b) and Rpc2Lsoft2b (c,d).

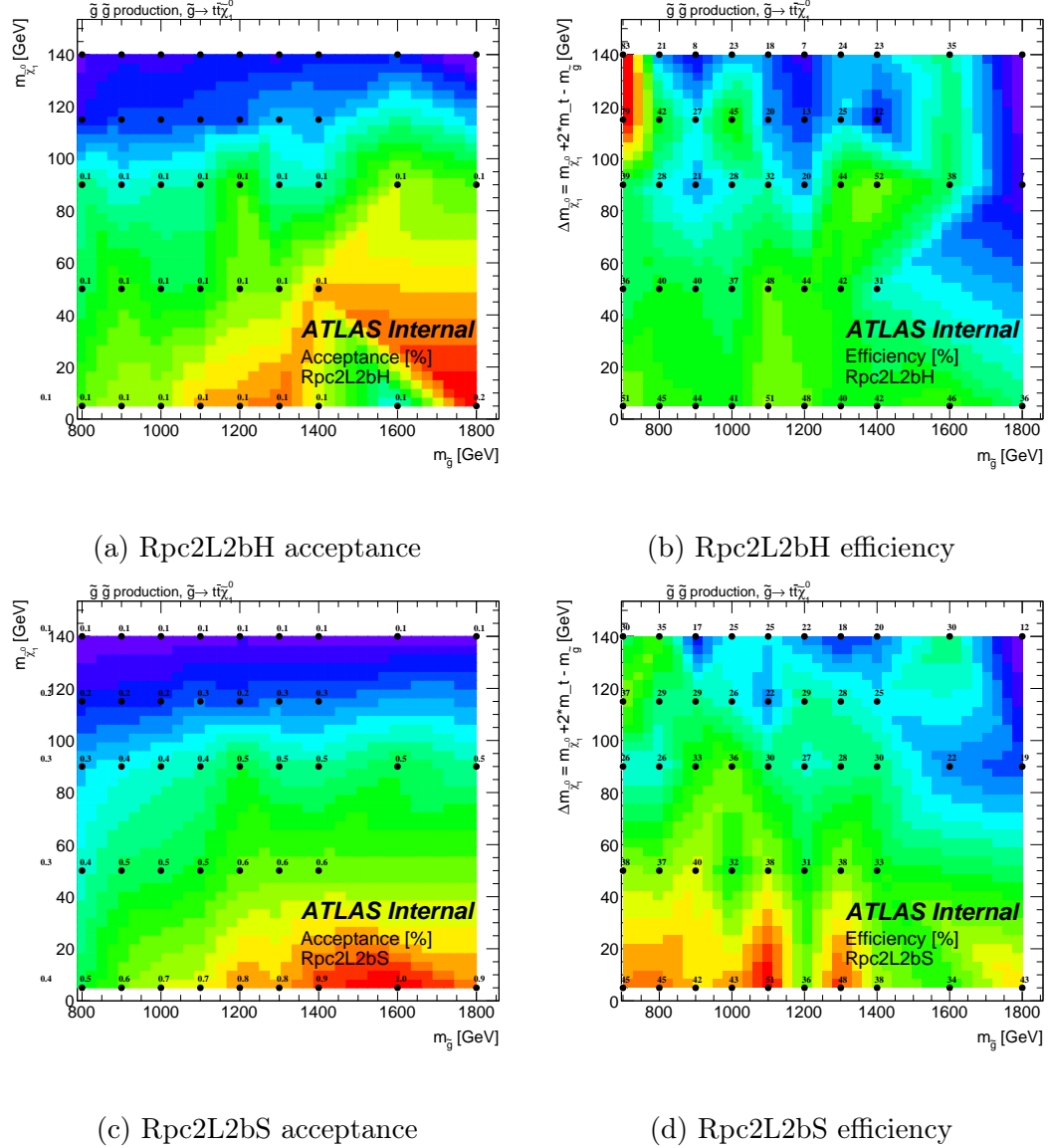


Figure A.7: Signal acceptance (a,c) and reconstruction efficiency (b,d) for simplified models of $\tilde{g}\tilde{g}$ production with $\tilde{g} \rightarrow tWb\tilde{\chi}_1^0$ decays (region with $\Delta m(\tilde{g}, \tilde{\chi}_1^0) < 2m_t$), in the signal regions Rpc2L2bH (a,b) and Rpc2L2bS (c,d).

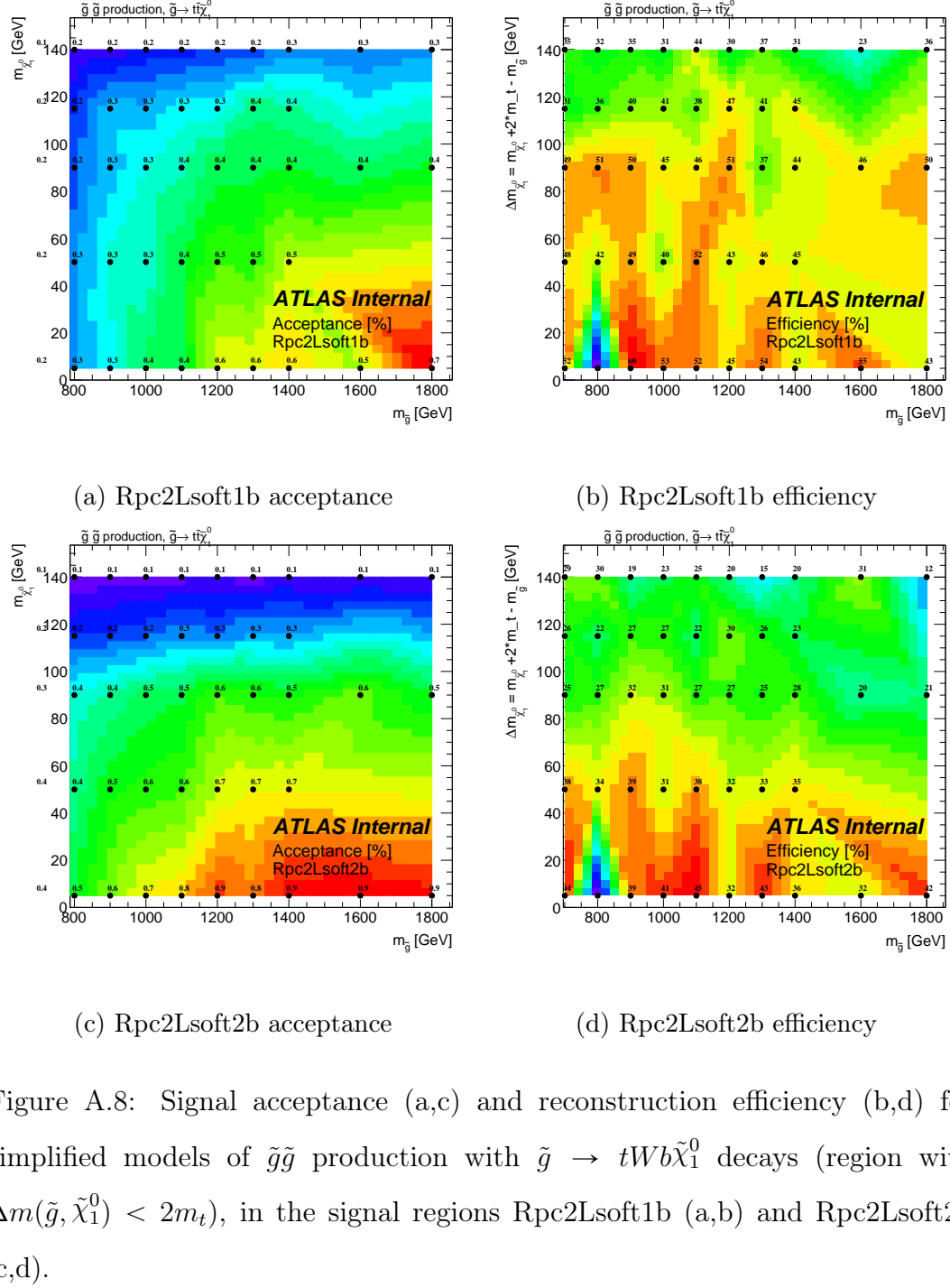


Figure A.8: Signal acceptance (a,c) and reconstruction efficiency (b,d) for simplified models of $\tilde{g}\tilde{g}$ production with $\tilde{g} \rightarrow tWb\tilde{\chi}_1^0$ decays (region with $\Delta m(\tilde{g}, \tilde{\chi}_1^0) < 2m_t$), in the signal regions Rpc2Lsoft1b (a,b) and Rpc2Lsoft2b (c,d).

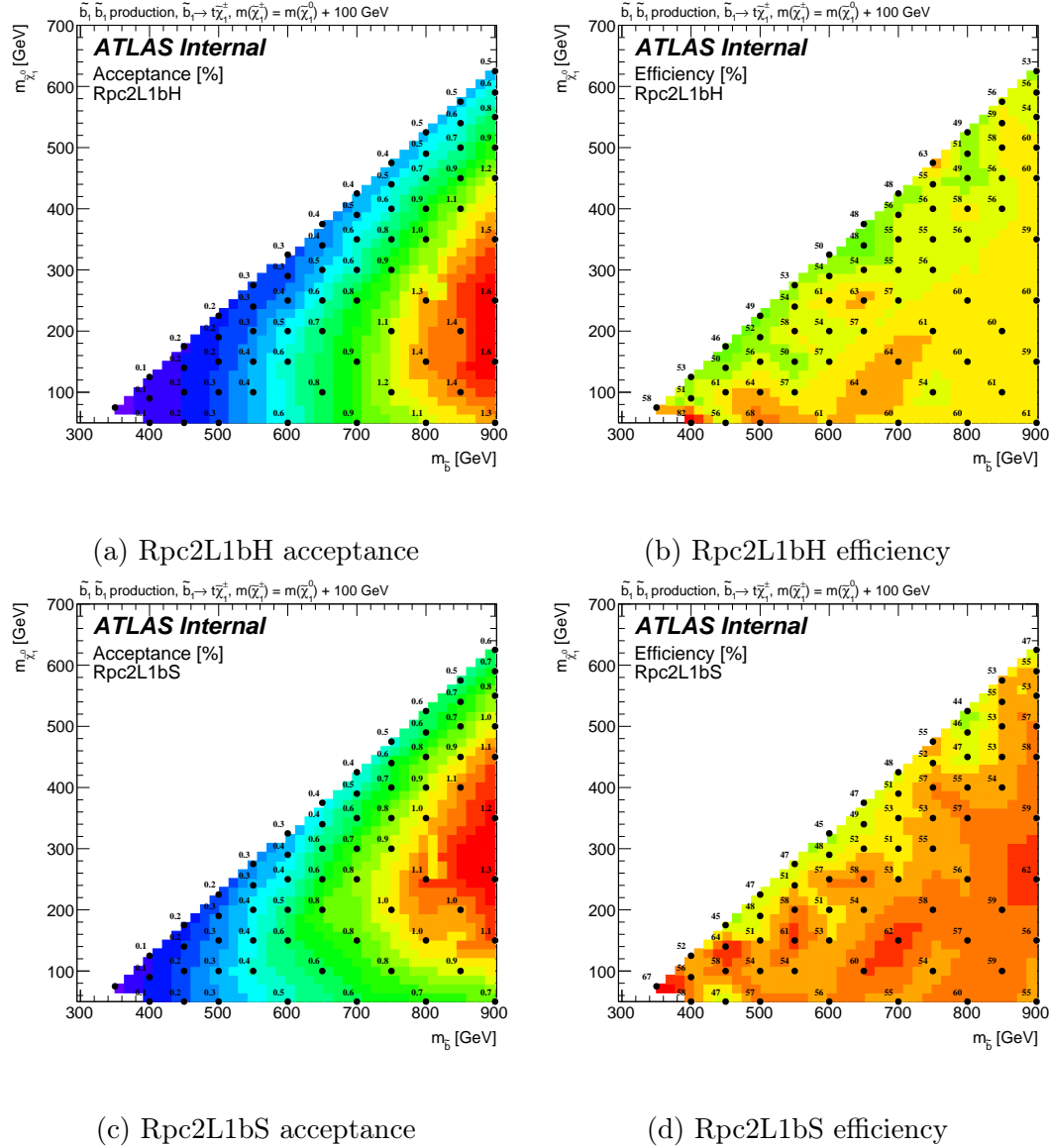


Figure A.9: Signal acceptance (a,c) and reconstruction efficiency (b,d) for simplified models of $\tilde{b}_1 \tilde{b}_1^*$ production with $\tilde{b}_1 \rightarrow tW^- \tilde{\chi}_1^0$ decays, in the signal regions Rpc2L1bH (a,b) and Rpc2L1bS (c,d).

Rpc2L2bH, $\tilde{g}\tilde{g}$ production in the NUHM2 model							
$m_{\tilde{g}}$ [GeV]	300	350	400	500	600	700	800
Acceptance	0.8%	1.6%	2.1%	3.2%	3.5%	4.4%	4.0%
Efficiency	43%	49%	50%	49%	48%	43%	49%

Table A.12: Rpc2L2bH signal region acceptance and reconstruction efficiency for $\tilde{g}\tilde{g}$ production in the NUHM2 model.

Rpc3LSS1b, $\tilde{t}_1\tilde{t}_1^*$ production, $\tilde{t}_1 \rightarrow t\tilde{\chi}_2^0$, $\tilde{\chi}_2^0 \rightarrow W^\mp\tilde{\chi}_1^\pm$						
$m_{\tilde{t}_1}$ [GeV]	550	600	650	700	750	800
Acceptance	0.3%	0.3%	0.3%	0.4%	0.4%	0.4%
Efficiency	36%	42%	44%	37%	33%	30%

Table A.13: Rpc3LSS1b signal region acceptance and reconstruction efficiency for $\tilde{t}_1\tilde{t}_1^*$ production with $\tilde{t}_1 \rightarrow t\tilde{\chi}_2^0$ ($\tilde{\chi}_2^0 \rightarrow W\tilde{\chi}_1^\pm$) decays.

3252 References

- 3253 [1] CDF Collaboration Collaboration, F. Abe et al., *Phys. Rev. Lett.* **74** (1995)
 3254 2626–2631,
 3255 <https://link.aps.org/doi/10.1103/PhysRevLett.74.2626>.
- 3256 [2] D0 Collaboration, S. Abachi et al., *Phys. Rev. Lett.* **74** (1995) 2632–2637,
 3257 [arXiv:hep-ex/9503003](https://arxiv.org/abs/hep-ex/9503003) [hep-ex].
- 3258 [3] ATLAS Collaboration, G. Aad et al., *Phys. Lett.* **B716** (2012) 1–29,
 3259 [arXiv:1207.7214](https://arxiv.org/abs/1207.7214) [hep-ex].
- 3260 [4] CMS Collaboration, S. Chatrchyan et al., *Phys. Lett.* **B716** (2012) 30–61,
 3261 [arXiv:1207.7235](https://arxiv.org/abs/1207.7235) [hep-ex].
- 3262 [5] F. Zwicky, *Helvetica Physica Acta* **6** (1933) 110–127.
- 3263 [6] W. Hu and S. Dodelson, *Ann. Rev. Astron. Astrophys.* **40** (2002) 171–216,
 3264 [arXiv:astro-ph/0110414](https://arxiv.org/abs/astro-ph/0110414) [astro-ph].
- 3265 [7] A. Challinor and H. Peiris, [arXiv:0903.5158](https://arxiv.org/abs/0903.5158) [astro-ph.CO].
- 3266 [8] G. Bertone, D. Hooper, and J. Silk, *Phys. Rept.* **405** (2005) 279–390,
 3267 [arXiv:hep-ph/0404175](https://arxiv.org/abs/hep-ph/0404175) [hep-ph].
- 3268 [9] Supernova Cosmology Project Collaboration, S. Perlmutter et al.,
 3269 *Astrophys. J.* **517** (1999) 565–586, [arXiv:astro-ph/9812133](https://arxiv.org/abs/astro-ph/9812133)
 3270 [astro-ph].
- 3271 [10] Planck Collaboration, R. Adam et al., *Astron. Astrophys.* **594** (2016) A1,
 3272 [arXiv:1502.01582](https://arxiv.org/abs/1502.01582) [astro-ph.CO].
- 3273 [11] Planck Collaboration, P. A. R. Ade et al., *Astron. Astrophys.* **594** (2016)
 3274 A13, [arXiv:1502.01589](https://arxiv.org/abs/1502.01589) [astro-ph.CO].
- 3275 [12] SDSS Collaboration, R. Scranton et al., [arXiv:astro-ph/0307335](https://arxiv.org/abs/astro-ph/0307335)
 3276 [astro-ph].
- 3277 [13] R. Brandelik et al., *Physics Letters B* **86** (1979) 243–249, <http://www.sciencedirect.com/science/article/pii/037026937990830X>.
- 3279 [14] ATLAS Collaboration, G. Aad et al., *Phys. Lett.* **B716** (2012) 1–29,
 3280 [arXiv:1207.7214](https://arxiv.org/abs/1207.7214) [hep-ex].
- 3281 [15] CMS Collaboration, S. Chatrchyan et al., *Phys. Lett.* **B716** (2012) 30–61,
 3282 [arXiv:1207.7235](https://arxiv.org/abs/1207.7235) [hep-ex].
- 3283 [16] Planck Collaboration, P. A. R. Ade et al., *Astron. Astrophys.* **571** (2014)
 3284 A16, [arXiv:1303.5076](https://arxiv.org/abs/1303.5076) [astro-ph.CO].

- 3285 [17] L. Canetti, M. Drewes, and M. Shaposhnikov, *New J. Phys.* **14** (2012)
 3286 095012, [arXiv:1204.4186 \[hep-ph\]](https://arxiv.org/abs/1204.4186).
- 3287 [18] Muon g-2 Collaboration Collaboration, G. W. Bennett et al., *Phys. Rev. D*
 3288 **73** (2006) 072003,
 3289 <https://link.aps.org/doi/10.1103/PhysRevD.73.072003>.
- 3290 [19] K. Hagiwara, R. Liao, A. D. Martin, D. Nomura, and T. Teubner, *J. Phys.*
 3291 **G38** (2011) 085003, [arXiv:1105.3149 \[hep-ph\]](https://arxiv.org/abs/1105.3149).
- 3292 [20] Particle Data Group Collaboration, K. A. Olive et al., *Chin. Phys.* **C38**
 3293 (2014) 090001.
- 3294 [21] H. Baer, V. Barger, and M. Savoy, *Phys. Scripta* **90** (2015) 068003,
 3295 [arXiv:1502.04127 \[hep-ph\]](https://arxiv.org/abs/1502.04127).
- 3296 [22] K. J. Bae, H. Baer, V. Barger, M. R. Savoy, and H. Serce, *Symmetry* **7**
 3297 (2015) 788–814, [arXiv:1503.04137 \[hep-ph\]](https://arxiv.org/abs/1503.04137).
- 3298 [23] S. R. Coleman and J. Mandula, *Phys. Rev.* **159** (1967) 1251–1256.
- 3299 [24] R. Haag, J. T. Lopuszanski, and M. Sohnius, *Nucl. Phys.* **B88** (1975) 257.
- 3300 [25] D. J. H. Chung, L. L. Everett, G. L. Kane, S. F. King, J. D. Lykken, and
 3301 L.-T. Wang, *Phys. Rept.* **407** (2005) 1–203, [arXiv:hep-ph/0312378](https://arxiv.org/abs/hep-ph/0312378)
 3302 [hep-ph].
- 3303 [26] R. Barbier et al., *Phys. Rept.* **420** (2005) 1–202, [arXiv:hep-ph/0406039](https://arxiv.org/abs/hep-ph/0406039)
 3304 [hep-ph].
- 3305 [27] H. Baer and T. Xerxes.
- 3306 [28] S. P. Martin, [arXiv:hep-ph/9709356](https://arxiv.org/abs/hep-ph/9709356), [Adv. Ser. Direct. High Energy
 3307 Phys.18,1(1998)].
- 3308 [29] J. Ellis, PoS **PLANCK2015** (2015) 041, [arXiv:1510.06204 \[hep-ph\]](https://arxiv.org/abs/1510.06204).
- 3309 [30] UA1 Collaboration, G. Arnison et al., *Phys. Lett.* **139B** (1984) 115.
- 3310 [31] UA2 Collaboration, P. Bagnaia et al., *Phys. Lett.* **B129** (1983) 130–140.
- 3311 [32] C. De Melis, <https://cds.cern.ch/record/2197559>, General Photo.
- 3312 [33] N. Garelli, *J. Phys.: Conf. Ser.* 513 (2014) 012007.
- 3313 [34] A. Negri, *J. Phys. Conf. Ser.* **396** (2012) 012033,
 3314 <http://stacks.iop.org/1742-6596/396/i=1/a=012033>.
- 3315 [35] ATLAS Collaboration, ATLAS-TDR-12, 1998.
- 3316 [36] ATLAS Collaboration, [CERN/LHCC/2003-022](https://cds.cern.ch/record/2003-022), CERN Geneva 2003.

- 3317 [37] A. Borga et al., PoS(TIPP2014)205, 2014.
- 3318 [38] A. Collaboration, *Technical Design Report for the Phase-I Upgrade of the*
 3319 *ATLAS TDAQ System*, Tech. Rep. CERN-LHCC-2013-018, Sep, 2013.
 3320 <https://cds.cern.ch/record/1602235>.
- 3321 [39] W. P. Vazquez et al., Nuclear and Particle Physics Proceedings **273 - 275**
 3322 (2016) 939 – 944, <http://www.sciencedirect.com/science/article/pii/S2405601415006355>.
- 3323 [40] A. Negri et al., Journal of Physics: Conference Series **396** (2012) 012033,
 3324 <http://stacks.iop.org/1742-6596/396/i=1/a=012033>.
- 3325 [41] *Luminosity Public Results in Run 2*, <https://twiki.cern.ch/twiki/bin/view/AtlasPublic/LuminosityPublicResultsRun2>. Accessed:
 3326 2016-08-01.
- 3327 [42] J. Alwall, R. Frederix, S. Frixione, V. Hirschi, F. Maltoni, O. Mattelaer,
 3328 H. S. Shao, T. Stelzer, P. Torrielli, and M. Zaro, **JHEP 07 (2014) 079**,
 3329 [arXiv:1405.0301 \[hep-ph\]](arXiv:1405.0301).
- 3330 [43] T. Sjöstrand, S. Mrenna, and P. Skands, **Comput. Phys. Commun. 178**
 3331 (2008) 852–867, [arXiv:0710.3820 \[hep-ph\]](arXiv:0710.3820).
- 3332 [44] GEANT4 Collaboration, S. Agostinelli et al., **Nucl. Instrum. Meth. A 506**
 3333 (2003) 250–303.
- 3334 [45] ATLAS Collaboration, ATL-PHYS-PUB-2010-013,
 3335 <http://cds.cern.ch/record/1300517>.
- 3336 [46] ATLAS Collaboration, ATLAS-CONF-2016-024, 2016,
 3337 <https://cds.cern.ch/record/2157687>.
- 3338 [47] M. Cacciari, G. P. Salam, and G. Soyez, **JHEP 0804 (2008) 063**,
 3339 [arXiv:0802.1189 \[hep-ph\]](arXiv:0802.1189).
- 3340 [48] ATLAS Collaboration, [arXiv:1603.02934 \[hep-ex\]](arXiv:1603.02934).
- 3341 [49] ATLAS Collaboration, G. Aad et al., [arXiv:1603.02934 \[hep-ex\]](arXiv:1603.02934).
- 3342 [50] ATLAS Collaboration, ATL-PHYS-PUB-2015-034, 2015,
 3343 <https://cds.cern.ch/record/2042098>.
- 3344 [51] ATLAS Collaboration, ATLAS Collaboration, **JINST 11 (2016) P04008**,
 3345 [arXiv:1512.01094 \[hep-ex\]](arXiv:1512.01094).
- 3346 [52] ATLAS Collaboration, ATL-PHYS-PUB-2015-022, 2015,
 3347 <https://cds.cern.ch/record/2037697>.
- 3348 [53] R. Blair et al., 2008 **JINST 3 P04001**.
- 3349

- 3351 [54] R. Blair et al., ATL-DQ-TR-0020, 2012.
- 3352 [55] CERN, <http://www.cerntech.hu/products/15-tilar-express.html>,
3353 October 15, 2015.
- 3354 [56] H. Engel and U. Kebschull, 2013 JINST 8 C12016.
- 3355 [57] A. Borga et al., 2015 JINST 10 C02022.
- 3356 [58] ATLAS Collaboration, JHEP **10** (2015) 054, [arXiv:1507.05525](https://arxiv.org/abs/1507.05525)
3357 [hep-ex].
- 3358 [59] ATLAS Collaboration, Eur. Phys. J. C **75** (2015) 510, [arXiv:1506.08616](https://arxiv.org/abs/1506.08616)
3359 [hep-ex].
- 3360 [60] ATLAS Collaboration, Atlas-conf-2015-066,
3361 <https://cds.cern.ch/record/2114833>.
- 3362 [61] P. Huang, A. Ismail, I. Low, and C. E. M. Wagner, Phys. Rev. D **92** (2015)
3363 075035, [arXiv:1507.01601](https://arxiv.org/abs/1507.01601) [hep-ph].
- 3364 [62] ATLAS Collaboration, Phys. Rev. **D88** (2013).
- 3365 [63] H. Baer, V. Barger, P. Huang, D. Mickelson, A. Mustafayev,
3366 W. Sreethawong, and X. Tata, JHEP **12** (2013) 013, [arXiv:1310.4858](https://arxiv.org/abs/1310.4858)
3367 [hep-ph], [Erratum: JHEP06,053(2015)].
- 3368 [64] H. Baer, V. Barger, P. Huang, D. Mickelson, A. Mustafayev,
3369 W. Sreethawong, and X. Tata, Phys. Rev. Lett. **110** (2013) 151801,
3370 [arXiv:1302.5816](https://arxiv.org/abs/1302.5816) [hep-ph].
- 3371 [65] H. Baer, V. Barger, M. Savoy, and X. Tata, Phys. Rev. **D94** (2016) 035025,
3372 [arXiv:1604.07438](https://arxiv.org/abs/1604.07438) [hep-ph].
- 3373 [66] ATLAS Collaboration, ATLAS Collaboration, Eur. Phys. J. C **76** (2016)
3374 653, [arXiv:1608.03953](https://arxiv.org/abs/1608.03953) [hep-ex].
- 3375 [67] D. J. Lange, Nucl. Instrum. Meth. A **462** (2001) 152.
- 3376 [68] R. D. Ball et al., Nucl. Phys. B **867** (2013) 244–289, [arXiv:1207.1303](https://arxiv.org/abs/1207.1303)
3377 [hep-ph].
- 3378 [69] ATLAS Collaboration, Atl-phys-pub-2014-021,
3379 <https://cds.cern.ch/record/1966419>.
- 3380 [70] LHC Higgs Cross Section Working Group Collaboration, D. de Florian
3381 et al., [arXiv:1610.07922](https://arxiv.org/abs/1610.07922) [hep-ph].
- 3382 [71] T. Gleisberg et al., JHEP **02** (2009) 007, [arXiv:0811.4622](https://arxiv.org/abs/0811.4622) [hep-ph].

- 3383 [72] ATLAS Collaboration, Atl-phys-pub-2016-002,
 3384 <http://cds.cern.ch/record/2119986>.
- 3385 [73] H.-L. Lai et al., *Phys. Rev. D* **82** (2010) 074024, [arXiv:1007.2241](https://arxiv.org/abs/1007.2241)
 3386 [[hep-ph](#)].
- 3387 [74] LHC Higgs Cross Section Working Group Collaboration, LHC Higgs Cross
 3388 Section Working Group, [arXiv:1201.3084](https://arxiv.org/abs/1201.3084) [[hep-ph](#)].
- 3389 [75] ATLAS Collaboration, *JHEP* **2014** (2014) 55, [arXiv:1406.3660](https://arxiv.org/abs/1406.3660)
 3390 [[hep-ex](#)].
- 3391 [76] M. Czakon and A. Mitov, *Comput. Phys. Commun.* **185** (2014) 2930,
 3392 [arXiv:1112.5675](https://arxiv.org/abs/1112.5675) [[hep-ph](#)].
- 3393 [77] P. Skands, *Phys. Rev. D* **82** (2010) 074018, [arXiv:1005.3457](https://arxiv.org/abs/1005.3457) [[hep-ph](#)].
- 3394 [78] ATLAS Collaboration, G. Aad et al., *Eur.Phys.J.* **C70** (2010) 823–874,
 3395 [arXiv:1005.4568](https://arxiv.org/abs/1005.4568) [[physics.ins-det](#)].
- 3396 [79] A. Sherstnev and R. Thorne, *Eur. Phys. J. C* **55** (2008) 553–575,
 3397 [arXiv:0711.2473](https://arxiv.org/abs/0711.2473) [[hep-ph](#)].
- 3398 [80] ATLAS Collaboration, Atl-phys-pub-2016-005,
 3399 <http://cds.cern.ch/record/2120826>.
- 3400 [81] G. Corcella et al., *JHEP* **01** (2001) 010, [arXiv:hep-ph/0011363](https://arxiv.org/abs/hep-ph/0011363).
- 3401 [82] J. Pumplin et al., *JHEP* **07** (2002) 012, [arXiv:hep-ph/0201195](https://arxiv.org/abs/hep-ph/0201195).
- 3402 [83] J. Alwall, M. Herquet, F. Maltoni, O. Mattelaer, and T. Stelzer, *JHEP* **06**
 3403 (2011) 128, [arXiv:1106.0522](https://arxiv.org/abs/1106.0522) [[hep-ph](#)].
- 3404 [84] LHC SUSY Cross Section Working Group, 2015, <https://twiki.cern.ch/twiki/bin/view/LHCPhysics/SUSYCrossSections>.
- 3405
- 3406 [85] S. Carrazza, S. Forte, and J. Rojo, *Parton distributions and event*
 3407 *generators*, pp. , 89–96. 2013. [arXiv:1311.5887](https://arxiv.org/abs/1311.5887) [[hep-ph](#)].
- 3408 [86] L. Lönnblad and S. Prestel, *JHEP* **03** (2012) 019, [arXiv:1109.4829](https://arxiv.org/abs/1109.4829)
 3409 [[hep-ph](#)].
- 3410 [87] C. Borschensky et al., *Eur. Phys. J. C* **74** (2014) 3174, [arXiv:1407.5066](https://arxiv.org/abs/1407.5066)
 3411 [[hep-ph](#)].
- 3412 [88] ATLAS Collaboration, ATL-PHYS-PUB-2015-026, 2015,
 3413 <https://cds.cern.ch/record/2037717>.
- 3414 [89] M. Cacciari and G. P. Salam, *Phys. Lett. B* **659** (2008) 119–126,
 3415 [arXiv:0707.1378](https://arxiv.org/abs/0707.1378) [[hep-ph](#)].

- 3416 [90] ATLAS Collaboration, ATLAS Collaboration, [arXiv:1703.09665](https://arxiv.org/abs/1703.09665)
 3417 [[hep-ex](#)].
- 3418 [91] ATLAS Collaboration, Atlas-conf-2014-018,
 3419 <https://cds.cern.ch/record/1700870>.
- 3420 [92] ATLAS Collaboration, ATL-PHYS-PUB-2016-012, 2016,
 3421 <https://cds.cern.ch/record/2160731>.
- 3422 [93] ATLAS Collaboration, ATLAS Collaboration, *Eur. Phys. J. C* **76** (2016)
 3423 292, [arXiv:1603.05598](https://arxiv.org/abs/1603.05598) [[hep-ex](#)].
- 3424 [94] ATLAS Collaboration, *Eur. Phys. J. C* **76** (2016) 666, [arXiv:1606.01813](https://arxiv.org/abs/1606.01813)
 3425 [[hep-ex](#)].
- 3426 [95] ATLAS Collaboration, ATL-PHYS-PUB-2015-027, 2015,
 3427 <https://cds.cern.ch/record/2037904>.
- 3428 [96] ATLAS Collaboration, ATL-PHYS-PUB-2015-023, 2015,
 3429 <https://cds.cern.ch/record/2037700>.
- 3430 [97] R. D. Cousins, K. E. Hymes, and J. Tucker, *Nucl.Instrum.Meth.Phys.Res.*
 3431 **A612** (2010) 388–398, [arXiv:0905.3831](https://arxiv.org/abs/0905.3831) [[physics.data-an](#)].
- 3432 [98] ATLAS Collaboration, ATLAS-CONF-2017-021, 2017,
 3433 <https://cds.cern.ch/record/2258143>.
- 3434 [99] ATLAS Collaboration, Atlas-conf-2016-037,
 3435 <http://cds.cern.ch/record/2205745>.
- 3436 [100] ATLAS Collaboration, Atlas-conf-2014-032,
 3437 <https://cds.cern.ch/record/1706245>.
- 3438 [101] G. Cowan, K. Cranmer, E. Gross, and O. Vitells, *Eur. Phys. J. C* **71** (2011)
 3439 1554, [arXiv:1007.1727](https://arxiv.org/abs/1007.1727) [[physics.data-an](#)], [Erratum: *Eur. Phys.*
 3440 *J.C73,2501(2013)*].
- 3441 [102] A. L. Read, *Journal of Physics G: Nuclear and Particle Physics* **28** (2002)
 3442 2693, <http://stacks.iop.org/0954-3899/28/i=10/a=313>.
- 3443 [103] F. James.
- 3444 [104] L. Moneta, K. Belasco, K. S. Cranmer, S. Kreiss, A. Lazzaro, D. Piparo,
 3445 G. Schott, W. Verkerke, and M. Wolf, PoS **ACAT2010** (2010) 057,
 3446 [arXiv:1009.1003](https://arxiv.org/abs/1009.1003) [[physics.data-an](#)].
- 3447 [105] I. Antcheva et al., *Comput. Phys. Commun.* **180** (2009) 2499–2512,
 3448 [arXiv:1508.07749](https://arxiv.org/abs/1508.07749) [[physics.data-an](#)].

- 3449 [106] J. Neyman and E. S. Pearson, *Philosophical Transactions of the Royal
3450 Society of London A: Mathematical, Physical and Engineering Sciences* **231**
3451 (1933) 289–337,
3452 <http://rsta.royalsocietypublishing.org/content/231/694-706/289.full.pdf>,
3453 <http://rsta.royalsocietypublishing.org/content/231/694-706/289>.
- 3455 [107] S. S. Wilks, *Annals Math. Statist.* **9** (1938) 60–62.
- 3456 [108] A. Wald, *Transactions of the American Mathematical Society* **54** (1943)
3457 426–482, <http://www.jstor.org/stable/1990256>.
- 3458 [109] I. Asimov, *Franchise*. Creative Education, 1 ed., May, 1989.
- 3459 [110] M. Baak et al., *Eur. Phys. J. C* **75** (2015) 153, [arXiv:1410.1280](https://arxiv.org/abs/1410.1280)
3460 [[hep-ex](#)].
- 3461 [111] K. Cranmer, G. Lewis, L. Moneta, A. Shibata, and W. Verkerke,
3462 Cern-open-2012-016, <http://cds.cern.ch/record/1456844>.
- 3463 [112] W. Verkerke and D. P. Kirkby, *eConf* **C0303241** (2003) MOLT007,
3464 [arXiv:physics/0306116](https://arxiv.org/abs/physics/0306116) [[physics](#)], [,186(2003)].
- 3465 [113] A. L. Read, *J. Phys. G* **28** (2002) 2693–2704.
- 3466 [114] J. Ellis, T. Falk, K. A. Olive, and Y. Santoso, *Nucl. Phys. B* **652** (2003)
3467 259–347, [arXiv:hep-ph/0210205](https://arxiv.org/abs/hep-ph/0210205).
- 3468 [115] J. Ellis, K. A. Olive, and Y. Santoso, *Phys. Lett. B* **539** (2002) 107–118,
3469 [arXiv:hep-ph/0204192](https://arxiv.org/abs/hep-ph/0204192).
- 3470 [116] ATLAS Collaboration, ATLAS Collaboration, *Eur. Phys. J. C* **76** (2016)
3471 259, [arXiv:1602.09058](https://arxiv.org/abs/1602.09058) [[hep-ex](#)].
- 3472 [117] ATLAS Collaboration, ATLAS Collaboration, *Phys. Lett. B* **757** (2016)
3473 334–355, [arXiv:1602.06194](https://arxiv.org/abs/1602.06194) [[hep-ex](#)].